Squeezing the Quantum Noise of LIGO below the Standard Quantum Limit

by

Wenxuan Jia

B.S., University of Southern California (2019)

Submitted to the Department of Physics
in partial fulfillment of the requirements for the degree of

Doctor of Philosophy in Physics

at the

MASSACHUSETTS INSTITUTE OF TECHNOLOGY

September 2024

© Wenxuan Jia 2024. All rights reserved.

The author hereby grants to MIT a nonexclusive, worldwide, irrevocable, royalty-free license to exercise any and all rights under copyright, including to reproduce, preserve, distribute and publicly display copies of the thesis, or release the thesis under an open-access license.

Author . . . . . .
Department of Physics
August 16, 2024

Certified by . . . . . .
Matthew Evans
Professor of Physics
Thesis Supervisor

Accepted by . . . . . .
Lindley Winslow
Associate Department Head of Physics

Squeezing the Quantum Noise of LIGO below the Standard Quantum Limit

by

Wenxuan Jia

Submitted to the Department of Physics
on August 16, 2024, in partial fulfillment of the
requirements for the degree of
Doctor of Philosophy in Physics

Abstract

The year 2015 marked the first detection of a gravitational wave signal from a pair of black holes located 410 megaparsecs (1.3 billion light-years) away. Their merger unleashed an immense amount of energy, with the peak emission rate surpassing the combined power of all luminous stars in the observable universe. Unlike stars, the merger of two black holes does not emit electromagnetic radiation like visible light but instead illuminates the universe with gravitational radiation. These waves traveled freely for over a billion years before being captured by the twin Laser Interferometer Gravitational-Wave Observatory (LIGO) detectors. Upon reaching Earth, these waves caused a minuscule length change between the LIGO mirrors, on the order of 10^{-18} m, a thousand times smaller than a proton.

The unprecedented sensitivity of LIGO requires an extremely low noise level. The design of LIGO as an interferometer converts the gravitational-wave signal to an optical signal, which is measured on photodiodes along with other noises. One of the noise sources is the quantum noise due to the quantum vacuum fluctuations of the light itself. Besides the light, the mirror also has quantum-mechanical features and experiences quantum back-actions when we probe it with light. Knowing the position of the mirror very well would inevitably perturb its momentum, which prevents us from precisely making the next measurement of the position. This is fundamental physics dictated by Heisenberg's uncertainty principle. In the case of continuous measurement like LIGO, the quantum back-action leads to an apparent sensitivity limit known as the Standard Quantum Limit (SQL). It tells us how precisely we can measure an object with light.

The SQL applies when using uncorrelated photons or coherent light to measure the object, such as a laser beam. However, introducing quantum correlations through squeezed light, a technique called squeezing (Chapter 2), can circumvent this limit. Squeezed vacuum, a non-classical light state, exploits quantum correlations between photon pairs to reduce vacuum fluctuations in one

quadrature at the cost of another. By manipulating the quantum correlation between light and the mirror, the squeezed vacuum can potentially reduce quantum noise below the SQL, a concept explored in frequency-dependent squeezing. This thesis develops a first-principle model of quantum noise in LIGO (Chapter 3) and investigates how squeezing can mitigate it while considering practical factors like optical losses and mode-mismatch (Chapter 4). These theories are constructed with a bottom-up approach. Experimental details on generating and utilizing frequency-dependent squeezing for LIGO are also discussed (Chapter 5), culminating in the observation of LIGO's quantum noise below the SQL (Chapter 6).

Besides squeezing, increasing optical power can also reduce quantum shot noise. Nevertheless, maintaining high power levels (fractions of megawatts) in LIGO is challenging due to experimental imperfections, such as unintended point absorbers on the mirror coating. This thesis analyzes the thermoelastic distortions caused by these absorbers, which limit achievable optical power in current and future gravitational-wave detectors (Chapter 7).

Thesis Supervisor: Matthew Evans
Title: Professor of Physics

Acknowledgments

The past five years of my PhD have been among the most challenging of my life. Amidst the pandemic and worsening domestic/international political situations, academia felt like an escape from reality. The support of these incredible people I met during my journey has been instrumental in completing all my work, including this thesis.

I am very fortunate to be one of Matt's students. His kindness and approachability always make me feel safe and comfortable to ask for help. Matt is more than a mentor who knows everything about LIGO; he is a true friend. I'm also deeply grateful for the guidance from Lisa, Nergis, and Peter. Lisa brought so much energy to me every time I ran out of gas, and it had always been inspiring to me whenever I talk with Nergis. I'm thankful for working with Slawek and Kevin, who taught me how to properly conduct an optical experiment and understand the complex LIGO system. Lee knows every detail about the squeezing system and loves to share them with me, pointing me in the right (sometimes not the easiest) direction. Myron and Marie are always there to help no matter how trivial my request sounds like. Hiro from Caltech has been a wonderful mentor to me since the very first time I worked on LIGO as an undergraduate student. I still don't know how he can quickly respond to my email while it's 3 AM on the west coast. I also appreciate Vladan and Ronald for their time to serve as members my thesis committee and evaluate my thesis research.

Of the total five years, I spent two years in pandemic lockdown, a year and half at MIT, and a year and half at LIGO observatories in Louisiana and Washington. Therefore, I cherish the time spent with people at LIGO sites as much as at MIT, if not more so. I'm very lucky to have the chance to work with Masayuki and Adam on the experimental upgrade at LIGO Livingston Observatory. I have learned so much from Masayuki on how to do experiments at real gravitational-wave detectors; he is surely one of the most skilled experts in terms of commissioning an interferometer. I will never forget the late nights in the control room with Masayuki, Adam, Anamaria, and Valera. I'm deeply grateful for the awesome staff at Livingston, including but not limited to Vlad, Pricilla,

Joe B, Mike, Keith, Karla, Huyen, TJ, Stuart, Matt, Gary, Brian, Janeen, Ed, and Danny. Besides work, I've also enjoyed the happiest moments in grad life with Masayuki & Maki and other fellows visiting from all over the world: Terrence, Juliédson, Sushant, Abhinav, Aaron, Liu, Leigh, Will, and Sumeet. Those hot pot and mahjong nights really made me feel like home.

Although I've only spent two months at LIGO Hanford Observatory, I am very appreciative of the support from the squeezing team there to get me started. Camilla was always the happiest person in the control room and brought me to fun events in the small town. Naoki and Nutsinee certainly knew the Hanford squeezing system much more than I do and helped me find all the knobs and buttons. I'm grateful for the trust Jenne, Sheila, and Daniel placed in me to make significant changes as a new commissioner. The amazing fellows: Elenna, Ross, Tony, Dripta, and Sudarshan gave colors to my life while I was at Hanford.

I want to give a special shout-out to Vicky and Haocun, without whom I would not be able to finish the most important work of my PhD career. Vicky is the most energetic person I have seen. She is always ready to tackle on anything, from fixing the experiment to resolving hundreds of comments on the manuscript. Her enthusiasm deeply encourages me to keep up the hard work and achieve our goal. Haocun is a great exemplar and predecessor of the squeezing work I've done. Having someone who has already experienced the similar challenges to talk to is such a blessing. I'm extremely lucky to have her as a role model and life advisor.

It has been an honor and pleasure to work with such amazing colleagues and friends at MIT. Our lab is undoubtedly one of the most enjoyable places to work and thrive. I wish to extend my appreciation to the group members, including Evan, Georgia, Vivishek, Junxin, Kentaro, Nick, Chris, Ben, Dhruva, Eva, Eugene, and Sylvia, whom I knew before the pandemic in 2019, and Deep, Dorotea, Eleonora, Hudson, Jack, Jacques, Masaya, Matt, Malina, Noah, Nikhil, Regina, Sidd, Swadha, and Xinghui, whom I only get to know after "re-joining" the group in 2023. My friends in the physics department, namely Tianyu, Anjie, Beili, Changnan, and Yuanjie brightened my days while being a student. My other friends from Pandemonium, including Avi, Max, Lucas, Shang, and Yuchen, really made Thursday my favorite day of the week.

I must not forget supports from my best friends on the other side of the Earth. I can't really describe how much I miss them: Mingzhong, Jiuchang, Yiying, Shengsen, ... the list can go on and on for another few pages. Although I haven't been back home for more than five years, the spacetime difference won't distance us. I'm forever indebted to the unconditional love from my parents and my family members. It's unfortunate that my grandpa, Ruimin Jia, would not be able to physically witness the day of my graduation, but I can fully imagine all his proud expressions if he saw everything now.

Published Content and Contributions

[1] **W. Jia**, V. Xu, K. Kuns, M. Nakano, L. Barsotti, M. Evans, N. Mavalvala, *et al.*, Squeezing the quantum noise of a gravitational-wave detector below the standard quantum limit, *Science* (in press), 2024. [Chapter 6]

[2] E. Capote*, **W. Jia***, N. Aritomi*, M. Nakano*, V. Xu*, *et al.* (LIGO O4 Detector List), Sensitivity and performance of the Advanced LIGO detectors in the fourth observing run, (in prep), 2024. [Chapter 5]

(*These authors contributed equally to this work)

[3] D. Ganapathy*, **W. Jia***, M. Nakano*, V. Xu*, *et al.* (LIGO O4 Detector List), Broadband quantum enhancement of the LIGO detectors with frequency-dependent squeezing, *Physical Review X* **13**, 041021, 2023. [Chapter 4, Chapter 5]

(*These authors contributed equally to this work)

[4] D. Ganapathy, V. Xu, **W. Jia**, C. Whittle, M. Tse, L. Barsotti, M. Evans, and L. McCuller, Probing squeezing for gravitational-wave detectors with an audio-band field, *Physical Review D* **105** (12), 122005, 2022.

[5] **W. Jia**, H. Yamamoto, K. Kuns, A. Effler, and M. Evans, *et al.* (LIGO O3 Detector List), Point absorber limits to future gravitational-wave detectors, *Physical Review Letters* **127**, 241102, 2021 [Chapter 7]

Contents

List of Figures

List of Tables

1 INTRODUCTION

It was in 1915 that Albert Einstein completed his general theory of relativity, ten years after he published his theory of special relativity. The new theory revolutionized our understanding of gravity, which impacts us every single second. Apples fall to the ground because of the curved spacetime caused by the mass of the Earth. General relativity brings us GPS navigation, precision timekeeping, and, most interestingly, gravitational-wave astronomy. However, it took another 60 years for humans to verify the existence of gravitational waves [21], and 100 years to directly observe them with Laser Interferometer Gravitational-Wave Detectors (LIGO) [22]. To observe the infinitesimal gravitational wave signals that are a thousand times smaller than the size of a proton, LIGO must tremendously reduce its other noises. In this thesis, we focus on one of the dominant sources of noise in LIGO, quantum noise, and ways to reduce it to achieve better instrument sensitivity and detect gravitational waves from deeper regions of the universe. I'll provide a phenomenological overview of my thesis in the introductory chapter before delving into more formal details in the following chapters.

1.1 Nature of Gravitational Waves

In Einstein's worldview, space and time are not separate entities. Instead, they form a 4-dimensional "spacetime" that treats 3-dimensional space and 1-dimensional time in equal footing.

The geometry of the spacetime tells objects how to move. Conversely, mass interacts with spacetime by telling it how to curve [23]. In a vacuum with no massive objects (an empty Universe), spacetime is flat as assumed in special relativity, and objects move in a straight line as expected from Newton's First Law. In a curved spacetime like those around the Earth, a mass falls freely to the Earth as if it's "attracted" by Earth's gravity. The stronger the mass, the more curved the spacetime is.

The 4-dimensional spacetime field has dynamics and follows wave equation analogous to the 3-dimensional electromagnetic fields. The vacuum allows for the propagation of gravitational waves at the speed of light, similar to the propagation of electromagnetic waves. Just like all accelerating charges emit electromagnetic waves, all accelerating masses emit gravitational waves; but only those from heavy bodies (several solar masses) with large accelerations (inspiral) have a large enough amplitude to be remotely detected. The primary example is the binary merger of compact objects. Consider a pair of black hole binary with mass m_1, m_2 in a circular orbit of distance a. The amplitude of gravitational wave (in units of strain) at a distance r away from the source is approximately

$$h \approx \frac{4G^2 m_1 m_2}{c^4 a}\frac{1}{r} = \frac{r_{S1} r_{S2}}{a}\frac{1}{r} \tag{1.1}$$

where $r_S = 2Gm/c^2$ is the Schwarzchild radius of the black hole, roughly 2.9 km for our Sun. For a pair of 30-solar mass black holes with a distance of 350 km away from each other and 400 Mpc away from Earth, the amplitude observed here is

$$h = \frac{(90\,\text{km})(90\,\text{km})}{350\,\text{km}}\frac{1}{(400)(3\times 10^{19}\,\text{km})} \approx 2\times 10^{-21} \tag{1.2}$$

which is an incredibly small number. When Einstein estimated the gravitational wave amplitude in 1916 [24, 25], he thought it was far too weak to be detectable. It indeed took a hundred years for the technology to develop until we made the first direct observation of gravitational waves [22].

1.2 Detecting Gravitational Waves with Advanced LIGO

When a gravitational wave sweeps across Earth, the spacetime we inhabit oscillates. This spacetime fabric dictates how particles move, including massless particles like photons. The travel time of a photon across a certain distance is determined by the local curvature of spacetime. Therefore, we can detect these perturbations in spacetime by measuring changes in the travel time of lasers. An interferometer is the perfect instrument for making such precise measurements.

A simple Michelson interferometer consists of two perpendicular arms with mirrors at the end. A beam splitter splits the light injected from one port into two beams and unites them back after two beams of light travel and reflect from the end mirror. As gravitational wave propagates through the interferometer with the perfect polarization, there will be a time difference between two beams of light traveling in their respective arm of the interferometer, which would be detected by measuring the phase difference, or the intensity fluctuation by interfering with the two beams re-united from the beam splitter. The time difference can be calibrated in the unit of gravitational-wave amplitude h, which is effectively the strain of the arm length, or the change of arm length ΔL divided by the length L itself.

LIGO is a complex interferometer designed to measure gravitational waves [26]. It essentially converts a gravitational wave signal to a laser intensity signal that can be measured on a photodiode. Accompanying the gravitational wave signal is the noise from other sources, one of the most dominant is the quantum noise.

Fig. 1-1 shows the total theoretical noise budget of the LIGO detector. The noise amplitude is in the unit of strain/$\sqrt{\text{Hz}}$, where the total root-mean-squared (RMS) strain noise of a time series is decomposed into frequency before taking the square root. The sensitivity of LIGO is limited by the quantum noise at both low frequencies (10–50 Hz) and high frequencies (>100 Hz), which contain important astrophysical information such as the inspiral signal of binary black hole mergers [22]. In general, our goal is to reduce the noise amplitude at all frequencies in the detection band (<6 kHz).

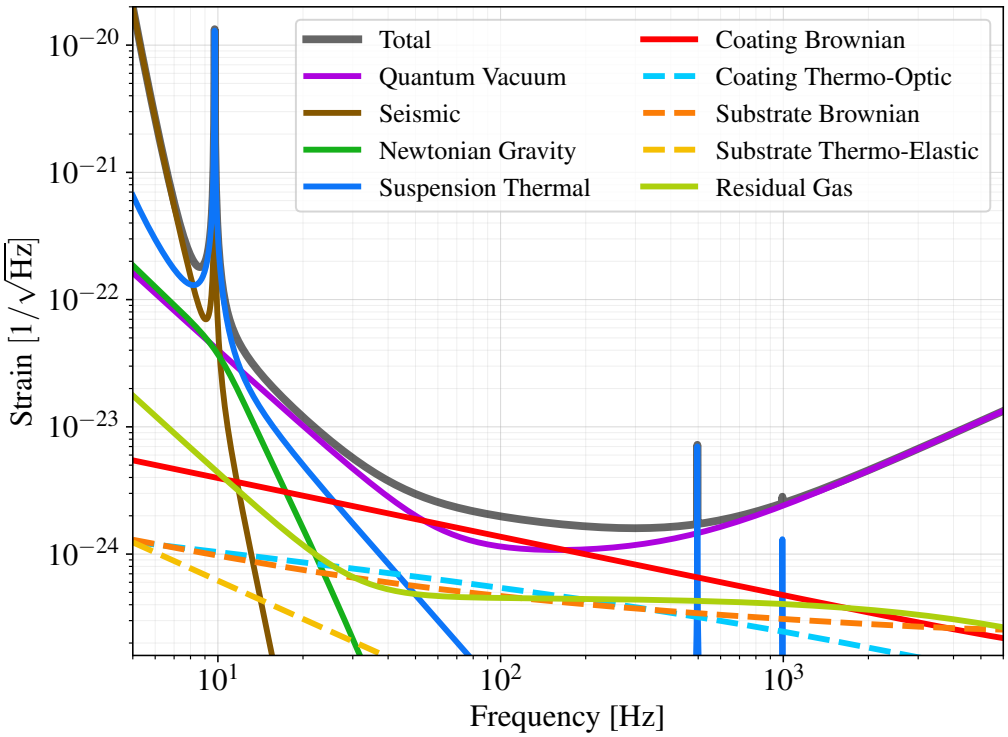

Figure 1-1: Noise budget of LIGO in the designed configuration known as "A+" [6].

1.3 Quantum Noise

Quantum noise is a fundamental noise due to the discrete nature of light. The photodiode sensor registers one photon at a time, giving the measured time series a fundamental shot noise limit. The discrete nature of photons leads to the counting of discrete independent events. Suppose the probability of counting one photon during time dt is adt, where a is the photon arrival rate. The probability of counting n photons in each measurement of duration τ is

$$\Pr(n) = \lim_{dt\to 0} \binom{\tau/dt}{n} (adt)^n (1-adt)^{\tau/dt-n} = \frac{(a\tau)^n e^{-a\tau}}{n!} \tag{1.3}$$

which is a Poisson process. The relative uncertainty of the ensemble average of $\langle n \rangle = a\tau$ counted photons is $1/\sqrt{\langle n \rangle}$. Therefore, the higher the laser power, the less the relative uncertainty or noise.

Alternatively, it is possible to reduce shot noise by squeezed states of light. The beam from a standard laser is unsqueezed, also known as the coherent state of light. The quantum noise can be depicted as extra fuzziness on the electromagnetic wave itself (Fig. 1-2).

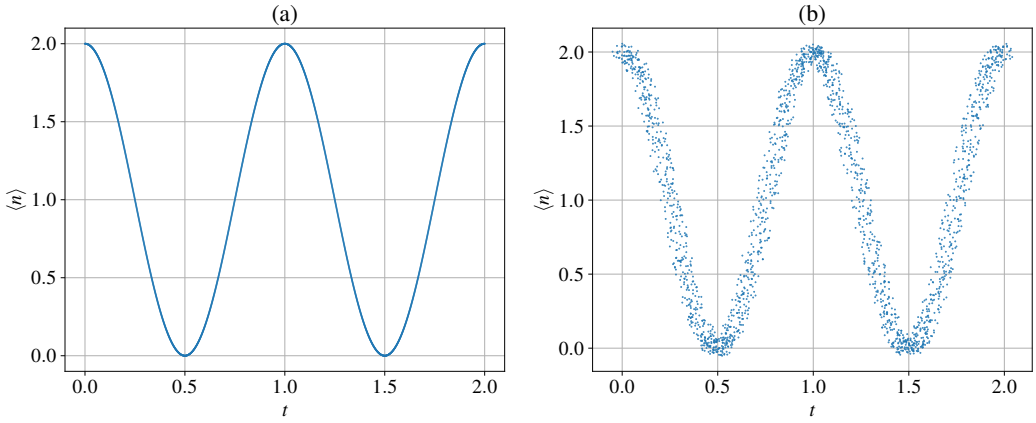

Figure 1-2: (a) An ideal electromagnetic wave without quantum noise versus (b) a realistic wave with quantum noise. Quantum noise is inherent to the light itself and can not be removed.

While we can't completely remove the quantum noise, we can re-distribute the noise in amplitude and phase quadratures. The unsqueezed light has a quantum noise that is evenly distributed in phase and amplitude, forming a round noise circle. The squeezed state of the light, however, could have the noise circle squeezed on one quadrature and anti-squeezed on the other side, making the total noise area unchanged without violating the Heisenberg uncertainty principle.

Since the measurement of the gravitational wave is a time measurement or a phase measurement, we reduce the quantum noise by squeezing the phase quadrature of the light. However, the amplitude quadrature would be anti-squeezed and become more noisy. The LIGO detector operates at very high optical power, so high that it converts some of the amplitude quadrature noise to phase quadrature noise at low frequencies (<100 Hz) by radiation pressure. Since the mirrors' force-to-displacement transfer function is frequency-dependent, it requires a frequency-dependent

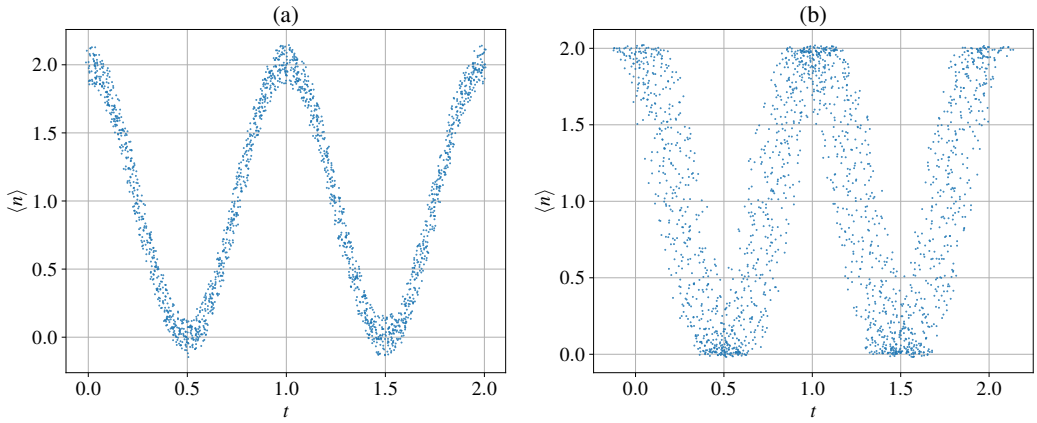

Figure 1-3: An electromagnetic wave with (a) phase squeezing and (b) amplitude squeezing. Phase-squeezed wave has less phase noise but more amplitude noise, and vice versa.

instrument to compensate.

Increment of optical power and injection of frequency-dependent squeezing are therefore two independent methods to reduce the quantum noise. Many experimental challenges need to be overcome to achieve the designed sensitivity and observe more exciting astrophysical events through the new window of gravitational waves. I will unfold these challenges in the following chapters.

2 SQUEEZED STATE OF LIGHT

Light was understood as classical waves until physicists revealed its quantum nature [27, 28]. The field of quantum optics was born to study the unique features and quantum-mechanical effects of light. Squeezed state of light is one type of quantum state of the light, which is useful for gravitational-wave detection. In this chapter, we discuss the quantum states of light in the language of quantum mechanics, including the squeezed states of light.

2.1 Coherent State

Before discussing the squeezed state, we have to introduce the coherent state. It was Erwin Schrödinger who first discovered the coherent state [29]. The coherent state is the state that resembles a classical counterpart the most [30]. It's also a minimum uncertainty state. The quantum state of the light emitted from a laser is best described as the coherent state. It is an eigenstate of annihilation operator a in quantum mechanics. Since

$$\partial_\alpha(e^{-\alpha a^\dagger} a e^{\alpha a^\dagger}) = [a, a^\dagger] = 1 \tag{2.1}$$

where a is the annihilation operator and $\alpha \in \mathbb{C}$. We have the eigenstate

$$a e^{\alpha a^\dagger}|0\rangle = \alpha e^{\alpha a^\dagger}|0\rangle \tag{2.2}$$

where $|0\rangle$ is the ground state of a quantum harmonic oscillator. The normalized coherent state is therefore

$$|\alpha\rangle = e^{-|\alpha|^2/2} e^{\alpha a^\dagger} |0\rangle = e^{-|\alpha|^2/2} \sum_n \frac{\alpha^n}{\sqrt{n!}} |n\rangle \tag{2.3}$$

This is a minimum uncertainty state with equal uncertainty in position and momentum $\Delta x \Delta p = 1/2$, the same as the vacuum state $|0\rangle$. The photon number statistic has

$$\langle N \rangle = \langle \alpha | a^\dagger a | \alpha \rangle = |\alpha|^2 \tag{2.4}$$

and the probability of finding n photon is

$$\Pr(n) = |\langle n|\alpha\rangle|^2 = e^{-|\alpha|^2} \frac{|\alpha|^{2n}}{n!} = \frac{\langle N \rangle^n e^{-\langle N \rangle}}{n!} \tag{2.5}$$

which is the Poisson distribution described in the introduction (Eq. (1.3)). Amazingly, both quantum mechanics and pure statistics have converged to the same statistical distribution.

Alternatively, we can create a unitary operator that acts on vacuum Eq. (2.3) to create a coherent state

$$D(\alpha) = e^{-|\alpha|^2/2} e^{\alpha a^\dagger} e^{-\alpha^* a} \tag{2.6}$$

There are no eigenstates for the displacement operator $D(\alpha)$, because it displaces any state on the phase space. The coherent states are not orthogonal

$$|\langle \alpha_1 | \alpha_2 \rangle|^2 = \exp\left(-|\alpha_1 - \alpha_2|^2\right) \neq 0 \tag{2.7}$$

but are complete

$$\int \frac{d^2\alpha}{\pi} |\alpha\rangle\langle\alpha| = 1 \tag{2.8}$$

2.2 Phase Space

In quantum mechanics, we define quadrature operator $X_1 = (a + a^\dagger)/2$ (real part, "position") and $X_2 = (a - a^\dagger)/2i$ (imaginary part, "momentum") and have the commutation relation

$$[X_1, X_2] = \frac{i}{2} \tag{2.9}$$

For a coherent state $|\alpha\rangle$, where α is a complex number

$$\alpha = |\alpha| e^{i\theta} \tag{2.10}$$

we get $\langle\alpha|X_1|\alpha\rangle = \Re(\alpha)$ and $\langle\alpha|X_2|\alpha\rangle = \Im(\alpha)$. The fluctuations are $\Delta X_1 = \Delta X_2 = 1/2$, independent of α. So the coherent state is like a circle on the complex plane, centered at $(X_1, X_2) = (\Re(\alpha), \Im(\alpha))$ with equal uncertainty of 1/2.

Alternatively, we can use "polar coordinate" to describe the state. The squared amplitude is obviously the number operator ($N = X_1^2 + X_2^2 = a^\dagger a + 1/2 \approx a^\dagger a$), so $\langle\alpha|N|\alpha\rangle = |\alpha|^2 + 1/2 \approx |\alpha|^2$ and $\Delta N^2 = |\alpha|^2$, followed from Poisson statistics.

The amplitude itself is $\sqrt{|\alpha|^2 + 1/2} \approx |\alpha|$. The phase operator is the Susskind–Glogower operator [31]

$$V = (aa^\dagger)^{-\frac{1}{2}} a = \sum_{n=0}^{\infty} |n\rangle\langle n+1| \tag{2.11}$$

with

$$VV^\dagger = 1 \qquad \text{and} \qquad V^\dagger V = 1 - |0\rangle\langle 0| \tag{2.12}$$

so it's not quite unitary. Its eigenstates are

$$V|\phi\rangle = e^{i\phi}|\phi\rangle \tag{2.13}$$

and we can construct $|\phi\rangle$ using number states

$$|\phi\rangle = \sum_{n=0}^{\infty} e^{in\phi}|n\rangle \tag{2.14}$$

Note these eigenstates are not normalizable nor are they orthogonal. But they are complete

$$\int_0^{2\pi} \frac{d\phi}{2\pi}|\phi\rangle\langle\phi| = \sum_{n,m} |n\rangle\langle m| \underbrace{\int_0^{2\pi} \frac{d\phi}{2\pi} e^{i(n-m)\phi}}_{\delta_{nm}} = 1 \tag{2.15}$$

so the probability $\Pr(\phi) = |\langle\psi|\phi\rangle|^2/2\pi$ sums up to 1. Technically, the completeness still holds if we pick any integration range of 2π difference

$$\int_{\delta-\pi}^{\delta+\pi} \frac{d\phi}{2\pi}|\phi\rangle\langle\phi| = 1 \tag{2.16}$$

For a coherent state, we have

$$\Pr(\phi) = \frac{1}{2\pi}|\langle\phi|\alpha\rangle|^2 = \frac{e^{-|\alpha|^2}}{2\pi}\left|\sum_{n=0}^{\infty}\frac{\alpha^n}{\sqrt{n!}}e^{-in\phi}\right|^2 = \frac{e^{-|\alpha|^2}}{2\pi}\sum_{n,m=0}^{\infty}\frac{|\alpha|^{n+m}}{\sqrt{n!m!}}\cos\left[(m-n)(\phi-\theta)\right] \tag{2.17}$$

The (i sin[...]) part is averaged out because it's anti-symmetric. The expectation value is

$$\langle\alpha|\phi|\alpha\rangle = \int_{\delta-\pi}^{\delta+\pi} d\phi \Pr(\phi)\phi = \theta + \int_{\delta-\pi}^{\delta+\pi} d\phi \Pr(\phi)(\phi-\theta) = \theta \tag{2.18}$$

where the even and odd functions of ϕ cancel each other. We've used the trick of translating the integration range even though it's not from $-\infty$ to ∞. The variance is

$$\Delta\phi^2 = \int_{\delta-\pi}^{\delta+\pi} d\phi \Pr(\phi)(\phi-\theta)^2 = \frac{e^{-|\alpha|^2}}{2\pi}\sum_{n,m=0}^{\infty}\frac{|\alpha|^{n+m}}{\sqrt{n!m!}}\left[\frac{2\pi^3}{3}\delta_{mn} + 4\pi\frac{(-1)^{n-m}}{(n-m)^2}(1-\delta_{mn})\right] \tag{2.19}$$

This result is exact but complicated. For very large $|\alpha| \gg 1$, we can make smart approximations on the probability density function

$$\begin{aligned}
\Pr(\phi, |\alpha| \gg 1) &= \frac{1}{2\pi} \left| \sum_{n=0}^{\infty} \left(\frac{(|\alpha|^2)^n e^{-|\alpha|^2}}{n!} \right)^{\frac{1}{2}} e^{-in\phi} \right|^2 \\
&\approx \frac{1}{2\pi} \left| \sum_{n=0}^{\infty} \left(\frac{1}{\sqrt{2\pi|\alpha|^2}} e^{-\frac{(n-|\alpha|)^2}{2|\alpha|^2}} \right)^{\frac{1}{2}} e^{in(\theta-\phi)} \right|^2 \\
&\approx \frac{1}{2\pi\sqrt{2\pi|\alpha|^2}} \left| \int_0^{\infty} dn e^{-\frac{(n-|\alpha|)^2}{4|\alpha|^2} - in(\theta-\phi)} \right|^2 \\
&= \sqrt{\frac{2|\alpha|^2}{\pi}} e^{-2|\alpha|^2(\phi-\theta)^2}
\end{aligned} \tag{2.20}$$

We've used the trick to approximate Poisson distribution with Gaussian distribution. The approximate variance can be directly read off $\Delta\phi \approx 1/(2|\alpha|)$, and the expectation is still θ.

For a number state $|n\rangle$, we have $\langle n|X_1|n\rangle = \langle n|X_2|n\rangle = 0$, but the variance is $\Delta X_1 = \Delta X_2 = \sqrt{2n+1}/2$. So the number state is located at the center of phase space. Its shape can be seen from polar coordinates. The amplitude has $\langle n|N|n\rangle = n$ and $\langle n|N^2|n\rangle = n^2$, so there's no fluctuation in the amplitude. Intuitively, there must be maximal fluctuations of phase. It's easy to show that the probability density is flat $\Pr(\phi) = 1/(2\pi)$ and $\Delta\phi = \pi/\sqrt{3}$.

The vacuum state $|0\rangle$ is has simply $\langle 0|X_1|0\rangle = \langle 0|X_2|0\rangle = 0$, $\Delta X_1 = \Delta X_2 = 1/2$. In polar coordinates, it has 1/2 amplitude with zero fluctuation and flat phase probability density $\Pr(\phi) = 1/(2\pi)$. This can be derived both from coherent states and number states.

Fig. 2-1 summarizes the distributions of quantum states in the phase space. The coherent state resembles the classical counterpart the most so it's the "most classical" quantum state, whereas the number state is the "least classical" quantum state. Squeezed state is somewhere in between, as we will show in the next section.

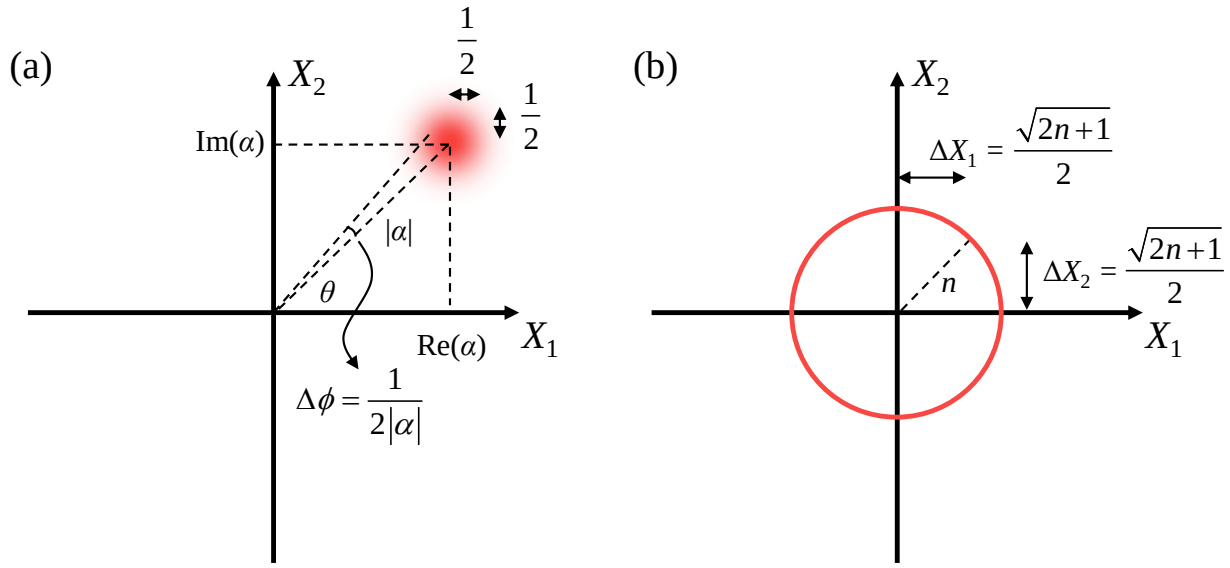

Figure 2-1: Phase space distribution of (a) a coherent state $|\alpha\rangle$ and (b) a number state $|n\rangle$. Note that the phase of the coherent state scales inversely with the amplitude $|\alpha|$, following the Heisenberg uncertainty principle. The phase is entirely random for the number state, which has zero uncertainty in amplitude.

2.3 Squeezed State

The squeeze operator is defined as [32]:

$$S(z) = e^{\frac{1}{2}(z^* a^2 - z(a^\dagger)^2)} \tag{2.21}$$

Compared with the displacement operator,

$$D(\alpha) = e^{\alpha a^\dagger - \alpha^* a} \tag{2.22}$$

both operators have a complex number as the parameter $\alpha = |\alpha|e^{i\theta}$, $z = |z|e^{i\varphi}$. As we will show, the squeeze operator will squeeze the vacuum fluctuation by a factor of $\exp(-|z|)$. The squeeze

operator is unitary obviously, but it doesn't have proper eigenstates. Sadly, the a^2, $(a^\dagger)^2$ on the exponential of $S(z)$ can't be separated because their commutations are not central up to any order. Some of the identities are listed here

$$S^\dagger(z) = S(-z) \tag{2.23}$$

$$S^\dagger(z) a S(z) = a \sum_{n=0}^{\infty} \frac{|z|^{2n}}{(2n)!} - a^\dagger \frac{z}{|z|} \sum_{n=0}^{\infty} \frac{|z|^{2n+1}}{(2n+1)!} = a \cosh|z| - a^\dagger e^{i\varphi} \sinh|z| \tag{2.24}$$

$$S(z) a S^\dagger(z) = a \sum_{n=0}^{\infty} \frac{|z|^{2n}}{(2n)!} + a^\dagger \frac{z}{|z|} \sum_{n=0}^{\infty} \frac{|z|^{2n+1}}{(2n+1)!} = a \cosh|z| + a^\dagger e^{i\varphi} \sinh|z| \tag{2.25}$$

$$S^\dagger(z) a^\dagger S(z) = a^\dagger \cosh|z| - a e^{-i\varphi} \sinh|z| \tag{2.26}$$

$$S(z) a^\dagger S^\dagger(z) = a^\dagger \cosh|z| + a e^{-i\varphi} \sinh|z| \tag{2.27}$$

Let's see what the squeeze operator does to the vacuum state $|0\rangle$ and coherent state $|\alpha\rangle$.

2.3.1 Squeezed vacuum state

Applying the squeeze operator to the vacuum state, we have

$$|z\rangle = S(z)|0\rangle \tag{2.28}$$

The quadrature operators X_1 and X_2 still have zero expectation, but their uncertainties change

$$\Delta X_1 = \sqrt{\frac{2\sinh^2|z| - 2\sinh|z|\cosh|z|\cos\varphi + 1}{4}} = \frac{1}{2}\sqrt{\sin^2\frac{\varphi}{2} e^{2|z|} + \cos^2\frac{\varphi}{2} e^{-2|z|}} \tag{2.29}$$

$$\Delta X_2 = \sqrt{\frac{2\sinh^2|z| + 2\sinh|z|\cosh|z|\cos\varphi + 1}{4}} = \frac{1}{2}\sqrt{\cos^2\frac{\varphi}{2} e^{2|z|} + \sin^2\frac{\varphi}{2} e^{-2|z|}} \tag{2.30}$$

So we can see that one of the quadratures is squeezed while the other one is anti-squeezed. The uncertainty principle still holds

$$\Delta X_1 \Delta X_2 = \frac{1}{4}\sqrt{1 + \frac{\cosh 4|z| - 1}{2}\sin^2\varphi} \geq \frac{1}{4} \tag{2.31}$$

The squeezed vacuum is at minimum uncertainty state only when it is squeezed along one of the quadratures ($\varphi = 0$ or π). The squeezed vacuum state can be represented as a squeezed ellipse in the phase space, as seen in Fig. 2-2.

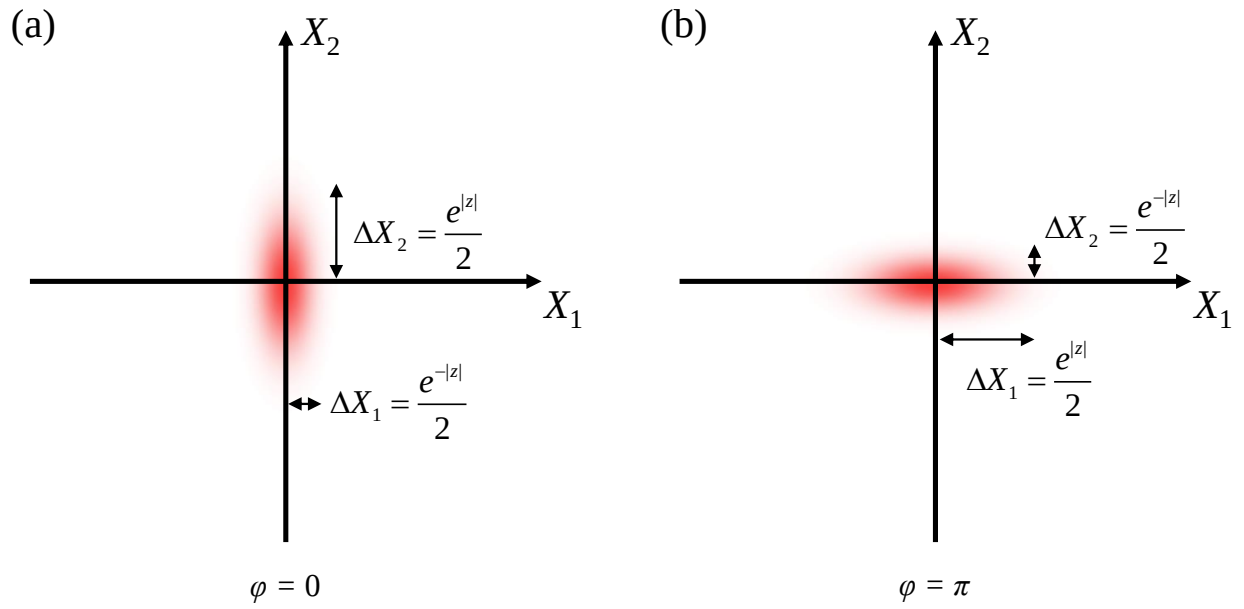

Figure 2-2: Phase space distribution of the squeezed vacuum state with (a) $\psi = 0$ and (b) $\psi = \pi$. The fluctuation of the squeezed quadrature can be reduced below the vacuum fluctuation by a factor of $e^{|z|}$. However, the other quadrature is anti-squeezed by the same factor allowed by Heisenberg uncertainty principle.

In polar coordinates, we have $\langle z|N|z\rangle = \sinh^2|z| + 1/2$ and $\Delta N = \sqrt{2}\,|\sinh|z|\cosh|z||$. They are phase-independent and always larger than pure vacuum for nonzero z. This implies that the squeezed vacuum state has a nonzero number of photons and can be measured on a photodiode.

To get the number statistics $\Pr(n)$, we need to decompose the squeezed vacuum state into number states.

$$|z\rangle = \sum_{n=0}^{\infty} \frac{(-e^{i\varphi}\tanh|z|)^n}{\sqrt{\cosh|z|}} \sqrt{(-1)^n \binom{-1/2}{n}} |2n\rangle \tag{2.32}$$

Only even number states exist in the squeezed vacuum state. The probability density is now

$$\Pr(2n) = \left| \frac{(-e^{i\varphi}\tanh|z|)^n}{\sqrt{\cosh|z|}} \frac{\sqrt{(2n)!}}{2^n n!} \right|^2 = \frac{\tanh^{2n}|z|}{\cosh|z|} \binom{-1/2}{n} \tag{2.33}$$

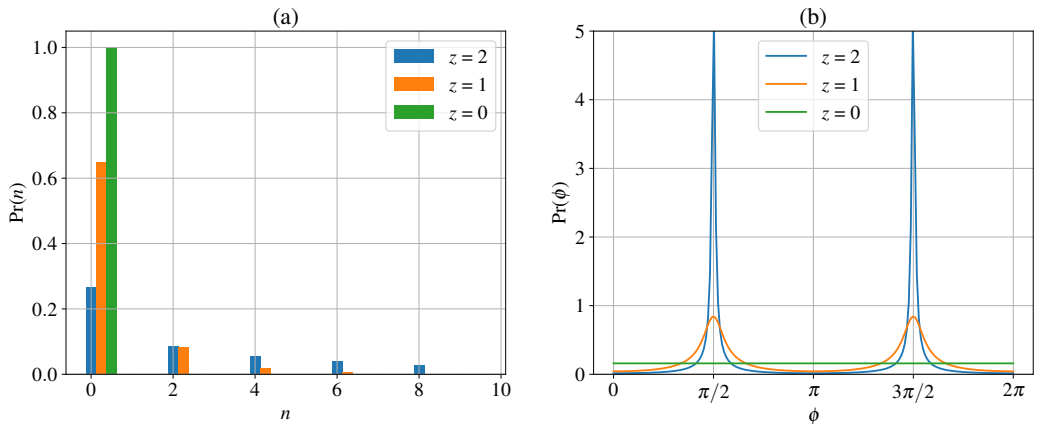

Figure 2-3: Probability density function of (a) the number operator ("amplitude") and (b) Susskind–Glogower operator ("phase") for the squeezed vacuum state $|z\rangle$. The complex number $z = |z|e^{i\varphi} = |z|$ in this case given $\varphi = 0$.

The phase probability density is

$$\begin{aligned}\Pr(\phi) &= \frac{1}{2\pi}\left|\sum_{n=0}^{\infty} e^{-i2n\phi}\frac{(-e^{i\varphi}\tanh|z|)^n}{\sqrt{\cosh|z|}}\frac{\sqrt{(2n)!}}{2^n n!}\right|^2 \\ &\approx \frac{1}{2\pi\cosh|z|}\left|1+\sum_{n=1}^{\infty}(-e^{i(\varphi-2\phi)}\tanh|z|)^n\frac{\sqrt{\sqrt{4\pi n}(2n/e)^{2n}}}{2^n\sqrt{2\pi n}(n/e)^n}\right|^2 \\ &= \frac{1}{2\pi\cosh|z|}\left|1+\frac{1}{\pi^{\frac{1}{4}}}\mathrm{Li}_{1/4}(-e^{i(\varphi-2\phi)}\tanh|z|)\right|^2\end{aligned} \tag{2.34}$$

where we used Stirling's approximation, and $\mathrm{Li}_{1/4}$ is the polylogarithm with order 1/4.

Fig. 2-3 shows the probability density function of the amplitude and phase operator. As the squeezing parameter $|z| \to \infty$, $\tanh|z| \to 1$, the amplitude probability spreads out and the phase probability becomes narrower. Note that the amplitude and phase here are just pictorial entities in the phase space and not referring to any of the actual fields.

2.3.2 Squeezed coherent state

Now that we know about the statistics of the squeezed vacuum state, let's squeeze the coherent state, namely the squeezed coherent state defined by

$$|\alpha, z\rangle = D(\alpha)S(z)|0\rangle \tag{2.35}$$

The squeezed coherent state still has the same centroid as the coherent state in the phase space. Their uncertainties equal to that of the squeezed vacuum state

$$\langle\alpha, z|\Delta X_1|\alpha, z\rangle = \langle z|\Delta X_1|z\rangle = \frac{1}{2}\sqrt{\sin^2\frac{\varphi}{2}e^{2|z|} + \cos^2\frac{\varphi}{2}e^{-2|z|}} \tag{2.36}$$

$$\langle \alpha, z|\Delta X_2|\alpha, z\rangle = \langle z|\Delta X_2|z\rangle = \frac{1}{2}\sqrt{\cos^2\frac{\varphi}{2}e^{2|z|} + \sin^2\frac{\varphi}{2}e^{-2|z|}} \tag{2.37}$$

If we squeeze the coherent state, for example, the light from a laser emitter, we can reduce its quantum fluctuation below the quantum vacuum, as seen in Fig. 2-4. Experimentally, we can't squeeze a coherent state, but we can displace a squeezed vacuum state. We will discuss more when we introduce input-output relations in Chapter 3.

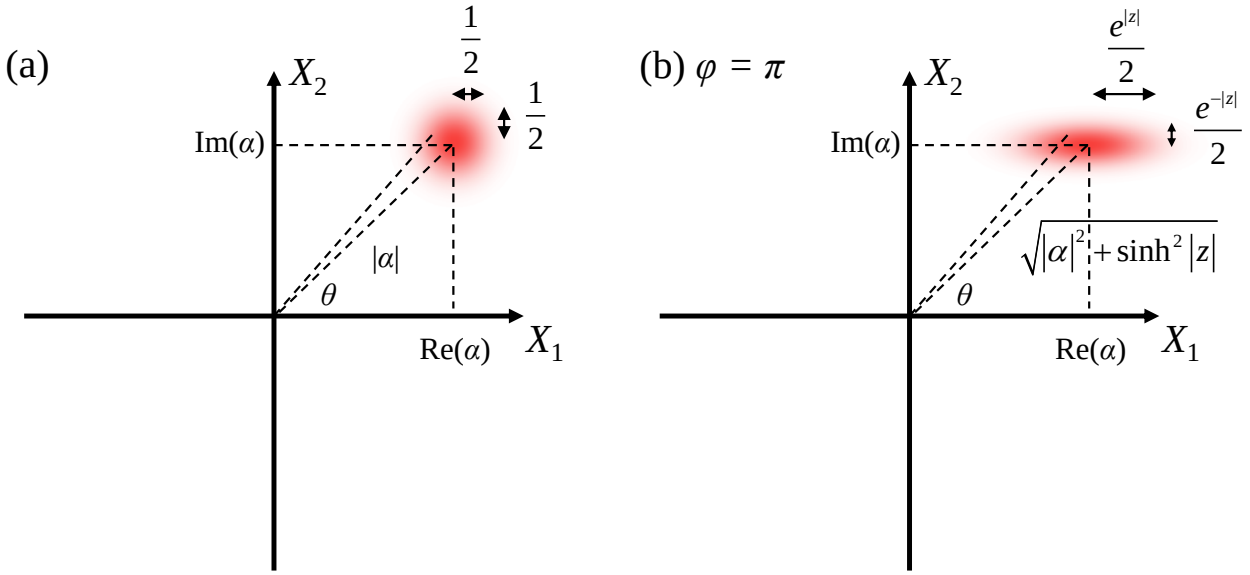

Figure 2-4: Phase space illustration of (a) the coherent state $|\alpha\rangle$ and (b) the squeezed coherent state $|\alpha, z\rangle$. The vacuum fluctuations of the squeezed coherent state are squeezed below vacuum fluctuations in one quadrature and anti-squeezed in the other. z has phase $\varphi = \pi$ to squeeze the X_2 quadrature.

In polar coordinates, we have

$$\langle \alpha, z|N|\alpha, z\rangle = |\alpha|^2 + \langle z|N|z\rangle = |\alpha|^2 + \sinh^2|z| + \frac{1}{2} \tag{2.38}$$

$$\langle \alpha, z|\Delta N^2|\alpha, z\rangle = \langle z|\Delta N^2|z\rangle + |\alpha|^2(2\sinh^2|z| - 2\sinh|z|\cosh|z|\cos(\varphi - 2\theta) + 1) \tag{2.39}$$

As $|\alpha| \to 0$, the fluctuation tends to squeezed vacuum state $\langle z|\Delta N^2|z\rangle = 2\sinh^2|z|\cosh^2|z|$. As

$|z| \to 0$, it tends to coherent state ($\langle\alpha|\Delta N^2|\alpha\rangle = |\alpha|^2$). So everything is consistent.

The squeezed coherent state can be decomposed to the number states:

$$|\alpha, z\rangle = \exp\left(-\frac{1}{2}|\alpha|^2 - \frac{1}{2}e^{i\varphi}\tanh|z|(\alpha^*)^2\right)\sum_{n=0}^{\infty}\sqrt{\frac{(e^{i\varphi}\tanh|z|)^n}{2^n n!\cosh|z|}}H_n\left(\frac{\alpha + e^{i\varphi}\tanh|z|\alpha^*}{\sqrt{2e^{i\varphi}\tanh|z|}}\right)|n\rangle \tag{2.40}$$

where H_n is the physicist's Hermite polynomials. A sanity check is to make α or z zero

$$\lim_{\alpha\to 0}|\alpha, z\rangle = \sum_{n=0}^{\infty}\sqrt{\frac{(e^{i\varphi}\tanh|z|)^n}{2^n n!\cosh|z|}}H_n(0)|n\rangle = \sum_{n=0}^{\infty}\frac{(e^{i\varphi}\tanh|z|)^n}{\sqrt{\cosh|z|2^{2n}(2n)!}}\frac{(-1)^n(2n)!}{n!}|2n\rangle = |z\rangle \tag{2.41}$$

where $H_n(0)$ are Hermite Numbers, only non-zero for even n.

$$\lim_{z\to 0}|\alpha, z\rangle = e^{-\frac{1}{2}|\alpha|^2}\sum_{n=0}^{\infty}\sqrt{\frac{(e^{i\varphi}\tanh|z|)^n}{2^n n!}}\left(2^n\left(\frac{\alpha}{\sqrt{2e^{i\varphi}\tanh|z|}}\right)^n + 0\cdots\right)|n\rangle = |\alpha\rangle \tag{2.42}$$

where only the first term of Hermite polynomials survive after taking $z \to 0$ limit. So everything is beautifully consistent.

The previous formalism is purely from a perspective of quantum mechanics. To relate to the actual quantum noise that is measurable, we have to connect these quantum operators to electromagnetic fields through second quantization.

2.4 Two-Photon Formalism

An ideal electromagnetic wave behaves like a pure sine wave, as we've seen in Fig. 1-2.

$$E(t) = \frac{A_0}{\sqrt{2}}e^{-i\omega_0 t} + \text{c.c.} \tag{2.43}$$

where c.c. stands for complex conjugate, and $\omega_0 = 2\pi f_0$ is the angular frequency of the wave. In real experiments, we can't measure the amplitude of a field, but the time-averaged power

$$P = \langle |E(t)|^2 \rangle = A_0^2 \tag{2.44}$$

A more complete picture of the field is to include all of its Fourier components if there are any

$$E(t) = \frac{A_0}{\sqrt{2}} e^{-i\omega_0 t} + \int_{-\infty}^{\infty} \frac{d\omega}{2\pi} \sqrt{\frac{\hbar\omega}{2}} a(\omega) e^{-i\omega t} + \text{h.c.} \tag{2.45}$$

$$\approx e^{-i\omega_0 t} \left(\frac{A_0}{\sqrt{2}} + \sqrt{\frac{\hbar\omega_0}{2}} \int_0^{\infty} \frac{d\Omega}{2\pi} \left(a(\omega_0 + \Omega) e^{-i\Omega t} + a(\omega_0 - \Omega) e^{i\Omega t} \right) \right) + \text{c.c.} \tag{2.46}$$

where I perform a change of variable $\omega = \omega_0 + \Omega$ and make an approximation $\hbar(\omega_0 + \Omega) \approx \hbar\omega_0$ because the sideband frequency $\Omega/2\pi$ is at most MHz of our interest while $\omega_0/2\pi = c/1064\,\text{nm} =$ THz. The classical part $A_0/\sqrt{2}$ is idealized as a Dirac delta function, and all the sideband oscillations are included in the Fourier modes $a(\omega)$. The integration range is also shifted by the carrier frequency ω_0, with upper and lower complex coefficients $a(\omega_0 + \Omega)$. Note that this convention is consistent with reference [33–36].

In the second quantization, the complex Fourier coefficients are promoted to the annihilation operators in quantum mechanics. The complex conjugate is promoted to Hermitian conjugate. These operators $a(\omega_0 + \Omega)$ are also known as quantum modes.

$$E(t) = e^{-i\omega_0 t} \left(\frac{A_0}{\sqrt{2}} + \sqrt{\frac{\hbar\omega_0}{2}} \int_0^{\infty} \frac{d\Omega}{2\pi} \left(a_+ e^{-i\Omega t} + a_- e^{i\Omega t} \right) \right) + \text{h.c.} \tag{2.47}$$

The above formalism is also known as "one-photon formalism" or the "sideband picture" of the electric field. In 1985, Caves proposed the two-photon formalism by changing the sideband basis

to the quadrature basis $a_\pm \to a_{1,2}$ [37, 38].

$$E(t) = \frac{A_0}{\sqrt{2}}\left(e^{-i\omega_0 t} + e^{i\omega_0 t}\right) + \tag{2.48}$$

$$\sqrt{\frac{\hbar\omega_0}{2}}\int_0^\infty \frac{d\Omega}{2\pi}\left[e^{-i\omega_0 t}\left(a_+ e^{-i\Omega t} + a_- e^{i\Omega t}\right) + e^{i\omega_0 t}\left(a_+^\dagger e^{i\Omega t} + a_-^\dagger e^{-i\Omega t}\right)\right] \tag{2.49}$$

$$= \sqrt{2}A_0\cos\omega_0 t + \sqrt{\hbar\omega_0}\int_0^\infty \frac{d\Omega}{2\pi}\left[\cos\omega_0 t\Big(\underbrace{\frac{a_+ + a_-^\dagger}{\sqrt{2}}}_{a_1} e^{-i\Omega t} + \frac{a_+^\dagger + a_-}{\sqrt{2}}e^{i\Omega t}\Big)\right. \tag{2.50}$$

$$\left. + \sin\omega_0 t\Big(\underbrace{-i\frac{a_+ - a_-^\dagger}{\sqrt{2}}}_{a_2} e^{-i\Omega t} + i\frac{a_+^\dagger - a_-}{\sqrt{2}}e^{i\Omega t}\Big)\right] \tag{2.51}$$

$$= \underbrace{\sqrt{2}\begin{bmatrix}\cos\omega_0 t & \sin\omega_0 t\end{bmatrix}}_{\vec{\omega}_0^{\intercal}(t)}\left(A_0\vec{v} + \sqrt{\frac{\hbar\omega_0}{2}}\int_0^\infty \frac{d\Omega}{2\pi}\left(\begin{bmatrix}a_1\\ a_2\end{bmatrix}e^{-i\Omega t} + \begin{bmatrix}a_1^\dagger\\ a_2^\dagger\end{bmatrix}e^{i\Omega t}\right)\right) \tag{2.52}$$

$$= \vec{\omega}_0^{\intercal}(t)\left(\vec{A}_0 + \sqrt{\frac{\hbar\omega_0}{2}}\int_{-\infty}^\infty \frac{d\Omega}{2\pi}\,\vec{a}e^{-i\Omega t}\right) \tag{2.53}$$

where vector $\vec{A}_0 = A_0\vec{v} = A_0[1\ \ 0]^{\intercal}$ is the classical part of the field and the vector $\vec{a} = [a_1\ \ a_2]^{\intercal}$ is the quantum mode. Notice that the integration range is changed again in Eq. (2.53). I will omit the integration range if it's the full $-\infty$ to ∞.

Without loss of generality, the convention of the Fourier transform is up to the author. Unfortunately, the convention has been mixed in literature commonly used in squeezing. In this thesis, we will follow the literature presented in [33, 34], which means that we have to flip the exponential in the previous equation.

$$E(t) \to \vec{\omega}_0^{\intercal}(t)\left(\vec{A}_0 + \sqrt{\frac{\hbar\omega_0}{2}}\int_{-\infty}^\infty \frac{d\Omega}{2\pi}\,\vec{a}e^{i\Omega t}\right) \tag{2.54}$$

The measured power of the laser field is thus

$$P(t) = \langle |E(t)|^2 \rangle \tag{2.55}$$

$$= \left(\vec{A_0}^{\dagger} + \sqrt{\frac{\hbar\omega_0}{2}} \int \frac{d\Omega}{2\pi} \vec{a}^{\dagger} e^{-i\Omega t} \right) \left\langle \vec{\omega}_0(t) \vec{\omega}_0^{\mathsf{T}}(t) \right\rangle \left(\vec{A_0} + \sqrt{\frac{\hbar\omega_0}{2}} \int \frac{d\Omega}{2\pi} \vec{a} e^{i\Omega t} \right) \tag{2.56}$$

$$= A_0^2 + \sqrt{2\hbar\omega_0} \int \frac{d\Omega}{2\pi} \vec{A_0}^{\dagger} \vec{a} e^{i\Omega t} + \mathcal{O}(\hbar) \tag{2.57}$$

where the brackets are time-averaging of the fast oscillations (the carrier frequency) to give

$$\left\langle \vec{\omega}_0(t) \vec{\omega}_0^{\mathsf{T}}(t) \right\rangle = \mathbf{1} \tag{2.58}$$

The final result is simplified using the properties of the operators

$$a_1(-\Omega) = a_1^{\dagger}(\Omega) \qquad \text{and} \qquad a_2(-\Omega) = a_2^{\dagger}(\Omega) \tag{2.59}$$

and the fact that $A\vec{v}$ is real.

It can be shown that if we propagate the field by changing $t \to t - x/c$, the electric field is

$$E(t,x) = \vec{\omega}_0^{\mathsf{T}}(t) \left(\mathbf{R}\left(\phi_x\right) \vec{A}_0 + \sqrt{\frac{\hbar\omega_0}{2}} \int \frac{d\Omega}{2\pi} \mathbf{R}\left(\phi_x\right) (\vec{a} e^{-i\varphi_x}) e^{-i\Omega t} \right) \tag{2.60}$$

where

$$\mathbf{R}\left(\phi\right) = \begin{bmatrix} \cos\phi & -\sin\phi \\ \sin\phi & \cos\phi \end{bmatrix} \tag{2.61}$$

is the rotation matrix and $\phi_x = \omega_0 x/c$ and $\varphi_x = \Omega x/c$. The classical part acquires the phase ϕ_x as usual and the quantum mechanical sidebands acquire an additional phase of φ_x. This is in full quadrature picture so the classical part $\mathbf{R}\left(\phi_x\right) \vec{A}_0$ is always real.

In this formalism, the quantum-mechanical parts are carried with classical parts of the field all

the time. The fluctuations of the power due to quantum modes can be expressed compactly in the frequency domain

$$P(\Omega) = \sqrt{2\hbar\omega_0}\vec{A}_0^{\dagger}\vec{a}(\Omega) \tag{2.62}$$

This is a very elegant expression of the power fluctuations, from which the quantum noise originates. It enables a very direct and intuitive way to calculate quantum noise, given all the experimental nonidealities like optical losses and mode-mismatches. I will discuss the formalism of directly calculating quantum noise in the next chapter.

3 DIRECT CALCULATION OF QUANTUM NOISE

In Chapter 1, I introduced the uncertainty when you measure the power of a light beam on a photodetector. The uncertainty of the measurement is calculated from the Poisson statistics of the discrete photons. This is the simplest picture of the quantum uncertainty. A slightly more complicated picture of the quantum uncertainty is the quantum-mechanical coherent state introduced in Chapter 2. In this theory, the Poisson nature of the photon detection process is derived from the photon statistics of the coherent state.

Notice that we have only discussed the quantum uncertainty but not the quantum noise itself. In this chapter, we will derive the quantum noise from Poisson statistics and quantum mechanics. Then we extend the analysis to describe the quantum noise of the LIGO optical system, which has been an active area of research for decades.

3.1 Simple Picture

The noise of a measured signal is represented by the power spectral density where the total variance is decomposed into frequencies. For a stationary and ergodic random process, the time series of the signal counts as proper measurements of the random process. It's simple to calculate the quantum noise assuming it's a white noise, meaning that it is independent of frequency.

The power of the light we measured is a random variable, equivalent to the time-averaged

number of photons $\langle n \rangle$ in the duration τ: $P = \hbar\omega n/\tau$. Thus, we have

$$\frac{\sigma_P}{P} = \frac{\sigma_n}{n} = \frac{1}{\sqrt{n}} = \sqrt{\frac{\hbar\omega}{\tau P}} \tag{3.1}$$

according to the Poisson statistics. Now we string these sets of τ-second measurements together to form a long time series of $P(t)$. The sampling frequency of such time series is $1/\tau$, which limits the bandwidth of our measurement. Therefore:

$$\sigma_P^2 = \frac{\hbar\omega P}{\tau} = \int_0^{1/2\tau} df\, S_P(f) \tag{3.2}$$

where $S_P(f)$ is the single-sided power spectral density of the power fluctuation. Assuming the shot noise is a white noise, we have

$$S_P(f) = S_P = 2\hbar\omega P \tag{3.3}$$

which has a unit of W^2/Hz and only depends on the power. It's essentially the same as the other types of shot noise like Schottky's shot noise in electronic devices.

3.2 Direct Calculation

There is extensive literature on the derivation and mitigation of quantum noise for gravitational wave detectors. The most seminal articles are "KLMTV" [36], "BnC" [39], and "DnD" [35]. We give each one a unique name from its authors or titles since they are very frequently used to discuss quantum noise. Their formulations are correct of course, but they are very analytical and lead to cumbersome equations if they are not performing approximations. In addition, it's difficult to add new optical systems on top of their analytical results. In this thesis, we utilize a direct way to calculate quantum noise. We obtain the full field information first, and the quantum noise can

be trivially calculated afterward. I'll show that this formalism doesn't require approximations to be physically intuitive, and it's very extensible to new systems, for example, the filter cavity that enables frequency-dependent squeezing.

In Section 2.4, I introduced two-photon formalism and presented the analytical expression of the field that contains classical and quantum-mechanical parts. The power of the field with amplitude A_0 and frequency ω_0 is (repeated from Eq. (2.55))

$$P(t) = A_0^2 + \sqrt{2\hbar\omega_0}\int_{-\infty}^{\infty}\frac{d\Omega}{2\pi}\,\vec{A_0}^{\dagger}\vec{a}(\Omega)e^{i\Omega t} + \mathcal{O}(\hbar) \tag{3.4}$$

The Fourier-transformed time series can be read-off directly

$$P(\Omega) = \sqrt{2\hbar\omega_0}\vec{A_0}^{\dagger}\vec{a}(\Omega) \tag{3.5}$$

The single-sided power spectral density can be calculated with standard formula [40, 41]

$$\frac{1}{2}S(f)\delta(f-f') = \langle P(f)P^*(f')\rangle \tag{3.6}$$

The bracket indicates time-averaging for complex numbers. For the quantum-mechanical operators, the bracket works by computing the expectation value of the symmetrized operators. From KLMTV [36], we have

$$\langle 0|a_j(\Omega)a_k^{\dagger}(\Omega')|0\rangle_{sym} = \frac{1}{2}2\pi\delta(\Omega-\Omega')\delta_{jk} \tag{3.7}$$

Since $\Omega = 2\pi f$ and thus $\delta(f - f') = 2\pi\delta(\Omega - \Omega')$, the power spectral density can be found

$$S(\Omega) = \frac{1}{2\pi\delta(\Omega - \Omega')/2}\langle 0|P(\Omega)P^{\dagger}(\Omega')|0\rangle_{sym} \tag{3.8}$$

$$= 2\hbar\omega_0 \frac{\langle 0|\vec{A}_0{}^{\dagger}\vec{a}(\Omega)\vec{a}^{\dagger}(\Omega')\vec{A}_0|0\rangle_{sym}}{2\pi\delta(\Omega - \Omega')/2} \tag{3.9}$$

$$= 2\hbar\omega_0 \vec{A}_0{}^{\dagger}\vec{A}_0 = 2\hbar\omega_0 P \tag{3.10}$$

which is identical to the calculation from Poisson statistics in Eq. (3.3).

In this thesis, we will simplify writing by denoting

$$\langle a_j a_k^{\dagger}\rangle = \frac{\langle 0|\vec{a}_j(\Omega)\vec{a}_k^{\dagger}(\Omega')|0\rangle_{sym}}{2\pi\delta(\Omega - \Omega')/2} = \delta_{jk} \tag{3.11}$$

If the beam propagates path length x and acquires additional phase $\phi = \omega_0 x/c$ and sideband phase $\varphi = \Omega x/c$, it is easy to check that transforming $\vec{A}_0 \to \mathbf{R}(\phi)\,\vec{A}_0$ and $\vec{a} \to \mathbf{R}(\phi)\,\vec{a}e^{-i\varphi}$ won't change the calculated quantum noise from Eq. (3.9). Now that we have obtained the quantum noise measured from a simple photodiode, it's time to calculate the quantum noise of a complicated optical or optomechanical system such as Advanced LIGO.

3.3 Input-Output Relations

Almost all of the optical systems are made of one thing - the beam splitter. Although the current Advanced LIGO is a complex dual-recycled Fabry-Pérot Michelson interferometer, it essentially is a bunch of beam splitters with carefully designed transmissions that are aligned perfectly together. We will start discussing input-output relations with the simplest instrument, namely beam splitter.

3.3.1 Beam splitter

Classically, the beam splitter is a simple device that splits a beam or mixes two beams. Quantum-mechanically, it also splits and mixes the quantum modes. However, the empty port in the classical context still has nonzero quantum vacuum fluctuations in the quantum regime. This is the mechanism of losses and how vacuum is mixed with squeezed states.

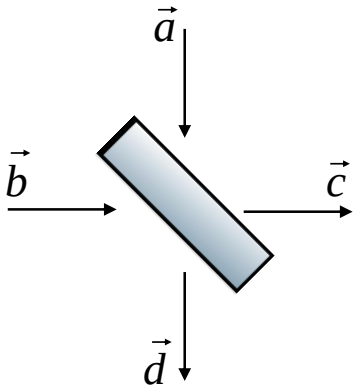

Figure 3-1: A quantum-mechanical beam splitter with input operators $\vec{a}$, $\vec{b}$ and output $\vec{c}$, $\vec{d}$.

The beam splitter can be represented as a unitary 4×4 matrix so it preserves the inner product and commutation relation. The input-output relation is written as follows

$$\begin{bmatrix} \vec{c} \\ \vec{d} \end{bmatrix} = \begin{bmatrix} r \cdot \mathbf{1} & t \cdot \mathbf{1} \\ t \cdot \mathbf{1} & -r \cdot \mathbf{1} \end{bmatrix} \begin{bmatrix} \vec{a} \\ \vec{b} \end{bmatrix} \quad \text{and} \quad |r|^2 + |t|^2 = 1 \tag{3.12}$$

where r and t are the amplitude reflectivity and transmissivity of the beam splitter. The identity matrix $\mathbf{1}$ will be omitted from now because it's easy to infer from the context. I used the convention where the minus sign is assigned to the bottom surface in Fig. 3-1. Other conventions put a minus sign on transmissions or break them into imaginary numbers, as long as the matrix is unitary.

For a lossy beam splitter, it can be thought of as two beam splitters with the first one acting as a source of loss with transmissivity $t = \sqrt{1 - L}$, where L is the power loss. Therefore, each beam

splitter is still a unitary matrix on the operators. In fact, all the optical losses can be modeled as a beam splitter on the path.

It is important to note that Eq. (3.12) also holds for the classical part of the field. Therefore, we only need to find one input-output relation that works for both the classical and quantum parts of the same field. Additionally, the diagram illustration also works for both classical and quantum parts.

3.3.2 Homodyne detector

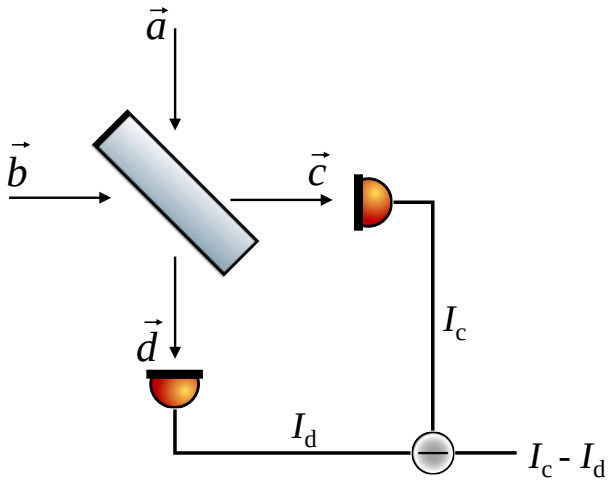

Figure 3-2: A homodyne detector with one input port being the measured beam and the other port being the local oscillator beam.

A homodyne detector is a device to detect squeezing. It's made of a beam splitter and two photodiodes, as shown in Fig. 3-2. If the beam splitter splits the beam into equal powers, the detector is the balanced homodyne detector. Suppose the measured field is

$$E(t,x) = \vec{\omega}_0^{\mathrm{T}}(t)\left(\vec{A} + \sqrt{\frac{\hbar\omega_0}{2}}\int_{-\infty}^{\infty}\frac{d\Omega}{2\pi}\,\vec{a}e^{i\Omega t}\right) \tag{3.13}$$

with classical amplitude A and quantum operators $\vec{a}$. The local oscillator field entering from the other port of the beam splitter has classical amplitude $\vec{B} = \mathbf{R}(\phi) B$ and quantum operators $\mathbf{R}(\phi) e^{-i\varphi}\vec{b}$, where ϕ is the relative phase difference and φ is the extra sideband phase.

$$E_{LO}(t,x) = \vec{\omega}_0^{\intercal}(t)\left(\vec{B} + \sqrt{\frac{\hbar\omega_0}{2}}\int_{-\infty}^{\infty}\frac{d\Omega}{2\pi}\mathbf{R}(\phi)(\vec{b}e^{-i\varphi})e^{i\Omega t}\right) \tag{3.14}$$

The field at output $\vec{C}$ of beam splitter is

$$\vec{C} = r\vec{A} + t\vec{B} \tag{3.15}$$

with quantum part

$$\vec{c} = r\vec{a} + t\mathbf{R}(\phi) e^{-i\varphi}\vec{b} \tag{3.16}$$

The measured photocurrent I_c is

$$I_c(t) = P_c(t) = \left(\vec{C}^{\dagger} + \sqrt{\frac{\hbar\omega_0}{2}}\int\frac{d\Omega}{2\pi}\vec{c}^{\dagger}e^{-i\Omega t}\right)\left\langle\vec{\omega}_0(t)\vec{\omega}_0^{\intercal}(t)\right\rangle\left(\vec{C} + \sqrt{\frac{\hbar\omega_0}{2}}\int\frac{d\Omega}{2\pi}\vec{c}e^{i\Omega t}\right) \tag{3.17}$$

$$= \vec{C}^{\dagger}\vec{C} + \sqrt{2\hbar\omega_0}\int\frac{d\Omega}{2\pi}\,\vec{C}^{\dagger}\vec{c}e^{i\Omega t} \tag{3.18}$$

Similarly, the photocurrent measured at photodiode D is

$$I_d(t) = \vec{D}^{\dagger}\vec{D} + \sqrt{2\hbar\omega_0}\int\frac{d\Omega}{2\pi}\,\vec{D}^{\dagger}\vec{d}e^{i\Omega t} \tag{3.19}$$

where $\vec{D} = t\vec{A} - r\vec{B}$ and $\vec{d} = t\vec{a} - r\mathbf{R}(\phi) e^{-i\varphi}\vec{b}$. It's apparent that each photodiode measures the shot noise of the power by itself, for example, $S_c = 2\hbar\omega_0\vec{C}^{\dagger}\vec{C}$. This makes sense because a beam splitter can not change the quantum noise of a beam. The homodyne signal subtracts the

photocurrents

$$I_{\text{diff}}(t) = I_c - I_d = (C^\dagger C - D^\dagger D) + \sqrt{2\hbar\omega_0}\int \frac{d\Omega}{2\pi}\,(C^\dagger \vec{c} - D^\dagger \vec{d})e^{i\Omega t} \tag{3.20}$$

Without squeezing, the expectation of symmetrized operators have

$$\langle 0|\vec{c}(\Omega)\vec{c}^\dagger(\Omega')|0\rangle_{sym} = \langle 0|r^2\vec{a}(\Omega)\vec{a}^\dagger(\Omega') + t^2\vec{b}(\Omega)\vec{b}^\dagger(\Omega')|0\rangle_{sym} \tag{3.21}$$

because the cross-spectral density of different quantum operators vanishes. The power spectral density of the difference signal is

$$S_{\text{diff}} = 2\hbar\omega_0(C^\dagger C + D^\dagger D) \tag{3.22}$$

This is equal to the total shot noises of individual photodiodes added in quadrature, even if the power $(C^\dagger C - D^\dagger D)$ is zero. This is expected when you have two incoherent noises added together.

When we squeeze one of the input beams, it can be shown that the measured noise from the homodyne detector is reduced. We will leave it in the next chapter when we introduce squeezing.

3.3.3 Fabry-Pérot cavity

A Fabry-Pérot cavity is an optical device made of two or more beam splitters (more commonly referred to as mirrors), as shown in Fig. 3-3. Let the amplitude reflectivity of two mirrors be r_1 and r_2. Using the representation of the beam splitter, we have

$$\begin{bmatrix} \vec{g} \\ \mathbf{R}(-\phi)\, e^{i\varphi}\vec{j} \end{bmatrix} = \begin{bmatrix} r_1 & t_1 \\ t_1 & -r_1 \end{bmatrix} \begin{bmatrix} \vec{f} \\ \vec{k} \end{bmatrix} \tag{3.23}$$

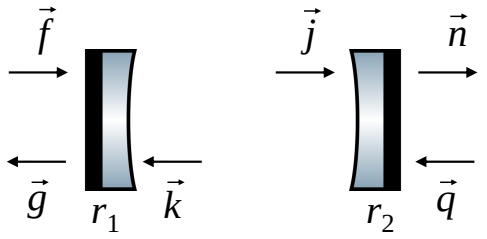

Figure 3-3: A Fabry-Pérot cavity constructed by two beam splitters with amplitude reflectivity r_1 and r_2. The input and output fields are labeled. The (-1) sign is assigned to the high-reflection surface of the beam splitter.

and

$$\begin{bmatrix} \vec{n} \\ \mathbf{R}(-\phi)\, e^{i\varphi}\vec{k} \end{bmatrix} = \begin{bmatrix} r_2 & t_2 \\ t_2 & -r_2 \end{bmatrix} \begin{bmatrix} \vec{q} \\ \vec{j} \end{bmatrix} \tag{3.24}$$

where $\phi = \omega_0 L/c$ ($\varphi = \Omega L/c$) is the single-trip phase and L is the length of the cavity.

When the cavity is locked on resonance. meaning that the fields inside the cavity are standing waves, we have the round-trip phase $\omega_0 2L/c = 2\pi N$ where $N \in \mathbb{N}$. Solving the two beam splitter equations, we have

$$\vec{g}(\Omega) = \underbrace{\frac{r_1 - r_2 e^{-i2\varphi}}{1 - r_1 r_2 e^{-i2\varphi}}}_{\mathbf{r}_{\text{cav}}(\Omega)} \vec{f} + \underbrace{\frac{t_1 t_2}{1 - r_1 r_2 e^{-i2\varphi}} \mathbf{R}(\pi N)\, e^{-i\varphi}}_{\mathbf{t}_{\text{cav}}(\Omega)} \vec{q} \tag{3.25}$$

where $\mathbf{r}_{\text{cav}}$ and $\mathbf{t}_{\text{cav}}$ are the equivalent amplitude reflectivity and transmissivity of the cavity. In a general case where the cavity is detuned from resonance ($\mathbf{R}(2\phi) \neq \mathbf{1}$), the reflection and transmission of the cavity are

$$\mathbf{r}_{\text{cav}}(\Omega) = r_1 \mathbf{1} - t_1 \mathbf{R}(\phi)\, e^{-i\varphi} r_2 \left[\mathbf{1} - r_1 r_2 \mathbf{R}(2\phi)\, e^{-i2\varphi}\right]^{-1} \mathbf{R}(\phi)\, e^{-i\varphi} t_1 \tag{3.26}$$

$$\mathbf{t}_{\text{cav}}(\Omega) = t_1 t_2 \mathbf{R}(\phi)\, e^{-i\varphi} + t_1 \mathbf{R}(\phi)\, e^{-i\varphi} r_2 \left[\mathbf{1} - r_1 r_2 \mathbf{R}(2\phi)\, e^{-i2\varphi}\right]^{-1} \mathbf{R}(2\phi)\, e^{-i2\varphi} r_1 t_2 \tag{3.27}$$

We can expand $\mathbf{r}_{\text{cav}}(\Omega)$

$$\mathbf{r}_{\text{cav}}(\Omega) = \begin{bmatrix} r_{11} & r_{12} \\ r_{21} & r_{22} \end{bmatrix} \tag{3.28}$$

where

$$r_{11} = \frac{r_1(1 - r_1 r_2 \cos 2\phi e^{-i2\varphi}) - r_2 e^{-i2\varphi}(\cos 2\phi - r_1 r_2 e^{-i2\varphi})}{1 - 2r_1 r_2 \cos 2\phi e^{-i2\varphi} + r_1^2 r_2^2 e^{-i4\varphi}} \tag{3.29}$$

$$r_{12} = -\frac{t_1^2 r_2 \sin 2\phi e^{-i2\varphi}}{1 - 2r_1 r_2 \cos 2\phi e^{-i2\varphi} + r_1^2 r_2^2 e^{-i4\varphi}} \tag{3.30}$$

$$r_{21} = r_{12} \tag{3.31}$$

$$r_{22} = r_{11} \tag{3.32}$$

The circulating field inside the cavity $\vec{j}$ is

$$\vec{j} = \underbrace{\frac{t_1}{1 - r_1 r_2 e^{-i2\varphi}} \mathbf{R}(\pi N) e^{-i\varphi}}_{\mathbf{g}_{\text{cav}}(\Omega)} \vec{f} - \frac{r_1 t_2 e^{-i2\varphi}}{1 - r_1 r_2 e^{-i2\varphi}} \vec{q} \tag{3.33}$$

where $\mathbf{g}_{\text{cav}}(\Omega)$ is the cavity's amplitude optical gain with a general form

$$\mathbf{g}_{\text{cav}}(\Omega) = t_1 \left[\mathbf{1} - r_1 r_2 \mathbf{R}(2\phi) e^{-i2\varphi}\right]^{-1} \mathbf{R}(\phi) e^{-i\varphi} \tag{3.34}$$

The exact solutions above can be approximated when the mirrors are highly reflective

$$r = \sqrt{1 - T} \approx e^{-T/2} \tag{3.35}$$

where $T \ll 1$ is the power transmission. For a resonant cavity, the amplitude reflectivity can be simplified as

$$r_{\text{cav}}(\Omega) = \frac{r_1 - r_2 e^{-i2\varphi}}{1 - r_1 r_2 e^{-i2\varphi}} \approx \frac{-T_1 + T_2 + i4\varphi}{T_1 + T_2 + i4\varphi} = \frac{-\gamma + \lambda + i\Omega}{\gamma + \lambda + i\Omega} \tag{3.36}$$

where

$$\gamma = \frac{T_1 c}{4L} \tag{3.37}$$

is the frequency (in rad/s) of the **half width at half maximum** of the resonance peak. $\gamma/(2\pi)$ is also known as (in Hz) **(half) linewidth, cavity pole, decay rate**, and **1/storage time**.

The other frequency (in rad/s) is

$$\lambda = \frac{T_2 c}{4L} \tag{3.38}$$

is the loss-limited bandwidth, dominated by loss.

The cavity gain in amplitude is approximately

$$g_{\rm cav}(\Omega) = \frac{t_1 e^{-i\varphi}}{1 - r_1 r_2 e^{-i2\varphi}} \approx \frac{2\sqrt{T_1}}{T_1 + T_2 + i4\varphi} = \frac{\sqrt{\gamma c/L}}{\gamma + \lambda + i\Omega} \tag{3.39}$$

For an overcoupled (low-loss) cavity, we have $T_1 \gg T_2$. The cavity gain in power is

$$G = g_{\rm cav}^2(0) \approx \frac{4}{T_1} \tag{3.40}$$

The finesse of the cavity is also defined as the full width at half maximum over the free spectral range (FSR = $c/(2L)$) of the cavity. The higher the finesse, the smaller the linewidth of the cavity (sharper resonance peaks).

$$\mathscr{F} = \frac{\pi\sqrt{r_1 r_2}}{1 - r_1 r_2} \approx \frac{\pi G}{2} \tag{3.41}$$

It is easy to check that (assuming an over-coupled cavity)

$$\mathscr{F} = \frac{2\pi(c/2L)}{2\gamma} = \frac{\pi G}{2} \tag{3.42}$$

A resonant cavity requires the round-trip phase of the circulating field to be the integer number of 2π, which means that the cavity length has to be stable at the scale of wavelength (1064 nm for LIGO). This requirement is even more stringent for high-finesse cavities. The reflected field $\vec{g}$ is

therefore very sensitive to cavity mirror motions.

To find the sensitivity of the reflected field to the cavity motion, one naive way is to take the derivative of the cavity's amplitude reflectivity with respect to the round-trip phase, $d\mathbf{r}_{\text{cav}}/d\phi$. However, it can be shown that the derivative is frequency-independent, which implies the cavity has infinite bandwidth and is sensitive up to infinite frequency. This is because we have assumed a steady-state cavity $\mathbf{r}_{\text{cav}}$, which is not fundamental and ignores the dynamics of the cavity. A more accurate picture of the cavity is that the reflection is the sum of all the fields traversed cavity at an integer number of times, as shown in Fig. 3-4.

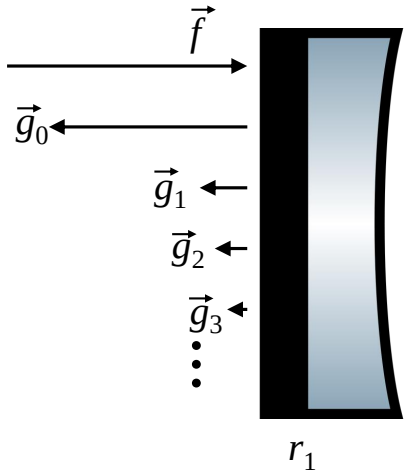

Figure 3-4: Reflected field from the cavity as a sum of individual fields.

The zeroth reflected field is just $\vec{g}_0 = r_1\vec{f}$. The first field traversed the cavity once and propagated back can be written as (note that all things the field sees are written from right to left)

$$\vec{g}_1 = t_1\mathbf{R}\left(\phi_0\right)e^{-i\varphi_0}(-r_2)\mathbf{R}\left(\phi_1\right)e^{-i\varphi_1}t_1\vec{f} = -r_2t_1^2e^{-i(\varphi_0+\varphi_1)}\mathbf{R}\left(\phi_0+\phi_1\right)\vec{f} \tag{3.43}$$

where

$$\phi_n = \frac{\omega_0}{c}L(t-\frac{nL}{c}) = \frac{\omega_0}{c}\left(L+\delta L(t-\frac{nL}{c})\right) = \phi+\frac{\omega_0}{c}\delta L(t-\frac{nL}{c}) \tag{3.44}$$

which is the single-trip phase in the past times $t - nL/c$. Same thing applies to φ.

$$\varphi_n = \frac{\Omega L}{c} + \frac{\Omega}{c}\delta L(t - \frac{nL}{c}) \tag{3.45}$$

The steady-state cavity reflection in Eq. (3.26) takes no information about the cavity in the past. It would make a difference at higher frequencies because a cavity has limited bandwidth.

The field traversed cavity twice is

$$\vec{g}_2 = t_1 \mathbf{R}\left(\phi_0\right) e^{-i\varphi_0}(-r_2)\mathbf{R}\left(\phi_1\right) e^{-i\varphi_1}\left[(-r_1)\mathbf{R}\left(\phi_2\right) e^{-i\varphi_2}(-r_2)\mathbf{R}\left(\phi_3\right) e^{-i\varphi_3}\right] t_1 \vec{f} \tag{3.46}$$

$$= -r_2 t_1^2 r_1 r_2 \prod_{k=0}^{3} e^{-i\varphi_k}\mathbf{R}\left(\phi_k\right)\vec{f} \tag{3.47}$$

Therefore, the summation of all fields give an equivalent $\mathbf{r}_{\text{cav}} = (\sum_n \vec{g}_n)/\vec{f}$

$$\mathbf{r}_{\text{cav}} = r_1 - r_2 t_1^2 \sum_{n=0}^{\infty}(r_1 r_2)^n \prod_{k=0}^{2n+1} e^{-i\varphi_k}\mathbf{R}\left(\phi_k\right) = r_1 - r_2 t_1^2 \sum_{n=0}^{\infty}(r_1 r_2)^n \exp\left(-i\sum_{k=0}^{2n+1}\varphi_k\right)\mathbf{R}\left(\sum_{k=0}^{2n+1}\phi_k\right) \tag{3.48}$$

Let's work on the terms one by one

$$\sum_{k=0}^{2n+1}\phi_k(t) = 2(n+1)\phi + \frac{\omega_0}{c}\sum_{k=0}^{2n+1}\delta L(t - \frac{kL}{c}) \tag{3.49}$$

It's easier to transfer it in frequency domain

$$\sum_{k=0}^{2n+1}\phi_k(\Omega) = 2(n+1)\phi + \frac{\omega_0}{c}\sum_{k=0}^{2n+1}\delta L(\Omega)(e^{-i\Omega L/c})^k \tag{3.50}$$

$$= 2(n+1)\phi + \frac{\omega_0}{c}\delta L(\Omega)\frac{1 - e^{-i\varphi 2(n+1)}}{1 - e^{-i\varphi}} \tag{3.51}$$

and thus

$$\mathbf{R}\left(\sum_{k=0}^{2n+1}\phi_k\right) = \mathbf{R}\left(2(n+1)\phi\right)\mathbf{R}\left(\frac{\omega_0}{c}\delta L(\Omega)\frac{1-e^{-i\varphi 2(n+1)}}{1-e^{-i\varphi}}\right) \tag{3.52}$$

$$= \mathbf{R}\left(2\phi\right)\mathbf{R}^n(2\phi)\left[\mathbf{1}+\mathbf{R}\left(\frac{\pi}{2}\right)\frac{\omega_0}{c}\delta L(\Omega)\frac{1-e^{-i\varphi 2(n+1)}}{1-e^{-i\varphi}}+\mathcal{O}(\delta L^2)\right] \tag{3.53}$$

Similarly, the term relating to sidebands are

$$\exp\left(-i\sum_{k=0}^{2n+1}\varphi_k\right) = e^{-i2\varphi}e^{i2\varphi n}\left[1-i\frac{\Omega}{c}\delta L(\Omega)\frac{1-e^{-i\varphi 2(n+1)}}{1-e^{-i\varphi}}+\mathcal{O}(\delta L^2)\right] \tag{3.54}$$

$$= 1-ie^{-i2\varphi}e^{-i2\varphi n}\frac{\Omega}{c}\delta L(\Omega)\frac{1-e^{-i\varphi 2(n+1)}}{1-e^{-i\varphi}}+\mathcal{O}(\delta L^2) \tag{3.55}$$

Notice that the last line of previous equation is not an approximation. The term $e^{-i2\varphi}e^{-i2\varphi n}$ only affects on sideband generated by the $\delta L(\Omega)$ and not on the classical part $\vec{F}$. If $e^{i2\varphi}$ acts on $\vec{F}$, the φ is zero. It's only nonzero when acting on $\mathbf{R}\left(\phi_k\right)\vec{F}$. Doing this will prevent its multiplication to the classical part $\vec{F}$. The ordering matters here.

The sum of infinite series is

$$\sum_{n=0}^{\infty}(r_1r_2)^n\exp\left(-i\sum_{k=0}^{2n+1}\varphi_k\right)\mathbf{R}\left(\sum_{k=0}^{2n+1}\phi_k\right) = \frac{\mathbf{R}\left(2\phi\right)}{1-r_1r_2\mathbf{R}\left(2\phi\right)}+\delta L(\Omega)(...) \tag{3.56}$$

and the total reflectivity is

$$\mathbf{r}_{\text{cav}}(\Omega) = r_1 - r_2t_1^2\sum_{n=0}^{\infty}(r_1r_2)^n\exp\left(-i\sum_{k=0}^{2n+1}\varphi_k\right)\mathbf{R}\left(\sum_{k=0}^{2n+1}\phi_k\right) \tag{3.57}$$

$$= \mathbf{r}_{\text{cav}}(0)+\frac{\delta\mathbf{r}_{\text{cav}}}{\delta\phi}(\Omega)\frac{\omega_0}{c}\delta L(t) \tag{3.58}$$

where

$$\frac{\delta \mathbf{r}_{\rm cav}}{\delta\phi}(\Omega) = -r_2 t_1 \frac{\mathbf{R}\,(2\phi)}{1-e^{-i\varphi}} \sum_{n=0}^{\infty} (r_1 r_2 \mathbf{R}\,(2\phi))^n (1-e^{-i\varphi 2(n+1)}) \left(\mathbf{R}\left(\frac{\pi}{2}\right) - i\frac{\Omega}{\omega_0} e^{-i\varphi 2(n+1)} \mathbf{1} \right) \tag{3.59}$$

$$= -(1+e^{-i\varphi})\mathbf{R}\,(2\phi)\, r_2 t_1^2 \left[\mathbf{R}\left(\frac{\pi}{2}\right) \frac{1}{(1-r_1 r_2 \mathbf{R}\,(2\phi))(1-r_1 r_2 \mathbf{R}\,(2\phi)\, e^{-i2\varphi})} - \right. \tag{3.60}$$

$$\left. i\frac{\Omega}{\omega_0} \frac{1}{(e^{i2\varphi} - r_1 r_2 \mathbf{R}\,(2\phi))(e^{i2\varphi} - r_1 r_2 \mathbf{R}\,(2\phi)\, e^{-i2\varphi})} \right] \tag{3.61}$$

$$= -r_2(1+e^{i\varphi})\mathbf{R}\left(\frac{\pi}{2}\right) \mathbf{g}_{\rm cav}(0)\mathbf{g}_{\rm cav}(\Omega) + \mathcal{O}\left(\frac{\Omega}{\omega_0}\right) \tag{3.62}$$

This is a surprisingly simple result. The fluctuation of the cavity reflected field can be thought of as if the classical part gets amplified once ($\mathbf{g}(0)$) before hitting the cavity end mirror, which modulates it into sidebands due to δL. The final signal is amplified again ($\mathbf{g}(\Omega)$) by the cavity when it exits.

3.4 Cavity Optomechanics

The cavity is a passive device in most cases. However, it can be a nonlinear device when the circulating power is so high that it couples the amplitude quadrature of the light to the phase quadrature, causing correlations between the two quadratures of the light. This is an optomechanical effect known as ponderomotive squeezing [42–45]. Such an effect is the cause for the quantum back-action noise, manifested as quantum radiation pressure noise in Advanced LIGO [46] and Advanced Virgo [47]. In this section, we will discuss cavity optomechanics in the context of LIGO, which is not necessarily the same language used in other contexts [48].

For a resonant cavity holding hundreds of kilowatts of power, the quantum noise of the circulating field would produce a noisy radiation pressure on the mirrors and thus a noisy motion. The motion then modulates the field circulating inside and thus converts noise from the amplitude quadrature to the phase quadrature.

In Fig. 3-3, the field power at mirror 1 has a classical part

$$\vec{J} = \frac{t_1}{1 - r_1 r_2} \mathbf{R}(\pi N)\, \vec{F} \tag{3.63}$$

with quantum-mechanical part

$$\vec{j} = \frac{t_1}{1 - r_1 r_2 e^{-i2\varphi}} \mathbf{R}(\pi N)\, e^{-i\varphi} \vec{f} - \frac{r_1 t_2 e^{-i2\varphi}}{1 - r_1 r_2 e^{-i2\varphi}} \vec{q} \tag{3.64}$$

Therefore, the radiation power on the mirror 1 is

$$P_1(t) = \vec{J}^{\dagger} \vec{J} + \sqrt{2\hbar\omega_0} \int \frac{d\Omega}{2\pi}\, \vec{J}^{\dagger} \vec{j} e^{i\Omega t} \tag{3.65}$$

so

$$P_1(\Omega) = \sqrt{2\hbar\omega_0} \vec{J}^{\dagger} \vec{j}(\Omega) \tag{3.66}$$

Similarly, the radiation power on the other mirror 2 is

$$P_2(\Omega) = \sqrt{2\hbar\omega_0} \vec{K}^{\dagger} \vec{k}(\Omega) \tag{3.67}$$

where

$$\vec{K} = -\frac{r_2 t_1}{1 - r_1 r_2} \vec{F} \tag{3.68}$$

and

$$\vec{k} = \frac{t_2}{1 - r_1 r_2 e^{-i2\varphi}} \mathbf{R}(\pi N)\, e^{-i\varphi} \vec{q} - \frac{r_2 t_1 e^{-i2\varphi}}{1 - r_1 r_2 e^{-i2\varphi}} \vec{f} \tag{3.69}$$

A simple formulation of the free motion of the mirror using Newtonian dynamics gives

$$\frac{d^2}{dt^2} X(t) = \frac{F(t)}{m} = \frac{2P(t)}{mc} \tag{3.70}$$

where m is the mirror mass, $\delta F(t)$ is the radiation force, and $\delta P(t)$ is the circulating radiation power.

In the frequency domain, the differential equation is rewritten as

$$X(\Omega) = -\frac{2P(\Omega)}{mc\Omega^2} \tag{3.71}$$

Therefore, the motions of each mirror caused by radiation pressure are

$$\delta X_1(\Omega) = -\frac{2(-P_1(\Omega))}{mc\Omega^2} \quad \text{and} \quad \delta X_2(\Omega) = -\frac{2P_2(\Omega)}{mc\Omega^2} \tag{3.72}$$

and they modulate the cavity length $L(t)$ to produce a field fluctuation.

$$L(t) = L + \delta L(t) \tag{3.73}$$

where $\delta L(t) = \delta X_2(t) - \delta X_1(t)$ is the dynamic part due to radiation pressure noise. In general, the fluctuation of the reflection field is

$$\vec{G}(t) = \left(\mathbf{r}_{\text{cav}}(\phi, \Omega = 0) + \frac{\delta \mathbf{r}_{\text{cav}}(\phi, \Omega = 0)}{\delta \phi} \delta\phi \right) \vec{F} \tag{3.74}$$

$$= \mathbf{r}_{\text{cav}} \vec{F} + \frac{\delta \mathbf{r}_{\text{cav}}}{\delta \phi}(\Omega = 0) \frac{\omega_0}{c} \delta L(t) \vec{F} \tag{3.75}$$

Including the quantum fluctuation parts, the total reflected field is

$$E_g(t, x) = \vec{\omega}_0^{\mathrm{T}}(t) \left[\vec{G}(t) + \sqrt{\frac{\hbar\omega_0}{2}} \int \frac{d\Omega}{2\pi} \, \vec{g} e^{i\Omega t} \right] \tag{3.76}$$

$$= \vec{\omega}_0^{\mathrm{T}}(t) \left[\mathbf{r}_{\text{cav}} \vec{F} + \frac{\delta \mathbf{r}_{\text{cav}}}{\delta \phi}(\Omega) \frac{\omega_0}{c} \vec{F} \int \frac{d\Omega}{2\pi} \, \delta L(\Omega) e^{i\Omega t} + \sqrt{\frac{\hbar\omega_0}{2}} \int \frac{d\Omega}{2\pi} \, \vec{g} e^{i\Omega t} \right] \tag{3.77}$$

The radiation pressure term can be merged with the shot noise term because they are of the

same order of magnitude, which will be shown.

$$\delta E_g(\Omega) = \sqrt{\frac{\hbar\omega_0}{2}}\vec{g}(\Omega) + \frac{\delta \mathbf{r}_{\text{cav}}}{\delta\phi}(\Omega)\frac{\omega_0}{c}\vec{F}\delta L(\Omega) \tag{3.78}$$

where

$$\delta L(\Omega) = -\frac{2}{mc\Omega^2}(P_1(\Omega) + P_2(\Omega)) \tag{3.79}$$

$$= -\frac{2}{mc\Omega^2}\sqrt{2\hbar\omega_0}[J^\dagger \vec{j}(\Omega) + K^\dagger \vec{k}(\Omega)] \tag{3.80}$$

$$= -\frac{2}{mc\Omega^2}\sqrt{2\hbar\omega_0}\vec{F}^\dagger \mathbf{g}_{\text{cav}}^\dagger \mathbf{g}_{\text{cav}}(\Omega)\left[(e^{-i\varphi} + r_2^2 e^{-i2\varphi})\vec{f} - (r_1 e^{-i\varphi} + r_2)\frac{t_2}{t_1}\mathbf{R}(\pi N)\, e^{-i\varphi}\vec{q}\right] \tag{3.81}$$

This is the full solution without any approximation, to the first order of the quantum fluctuations. Plug it back to Eq. (3.76) and we have

$$\delta E_g(\Omega) = \sqrt{\frac{\hbar\omega_0}{2}}\vec{g}(\Omega) + \frac{\delta \mathbf{r}_{\text{cav}}}{\delta\phi}(\Omega)\frac{\omega_0}{c}\vec{F}\delta L(\Omega) + (...)\vec{q} \tag{3.82}$$

$$= \sqrt{\frac{\hbar\omega_0}{2}}\left[\mathbf{r}_{\text{cav}}(\Omega)\vec{f} - \underbrace{\frac{4\omega_0}{mc^2\Omega^2}\frac{\delta \mathbf{r}_{\text{cav}}}{\delta\phi}(\Omega)\vec{F}\vec{F}^\dagger \mathbf{g}_{\text{cav}}^\dagger \mathbf{g}_{\text{cav}}(\Omega)(e^{-i\varphi} + r_2^2 e^{-i2\varphi})\,\vec{f}}_{\mathscr{K}(\Omega)}\right] + (...)\vec{q} \tag{3.83}$$

$$= \sqrt{\frac{\hbar\omega_0}{2}}\mathbf{r}_{opto}(\Omega)\vec{f} + (...)\vec{q} \tag{3.84}$$

where

$$\mathbf{r}_{opto}(\Omega) = \mathbf{r}_{\text{cav}}(\Omega) - \mathscr{K}(\Omega) \tag{3.85}$$

The exact solution above can be approximated assuming $\mathbf{R}(2\phi) = \mathbf{1}$ for a resonant cavity.

$$\mathbf{r}_{opto}(\Omega) \approx \begin{bmatrix} r_{\rm cav}(\Omega) & 0 \\ -\mathcal{K}(\Omega) & r_{\rm cav}(\Omega) \end{bmatrix} \tag{3.86}$$

where $\mathbf{r}_{\rm cav}$ reduces to a diagonal matrix with diagonal element

$$r_{\rm cav}(\Omega) = \frac{r_1 - r_2 e^{-i2\varphi}}{1 - r_1 r_2 e^{-i2\varphi}} = \frac{r_1 - r_2 e^{i2\Omega L/c}}{1 - r_1 r_2 e^{i2\Omega L/c}} \tag{3.87}$$

and $\boldsymbol{\mathcal{K}}$ reduces to $[0 \;\; \mathcal{K}]^{\mathsf{T}}$ because

$$\mathbf{R}(\pi/2)\,\vec{F}\vec{F}^{\dagger} = F^2 \mathbf{R}(\pi/2) \begin{bmatrix} 1 & 0 \\ 0 & 0 \end{bmatrix} = F^2 \begin{bmatrix} 0 & 0 \\ 1 & 0 \end{bmatrix} \tag{3.88}$$

Assuming $\varphi \ll 1$ for a short cavity length, the optomechanical coupling coefficient can be approximated as

$$\mathcal{K}(\Omega) \approx \frac{8F^2\omega_0}{mc^2\Omega^2} \frac{\delta \mathbf{r}_{\rm cav}}{\delta\phi}(\Omega)\mathbf{g}_{\rm cav}\mathbf{g}_{\rm cav}(\Omega) \approx \frac{16P_{arm}\omega_0}{mc^2\Omega^2} g_{\rm cav}^2(\Omega) \tag{3.89}$$

using Eq. (3.59) and $P_{arm} = g_{\rm cav}^2 F^2$. We will derive the terms in the parenthesis before $\vec{q}$ later. Notice that the optomechanical coupling coefficient is consistent with KLMTV [36] and [33], which are written here

$$\mathcal{K}_{\rm KLMTV}(\Omega) = \frac{16P_{arm}\omega_0}{mc^2\Omega^2} g_{arm}^2(\Omega) \tag{3.90}$$

The extra minus sign comes from the phase convention or equivalently the Fourier transform convention.

The optomechanical coupling $\mathcal{K}$ is shown in Fig. 3-5. It's usually negligible when the cavity has a low finesse and a low circulating power. Observing back action is typically difficult and requires specific experimental design [42, 49]. The characteristic frequency where $\mathcal{K}(\Omega) = 1$ is

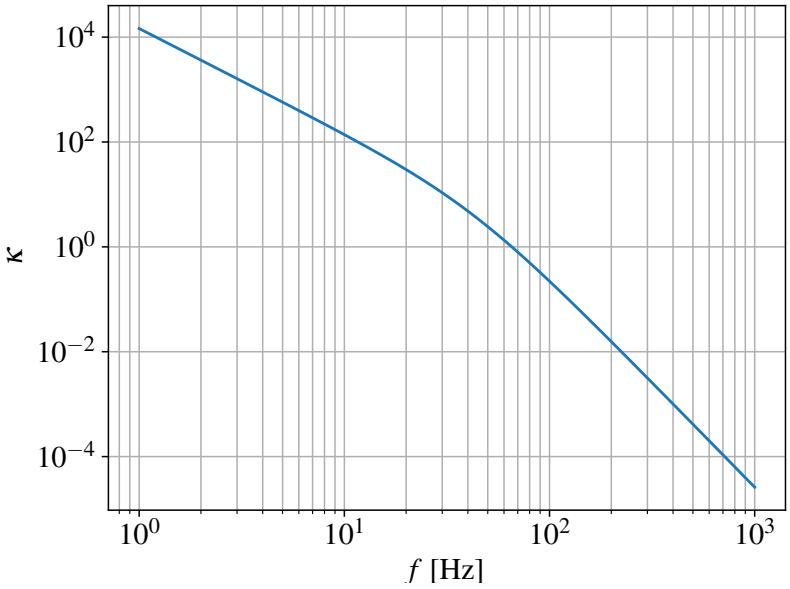

Figure 3-5: The magnitude of optomechanical coupling versus frequency. The parameters used to plot are from LIGO arm cavities. Note that $\mathcal{K} \sim 1/f^2$ at low frequencies where $\mathcal{K} \ll 1$, and $\mathcal{K} \sim 1/f^4$ at high frequencies where $\mathcal{K} \gg 1$.

defined as the SQL frequency Ω_{SQL} where SQL stands for Standard Quantum Limit. We will see where the name comes from in the next chapters.

There is one subtlety between this formalism (Eq. (3.89)) and KLMTV (Eq. (3.90)): the cavity gain $g(\Omega)$. In KLMTV, there is no signal-recycling cavity at the anti-symmetric port of the interferometer. The Advanced LIGO detector has a signal-recycling cavity, which forms an effective coupled cavity with arm cavities [50, 51]. The coupled cavity can be approximated with a single-cavity equation

$$g_{\mathrm{cav}}(\Omega) \approx \frac{\sqrt{\gamma_0 c/L}}{\gamma_0 + i\Omega} \tag{3.91}$$

Plug it back to Eq. (3.89) to approximate the SQL frequency assuming it is much less than the

linewidth of the coupled cavity $\Omega_{\mathrm{SQL}} \ll \gamma_0$

$$\Omega_{\mathrm{SQL}} \approx \sqrt{\frac{16 k_0 P_{arm}}{m \gamma_0 L}} = 2\pi \times 37\,\mathrm{Hz} \tag{3.92}$$

where $k_0 = \omega_0/c$. $P_{arm} = 260\,\mathrm{kW}$, $L_{arm} = 4000\,\mathrm{m}$, $m = 40\,\mathrm{kg}$, and $\gamma_0 \approx 2\pi \times 450\,\mathrm{Hz}$.

Conversely, the cavity has to have a high enough circulating power to see the quantum back action at frequencies where it's not submerged by other noises at low frequency, for example, seismic noises [52].

Besides the reflected field $\vec{f}$, the vacuum fluctuations $\vec{q}$ entering from the end mirror also experience the optomechanical effects that I didn't derive in Eq. (3.84). It can read off from Eq. (3.81)

$$\delta E_g(\Omega) = \sqrt{\frac{\hbar\omega_0}{2}} \left[\mathbf{r}_{opto}(\Omega)\vec{f} + \mathbf{t}_{\mathrm{cav}}(\Omega)\mathbf{R}(\pi N)\,\vec{q} - \mathscr{K}(\Omega)\frac{r_1 e^{-i\varphi} + r_2}{e^{-i\varphi} + r_2^2 e^{-i2\varphi}}\frac{t_2}{t_1}\mathbf{R}(\pi N)\, e^{-i\varphi}\vec{q} \right] \tag{3.93}$$

$$= \sqrt{\frac{\hbar\omega_0}{2}} \left[\mathbf{r}_{opto}(\Omega)\vec{f} + \mathbf{t}_{opto}(\Omega)\vec{q} \right] \tag{3.94}$$

where (assuming short cavity $e^{-i\varphi} \approx 1$)

$$\mathbf{t}_{opto}(\Omega) \approx \mathbf{R}(\pi N) \begin{bmatrix} \mathbf{t}_{\mathrm{cav}}(\Omega) & 0 \\ \dfrac{t_2}{t_1}\mathscr{K}(\Omega) & \mathbf{t}_{\mathrm{cav}}(\Omega) \end{bmatrix} \tag{3.95}$$

The optomechanical coupling for the vacuum entering from end mirror is reduced by a factor of t_2/t_1 for an overcoupled cavity.

In summary, the input-output relation for a Fabry-Pérot cavity, including optomechanical coupling, is

$$\vec{g}(\Omega) = \mathbf{r}_{opto}(\Omega)\vec{f} + \mathbf{t}_{opto}(\Omega)\vec{q} \tag{3.96}$$

where $\mathbf{r}_{opto}$ is Eq. (3.85) with approximation in Eq. (3.86), and $\mathbf{t}_{opto}$ is Eq. (3.93) approximated in Eq. (3.95).

3.5 Advanced LIGO

The Advanced LIGO is a dual-recycled Fabry-Pérot Michelson interferometer. We can derive its full input-output relations from the tools developed in the previous section.

3.5.1 Lossy Fabry-Pérot cavity

For a lossy cavity, it can be thought as a cavity with a beam splitter inserted inside. If we only care about the reflected fields for an overcoupled cavity ($t_3 \sim t_2 \ll t_1$), we can assign the transmission to the end mirror because they are degenerate. However, the vacuum leaked from the free space is different from those from the end mirror. It is not correct to attribute diffraction loss to the end mirror. The better model of a lossy cavity is shown in Fig. 3-6. Besides the two equations

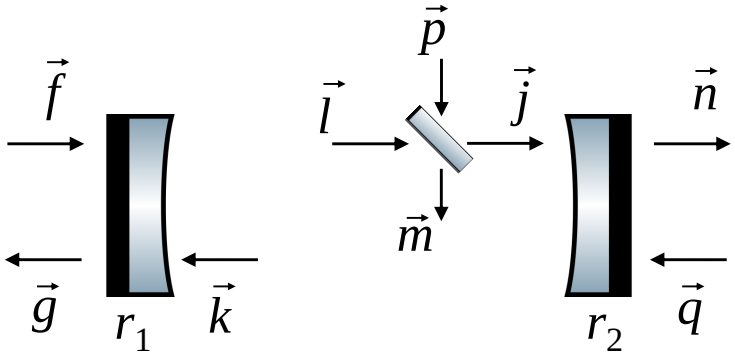

Figure 3-6: Lossy Fabry-Pérot cavity with input and output fields. An additional mirror 3 is inserted to act as a loss source. The (-1) is assigned to the anti-reflective surface of the middle mirror, unlike other mirrors.

written for the two mirrors of the cavity in Eq. (3.23) and Eq. (3.24), there is an extra one for the

beam splitter inside.

$$\begin{bmatrix} \vec{g} \\ \mathbf{R}(-\phi)\, e^{i\varphi}\vec{l} \end{bmatrix} = \begin{bmatrix} r_1 & t_1 \\ t_1 & -r_1 \end{bmatrix} \begin{bmatrix} \vec{f} \\ \vec{k} \end{bmatrix} \tag{3.97}$$

$$\begin{bmatrix} \vec{n} \\ \mathbf{R}(-\phi)\, e^{i\varphi}\vec{k} \end{bmatrix} = \begin{bmatrix} r_2 & t_2 \\ t_2 & -r_2 \end{bmatrix} \begin{bmatrix} \vec{q} \\ \vec{j} \end{bmatrix} \tag{3.98}$$

$$\begin{bmatrix} \vec{j} \\ \vec{m} \end{bmatrix} = \begin{bmatrix} r_3 & t_3 \\ t_3 & -r_3 \end{bmatrix} \begin{bmatrix} \vec{l} \\ \vec{p} \end{bmatrix} \tag{3.99}$$

where $t_3 = \sqrt{\text{loss}}$ is the loss source and at the same order of magnitude as t_2 ($t_2 \ll 1$). Here we assume the round-trip loss is due to the diffraction clipping of the end mirror. So the inserted beam splitter is infinitely closed to the end mirror. The new cavity reflection, transmission, and gain when on resonance are

$$\mathbf{r}_{\text{cav}}(\Omega) = \left(r_1\mathbf{1} - r_2 r_3 \mathbf{R}(2\phi)\, e^{-i2\varphi}\right)\left[\mathbf{1} - r_1 r_2 r_3 \mathbf{R}(2\phi)\, e^{-i2\varphi}\right]^{-1} \approx \frac{r_1 - r_2 r_3 e^{-i2\varphi}}{1 - r_1 r_2 r_3 e^{-i2\varphi}}\mathbf{1} \tag{3.100}$$

$$\mathbf{t}_{\text{cav}}(\Omega) = t_1 t_2 \mathbf{R}(\phi)\, e^{-i\varphi}\left[\mathbf{1} - r_1 r_2 r_3 \mathbf{R}(2\phi)\, e^{-i2\varphi}\right]^{-1} \approx \frac{t_1 t_2 e^{-i\varphi}}{1 - r_1 r_2 r_3 e^{-i2\varphi}}\mathbf{R}(\pi N) \tag{3.101}$$

$$\mathbf{g}_{\text{cav}}(\Omega) = t_1 r_3 \mathbf{R}(\phi)\, e^{-i\varphi}\left[\mathbf{1} - r_1 r_2 r_3 \mathbf{R}(2\phi)\, e^{-i2\varphi}\right]^{-1} \approx \frac{t_1 r_3 e^{-i\varphi}}{1 - r_1 r_2 r_3 e^{-i2\varphi}}\mathbf{R}(\pi N) \tag{3.102}$$

with approximation applied when the cavity is on resonance. Note that the operations with $f(\mathbf{R})$ commutes with $\mathbf{R}$, just like the complex numbers commute (you can prove it using Taylor expansions). It's slightly different from previous equations (Eq. (3.25), Eq. (3.33)) by adding a r_3 to the r_2 to make for the total optics seen in a round-trip. Knowing the cavity elements, one can easily write out the reflection and transmission by observing the round trip traveled by light and putting them in the numerator. The denominator is the same $1 -$ (round trip).

The fields circulating in the cavity are

$$\vec{J} = \mathbf{g}_{\rm cav}\vec{F} \tag{3.103}$$

with quantum-mechanical part

$$\vec{j} = \mathbf{g}_{\rm cav}(\Omega)\left[\vec{f} - \frac{r_1 t_2}{t_1}\mathbf{R}(\phi)\, e^{-i\varphi}\vec{q} + \frac{t_3}{t_1 r_3}\mathbf{R}(-\phi)\, e^{i\varphi}\vec{p}\right] \tag{3.104}$$

and

$$\vec{K} = -r_2\mathbf{g}_{\rm cav}\mathbf{R}(\phi)\,\vec{F} \tag{3.105}$$

with quantum part

$$\vec{k} = \mathbf{g}_{\rm cav}(\Omega)\left[-r_2\mathbf{R}(\phi)\, e^{-i\varphi}\vec{f} + \frac{t_2}{t_1 r_3}\vec{q} - \frac{r_2 t_3}{t_1 r_3}\vec{p}\right] \tag{3.106}$$

These two fields are contributing to the radiation pressure on the cavity mirrors, whereas $\vec{L}$ doesn't.

The cavity length fluctuation due to the radiation pressure is

$$\delta L(\Omega) = -\frac{2}{mc\Omega^2}(P_1(\Omega) + P_2(\Omega)) = -\frac{2}{mc\Omega^2}\sqrt{2\hbar\omega_0}[\vec{J}^\dagger\vec{j}(\Omega) + \vec{K}^\dagger\vec{k}(\Omega)] \tag{3.107}$$

$$= -\frac{2}{mc\Omega^2}\sqrt{2\hbar\omega_0}\vec{F}^\dagger\mathbf{g}_{\rm cav}^\dagger\mathbf{g}_{\rm cav}(\Omega)\times \tag{3.108}$$

$$\left[(1 + r_2^2 e^{-i\varphi})\vec{f} - \frac{t_2}{t_1}\left(r_1\mathbf{R}(\phi)\, e^{-i\varphi} + \frac{r_2}{r_3}\mathbf{R}(-\phi)\right)\vec{q} + (e^{i\varphi} + r_2^2)\frac{t_3}{t_1 r_3}\mathbf{R}(-\phi)\,\vec{p}\right] \tag{3.109}$$

The ratio between cavity round-trip loss and end mirror transmission is roughly t_3/t_2, as seen from

the previous equation. The sidebands of the reflected field caused by cavity length fluctuation is

$$\delta E(\Omega) = \frac{\delta \mathbf{r}_{\text{cav}}}{\delta \phi}(\Omega)\frac{\omega_0}{c}\vec{F}\delta L(\Omega) \tag{3.110}$$

$$= -\sqrt{\frac{\hbar\omega_0}{2}}\frac{4\omega_0}{mc^2\Omega^2}\frac{\delta \mathbf{r}_{\text{cav}}}{\delta \phi}(\Omega)\vec{F}\vec{F}^{\dagger}g_{\text{cav}}^{\dagger}\mathbf{g}_{\text{cav}}(\Omega)\times \tag{3.111}$$

$$\left[(1+r_2^2e^{-i\varphi})\vec{f} - \frac{t_2}{t_1}\left(r_1\mathbf{R}(\phi)\,e^{-i\varphi} + \frac{r_2}{r_3}\mathbf{R}(-\phi)\right)\vec{q} + (e^{i\varphi}+r_2^2)\frac{t_3}{t_1 r_3}\mathbf{R}(-\phi)\,\vec{p}\right] \tag{3.112}$$

where

$$\frac{\delta \mathbf{r}_{\text{cav}}}{\delta \phi}(\Omega) = -r_2 r_3(1+e^{i\varphi})\mathbf{R}\left(\frac{\pi}{2}\right)\mathbf{g}_{\text{cav}}(0)\mathbf{g}_{\text{cav}}(\Omega) + \mathcal{O}\left(\frac{\Omega}{\omega_0}\right) \tag{3.113}$$

Summing it up with the cavity reflection without optomechanical coupling, the final reflected field is

$$\vec{g}(\Omega) = \mathbf{r}_{opto}(\Omega)\vec{f} + \mathbf{t}_{opto}(\Omega)\vec{q} + \mathbf{l}_{opto}(\Omega)\vec{p} \tag{3.114}$$

where $\mathbf{r}_{opto}$ is identical to Eq. (3.85)

$$\mathbf{r}_{opto}(\Omega) = \mathbf{r}_{\text{cav}}(\Omega) - \mathscr{K}_r(\Omega) \tag{3.115}$$

with

$$\mathscr{K}_r(\Omega) = \frac{4\omega_0}{mc^2\Omega^2}(1+r_2^2e^{-i\varphi})\frac{\delta \mathbf{r}_{\text{cav}}}{\delta \phi}(\Omega)\vec{F}\vec{F}^{\dagger}g_{\text{cav}}^{\dagger}\mathbf{g}_{\text{cav}}(\Omega) \tag{3.116}$$

The transmission matrix is

$$\mathbf{t}_{opto}(\Omega) = \mathbf{t}_{\text{cav}}(\Omega) - \mathscr{K}_t(\Omega) \tag{3.117}$$

with

$$\mathscr{K}_t(\Omega) = -\frac{4\omega_0}{mc^2\Omega^2}\frac{t_2}{t_1}\left(r_1\mathbf{R}(\phi)\,e^{-i\varphi} + \frac{r_2}{r_3}\mathbf{R}(-\phi)\right)\frac{\delta \mathbf{r}_{\text{cav}}}{\delta \phi}(\Omega)\vec{F}\vec{F}^{\dagger}g_{\text{cav}}^{\dagger}\mathbf{g}_{\text{cav}}(\Omega) \tag{3.118}$$

and the loss matrix is

$$\mathbf{l}_{opto}(\Omega) = \mathbf{l}_{\mathrm{cav}}(\Omega) - \mathscr{K}_l(\Omega) \tag{3.119}$$

where

$$\mathbf{l}_{\mathrm{cav}}(\Omega) = t_1 r_2 t_3 \mathbf{R}(\phi)\, e^{-i\varphi} \left[\mathbf{1} - r_1 r_2 r_3 \mathbf{R}(2\phi)\, e^{-i2\varphi}\right]^{-1} \approx -\frac{t_1 r_2 t_3 e^{-i\varphi}}{1 - r_1 r_2 r_3 e^{-i2\varphi}}\mathbf{1} \tag{3.120}$$

and

$$\mathscr{K}_l(\Omega) = \frac{4\omega_0}{mc^2\Omega^2}(e^{i\varphi} + r_2^2)\frac{t_3}{t_1 r_3}\mathbf{R}(-\phi)\,\frac{\delta \mathbf{r}_{\mathrm{cav}}}{\delta\phi}(\Omega)\vec{F}\vec{F}^{\dagger} g_{\mathrm{cav}}^{\dagger}\mathbf{g}_{\mathrm{cav}}(\Omega) \tag{3.121}$$

Again, the ratio between vacuum from loss and that from end mirror transmission is $\mathscr{K}_l/\mathscr{K}_t \sim t_3/t_2$. Approximately, the total vacuum leaked is the sum of these two as if they are degenerate. Notice that even though the loss vacuum didn't enter the cavity through one of the massive mirrors, it is still imprinted by the optomechanical coupling.

3.5.2 Michelson interferometer

The Michelson interferometer is the last puzzle for the Advanced LIGO topology. An interferometer is an extremely sensitive device relying on the interference of two beams traveling in different paths, as shown in Fig. 3-7.

There are two input-output relations for the center beam splitter

$$\begin{bmatrix} \vec{f}_y \\ \vec{f}_x \end{bmatrix} = \frac{1}{\sqrt{2}}\begin{bmatrix} \mathbf{1} & \mathbf{1} \\ \mathbf{1} & -\mathbf{1} \end{bmatrix}\begin{bmatrix} \vec{d} \\ \vec{a} \end{bmatrix} = \mathbf{H}_{\mathrm{BS}}\begin{bmatrix} \vec{d} \\ \vec{a} \end{bmatrix} \tag{3.122}$$

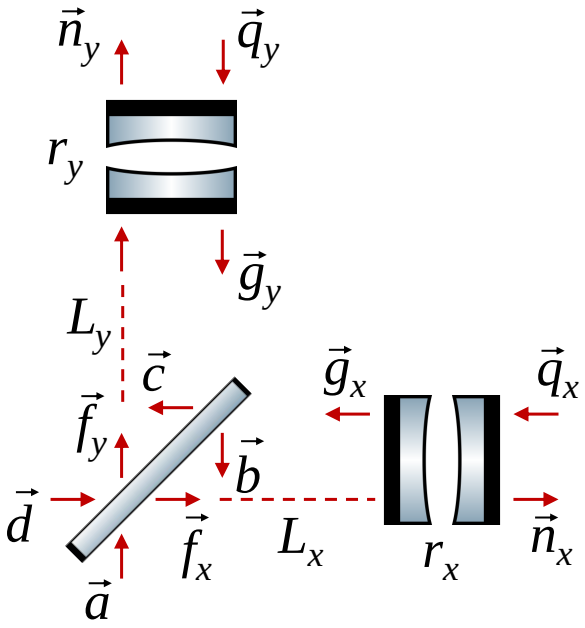

Figure 3-7: Michelson interferometer with path length L_x and L_y. The arm cavity can be thought of as a simple mirror with a frequency-dependent reflectivity.

The center beam splitter is balanced for Michelson.

$$\begin{bmatrix} \vec{c} \\ \vec{b} \end{bmatrix} = \mathbf{H}_{\mathrm{BS}} \begin{bmatrix} \mathbf{R}\left(\phi_y\right) e^{-i\varphi_y} \vec{g}_y \\ \mathbf{R}\left(\phi_x\right) e^{-i\varphi_x} \vec{g}_x \end{bmatrix} \tag{3.123}$$

where $\phi_y = \omega_0 L_y/c$ and $\varphi_y = \Omega L_y/c$. The symmetric or bright port of the Michelson is $\vec{c}$, and the anti-symmetric or dark port is $\vec{b}$. The equation for end mirrors are

$$\begin{bmatrix} \vec{g}_y \\ \vec{n}_y \end{bmatrix} = \begin{bmatrix} r_y & t_y \\ t_y & -r_y \end{bmatrix} \begin{bmatrix} \mathbf{R}\left(\phi_y\right) e^{-i\varphi_y} \vec{f}_y \\ \vec{q}_y \end{bmatrix} \tag{3.124}$$

$$\begin{bmatrix} \vec{g}_x \\ \vec{n}_x \end{bmatrix} = \begin{bmatrix} r_x & t_x \\ t_x & -r_x \end{bmatrix} \begin{bmatrix} \mathbf{R}\left(\phi_x\right) e^{-i\varphi_x} \vec{f}_x \\ \vec{q}_x \end{bmatrix} \tag{3.125}$$

For the Advanced LIGO, the end mirrors are 4-km long Fabry-Pérot cavities, also known as the arm cavities. Therefore, we can simplify Eq. (3.124) and Eq. (3.125) using Eq. (3.114).

$$\begin{bmatrix} \vec{g}_y \\ \vec{g}_x \end{bmatrix} = \begin{bmatrix} \mathbf{r}_{optoy}\mathbf{R}\left(\phi_y\right) e^{-i\varphi_y} & 0 \\ 0 & \mathbf{r}_{optox}\mathbf{R}\left(\phi_x\right) e^{-i\varphi_x} \end{bmatrix} \begin{bmatrix} \vec{f}_y \\ \vec{f}_x \end{bmatrix} + \begin{bmatrix} \mathbf{t}_{optoy} & 0 \\ 0 & \mathbf{t}_{optox} \end{bmatrix} \begin{bmatrix} \vec{q}_y \\ \vec{q}_x \end{bmatrix} + \begin{bmatrix} \mathbf{l}_{optoy} & 0 \\ 0 & \mathbf{l}_{optox} \end{bmatrix} \begin{bmatrix} \vec{p}_y \\ \vec{p}_x \end{bmatrix} \tag{3.126}$$

If both $\vec{q}$ and $\vec{p}$ are just unsqueezed vacuum, they can be combined to give an effective loss. The total input-output relation is

$$\begin{bmatrix} \vec{c} \\ \vec{b} \end{bmatrix} = \mathbf{h}_{\mathrm{MICH}} \begin{bmatrix} \vec{d} \\ \vec{a} \end{bmatrix} + \mathbf{l}_{\mathrm{MICHq}} \begin{bmatrix} \vec{q}_y \\ \vec{q}_x \end{bmatrix} + \mathbf{l}_{\mathrm{MICHp}} \begin{bmatrix} \vec{p}_y \\ \vec{p}_x \end{bmatrix} \tag{3.127}$$

where the Michelson transfer function is

$$\mathbf{h}_{\mathrm{MICH}} = \mathbf{H}_{\mathrm{BS}} \begin{bmatrix} \mathbf{R}\left(\phi_y\right) \mathbf{r}_{optoy} \mathbf{R}\left(\phi_y\right) e^{-i2\varphi_y} & 0 \\ 0 & \mathbf{R}\left(\phi_x\right) \mathbf{r}_{optox} \mathbf{R}\left(\phi_x\right) e^{-i2\varphi_x} \end{bmatrix} \mathbf{H}_{\mathrm{BS}} \tag{3.128}$$

and the loss transfer functions are

$$\mathbf{l}_{\mathrm{MICHq}} = \mathbf{H}_{\mathrm{BS}} \begin{bmatrix} \mathbf{R}\left(\phi_y\right) \mathbf{t}_{optoy} e^{-i\varphi_y} & 0 \\ 0 & \mathbf{R}\left(\phi_x\right) \mathbf{t}_{optox} e^{-i\varphi_x} \end{bmatrix} \tag{3.129}$$

$$\mathbf{l}_{\mathrm{MICHp}} = \mathbf{H}_{\mathrm{BS}} \begin{bmatrix} \mathbf{R}\left(\phi_y\right) \mathbf{l}_{optoy} e^{-i\varphi_y} & 0 \\ 0 & \mathbf{R}\left(\phi_x\right) \mathbf{l}_{optox} e^{-i\varphi_x} \end{bmatrix} \tag{3.130}$$

I use **h** for transfer functions relating to the quantum parts and **H** are for the classical transfer functions. The classical parts are easier to derive by removing the quantum-mechanical dependence such as the additional sideband phase φ.

$$\begin{bmatrix} C \\ B \end{bmatrix} = \mathbf{H}_{\mathrm{MICH}} \begin{bmatrix} D \\ A \end{bmatrix} \tag{3.131}$$

where

$$\mathbf{H}_{\mathrm{MICH}} = \mathbf{H}_{\mathrm{BS}} \begin{bmatrix} r_{yarm}\mathbf{R}\left(2\phi_y\right) & 0 \\ 0 & r_{xarm}\mathbf{R}\left(2\phi_x\right) \end{bmatrix} \mathbf{H}_{\mathrm{BS}} \tag{3.132}$$

3.5.3 Recycling cavities

The core optics of the Advanced LIGO is a dual-recycled Fabry-Pérot Michelson interferometer (DRFPMI), as shown in Fig. 3-8. The dual-recycling means power-recycling and signal-recycling, although the latter of which should be called resonant sideband extraction. That's also the reason why the signal-recycling cavity is sometimes referred to as the signal extraction cavity. The dual-cycling cavities are enabled by the two extra mirrors (beam splitters) at the symmetric and anti-symmetric ports.

Denote the single-trip phase as $\phi_p = \omega_0 L_p/c$ and $\varphi_p = \Omega L_p/c$, where L_p is the power-recycling cavity length. Denote ϕ_s for the signal-recycling cavity length L_s. The input-output relation for a

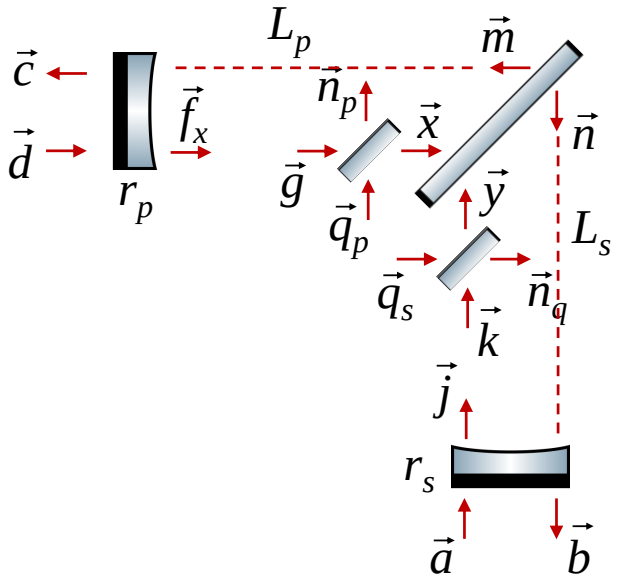

Figure 3-8: The dual recycling cavities. The Michelson part is simplified as a central beam splitter

Michelson interferometer has been worked out in the previous section (Eq. (3.127)).

$$\begin{bmatrix} \vec{m} \\ \vec{n} \end{bmatrix} = \mathbf{h}_{\mathrm{MICH}} \begin{bmatrix} \vec{x} \\ \vec{y} \end{bmatrix} + \mathbf{l}_{\mathrm{MICHq}} \begin{bmatrix} \vec{q}_y \\ \vec{q}_x \end{bmatrix} + \mathbf{l}_{\mathrm{MICHp}} \begin{bmatrix} \vec{p}_y \\ \vec{p}_x \end{bmatrix} = \mathbf{h}_{\mathrm{MICH}} \begin{bmatrix} \vec{x} \\ \vec{y} \end{bmatrix} + \sum_i \mathbf{l}_i \vec{q}_i \tag{3.133}$$

where $\vec{q}$ and $\vec{p}$ are vacuum fields introduced due to loss in the arm cavity. The equations for the two recycling mirrors are

$$\begin{bmatrix} \vec{c} \\ \vec{f} \end{bmatrix} = \begin{bmatrix} r_p & t_p \\ t_p & -r_p \end{bmatrix} \begin{bmatrix} \vec{d} \\ \mathbf{R}(\phi_p)\, e^{-i\varphi_p} \vec{m} \end{bmatrix} \tag{3.134}$$

$$\begin{bmatrix} \vec{x} \\ \vec{n}_p \end{bmatrix} = \begin{bmatrix} r_{pl} & t_{pl} \\ t_{pl} & -r_{pl} \end{bmatrix} \begin{bmatrix} \mathbf{R}(\phi_p)\, e^{-i\varphi_p} \vec{f} \\ \vec{q}_p \end{bmatrix} \tag{3.135}$$

where $t_{pl} = \sqrt{\text{loss}}$ acts as an effective loss in the power-recycling cavity. Similarly, the signal-recycling cavity has

$$\begin{bmatrix} \vec{b} \\ \vec{j} \end{bmatrix} = \begin{bmatrix} r_s & t_s \\ t_s & -r_s \end{bmatrix} \begin{bmatrix} \vec{a} \\ \mathbf{R}\left(\phi_s\right) e^{-i\varphi_s} \vec{n} \end{bmatrix} \tag{3.136}$$

$$\begin{bmatrix} \vec{y} \\ \vec{n}_q \end{bmatrix} = \begin{bmatrix} r_{sl} & t_{sl} \\ t_{sl} & -r_{sl} \end{bmatrix} \begin{bmatrix} \mathbf{R}\left(\phi_s\right) e^{-i\varphi_s} \vec{j} \\ \vec{q}_s \end{bmatrix} \tag{3.137}$$

The power recycling cavity is always locked on resonance to maximize the circulating power in the arm cavity ($\phi_p = \pi N$). The signal-recycling cavity, however, can be locked with carefully selected offset to maximize the sensitivity at certain frequency bands [53]. The two common configurations are $\phi_s = 0$ for extreme signal-recycling and $\phi_s = \pi/2$ for extreme resonant-sideband extraction [39].

It's possible to write out the transfer function by the trick of propagating each element in the cavity loop. However, the order of the elements matters in this double cavity calculation. Therefore, I will still derive the relations from the equations given above.

The equation for the effective lossy mirror is

$$\begin{bmatrix} \vec{x} \\ \vec{y} \end{bmatrix} = \mathbf{r_l e} \begin{bmatrix} \vec{f} \\ \vec{j} \end{bmatrix} + \mathbf{t_l} \begin{bmatrix} \vec{q}_p \\ \vec{q}_s \end{bmatrix} \tag{3.138}$$

where the reflection and transmission matrices are all diagonal

$$\mathbf{r_l} = \begin{bmatrix} r_{pl} & 0 \\ 0 & r_{sl} \end{bmatrix} \tag{3.139}$$

$$\mathbf{t_l} = \begin{bmatrix} t_{pl} & 0 \\ 0 & t_{sl} \end{bmatrix} \tag{3.140}$$

and the propagation matrix is also diagonal

$$\mathbf{e} = \begin{bmatrix} \mathbf{R}\left(\phi_p\right) e^{-i\varphi_p} & 0 \\ 0 & \mathbf{R}\left(\phi_s\right) e^{-i\varphi_s} \end{bmatrix} \tag{3.141}$$

The round-trip transfer function is

$$\begin{bmatrix} \vec{f} \\ \vec{j} \end{bmatrix} = -\mathbf{re} \begin{bmatrix} \vec{m} \\ \vec{n} \end{bmatrix} + \mathbf{t} \begin{bmatrix} \vec{d} \\ \vec{a} \end{bmatrix} \tag{3.142}$$

where the recycling mirrors' reflection and transmission are

$$\mathbf{r} = \begin{bmatrix} r_p & 0 \\ 0 & r_s \end{bmatrix} \tag{3.143}$$

$$\mathbf{t} = \begin{bmatrix} t_p & 0 \\ 0 & t_s \end{bmatrix} \tag{3.144}$$

Using Eq. (3.127), we have

$$\begin{bmatrix} \vec{f} \\ \vec{j} \end{bmatrix} = (1 + \mathbf{reh}_{\mathrm{MICH}}\mathbf{r_l e})^{-1} \left(\mathbf{t} \begin{bmatrix} \vec{d} \\ \vec{a} \end{bmatrix} - \mathbf{reh}_{\mathrm{MICH}}\mathbf{t_l} \begin{bmatrix} \vec{q}_p \\ \vec{q}_s \end{bmatrix} - \mathbf{re} \sum_i \mathbf{l}_i \vec{q}_i \right) \tag{3.145}$$

Therefore, the input-output relation for the double cavity is

$$\begin{bmatrix} \vec{c} \\ \vec{b} \end{bmatrix} = \mathbf{r} \begin{bmatrix} \vec{d} \\ \vec{a} \end{bmatrix} + \mathbf{te} \begin{bmatrix} \vec{m} \\ \vec{n} \end{bmatrix} \tag{3.146}$$

$$= \mathbf{h}_{\mathrm{DC}}(\Omega) \begin{bmatrix} \vec{d} \\ \vec{a} \end{bmatrix} + \mathbf{l}_{\mathrm{DCq}} \begin{bmatrix} \vec{q}_p \\ \vec{q}_s \end{bmatrix} + \mathbf{l}_{\mathrm{DCm}} \sum_i \mathbf{l}_i \vec{q}_i \tag{3.147}$$

where

$$\mathbf{h}_{\mathrm{DC}}(\Omega) = \mathbf{r} + \mathbf{teh}_{\mathrm{MICH}}\mathbf{r_l e}(1 + \mathbf{reh}_{\mathrm{MICH}}\mathbf{r_l e})^{-1}\mathbf{t} = \frac{\mathbf{r} + \mathbf{eh}_{\mathrm{MICH}}\mathbf{r_l e}}{\mathbf{1} + \mathbf{reh}_{\mathrm{MICH}}\mathbf{r_l e}} + \text{Commutators} \tag{3.148}$$

is the transfer function for the doubly coupled cavity, and

$$\mathbf{l}_{\mathrm{DCq}} = \mathbf{te}\left(\mathbf{1} - \mathbf{h}_{\mathrm{MICH}}\mathbf{r_l e}(1 + \mathbf{reh}_{\mathrm{MICH}}\mathbf{r_l e})^{-1}\mathbf{re}\right)\mathbf{h}_{\mathrm{MICH}}\mathbf{t_l} = \frac{\mathbf{teh}_{\mathrm{MICH}}\mathbf{t_l}}{\mathbf{1} + \mathbf{reh}_{\mathrm{MICH}}\mathbf{r_l e}} + \text{Commutators} \tag{3.149}$$

$$\mathbf{l}_{\mathrm{DCm}} = \mathbf{te}\left(\mathbf{1} - \mathbf{h}_{\mathrm{MICH}}\mathbf{r_l e}(1 + \mathbf{reh}_{\mathrm{MICH}}\mathbf{r_l e})^{-1}\mathbf{re}\right) = \frac{\mathbf{te}}{\mathbf{1} + \mathbf{reh}_{\mathrm{MICH}}\mathbf{r_l e}} + \text{Commutators} \tag{3.150}$$

are the transfer functions for the losses from Michelson or the recycling cavities themselves. Note that the approximated form ignoring the commutators of Michelson matrix $\mathbf{h}_{\mathrm{MICH}}$ gives the identical form as if it's a single cavity, except for an extra minus sign absorbed in $\mathbf{h}_{\mathrm{MICH}}$. For example, let $\mathbf{h}_{\mathrm{MICH}} = -\mathbf{1}$ as if the Michelson is just a perfectly-reflective mirror. It can be shown that the transfer function of the double cavity is a diagonal matrix with no cross terms, which means that the two recycling cavities are totally independent of each other. They are just two separate cavities written together. Of course, the Michelson interferometer mixes the signals from bright and dark ports, and the ordering of matrices matters.

3.5.4 Readout chain

Besides DRFPMI, the readout chain of Advanced LIGO is composed of output mode cleaners and Faraday isolators. They can be simplified as beam splitters with some transmissions acting as losses. The output field before the mode cleaner is

$$\vec{b} = \begin{bmatrix} \mathbf{0} & \mathbf{1} \end{bmatrix} \begin{bmatrix} \vec{c} \\ \vec{b} \end{bmatrix} = \begin{bmatrix} \mathbf{0} & \mathbf{1} \end{bmatrix} \left(\mathbf{h}_{\mathrm{DC}}(\Omega) \begin{bmatrix} \vec{d} \\ \vec{a} \end{bmatrix} + \mathbf{l}_{\mathrm{DCq}} \begin{bmatrix} \vec{q}_p \\ \vec{q}_s \end{bmatrix} + \mathbf{l}_{\mathrm{DCm}} \sum_i \mathbf{l}_i \vec{q}_i \right) \tag{3.151}$$

$$= \begin{bmatrix} \mathbf{0} & \mathbf{1} \end{bmatrix} \left(\mathbf{h}_{\mathrm{DC}}(\Omega) \begin{bmatrix} \mathbf{1} \\ \mathbf{0} \end{bmatrix} \vec{d} + \mathbf{h}_{\mathrm{DC}}(\Omega) \begin{bmatrix} \mathbf{0} \\ \mathbf{1} \end{bmatrix} \vec{a} + \mathbf{l}_{\mathrm{DCq}} \begin{bmatrix} \mathbf{1} \\ \mathbf{0} \end{bmatrix} \vec{q}_p + \dots \right) \tag{3.152}$$

Inserting a beam splitter as the lossy source, we have the final quantum-mechanical part observed by the readout photodiode:

$$\vec{b} \to r_{\mathrm{RO}} \vec{b} + t_{\mathrm{RO}} \vec{q} \tag{3.153}$$

where $\vec{q}$ is the vacuum mixed and $t_{\mathrm{RO}} = \sqrt{\mathrm{loss}}$ is the readout loss. Interestingly, we still haven't touched the gravitational-wave signals yet, which will be discussed in the next section.

3.6 DC Readout Scheme

One of the famous questions on gravitational wave measurement is to identify the stretch of laser wavelength from the stretch of the 4-km arm cavity. It's like measuring a changing length with a changing ruler. The answer is that we are essentially measuring a time difference with a limited bandwidth. We won't be sensible at very high frequencies above the arm cavity pole. The time measurement will be calibrated to a gravitational wave strain measurement.

Suppose the gravitational wave enters the Advanced LIGO detector with amplitude h and perfect polarization and direction. One of the arm cavity length L would experience a stretch $hL/2$

and the other one would experience a contraction with the same amplitude.

$$\delta L \to \delta L \pm \frac{hL}{2} \tag{3.154}$$

Using Eq. (3.110), the additional field fluctuations due to gravitational wave is

$$\delta E(\Omega) \to \delta E(\Omega) + \frac{\delta \mathbf{r}_{\rm cav}}{\delta \phi}(\Omega)\frac{\omega_0}{c}\vec{F}\frac{hL}{2} \tag{3.155}$$

It's a purely classical effect, but it can be grouped into quantum-mechanical parts due to its infinitesimal nature. Using Eq. (3.114), the additional term from gravitational wave is

$$\vec{g}(\Omega) \to \vec{g}(\Omega) + h\mathbf{g}_{\rm GW}(\Omega) \tag{3.156}$$

where

$$\mathbf{g}_{\rm GW}(\Omega) = \sqrt{\frac{2}{\hbar\omega_0}}\frac{\omega_0 L}{2c}\frac{\delta \mathbf{r}_{\rm cav}}{\delta \phi}(\Omega)\vec{F} \tag{3.157}$$

If we apply the approximation with $r_i \sim 1$ and the classical laser is infinitely thin, we have

$$\mathbf{g}_{\rm GW} = \frac{\sqrt{\mathcal{K}}}{h_{\rm SQL}}\begin{bmatrix} 0 \\ 1 \end{bmatrix} \tag{3.158}$$

where $\mathcal{K}$ is the approximated in Eq. (3.83) and $h_{\rm SQL}$ is the standard quantum limit

$$h_{\rm SQL}(\Omega) = \sqrt{\frac{8\hbar}{m\Omega^2 L^2}} \tag{3.159}$$

The other arm, for example, X arm without loss of generality, experiences negative $hL/2$ and has

$$\vec{g}_x(\Omega) \to \vec{g}_x(\Omega) - h\mathbf{g}_{{\rm GW}x}(\Omega) \tag{3.160}$$

Therefore, the Michelson output Eq. (3.127) has an additional term

$$\begin{bmatrix} \vec{c} \\ \vec{b} \end{bmatrix} \to \begin{bmatrix} \vec{c} \\ \vec{b} \end{bmatrix} + h\mathbf{l}_{\mathrm{MICHh}} \begin{bmatrix} \mathbf{g}_{\mathrm{GW}y} \\ -\mathbf{g}_{\mathrm{GW}x} \end{bmatrix} \tag{3.161}$$

where

$$\mathbf{l}_{\mathrm{MICHh}} = \mathbf{H}_{\mathrm{BS}} \begin{bmatrix} \mathbf{R}\left(\phi_y\right) e^{-i\varphi_y} & 0 \\ 0 & \mathbf{R}\left(\phi_x\right) e^{-i\varphi_x} \end{bmatrix} \tag{3.162}$$

is analogous to the transfer function of loss in arm cavity Eq. (3.129). The final output of the DRFPMI is thus

$$\begin{bmatrix} \vec{c} \\ \vec{b} \end{bmatrix} = \mathbf{h}_{\mathrm{DC}}(\Omega) \begin{bmatrix} \vec{d} \\ \vec{a} \end{bmatrix} + \mathbf{l}_{\mathrm{DCq}} \begin{bmatrix} \vec{q}_p \\ \vec{q}_s \end{bmatrix} + \mathbf{l}_{\mathrm{DCm}} \sum_i \mathbf{l}_i \vec{q}_i + h\mathbf{l}_{\mathrm{DCm}}\mathbf{l}_{\mathrm{MICHh}} \begin{bmatrix} \mathbf{g}_{\mathrm{GW}y} \\ -\mathbf{g}_{\mathrm{GW}x} \end{bmatrix} \tag{3.163}$$

To calibrate the quantum noise to the gravitational wave signal, we need to isolate the contribution to the output field from gravitational waves.

$$\vec{b}\Big|_{\mathrm{GW}} = hr_{\mathrm{RO}} \begin{bmatrix} \mathbf{0} & \mathbf{1} \end{bmatrix} \mathbf{l}_{\mathrm{DCm}}\mathbf{l}_{\mathrm{MICHh}} \begin{bmatrix} \mathbf{g}_{\mathrm{GW}y} \\ -\mathbf{g}_{\mathrm{GW}x} \end{bmatrix} \tag{3.164}$$

The power fluctuation observed on the readout photodiode is

$$P(\Omega) = \sqrt{2\hbar\omega_0}\vec{B}_0^{\dagger}\vec{b}(\Omega) = hg_{\mathrm{cal}} \tag{3.165}$$

where g_{cal} is the calibration coefficient with the unit of Watt and $\vec{B}$ is the DC power leaked from the anti-symmetric port (therefore the DC readout) [54]. Therefore, the quantum noise calibrated

to strain is

$$S_h(\Omega) = \frac{S_P(\Omega)}{g_{\rm cal}^2} \tag{3.166}$$

where

$$S_P(\Omega) = 2\hbar\omega_0 \frac{\langle 0|\vec{B}^\dagger \vec{b}(\Omega)\vec{b}^\dagger(\Omega')\vec{B}|0\rangle_{sym}}{2\pi\delta(\Omega-\Omega')/2} \tag{3.167}$$

and

$$\vec{b} = \vec{b}\Big|_{\rm QN} = r_{\rm RO}\begin{bmatrix}\mathbf{0} & \mathbf{1}\end{bmatrix}\left(\mathbf{h}_{\rm DC}(\Omega)\begin{bmatrix}\vec{d}\\ \vec{a}\end{bmatrix} + \mathbf{l}_{\rm DCq}\begin{bmatrix}\vec{q}_p\\ \vec{q}_s\end{bmatrix} + \mathbf{l}_{\rm DCm}\sum_i \mathbf{l}_i\vec{q}_i\right) + t_{\rm RO}\vec{q}_{\rm RO} \tag{3.168}$$

The first step to calculate quantum noise is to find the classical field $\vec{F}_{x,y}$ required to get optomechanical coupling coefficients $\mathscr{K}$. Fortunately, everything is laid out and the classical field is just a special case with $\Omega = 0$. Using Eq. (3.122), Eq. (3.138), Eq. (3.145), we have

$$\begin{bmatrix}\vec{F}_y\\ \vec{F}_x\end{bmatrix} = \mathbf{H}_{\rm BS}\mathbf{r_l e}(1+\mathbf{reh}_{\rm MICH}\mathbf{r_l e})^{-1}\mathbf{t}\Big|_{\Omega=0}\begin{bmatrix}\vec{D}\\ \vec{A}\end{bmatrix} \tag{3.169}$$

where $\vec{D}$ and $\vec{A}$ are classical fields entering the symmetric and asymmetric port of Advanced LIGO.

Although Eq. (3.166) tells us exactly how to convert the measured quantum noise from W^2/Hz to strain^2/Hz, it is experimentally challenging to find the numerical values of g_{cal}. The process of measuring parameters of g_{cal} is called calibration, which is detailed in the next section.

3.7 Calibration

In Advanced LIGO, we use the photon calibrator (Pcal) to actively calibrate the response of the interferometer to a differential arm length at a specific frequency [55, 56]. Specifically, Pcal sends an intensity-modulated laser beam with a known power to the arm cavity mirror. The radiation pressure of the Pcal laser beam will drive the motion of the mirror at a very precise amplitude and frequency.

It's similar to the sensing of gravitational wave, but the Pcal line is only injected into one arm to create a displacement δL_{Pcal}.

$$\delta L \rightarrow \delta L + \delta L_{Pcal} \tag{3.170}$$

where

$$\delta L_{Pcal}(t) = A_{Pcal}\cos(\Omega_{Pcal} t) \tag{3.171}$$

$$\delta L_{Pcal}(\Omega) = A_{Pcal}\delta(\Omega - \Omega_{Pcal}) \tag{3.172}$$

Using Eq. (3.110), the additional field fluctuations due to the Pcal line is

$$\delta E(\Omega) \rightarrow \delta E(\Omega) + \frac{\delta \mathbf{r}_{\rm cav}}{\delta \phi}(\Omega)\frac{\omega_0}{c}\vec{F}\delta L_{Pcal}(\Omega) \tag{3.173}$$

Using Eq. (3.114), the additional term of the reflected field is

$$\vec{g}(\Omega) \rightarrow \vec{g}(\Omega) + \delta L_{Pcal}(\Omega)\mathbf{g}_{Pcaly}(\Omega) \tag{3.174}$$

where

$$\mathbf{g}_{Pcaly}(\Omega) = \sqrt{\frac{2}{\hbar\omega_0}}\frac{\omega_0}{c}\frac{\delta \mathbf{r}_{\rm cav}}{\delta \phi}(\Omega)\vec{F} = \frac{L}{2}\mathbf{g}_{\rm GW}(\Omega) \tag{3.175}$$

Therefore, the Michelson output Eq. (3.127) has an additional term

$$\begin{bmatrix} \vec{c} \\ \vec{b} \end{bmatrix} \rightarrow \begin{bmatrix} \vec{c} \\ \vec{b} \end{bmatrix} + \delta L_{Pcal}(\Omega) \mathbf{l}_{\mathrm{MICHh}} \begin{bmatrix} \mathbf{g}_{Pcaly} \\ 0 \end{bmatrix} \tag{3.176}$$

where

$$\mathbf{l}_{\mathrm{MICHh}} = \mathbf{H}_{\mathrm{BS}} \begin{bmatrix} \mathbf{R}\left(\phi_y\right) e^{-i\varphi_y} & 0 \\ 0 & \mathbf{R}\left(\phi_x\right) e^{-i\varphi_x} \end{bmatrix} \tag{3.177}$$

is analogous to the transfer function of loss in the arm cavity (Eq. (3.129)). The output of the interferometer has the contribution of Pcal injection

$$\vec{b}\Big|_{Pcal} = \delta L_{Pcal}(\Omega) r_{QE} t_{OMC} \mathbf{U}_{OMC} r_{\mathrm{RO}} \begin{bmatrix} \mathbf{0} & \mathbf{1} \end{bmatrix} \mathbf{l}_{\mathrm{DCm}} \mathbf{l}_{\mathrm{MICHh}} \begin{bmatrix} \mathbf{g}_{Pcaly} \\ 0 \end{bmatrix} \tag{3.178}$$

The power fluctuation observed on the readout photodiode is

$$P(\Omega) = \sqrt{2\hbar\omega_0} \vec{B}_0^{\dagger} \vec{b}(\Omega) = \delta L_{Pcal}(\Omega) g_{\mathrm{Pcal}} \tag{3.179}$$

where $\vec{B}$ is the classical part and g_{Pcal} is the calibration coefficient with the unit of Watt/meter. It can be read off from the root mean square of the photodiode current in mA and that of the Pcal line in meter.

Another piece of information from the Pcal line is the coupled cavity pole frequency. Assuming a simple single cavity pole, the transfer function is

$$G(f) = \frac{A}{1 + if/f_{CC}} \tag{3.180}$$

The pole frequency can be derived if we have a complex gain at a certain frequency

$$f_{CC} = -f \frac{\text{real}(\boldsymbol{G}(f))}{\text{imag}(\boldsymbol{G}(f))} \tag{3.181}$$

However, the actual system is a coupled cavity with unknown loss and detuning of the signal-recycling cavity. The mode-mismatches in the system would also break the single-pole approximation. We will explain more in the next few chapters why the coupled-cavity pole frequency isn't a good quantity to fit.

Here concludes the chapter on quantum noise. In this chapter, we provided a direct calculation of quantum noise from first principles. Then we derive input-output relations for the full Advanced LIGO detector, including all the optical losses happening everywhere. The formalism in this chapter is still limited to the field in the fundamental spatial mode of each cavity, assuming no mode-mismatches. We will show in the next chapter how to easily incorporate mode-mismatch in the quantum noise calculation by extending the field to the next higher-order spatial mode. We will also discuss how mode-mismatch would affect squeezing separately from optical losses.

4 FREQUENCY-DEPENDENT SQUEEZING

In Chapter 2, we discussed the squeezed states of light and examined how it is possible to reduce the quantum uncertainty without violating the Heisenberg uncertainty principle, by "squeezing" one quadrature of the light while "anti-squeezing" the conjugate quadrature. In Chapter 3, we introduced the formalism that directly calculates the quantum noise of the light. In this chapter, we will combine the knowledge from previous chapters and theoretically start squeezing the quantum noise of the LIGO detector.

4.1 Generation of Squeezing

The quantum mechanics of squeezing was introduced in Chapter 2; here we briefly recapitulate the theory. The squeezing operator is defined as

$$S(z) = e^{\frac{1}{2}(z^* a^2 - z(a^\dagger)^2)} \tag{4.1}$$

And here are some of its useful properties.

$$S^\dagger(z) = S(-z) \tag{4.2}$$

$$S^\dagger(z) a S(z) = a \cosh|z| - a^\dagger e^{-i\varphi} \sinh|z| \tag{4.3}$$

$$S(z)aS^{\dagger}(z) = a\cosh|z| + a^{\dagger}e^{-i\varphi}\sinh|z| \tag{4.4}$$

$$S^{\dagger}(z)a^{\dagger}S(z) = a^{\dagger}\cosh|z| - ae^{i\varphi}\sinh|z| \tag{4.5}$$

$$S(z)a^{\dagger}S^{\dagger}(z) = a^{\dagger}\cosh|z| + ae^{i\varphi}\sinh|z| \tag{4.6}$$

While Chapter 2 introduced squeezing in Schrödinger's picture, it is often useful to use Heisenberg's picture where the operators are evolving.

Since the light itself is made of infinite harmonic oscillators (Eq. (2.53))

$$E(t) = \vec{\omega}_0^{\mathrm{T}}(t)\left(\vec{A}_0 + \sqrt{\frac{\hbar\omega_0}{2}}\int\frac{d\Omega}{2\pi}\,\vec{a}(\Omega)e^{i\Omega t}\right) \tag{4.7}$$

where the quantum mode is

$$\vec{a} = \begin{bmatrix} a_1 \\ a_2 \end{bmatrix} = \underbrace{\frac{1}{\sqrt{2}}\begin{bmatrix} 1 & 1 \\ -i & i \end{bmatrix}}_{\mathbf{A}_2}\begin{bmatrix} a_+ \\ a_-^{\dagger} \end{bmatrix} \tag{4.8}$$

The squeezing operator is redefined as annihilating sideband at frequency $(\omega_0 \pm \Omega)$ and copying it over to the other side $(\omega_0 \mp \Omega)$

$$S(z) = e^{z^* a_+ a_- - z a_+^{\dagger} a_-^{\dagger}} \tag{4.9}$$

where $z = |z|e^{i2\phi}$. The re-definition of the phase can be understood from Eq. (2.29) in Chapter 2. The new properties are

$$S^{\dagger}(z) = S(-z) \tag{4.10}$$

$$S(z)a_{\pm}S^{\dagger}(z) = a_{\pm}\cosh|z| + a_{\mp}^{\dagger}e^{i2\phi}\sinh|z| \tag{4.11}$$

$$S^{\dagger}(z)a_{\pm}S(z) = S(-z)a_{\pm}S^{\dagger}(-z) = a_{\pm}\cosh|z| - a_{\mp}^{\dagger}e^{i2\phi}\sinh|z| \tag{4.12}$$

It can be shown that

$$S^{\dagger}(z)\vec{a}S(z) = \mathbf{R}(\phi)\,\mathbf{S_1}(|z|)\mathbf{R}(-\phi)\,\vec{a} \tag{4.13}$$

where

$$\mathbf{S_1} = \begin{bmatrix} e^{|z|} & \\ & e^{-|z|} \end{bmatrix} \tag{4.14}$$

The squeezing matrix $\mathbf{S_1}$ represents a one-time squeezing operation. It can be thought of as a single-pass of the nonlinear crystal in a real experiment. To enhance the squeezing, we put the crystal inside a resonant cavity to drastically increase the number of passes of light through the nonlinear medium.

Fig. 4-1 shows the nonlinear crystal sitting inside a resonant cavity. When the end mirror isn't perfectly reflective $r_2 < 1$, there is some vacuum $\vec{q}_2$ leaked into the squeezer cavity. The input-

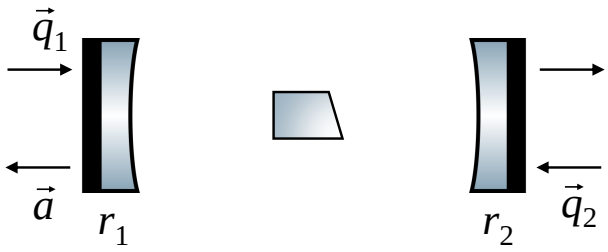

Figure 4-1: Vacuum $\vec{q}_1$ and $\vec{q}_2$ entering from different ports of the squeezer cavity, which enhances the nonlinear interaction by increasing the number of passes of the light through the crystal.

output relations give the reflectivity of the light from the input port of the squeezer

$$H_{\text{refl}} = (\mathbf{1} - (-r_1)(-r_2)\mathbf{S_1})^{-1} t_1^2 \mathbf{S_1}(-r_2) + r_1 \mathbf{1} \tag{4.15}$$

$$= \begin{bmatrix} r_1 - \dfrac{r_2 t_1^2 e^{z_1}}{1 - r_1 r_2 e^{z_1}} & \\ & r_1 - \dfrac{r_2 t_1^2 e^{-z_1}}{1 - r_1 r_2 e^{-z_1}} \end{bmatrix} \tag{4.16}$$

$$= \mathbf{S}_r \tag{4.17}$$

Similarly, the transfer function of the vacuum $\vec{q}_2$ transmission is

$$H_{\text{trans}} = (\mathbf{1} - (-r_1)(-r_2)\mathbf{S_1})^{-1} t_2 \mathbf{S_1} t_1 \tag{4.18}$$

$$= \begin{bmatrix} \dfrac{t_1 t_2 e^{z_1}}{1 - r_1 r_2 e^{z_1}} & \\ & \dfrac{t_1 t_2 e^{-z_1}}{1 - r_1 r_2 e^{-z_1}} \end{bmatrix} \tag{4.19}$$

$$= \mathbf{S}_t \tag{4.20}$$

Thus, the total output of the squeezed vacuum is

$$\vec{a} = H_{\text{refl}} \vec{q}_1 + H_{\text{trans}} \vec{q}_2 \tag{4.21}$$

and the variance measured is

$$\langle \vec{a} \vec{a}^\dagger \rangle = (\mathbf{S}_r^2 + \mathbf{S}_t^2) \tag{4.22}$$

Now let's focus on the diagonal elements of the diagonal matrix $\mathbf{S}_r^2 + \mathbf{S}_t^2$. At the lossless limit $r_2 = 1, t_2 = 0$, the upper diagonal element (anti-squeezing) is

$$\left(\frac{r_1 - e^{z_1}}{1 - r_1 e^{z_1}} \right)^2 = e^{2z} \tag{4.23}$$

which connects single-pass squeezing parameter z_1 to the total squeezing observed z outside the cavity. This also holds for the lower diagonal element (e^{-2z}).

When there is loss ($T_2 > 0$), the anti-squeezing becomes

$$e^{2z} \eta_+ + (1 - \eta_+) \tag{4.24}$$

where

$$\eta_+ = 1 - \frac{2 r_1 (1 - r_2) e^{z_1} - r_1^2 T_2 e^{2 z_1}}{(1 - r_1 e^{z_1})^2} \tag{4.25}$$

Similarly, the squeezing is

$$e^{-2z}\eta_- + (1-\eta_-) \tag{4.26}$$

where

$$\eta_- = 1 - \frac{2r_1(1-r_2)e^{-z_1} - r_1^2 T_2 e^{-2z_1}}{(1-r_1 e^{-z_1})^2} \tag{4.27}$$

The new escape efficiencies can also be re-written as

$$(1-\eta_\pm) = (1-\eta)(r_1^2 + r_1 e^{\pm z}) + \mathcal{O}(T_2^2) \tag{4.28}$$

where T_2 acts as an effective loss term. The losses decrease squeezing by mixing the unsqueezed vacuum in it, as expected. Therefore, the measured variance is

$$\langle \vec{a}\vec{a}^\dagger \rangle = \begin{bmatrix} \eta_+ e^{2z} + (1-\eta_+) & \\ & \eta_- e^{-2z} + (1-\eta_-) \end{bmatrix} \tag{4.29}$$

which is a more generalized form. The unsqueezed vacuum due to loss is not identical to both anti-squeezing and squeezing. The loss is also squeezing-level dependent, which is different from the Quantum Langevin approach [57].

At the low-squeezing limit $e^{z_1} \approx 1$, the loss terms are identical for squeezing and anti-squeezing $\eta_+ \approx \eta_- = \eta$, giving the familiar equation when there's losses

$$\langle \vec{a}\vec{a}^\dagger \rangle \approx \eta \begin{bmatrix} e^{2z} & \\ & e^{-2z} \end{bmatrix} + (1-\eta)\mathbf{1} = \eta \mathbf{S}(z) + (1-\eta)\mathbf{1} \tag{4.30}$$

4.2 Frequency-Independent Squeezing

Before discussing frequency-dependent squeezing, we need to understand its preliminary work known as frequency-independent squeezing. Even before that, we need to quantitatively analyze the unsquezeed quantum noise of LIGO.

4.2.1 Homodyne revisited

In Section 3.3.2, we introduced the balanced homodyne detector that is typically used to observe squeezing. The measured photocurrent difference is

$$I_{\mathrm{diff}}(t) = I_c - I_d = (C^\dagger C - D^\dagger D) + \sqrt{2\hbar\omega_0}\int \frac{d\Omega}{2\pi}\,(C^\dagger \vec{c} - D^\dagger \vec{d})e^{i\Omega t} \tag{4.31}$$

where the output fields are from a beam splitter (Eq. (3.12))

$$\begin{bmatrix}\vec{c}\\ \vec{d}\end{bmatrix} = \begin{bmatrix} r\cdot\mathbf{1} & t\cdot\mathbf{1}\\ t\cdot\mathbf{1} & -r\cdot\mathbf{1}\end{bmatrix}\begin{bmatrix}\vec{a}\\ \vec{b}\end{bmatrix} \quad \text{and} \quad |r|^2 + |t|^2 = 1 \tag{4.32}$$

Let $\vec{a} \to \mathbf{R}\left(\phi_s\right)\mathbf{S}\left(z\right)\mathbf{R}\left(-\phi_s\right)$ be the squeezed field with zero classical part $A = 0$. The other input port of the beam splitter is the readout field $\vec{B}$, also known as the local oscillator (LO) field, with unsqueezed quantum modes $\vec{b}$.

Re-write Eq. (4.31) into input fields, and the power fluctuations due to quantum modes are

$$P_{\mathrm{diff}}(\Omega) = \sqrt{2\hbar\omega_0}\,\vec{B}[2rt\vec{a} + (t^2 - r^2)\vec{b}] \tag{4.33}$$

For a perfect beam splitter ($r^2 = t^2 = 1/2$), the vacuum of the local oscillator field gets subtracted out, leaving only the squeezed vacuum, which gets "read out" by the classical part of the LO field

$\vec{B}$.

$$S_{\text{diff}} = 2\hbar\omega_0 \frac{\langle 0|\vec{B}^\dagger \vec{a}(\Omega)\vec{a}^\dagger(\Omega')\vec{B}|0\rangle_{sym}}{2\pi\delta(\Omega-\Omega')/2} \tag{4.34}$$

$$= 2\hbar\omega_0 B^2 \vec{v}^\dagger \mathbf{R}^\dagger\left(\phi_{\text{LO}}\right)\mathbf{R}\left(\phi_s\right)\mathbf{S}^2(z)\mathbf{R}^\dagger\left(\phi_s\right)\mathbf{R}\left(\phi_{\text{LO}}\right)\vec{v} \tag{4.35}$$

$$= 2\hbar\omega_0 B^2(e^{2z}\cos^2(\phi_{\text{LO}}-\phi_s) + e^{-2z}\sin^2(\phi_{\text{LO}}-\phi_s)) \tag{4.36}$$

where $\vec{v} = [1 \;\; 0]^T$ is the reference vector.

The most important point is that the measured quantum noise depends heavily on the phase difference $\phi_{\text{LO}}-\phi_s$. It's possible to read out either desired squeezing $S = 2\hbar\omega_0 B^2 e^{-2z}$ or undesired anti-squeezing $S = 2\hbar\omega_0 B^2 e^{2z}$, depending on if you are reading out the squeezed quadrature or the anti-squeezed quadrature.

4.2.2 Unsqueezed LIGO

In Section 3.6, we introduced the full solution of the quantum noise for a full LIGO system. It is often useful to have a simplified and approximated solution to reveal the essential part of physics.

Assuming a lossless arm cavity, the amplitude reflectivity is

$$\vec{g}(\Omega) \approx \mathbf{r}_{opto}(\Omega)\vec{f} \tag{4.37}$$

where

$$\mathbf{r}_{opto}(\Omega) \approx \begin{bmatrix} r_{arm}(\Omega) & 0 \\ -\mathcal{K}(\Omega) & r_{arm}(\Omega) \end{bmatrix} \tag{4.38}$$

and

$$\mathcal{K}(\Omega) \approx \frac{16P_{arm}\omega_0}{mc^2\Omega^2} g_{arm}^2(\Omega) \tag{4.39}$$

are from Eq. (3.86) and Eq. (3.89).

The lossless assumption continues to the dual-recycled Michelson with symmetric arms $\mathbf{r}_{optoy}(\Omega) = \mathbf{r}_{optox}(\Omega)$, which has a simplified transfer function from Eq. (3.150)

$$\mathbf{h}_{\mathrm{DC}}(\Omega) \approx \mathbf{r} + \mathbf{teh}_{\mathrm{MICH}}\mathbf{e}(1 + \mathbf{reh}_{\mathrm{MICH}}\mathbf{e})^{-1}\mathbf{t} \tag{4.40}$$

with a lossless Michelson interferometer simplified from Eq. (3.127)

$$\mathbf{h}_{\mathrm{MICH}}(\Omega) \approx \mathbf{H}_{\mathrm{BS}}\begin{bmatrix} \mathbf{r}_{optoy}(\Omega) & 0 \\ 0 & \mathbf{r}_{optox}(\Omega) \end{bmatrix}\mathbf{H}_{\mathrm{BS}} = \begin{bmatrix} \mathbf{r}_{opto}(\Omega) & 0 \\ 0 & \mathbf{r}_{opto}(\Omega) \end{bmatrix} \tag{4.41}$$

A diagonal $\mathbf{h}_{\mathrm{MICH}}$ implies that the power-recycling and signal-recycling are completely decoupled from each other. Mathematically, the double cavity transfer function $\mathbf{h}_{\mathrm{DC}}(\Omega)$ becomes diagonal. The output field $\vec{b}$ at LIGO's anti-symmetric (dark) port only depends on the input field at the same port $\vec{a}$ and decouples from the input field at the symmetric (bright) port.

$$\vec{b} = \vec{a}\left[r_s\mathbf{1} + t_s^2\mathbf{R}\left(\phi_s\right)e^{-i\varphi_s}\mathbf{r}_{opto}(\Omega)\mathbf{R}\left(\phi_s\right)e^{-i\varphi_s}(\mathbf{1} + r_s\mathbf{R}\left(\phi_s\right)e^{-i\varphi_s}\mathbf{r}_{opto}(\Omega)\mathbf{R}\left(\phi_s\right)e^{-i\varphi_s})^{-1}\right] \tag{4.42}$$

$$= \vec{a}\left[r_s\mathbf{1} - t_s^2e^{-i2\varphi_s}\mathbf{r}_{opto}(\Omega)(\mathbf{1} - r_se^{-i2\varphi_s}\mathbf{r}_{opto}(\Omega))^{-1}\right] \tag{4.43}$$

This is just a reflectivity of a double cavity. The double cavity can be further approximated to a single cavity by replacing $r_{arm}(\Omega)$ in Eq. (4.38) to $r_{\mathrm{DC}}(\Omega)$.

$$r_{\mathrm{DC}}(\Omega) \approx \frac{-\gamma_{\mathrm{DC}} + \lambda + i\Omega}{\gamma_{\mathrm{DC}} + \lambda + i\Omega} \approx \frac{-\gamma_{\mathrm{DC}} + i\Omega}{\gamma_{\mathrm{DC}} + i\Omega} \tag{4.44}$$

where γ_{DC} is the coupled-cavity pole in rad/s and $\lambda = 0$ in the lossless case. The quantum mode at

the LIGO output port is effectively

$$\vec{b} = \begin{bmatrix} r_{\mathrm{DC}}(\Omega) & 0 \\ -\mathcal{K}_{\mathrm{DC}}(\Omega) & r_{\mathrm{DC}}(\Omega) \end{bmatrix} \vec{a} = \mathbf{r}_{\mathrm{DC}}(\Omega)\vec{a} \tag{4.45}$$

The gravitational wave contributes to the output signal as

$$\vec{b}\Big|_{\mathrm{GW}} = h \begin{bmatrix} \mathbf{0} & \mathbf{1} \end{bmatrix} \mathbf{l}_{\mathrm{DCm}} \mathbf{l}_{\mathrm{MICHh}} \begin{bmatrix} \mathbf{g}_{\mathrm{GW}} \\ -\mathbf{g}_{\mathrm{GW}} \end{bmatrix} \approx h\sqrt{2}\mathbf{g}_{\mathrm{GW}} \tag{4.46}$$

where

$$\mathbf{l}_{\mathrm{MICHh}} = \mathbf{H}_{\mathrm{BS}} \begin{bmatrix} \mathbf{R}\left(\phi_y\right) e^{-i\varphi_y} & 0 \\ 0 & \mathbf{R}\left(\phi_x\right) e^{-i\varphi_x} \end{bmatrix} \approx \mathbf{H}_{\mathrm{BS}} \tag{4.47}$$

and

$$\mathbf{l}_{\mathrm{DCm}} = \mathbf{te}\left(\mathbf{1} - \mathbf{h}_{\mathrm{MICH}}\mathbf{e}(1 + \mathbf{reh}_{\mathrm{MICH}}\mathbf{e})^{-1}\mathbf{re}\right) \approx \mathbf{1} \tag{4.48}$$

in single-cavity approximation. The coupling from gravitational waves is from Eq. (3.158)

$$\mathbf{g}_{\mathrm{GW}} = \frac{\sqrt{\mathcal{K}}}{h_{\mathrm{SQL}}} \begin{bmatrix} 0 \\ 1 \end{bmatrix} \tag{4.49}$$

Therefore, we need the phase of the local oscillator field to be $\vec{B} = B[0 \;\; 1]^{\mathsf{T}}$ to read out gravitational waves. The uncalibrated quantum noise in W^2/Hz is

$$S_P(\Omega) = 2\hbar\omega_0 \vec{B}^{\dagger} \langle \vec{b}(\Omega)\vec{b}^{\dagger}(\Omega') \rangle \vec{B} = 2\hbar\omega_0 B^2 (\mathcal{K}^2_{\mathrm{DC}}(\Omega) + 1) \tag{4.50}$$

and the signal from gravitational wave has

$$S_{\mathrm{GW}}(\Omega) = 2\hbar\omega_0 \vec{B}^{\dagger}\langle \vec{b}_{\mathrm{GW}}(\Omega)\vec{b}^{\dagger}_{\mathrm{GW}}(\Omega')\rangle \vec{B} = 2\hbar\omega_0 B^2 2|\mathscr{K}_{\mathrm{DC}}(\Omega)|\frac{h^2}{h^2_{\mathrm{SQL}}} = h^2 g^2_{\mathrm{cal}} \tag{4.51}$$

Therefore, the unsqueezed quantum noise calibrated in strain^2/Hz is

$$S_h(\Omega) = \frac{S_P(\Omega)}{g^2_{\mathrm{cal}}} = \frac{h^2_{\mathrm{SQL}}}{2}\left(|\mathscr{K}_{\mathrm{DC}}(\Omega)| + \frac{1}{|\mathscr{K}_{\mathrm{DC}}(\Omega)|}\right) \tag{4.52}$$

where

$$h_{\mathrm{SQL}}(\Omega) = \sqrt{\frac{8\hbar}{m\Omega^2 L^2}} \tag{4.53}$$

and

$$\mathscr{K}_{\mathrm{DC}}(\Omega) = \frac{16kP_{arm}}{m\gamma_{\mathrm{DC}}L_{arm}}\frac{1}{\Omega^2}\left(1 + \frac{\Omega^2}{\gamma^2_{\mathrm{DC}}}\right)^{-1} \tag{4.54}$$

k is the wavenumber of the 1064-nm field. As we can see, the first term in S_h is due to quantum back-action from radiation pressure noise, whereas the second term is shot noise. The total quantum noise also never breaks h_{SQL} for any given $|\mathscr{K}|$.

4.2.3 Squeezed LIGO

When we squeeze the quantum noise of LIGO, we actually squeeze the quantum modes entering from the anti-symmetric port $\vec{a}$, such that (ignoring all losses)

$$\vec{a} \rightarrow \mathbf{R}(\phi)\,\mathbf{S}(r)\mathbf{R}(-\phi)\,\vec{a} \tag{4.55}$$

This will modify Eq. (4.50) to be

$$S_P(\Omega) = 2\hbar\omega_0 \vec{B}^\dagger \langle \vec{b}(\Omega)\vec{b}^\dagger(\Omega')\rangle \vec{B} \tag{4.56}$$

$$= 2\hbar\omega_0 \vec{B}^\dagger \mathbf{r}_{\rm DC}(\Omega)\mathbf{R}(\phi)\,\mathbf{S}^2(z)\mathbf{R}(-\phi)\,\mathbf{r}_{\rm DC}^\dagger(\Omega)\vec{B} \tag{4.57}$$

$$= 2\hbar\omega_0 B^2[e^{2r}(\cos^2\phi|\mathcal{K}|^2 + \sin^2\phi - \cos\phi\sin\phi\mathcal{K}r_{\rm DC}^\dagger - \cos\phi\sin\phi\mathcal{K}^\dagger r_{\rm DC}) + \tag{4.58}$$

$$e^{-2r}(\sin^2\phi|\mathcal{K}|^2 + \cos^2\phi + \cos\phi\sin\phi\mathcal{K}r_{\rm DC}^\dagger + \cos\phi\sin\phi\mathcal{K}^\dagger r_{\rm DC})] \tag{4.59}$$

Using approximations Eq. (3.36) and Eq. (3.39), we have

$$\mathcal{K} = |\mathcal{K}|e^{-i2\tan^{-1}(\Omega/\gamma)} \tag{4.60}$$

and

$$r_{\rm DC} = e^{-i2\tan^{-1}(\Omega/\gamma)} \tag{4.61}$$

Note that they have the same complex phase. Thus, we can further re-write Eq. (4.56) to

$$S_P(\Omega) = 2\hbar\omega_0 B^2[e^{2r}(\cos\phi|\mathcal{K}| - \sin\phi)^2 + e^{-2r}(\cos\phi|\mathcal{K}| + \sin\phi)^2] \tag{4.62}$$

$$= 2\hbar\omega_0 B^2(|\mathcal{K}|^2+1)[e^{2r}\sin^2(\phi-\theta) + e^{-2r}\cos^2(\phi-\theta)] \tag{4.63}$$

where

$$\theta(\Omega) = \tan^{-1}|\mathcal{K}(\Omega)| \tag{4.64}$$

In the strain unit, the squeezed quantum noise is

$$S_h(\Omega) = \frac{h_{\rm SQL}^2}{2}\left(|\mathcal{K}_{\rm DC}(\Omega)| + \frac{1}{|\mathcal{K}_{\rm DC}(\Omega)|}\right)[e^{2r}\sin^2(\phi-\theta) + e^{-2r}\cos^2(\phi-\theta)] \tag{4.65}$$

It is easy to see that enforcing $\phi = \phi(\Omega) = \theta(\Omega)$ will give a broadband quantum noise reduction by a factor of e^{-2r}. However, the squeezing angle produced by a squeezer has a constant ϕ, which

is frequency-independent. This motivates us to find a way to add frequency dependence to the squeezing angle, namely producing frequency-dependent squeezing.

4.3 Detuned Fabry-Pérot Cavity

The goal of frequency-dependent squeezing is to change the phase ϕ of the squeezed beam such that

$$\phi \to \phi(\Omega) = \tan^{-1} |\mathcal{K}(\Omega)| \tag{4.66}$$

without reducing the amplitude of the squeezed beam. This phase-shifting "filtering" effect can be approximately produced by a lossless over-coupled Fabry-Pérot cavity operated at a detuned frequency $\Delta\omega$. The amplitude reflectivity of the filter cavity is (at the low-loss limit)

$$r_{\mathrm{fc}}(\Omega) \approx \frac{-\gamma + \lambda + i(\Omega - \Delta\omega)}{\gamma + \lambda + i(\Omega - \Delta\omega)} \tag{4.67}$$

Following Eq. (7) in the optimal detuning paper [34], the filter cavity will produce an effective phase-shifting

$$\phi(\Omega) \approx \tan^{-1} \frac{2\gamma\Delta\omega}{\gamma^2 - \lambda^2 + \Omega^2 - \Delta\omega^2} \tag{4.68}$$

Equalizing it with

$$\theta(\Omega) = \tan^{-1} |\mathcal{K}(\Omega)| \approx \tan^{-1} \frac{\Omega_{\mathrm{SQL}}^2}{\Omega^2} \tag{4.69}$$

because $\Omega_{\mathrm{SQL}} \ll \gamma_{\mathrm{DC}}$, we have

$$\begin{cases} 2\gamma\Delta\omega = \Omega_{\mathrm{SQL}}^2 \\ \gamma^2 = \Delta\omega^2 + \lambda^2 \end{cases} \tag{4.70}$$

where Ω_{SQL} is the frequency where $|\mathcal{K}(\Omega_{\mathrm{SQL}})| = 1$

$$\Omega_{\mathrm{SQL}} \approx \sqrt{\frac{16kP_{arm}}{mL_{arm}\gamma_{\mathrm{DC}}}} \tag{4.71}$$

In the lossless case, an optimal filter cavity would have

$$\gamma = \Delta\omega = \frac{\Omega_{\mathrm{SQL}}}{\sqrt{2}} \tag{4.72}$$

Current LIGO has $\Omega_{\mathrm{SQL}} = 2\pi \times 37\,\mathrm{Hz}$ at $P_{arm} = 260\,\mathrm{kW}$. This requires the filter cavity to have a very small linewidth, which is experimentally challenging.

In the formalism of direct calculation of quantum noise, it is very easy to model the detuned filter cavity. Unlike the arm cavity, the filter cavity has negligible optomechanical interaction but always stays detuned from resonance. The optomechanical coupling $\mathcal{K}$ is totally negligible because of the very low power of squeezed light.

The detuning frequency of the cavity $\Delta\omega = 2\pi\Delta f$ is the frequency difference between the cavity resonance frequency and the carrier frequency ω_0.

$$\frac{(\omega_0 + \Delta\omega)2(L + \Delta L)}{c} = \frac{\omega_0 2L}{c} = 2\pi\mathbb{N} \tag{4.73}$$

where the length detuning is

$$\Delta L = -\frac{\Delta\omega}{\omega_0}L + \mathcal{O}(\Delta\omega^2) \tag{4.74}$$

Therefore, the round-trip phase is

$$\mathbf{R}\,(2\phi) = \mathbf{R}\left(\frac{2\omega_0(L + \Delta L)}{c}\right) = \mathbf{R}\left(2\pi\mathbb{N} - \frac{2\Delta\omega L}{c}\right) = \mathbf{R}\left(-\frac{2\Delta\omega L}{c}\right) \tag{4.75}$$

and

$$\mathbf{R}\,(2\varphi) = \mathbf{R}\left(\frac{2\Omega(L + \Delta L)}{c}\right) \approx \mathbf{R}\left(\frac{2\Omega L}{c}\right) \tag{4.76}$$

Only the ϕ is affected and that's all. The rest is identical to the standard input-output relation of an optical cavity introduced in Section 3.3.3.

4.4 Mode-Mismatch

Besides optical losses, mismatches between spatial modes of two cavities are also significant degradation to squeezing. However, it manifests as a "frequency-dependent loss" in contrast to regular losses that affect squeezed vacuum equally at all frequencies. Mode-mismatch was known to affect squeezing in Observing Run 3 (2020), but we didn't have the theory to model it. The formalism was finally available before Observing Run 4 (2023) [33], and it has been added to the Gravitational Wave Interferometer Noise Calculator (GWINC) [58]. We will explain the physics in this chapter.

4.4.1 A more complete picture of light

We have already known the electric field after the second quantization (Eq. (2.54)).

$$E(t) \to \vec{\omega}_0^{\mathsf{T}}(t)\left(\vec{A}_0 + \sqrt{\frac{\hbar\omega_0}{2}}\int_{-\infty}^{\infty}\frac{d\Omega}{2\pi}\,\vec{a}e^{i\Omega t}\right) \tag{4.77}$$

This is the temporal picture of the light with quantum modes. The spatial picture of the light is to decompose the field into higher-order spatial modes (orthogonal Hermite-Gaussian or Laguerre-Gaussian modes). Here we use Hermite-Gaussian (HG) modes, for example.

$$E(x,y,z) = A_0\sum_{l,m} H_{l,m}(x,y)e^{i\psi_{l,m}(z)}e^{-ikz} \tag{4.78}$$

The straightforward way to unite these two pictures is just to multiply them.

$$E_{\text{full}}(x, y, z, t) = E(t)E(x, y, z) \tag{4.79}$$

The spatial terms $H_{l,m}(x, y)$ are not important to us because we usually don't measure the spatial distribution of the power. The Gouy phase $\psi_{l,m}(z)$ is very important because it carries the phase information of the squeezed vacuum.

As aforementioned, one advantage of the direct calculation formalism is that it is trivial to extend from the fundamental spatial mode to any higher-order mode. Suppose we want to extend to the n-th order. The classical part is promoted to

$$\vec{A} \to [\vec{A}_{00} \cdots \vec{A}_n]^\intercal \tag{4.80}$$

The propagation matrix is promoted accordingly

$$\mathbf{R}(\phi) \to \begin{bmatrix} \mathbf{R}(\phi) & & \\ & \ddots & \\ & & \mathbf{R}\left(\phi - \psi_n\right) \end{bmatrix} \tag{4.81}$$

Besides these two, the quantum modes are also generalized. If we have squeezing, the output field from the squeezer is expressed as

$$\vec{a} \to [\mathbf{R}\mathbf{S}\mathbf{R}^\dagger \vec{a}_{00} \cdots \vec{a}_n]^\intercal \tag{4.82}$$

Only the fundamental mode is squeezed in the squeezer cavity's basis.

To generate mode-mismatch, we need a scattering matrix among spatial modes

$$\mathbf{U} = \begin{bmatrix} \sqrt{1-\Upsilon} & \cdots & \mathbf{R}\left(-\theta_n\right)\sqrt{\Upsilon_n} \\ \vdots & \ddots & \vdots \\ -\mathbf{R}\left(\theta_n\right)\sqrt{\Upsilon_n} & \cdots & \sqrt{1-\Upsilon} \end{bmatrix}, \text{ and } \mathbf{U}\mathbf{U}^\dagger = \mathbf{U}^\dagger\mathbf{U} = \mathbf{1} \tag{4.83}$$

This is it! All the equations in Chapter 3 still hold when we introduce mode-mismatches.

The exact equations after we promote these fields and matrices are presented in the next section. You can skip this part and jump to Section 4.4.3 to see an example of mode-mismatch in practice.

4.4.2 Equations of mode-mismatch

The cavity responses for n-th order higher-order mode (HOM) are

$$\mathbf{r}_{\text{cav}}(\Omega, n) = \left(r_1\mathbf{1} - r_2 r_3 \mathbf{R}\left(2(\phi - n\psi)\right)e^{-i2\varphi}\right)\left[\mathbf{1} - r_1 r_2 r_3 \mathbf{R}\left(2(\phi - n\psi)\right)e^{-i2\varphi}\right]^{-1} \tag{4.84}$$

$$\mathbf{t}_{\text{cav}}(\Omega, n) = t_1 t_2 \mathbf{R}\left(\phi - n\psi\right)e^{-i\varphi}\left[\mathbf{1} - r_1 r_2 r_3 \mathbf{R}\left(2(\phi - n\psi)\right)e^{-i2\varphi}\right]^{-1} \tag{4.85}$$

$$\mathbf{g}_{\text{cav}}(\Omega, n) = t_1 r_3 \mathbf{R}\left(\phi - n\psi\right)e^{-i\varphi}\left[\mathbf{1} - r_1 r_2 r_3 \mathbf{R}\left(2(\phi - n\psi)\right)e^{-i2\varphi}\right]^{-1} \tag{4.86}$$

where ψ is the single-trip Gouy phase of the cavity, and we've ignored the Gouy phase of the 00 mode since the round-trip phase $2\phi = 2\pi\mathbb{N}$ when on-resonance. The Gouy phase is only accounted for in the classical field instead of the quantum modes. It's also only accounted for once in two-photon formalism. This is also the cavity response without any optomechanical coupling.

The squeezer outputs squeezed vacuum only in 00 and not in other HOMs.

$$\vec{a}_{\text{SQZ}} = \begin{bmatrix} \mathbf{R}\mathbf{S}\mathbf{R}^\dagger\vec{q}_1 \\ \\ \vec{q}_2 \end{bmatrix} \tag{4.87}$$

where $\vec{q}_i$ are vacuum fields. If the squeezed beam isn't mode-matched to the cavity, aka $\mathbf{U} \neq \mathbf{1}$, then the squeezing can be scattered into HOM, which would see a detuned cavity response due to extra Gouy phase. The 4x4 cavity response matrix is (only considering 2nd order mode because 4th is higher order correction)

$$\mathbf{r}_{\text{cav}} = \begin{bmatrix} \mathbf{r}_{\text{cav}}^{00}(\Omega) & 0 \\ 0 & \mathbf{r}_{\text{cav}}^{\text{HOM}}(\Omega) \end{bmatrix} = \begin{bmatrix} \mathbf{r}_{\text{cav}}(\Omega, 0) & 0 \\ 0 & \mathbf{r}_{\text{cav}}(\Omega, 2) \end{bmatrix} \tag{4.88}$$

acting on $\mathbf{U}\vec{a}_{\text{SQZ}}$. Note that it's a 4x4 matrix instead of an 8x8 like a beam splitter because we don't care about the transmission vacuum. The other two cavity responses are analogous.

$$\mathbf{g}_{\text{cav}} = \begin{bmatrix} \mathbf{g}_{\text{cav}}(\Omega, 0) & 0 \\ 0 & \mathbf{g}_{\text{cav}}(\Omega, 2) \end{bmatrix} \tag{4.89}$$

$$\mathbf{t}_{\text{cav}} = \begin{bmatrix} \mathbf{t}_{\text{cav}}(\Omega, 0) & 0 \\ 0 & \mathbf{t}_{\text{cav}}(\Omega, 2) \end{bmatrix} \tag{4.90}$$

Essentially, we just promote the rotation matrix to 4x4

$$\mathbf{R}(\phi) \rightarrow \begin{bmatrix} \mathbf{R}(\phi) & \\ & \mathbf{R}(\phi - n\psi) \end{bmatrix} \tag{4.91}$$

and insert mode conversion matrix $\mathbf{U}$ to the appropriate places in the previous formulation. The cavity response including optomechanical coupling remains the same. The change of cavity reflection

due to radiation pressure is

$$\frac{\delta \mathbf{r}_{\rm cav}}{\delta \phi}(\Omega) = -r_2 r_3 (1 + e^{i\varphi}) \begin{bmatrix} \mathbf{R}\left(\frac{\pi}{2}\right) & \\ & \mathbf{R}\left(\frac{\pi}{2}\right) \end{bmatrix} \mathbf{g}_{\rm cav}(0) \mathbf{g}_{\rm cav}(\Omega) + \mathcal{O}\left(\frac{\Omega}{\omega_0}\right) \tag{4.92}$$

The only difference is $\mathbf{R}$ becomes 4x4. The cavity reflection is still

$$R_{opto}(\Omega) = \mathbf{r}_{\rm cav}(\Omega) - \mathscr{K}_r(\Omega) \tag{4.93}$$

with

$$\mathscr{K}_r(\Omega) = \frac{4\omega_0}{mc^2\Omega^2}(1 + r_2^2 e^{-i\varphi}) \frac{\delta \mathbf{r}_{\rm cav}}{\delta \phi}(\Omega) \vec{F} \vec{F}^\dagger g_{\rm cav}^\dagger \mathbf{g}_{\rm cav}(\Omega) \tag{4.94}$$

This also becomes 4x4 naturally. Same for other $\mathscr{K}$ for losses.

The Michelson transfer function is the same with some $\mathbf{U}$ plugged in. The X-arm and Y-arm might not have the same cavity basis due to non-idealities. Define the Michelson mode to be perfectly matched to X-arm without losing generalities. The Michelson transfer function is

$$\mathbf{h}_{\rm MICH} = \mathbf{H}_{\rm BS} \begin{bmatrix} \mathbf{R}\left(\phi_y\right) \mathbf{U}_{XY}^\dagger R_{optoy} \mathbf{U}_{XY} \mathbf{R}\left(\phi_y\right) e^{i2\varphi_y} & \\ & \mathbf{R}\left(\phi_x\right) R_{optox} \mathbf{R}\left(\phi_x\right) e^{i2\varphi_x} \end{bmatrix} \mathbf{H}_{\rm BS} \tag{4.95}$$

where $\mathbf{U}_{XY}$ is responsible for the mismatch. It's easy to see that if the Y-arm cavity is simply a mirror $r\mathbf{1}$, the mode-mismatch would cancel each other because it doesn't matter.

There could also be mode-mismatch between the power-recycling cavity to arms, and the signal-recycling cavity to arm cavities. It's taken care of by changing

$$\mathbf{h}_{\rm MICH} \to \mathbf{U}_{\rm DC}^\dagger \mathbf{h}_{\rm MICH} \mathbf{U}_{\rm DC} \tag{4.96}$$

where

$$\mathbf{U}_{\mathrm{DC}} = \begin{bmatrix} \mathbf{U}_p & \\ & \mathbf{U}_s \end{bmatrix} \tag{4.97}$$

and $\mathbf{U}_p$ is the mismatch between power-recycling cavity and X-arm, and $\mathbf{U}_s$ is the mismatch between signal-recycling cavity and X-arm.

4.4.3 Homodyne re-revisited

The balanced homodyne detection introduced (Section 3.3.2) to measure squeezing (Section 4.2.1) is also an excellent example to evaluate mode-mismatch. The homodyne visibility ν is fundamentally a mode-mismatch effect. It's the square root of the mode-matching coefficient or efficiency in power

$$\nu = \sqrt{\eta} \tag{4.98}$$

When we try to measure the visibility, we send a coherent beam co-aligned with the squeezed vacuum (known as seed) to the homodyne $A_{\mathrm{SQZ}} = A_{\mathrm{seed}} > 0$. If it is not mode-matched to the local oscillator (LO) beam, it can be converted to LO basis as

$$\vec{A}_{\mathrm{SQZ}} = \begin{bmatrix} \mathbf{R}\left(\phi_{\mathrm{SQZ}}\right)\vec{A}_0 \\ 0 \end{bmatrix} \rightarrow \mathbf{U}\vec{A}_{\mathrm{SQZ}} \tag{4.99}$$

where

$$\mathbf{U} = \begin{bmatrix} \nu\mathbf{1} & \mathbf{R}\left(-\phi_{mm}\right)\sqrt{1-\nu^2} \\ -\mathbf{R}\left(\phi_{mm}\right)\sqrt{1-\nu^2} & \nu\mathbf{1} \end{bmatrix} \tag{4.100}$$

is an orthonormal basis-conversion matrix, or scattering matrix. It doesn't have to be complex

because the mode-mismatch is a classical effect. The mode-mismatch angle is

$$\phi_{mm} = \frac{\pi}{2} + \sqrt{1 - \nu^2} \tag{4.101}$$

It's the additional phase scattered to the higher-order mode (HOM) from the fundamental TEM_{00} mode. Its sign is arbitrary because we don't know if the waist location mismatch is positive or negative. The HOM is naturally incorporated by extending the 2-by-1 classical field vector to a 4-by-1 vector with the top being 00 mode and the bottom being HOM. The LO field in its own LO basis is

$$\vec{A}_{\mathrm{LO}} = \begin{bmatrix} \mathbf{R}\left(\phi_{\mathrm{LO}}\right)\vec{A}_0 \\ 0 \end{bmatrix} \tag{4.102}$$

Since the field is already 4-by-1, the beam splitter is now upgraded to 8x8 matrix

$$h_{BS} = \begin{bmatrix} r\mathbf{1} & t\mathbf{1} \\ t\mathbf{1} & -r\mathbf{1} \end{bmatrix} \tag{4.103}$$

with $\mathbf{1} = \mathbf{1}_{4\times4}$ and the input-output relation is

$$\begin{bmatrix} \vec{A}_1 \\ \vec{A}_2 \end{bmatrix} = h_{BS} \begin{bmatrix} \mathbf{U}\vec{A}_{\mathrm{SQZ}} \\ \vec{A}_{\mathrm{LO}} \end{bmatrix} \tag{4.104}$$

The measured power at one photodiode, for example, is

$$\vec{A}_1^{\mathrm{T}}\vec{A}_1 = \left(\begin{bmatrix} \mathbf{1} & \mathbf{0} \end{bmatrix} h_{BS} \begin{bmatrix} \mathbf{U}\vec{A}_{\mathrm{SQZ}} \\ \vec{A}_{\mathrm{LO}} \end{bmatrix} \right)^2 \tag{4.105}$$

$$= \frac{1}{2}\left(\mathbf{U}\vec{A}_{\mathrm{SQZ}} + \vec{A}_{\mathrm{LO}}\right)^2 = \frac{A_0^2}{2}\left((\nu^2 + 2\nu\cos(\phi_{\mathrm{SQZ}} - \phi_{\mathrm{LO}}) + 1) + 1 - \nu^2\right) \tag{4.106}$$

which ranges between $P_{min} = A_0^2(1-v)$ and $P_{max} = A_0^2(1+v)$. Therefore, we have

$$\frac{P_{max} - P_{min}}{P_{max} + P_{min}} = v \tag{4.107}$$

which recovers the definition of visibility.

When we send squeezing to the homodyne, we have $A_{\mathrm{SQZ}} = 0$ and $\vec{a}_{\mathrm{SQZ}} = \mathbf{RSR}^\dagger \vec{a}$. Similarly, the quantum-mechanical parts can also be represented in this way. The great thing about this formalism is that it's compatible with both classical and quantum fields. The quantum vacuum at the photodiode is

$$\vec{a}_1 = \begin{bmatrix} \mathbf{1} & \mathbf{0} \end{bmatrix} h_{BS} \begin{bmatrix} \mathbf{U}\vec{a}_{\mathrm{SQZ}} \\ \vec{a}_{\mathrm{LO}} \end{bmatrix} \tag{4.108}$$

with

$$\begin{bmatrix} \mathbf{U}\vec{a}_{\mathrm{SQZ}} \\ \vec{a}_{\mathrm{LO}} \end{bmatrix} = \begin{bmatrix} \mathbf{1} \\ \mathbf{0} \end{bmatrix} \mathbf{U}\vec{a}_{\mathrm{SQZ}} + \begin{bmatrix} \mathbf{0} \\ \mathbf{1} \end{bmatrix} \vec{a}_{\mathrm{LO}} \tag{4.109}$$

$$= \begin{bmatrix} \mathbf{1}_{4\times4} \\ \mathbf{0}_{4\times4} \end{bmatrix} \mathbf{U} \left(\begin{bmatrix} \mathbf{1}_{2\times2} \\ \mathbf{0}_{2\times2} \end{bmatrix} \vec{a}_{\mathrm{SQZ}}^{(00)} + \begin{bmatrix} \mathbf{0}_{2\times2} \\ \mathbf{1}_{2\times2} \end{bmatrix} \vec{a}_{\mathrm{SQZ}}^{(\mathrm{HOM})} \right) + \begin{bmatrix} \mathbf{0}_{4\times4} \\ \mathbf{1}_{4\times4} \end{bmatrix} \left(\left(\begin{bmatrix} \mathbf{1}_{2\times2} \\ \mathbf{0}_{2\times2} \end{bmatrix} \vec{a}_{\mathrm{LO}}^{(00)} + \begin{bmatrix} \mathbf{0}_{2\times2} \\ \mathbf{1}_{2\times2} \end{bmatrix} \vec{a}_{\mathrm{LO}}^{(\mathrm{HOM})} \right) \right) \tag{4.110}$$

(4.111)

Note that the spatial 00 mode and spatial HOM of the same quantum mode have zero cross-spectral density.

$$\langle \vec{a}_{(00)}^\dagger \vec{a}_{(\mathrm{HOM})}^\dagger \rangle = 0 \tag{4.112}$$

and

$$\langle \vec{a}_{\mathrm{SQZ}} \vec{a}^{\dagger}_{\mathrm{SQZ}} \rangle = \mathbf{1} \tag{4.113}$$

The measured power fluctuation on the difference of photocurrents is

$$P_{\mathrm{diff}}(\Omega) = \sqrt{2\hbar\omega_0}\vec{B}\mathbf{U}\vec{a}_{\mathrm{SQZ}} = \sqrt{2\hbar\omega_0}\begin{bmatrix}0 & 1\end{bmatrix}(\nu\vec{a}^{(00)}_{\mathrm{SQZ}} + \mathbf{R}\left(-\phi_{mm}\right)\sqrt{1-\nu^2}\vec{a}^{(\mathrm{HOM})}_{\mathrm{SQZ}}) \tag{4.114}$$

Note that the LO classical part $\vec{B} = [0 \;\; 1 \;\; 0 \;\; 0]^{\mathsf{T}}$ only has power in the fundamental mode of its own basis. When we have the right squeezing angle, the measured quantum noise is

$$S_{\mathrm{diff}}(\Omega) = 2\hbar\omega_0 B^2(\nu^2 e^{-2r} + (1-\nu^2)) \tag{4.115}$$

Here we recover visibility ν from mode-mismatch as effectively the efficiency to the squeezing (4.98).

In this example, the mode-mismatch acts the same as optical loss to squeezing. However, it becomes more interesting when we have more than one mode-mismatch along the squeezed path. Physically, the squeezed vacuum will be scattered to the HOM in the first mode-mismatch, and then scattered back to 00 in the second mode-mismatch down the path. The final squeezed vacuum that gets read out will be the coherent sum of the original squeezing from the squeezer and the squeezing scattered back, which will have a different phasing due to the Gouy phase.

In this chapter, we discussed how squeezing will alter the quantum noise in LIGO. When injected with frequency-dependent squeezing, the quantum noise will reduce by a factor of e^{-2r} at all frequencies. However, the experimental degradations like optical losses and mode-mismatch will prevent us from seeing the amount of squeezing generated from the squeezer.

We also finish all the formalism we need to fully understand the physics of squeezing and how it will affect LIGO's quantum noise. In the next chapter, we will delve into the experimental land and discuss how we implement the squeezing system in real gravitational-wave detectors.

5 SQUEEZING EXPERIMENT IN LIGO

In previous chapters, we introduced the squeezed vacuum state of light and understood how it can reduce quantum noise, especially for gravitational-wave detectors like LIGO. Experimentally, frequency-independent squeezing has been deployed to reduce quantum noise of gravitational-wave detectors [59, 60], for example, in LIGO [61, 62], Virgo [63], and GEO600 [64–66]. This chapter will describe the experimental work to realize frequency-dependent squeezing in real LIGO interferometers.

Since I spent most of my time at LIGO Livingston Observatory (L1), the experiment presented in this chapter will be focused on L1. The stories here will be closely related to our published work [3].

5.1 System Overview

As introduced in Chapter 4, the frequency-dependent squeezing requires three key components:

- Squeezer: generating squeezed vacuum states, which is physically a beam of correlated photons.
- Filter cavity: producing the frequency-dependent phase shift of the squeezed beam.
- Detection: observing a reduced quantum noise thanks to squeezing.

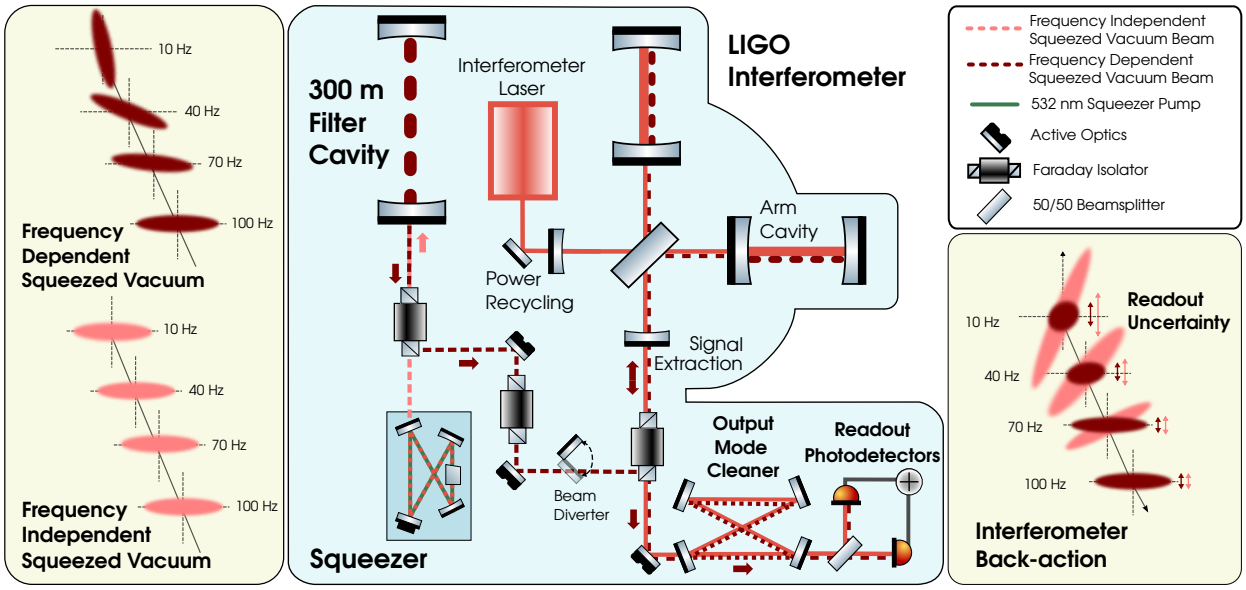

Figure 5-1: Experimental setup of frequency-dependent squeezing in LIGO [3].

In LIGO, the detection part already exists as we detect incoming gravitational waves. Fig. 5-1 shows the experimental overview of the squeezing subsystem.

The blue panel shows a simplified overview of the main experimental components. The LIGO detector is the dual-recycled Michelson interferometer with two Fabry-Pérot arm cavities. The LIGO squeezer [62] generates the squeezed vacuum at 1064 nm using a sub-threshold optical parametric amplifier, pumped at 532 nm. The frequency-independent squeezed beam reflects from the 300 m filter cavity and becomes frequency-dependent. Three Faraday isolators are in place to block any interfering light from reaching the squeezer and filter cavity. The use of active steering optics facilitates the alignment and mode-matching between the squeezed beam and the filter cavity & interferometer [8]. The squeezed beam travels alongside the outgoing interferometer beam through the output mode cleaner cavity, where it is measured by the readout photodetectors, as outlined in the LIGO design [67].

The yellow panels display uncertainty ellipses representing squeezed states in phase space [36]. These ellipses demonstrate how vacuum fluctuations are squeezed along the vertical readout quadra-

ture. In the left panel, the illustration portrays the frequency-dependent rotation caused by the filter cavity resonance (upper) on the generated squeezed vacuum state (lower). The right panel illustrates how the interferometer back-action impacts the injected squeezed state, which can be either frequency-independent (light) or frequency-dependent (dark). In both scenarios, the ellipse undergoes rotation and stretching, indicating the rotation and squeezing of the squeezed state. In the case of frequency-independent squeezing, there's an increase in uncertainty in the readout quadrature at low frequencies, as highlighted by the vertical red arrows. Conversely, for frequency-dependent squeezing where the appropriate rotation is applied to counteract back-action, a reduction in uncertainty in the readout quadrature is observed at low frequencies.

We will discuss each component in the following sections.

5.2 Squeezer

The LIGO squeezer generates correlated photon pairs through spontaneous parametric down-conversion (SPDC), which is a physical process enabled by a nonlinear $\chi^{(2)}$ crystal made of periodically poled potassium titanyl phosphate (PPKTP) [62, 68, 69]. SPDC essentially splits one green 532 nm photon to a pair of entangled red 1064 nm photons, allowed by the conservation of energy [70]. Since the signal in the squeezer is the vacuum as we are doing vacuum squeezing, we also call SPDC in a cavity an optical parametric amplifier because it operates below the lasing threshold.

SPDC is a $\chi^{(2)}$ process, which is from the second-order nonlinearity in the crystal. The displacement electric field $\vec{D}$ in the crystal can be expressed as

$$\vec{D} = \varepsilon_0 \vec{E} + \vec{P} \tag{5.1}$$

Taking a divergence, we have

$$\nabla \cdot \vec{D} = \rho_f = \rho - \rho_b \tag{5.2}$$

namely, the free charge is equal to the total charge minus the bound charge.

For a nonlinear crystal, we have

$$\vec{D} = \varepsilon_0[(1 + \chi^{(1)})\vec{E} + \chi^{(2)}\vec{E}^2 + \cdots] \tag{5.3}$$

The $\chi^{(2)}$ term generates sum and difference frequency photon. This allows us to write the Hamiltonian of the nonlinear process

$$H = \hbar\omega_a a \dagger a + \hbar\omega_b b^\dagger b + \frac{i\hbar}{2}(\epsilon(a^\dagger)^2 b - \epsilon^* a^2 b^\dagger) \tag{5.4}$$

where a is the fundamental field in 1064 nm, b is pump field 532 nm, and ϵ is the nonlinear coupling parameter. The down conversion can be seen as we annihilate one pump photon b and create two entangled red photon $(a^\dagger)^2$.

Assuming the process is parametric (no depletion of the pump field), we can write the pump field as a strong coherent field $b \to \beta e^{i\omega_b t}$ and $\omega_b = 2\omega_a = 2\omega$. The Hamiltonian is

$$H = \underbrace{\hbar\omega a^\dagger a}_{H_0} + \underbrace{\frac{i\hbar\epsilon}{2}(\beta e^{i2\omega t}(a^\dagger)^2 - \beta^* e^{-i2\omega t} a^2)}_{H_1} \tag{5.5}$$

The Hamiltonian in the interaction picture is

$$H_I = U_0^\dagger H_1 U_0 = \frac{i\hbar\epsilon}{2}(\beta(a^\dagger)^2 - \beta^* a^2) \tag{5.6}$$

where

$$U_0 = e^{-iH_0 t/\hbar} \tag{5.7}$$

Therefore, the state evolves with

$$|t\rangle_I = e^{-iH_I t/\hbar}|t_0\rangle_I = \underbrace{e^{\frac{\epsilon t}{2}(\beta(a^\dagger)^2 - \beta^* a^2)}}_{S(z)}|t_0\rangle_I \tag{5.8}$$

which recovers the squeezing operator $S(z)$ introduced in the previous chapters.

The formalism above stands for the SPDC. The LIGO squeezer cavity has the SPDC process in a lossy Fabry-Pérot cavity to increase the interaction time t. The full input-output relations are derived from Quantum Langevin equations, which can be found in previous theses [71]. The results are summarized here.

The nonlinear interaction strength x is

$$x = \frac{\epsilon\beta}{\gamma} = \sqrt{\frac{P_{\text{pump}}}{P_{\text{threshold}}}} \tag{5.9}$$

where γ is the linewidth of the cavity in red 1064 nm. The parameter x is analogous to z in the squeezing operator $S(z)$ derived above. The higher x, the more generated squeezing. When the pump power surpasses the threshold $x > 1$, the cavity starts lasing. Therefore, we always operate the squeezer below threshold power.

There are three other useful quantities that describe nonlinearity and are determined by the interaction strength x:

- Nonlinear gain: NLG = $\dfrac{1}{(1-x)^2}$
- Nonlinear attenuation: NLA = $\dfrac{1}{(1+x)^2}$
- Nonlinear ratio NLR = $\dfrac{(1+x)^2}{(1-x)^2} = e^{2r}$

where $e^{\pm 2r}$ are the (anti)squeezing diagonal elements in the squeezing matrix $\mathbf{S}(\mathbf{r})$

The squeezer cavity is suspended and situated in the ultra-high vacuum chamber [72]. The double suspension will isolate the squeezer from ground motions to reduce the phase fluctuation of

the squeezed beam. The vacuum chamber is coupled with the main interferometer vacuum system to prevent air currents from causing fluctuations in the index of refraction of the medium that also leads to phase noises. Compared to the cavity parameters of Observing Run 3, the finesse has been increased from 37 (17.6) to 85 (110) for fundamental 1064 nm (pump 532 nm) [68, 73, 74].

The squeezed vacuum beam generated from the squeezer is directed to the filter cavity by relay optics, some of which have deformable surfaces to allow for optimization of the mode-matching between the squeezer cavity and filter cavity. We will discuss these deformable mirrors in the next section.

5.3 Active Mode-Matching Optics

The relay optics from the squeezer to the filter cavity and from the filter cavity to the interferometer are called Suspended Active Matching Stages (SAMS). They are suspended in the vacuum chamber with actuators on pitch and yaw.

The deformable optics can be actuated by piezoelectric [8] or thermoelastic force [75, 76]. Fig. 5-2a shows the diagram of the piezo-deformable optics suspended on active matching stages (PSAMS). PSAMS refers to the whole assembly, but it is often used to refer to the deformable mirror itself. The radius of curvature of the mirror can be actively changed by stress-deforming it with a piezoelectric transducer (PZT).

Fig. 5-2b shows the actual PSAMS optics with a 2-inch diameter and 5-mm thickness. The cross-section of the whole optics assembly is shown in Fig. 5-2c. The axis of the mirror is aligned with the axis of the PZT, which transduces a DC voltage to a normal stress on the mirror. It pushes the inverted hat-shaped axisymmetric flexure that distributes the bending moment around the mirror circumference, deforming its radius of curvature [8].

At the bottom of the assembly, we have a pre-loading plate that can be screwed in to increase the normal stress on the mirror without applying any voltage to PZT. Since the dynamic range of

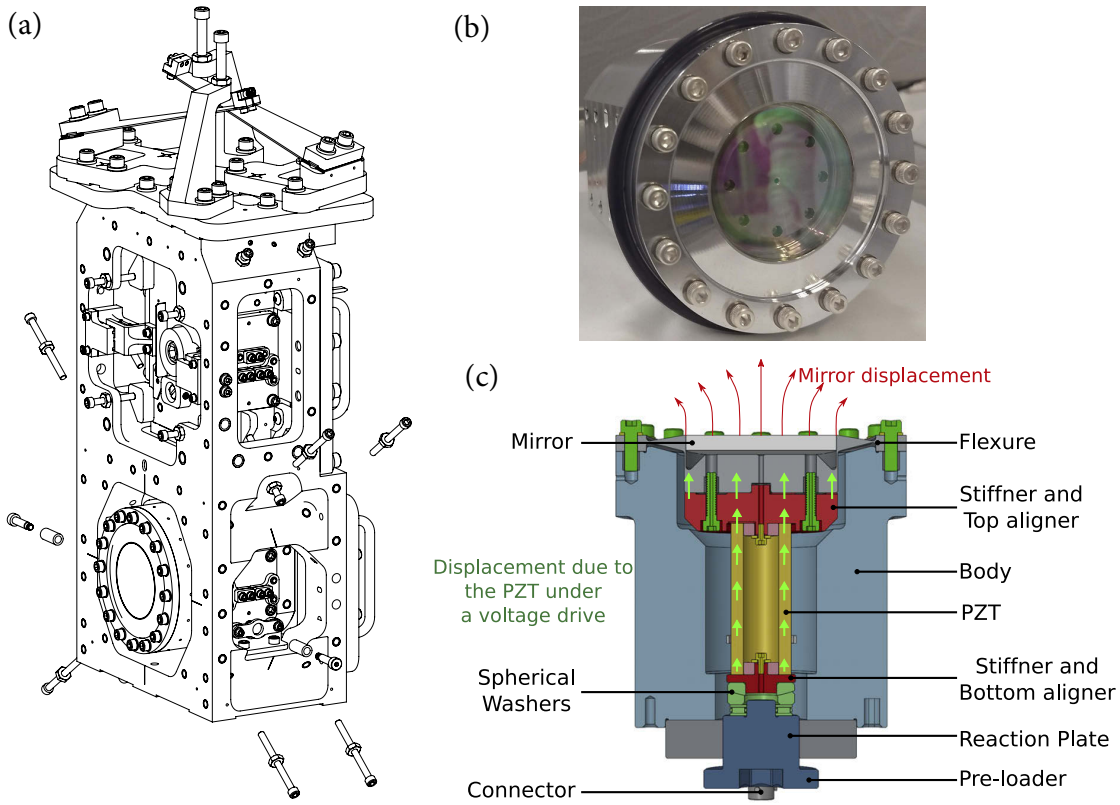

Figure 5-2: Illustration of the piezo-deformable suspended optics (PSAMS). (a) shows the drawing of the assembly [7] that suspends the (b) deformable mirror with (c) picture of cross-section [8].

the PSAMS is limited by the actuator, pre-loading allows us to choose the range of operation.

5.3.1 Defocus characterization

The physics intuition for PSAMS is very simple. Define the complex beam parameter q for a Gaussian beam

$$\frac{1}{q} = \frac{1}{R(z)} - \frac{i\lambda}{n\pi w^2(z)} \tag{5.10}$$

where $R(z)$ is the radius of curvature (ROC) of the beam, $w(z)$ is beam width, λ is the wavelength, and n is the index of refraction of the medium (assume $n = 1$). The ABCD transfer matrix for the

PSAMS optics is

$$\begin{bmatrix} A & B \\ C & D \end{bmatrix} = \begin{bmatrix} 1 & 0 \\ \frac{1}{f} & 1 \end{bmatrix} = \begin{bmatrix} 1 & 0 \\ \frac{2}{R} & 1 \end{bmatrix} \tag{5.11}$$

where $R < 0$ is the ROC of the convex mirror, and f is focal length.

The reflected beam q_2 given the input beam q_1 is

$$\frac{1}{q_2} = \frac{C + D/q_1}{A + B/q_1} \tag{5.12}$$

which gives

$$\frac{1}{R_2} = \frac{1}{R_1} + \frac{2}{R} \tag{5.13}$$

where R_1 and R_2 are the ROC of the beam just before and after reflected by the mirror. The beam width is not altered by reflection as expected.

We usually use optical power P to describe the curvature of the mirror. It's defined as

$$P\ [\mathrm{D}] = \frac{1}{f\ [\mathrm{m}]} = \frac{2}{R\ [\mathrm{m}]} \tag{5.14}$$

where D stands for diopter.

To measure the mirror deformation, we set up a simple Michelson interferometer to measure the displacement of the center of the optics under various input voltages to PZT. The deformation is measured versus the input PZT voltage at various pre-loading forces, as seen in Fig. 5-3. At each pre-loading in in-lb, we swept the PZT from 0 to 100 V to load the stress on the mirror and then swept down the voltage to unload it. The response of the optics is very linear, which is expected as we should operate in the linear or elastic region of the deformation. However, we did observe a significant hysteresis as the loading and unloading curves are different. More in-depth testing was carried out on the Zygo interferometer at Caltech and can be found in [8].

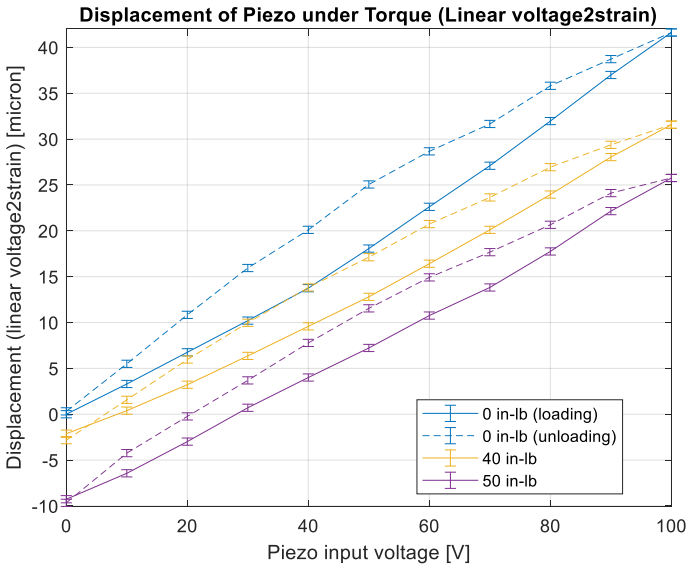

Figure 5-3: Measurement of the displacement of the mirror center due to deformation caused by PZT actuator.

5.3.2 Displacement noise

Besides measuring the deformation, we also need to quantify the noise of the displacement as the PZT is set at a constant voltage. Therefore, we set up a simple Michelson interferometer with the end mirror of one arm replaced by the PSAMS. The schematics of the set-up are shown in Fig. 5-4.

The intensity stabilization servo (ISS) is employed to reduce the relative intensity noise (RIN) of the laser before sending it to the vacuum chamber, which hosts the simple Michelson interferometer. One arm of the Michelson is folded to increase the displacement sensitivity of the PSAMS by a factor of two. The other arm is shorter so we put a lens to mode-match two beams from two arms. Note that the reflection path of each arm is misaligned on purpose because the lens is partially reflective and forms an etalon with the end mirror.

The visibility ν measures the mode-matching between two beams of the interferometer. It de-

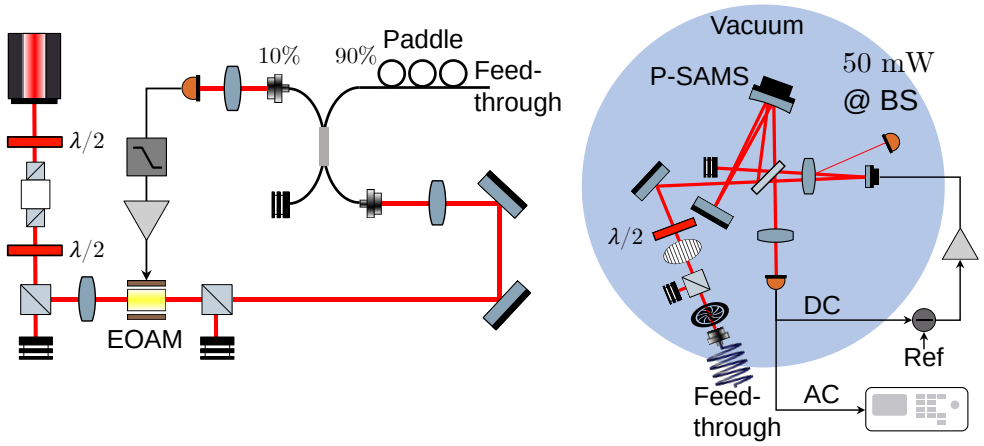

Figure 5-4: Schematics of the simple Michelson interferometer. The left side shows the laser intensity stabilization servo. The laser is then coupled to the fiber and sent to the interferometer in the vacuum chamber [9].

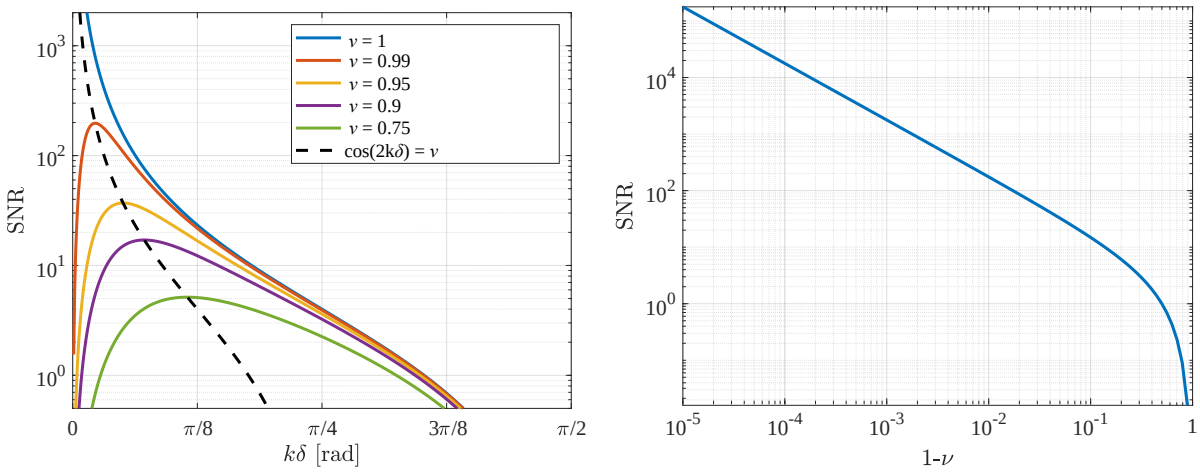

(a) (b)

Figure 5-5: (a) SNR of signal to RIN as a function of operating offset δ at various visibility ν. (b) The maximum achievable SNR as a function of visibility [9].

termines the sensitivity of the output power $P(t)$ to the displacement $x(t)$ and the coupling of RIN.

$$P = P_0(1 + \text{RIN})\left(\frac{1}{2} + \frac{1}{2}\nu\cos\left(2k\left(\frac{\lambda}{4} + \delta + x(t)\right)\right)\right) \tag{5.15}$$

$$= P_0\left[\frac{1}{2}(1 - \nu\cos(2k\delta)) + \nu\sin(2k\delta)kx(t) + \frac{1}{2}(1 - \nu\cos(2k\delta))(\text{RIN}) + \mathcal{O}(k^2x^2)\right] \tag{5.16}$$

where δ is the offset from the dark fringe. If we define the signal-to-noise ratio (SNR) of signal to RIN

$$\text{SNR} = \left(\frac{2\nu \sin(2k\delta)}{1 - \nu \cos(2k\delta)} \right)^2 \tag{5.17}$$

We can plot it as a function of ν, as shown in Fig. 5-5.

The key takeaway is that there exists an optimal operating DC offset from dark fringe given the visibility and RIN. If the total noise is limited by RIN, the optimal offset δ_m is

$$\cos 2k\delta_m = \nu \tag{5.18}$$

This motivates us to optimize visibility as much as possible. Besides alignment, we find the polarization to be the last hindrance from achieving a 99% visibility. While one arm is the PSAMS, the end mirror of the other arm is a PZT actuator to lock the Michelson at the correct offset.

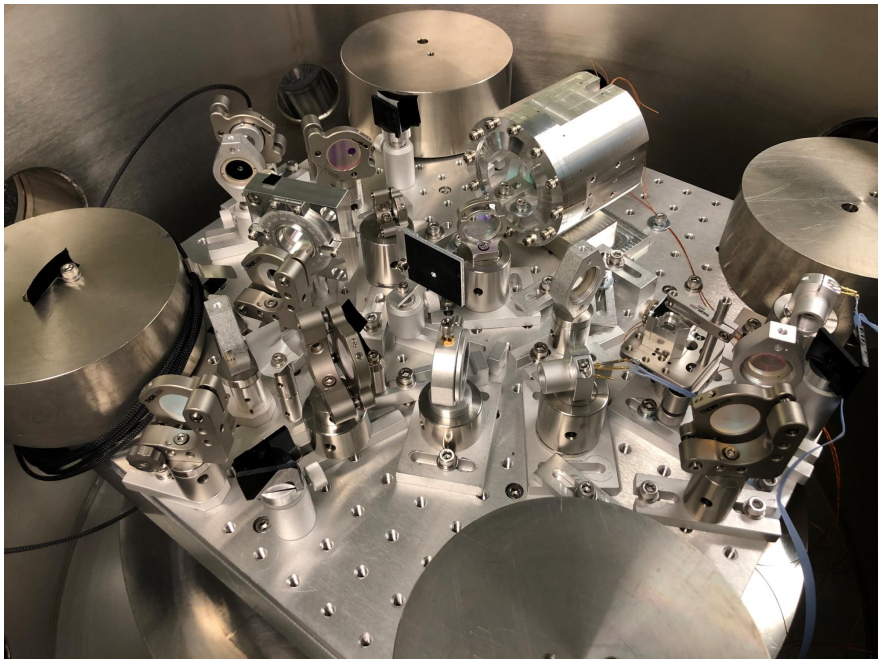

Figure 5-6: Picture of the Michelson interferometer inside a vacuum chamber. The PSAMS mirror is on the Y arm [9].

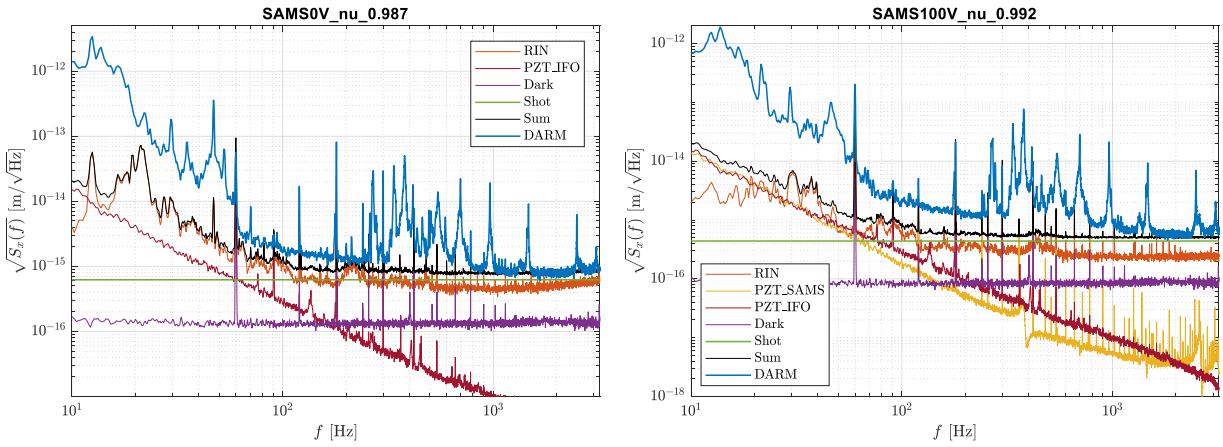

Figure 5-7: Noise budget of the Michelson interferometer at (a) 0 V and (b) input voltage 100 V to PSAMS. It is sensitive at the scale of femtometer [9].

The actual experimental set-up is shown in Fig. 5-6. Here are the key experimental techniques to reduce various noise sources:

- Seismic noise: we add four springs at each corner of the bottom of the optical table to isolate the 48-Hz vertical mode of the vacuum chamber. The Viton pads are attached at both ends of the spring to add damping. Four weights are also put at each corner of the top of the optical table to press against the spring.

- Laser noise: the frequency noise is higher-order than intensity noise. We deploy the ISS loop to stabilize intensity. The out-loop witness of RIN is below 10^{-7} $1/\sqrt{\text{Hz}}$.

- Acoustic noise: the interferometer resides in the vacuum chamber with a pressure of 7×10^{-6} mbar.

- Scattered light noise: we used an IR camera to find all the stray light and added Acktar-coated films everywhere to block them.

- Control noise: the noise from the PZT actuator is the main control noise. We replace the standard Thorlabs MDT693A high-voltage driver with HP E3612A high-voltage driver.

Fig. 5-7 shows the noise budget of the Michelson interferometer calibrated in m/$\sqrt{\text{Hz}}$. At low frequency (10–50 Hz), we have a lot of extra noises that are not budgeted, most of which are from ground motion because we didn't suspend any of our optics. At high frequency > 1 kHz, we are dominated by shot noise. In the mid-frequency band, we are limited by RIN and unknown noises near 400 Hz (probably acoustic noise coupled through optical fiber).

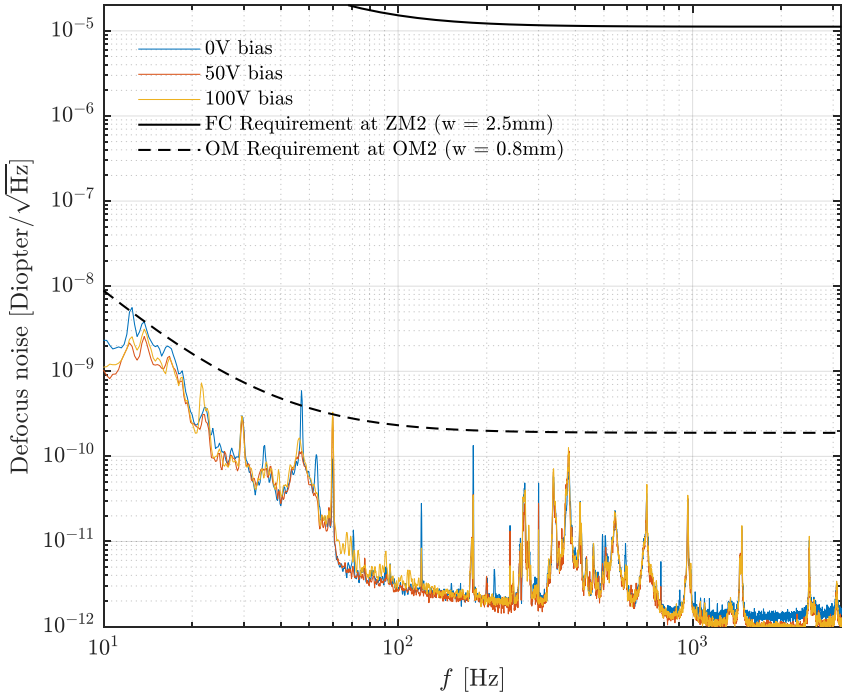

Figure 5-8: Qualification of PSAMS displacement noise that fulfills the LIGO's requirements of, for example, filter cavity (FC) optics and output mirror (OM2) [9].

Fig. 5-8 compares the measured displacement noise with LIGO's stringent requirement. It is below the requirement at all frequencies by up to a factor of 100 at high frequencies. The addition of PSAMS will not introduce noticeable phase noise to the squeezed beam.

5.4 Low-Loss Faraday Isolator

Besides relay optics, we have installed Faraday isolators on the path of the squeezed beam to block the stray light scattered back from the interferometer. This spurious light will propagate to the filter cavity and reflect back to the interferometer [77]. Reducing the backscattered light in Observing Run 3 (without filter cavity) was part of the reason why the squeezer was designed to be a bow-tie-shaped cavity. The addition of a linear filter cavity in the backscatter path poses a severe challenge to backscattered light mitigation.

Three low-loss Faraday isolators are installed in the squeezed beam path to provide a total of 103 dB reduction of the backscatter [78], as seen in Fig. 5-9. The addition of isolators also comes with the price of introducing losses in the squeezing. For Observing Run 4, the newly developed Faraday isolators are measured to have 99%-99.5% throughput or less than 1% loss in a single-pass [79]. These technological improvements are the key steps to enable high-dB squeezing in LIGO.

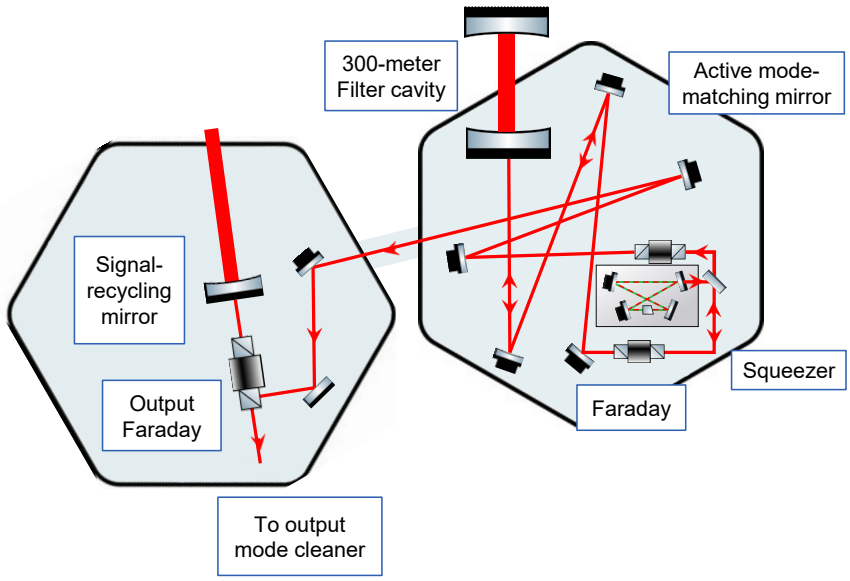

Figure 5-9: Simplified layout of the squeezing system in LIGO.

5.5 Filter Cavity

As discussed in Section 4.3, the goal of the filter cavity is to produce a frequency-dependent phase shift $\phi(\Omega)$ on the squeezed vacuum

$$\phi \rightarrow \phi(\Omega) = \tan^{-1} |\mathcal{K}(\Omega)| \tag{5.19}$$

which requires the filter cavity to have a half linewidth γ and frequency detuning $\Delta\omega$ such that

$$\gamma = \Delta\omega = \frac{\Omega_{\mathrm{SQL}}}{\sqrt{2}} \tag{5.20}$$

assuming a lossless cavity. The SQL frequency Ω_{SQL} for LIGO is at the order of tens of Hz, so the filter cavity must have a very thin linewidth to be operational. This requires the cavity to have either a small FSR (long length) or a very high finesse. The filter cavity has been demonstrated at various length across experiments all over the world [80–84].

A high-finesse cavity would lead to several problems [85].

- The stray light scattered back to the filter cavity would see higher amplification for a higher finesse, which requires a higher dB of backscatter isolation.
- High-finesse cavity is harder to control than low-finesse cavity
- It's more difficult to achieve a high finesse given realistic loss estimates.

Therefore, the designed filter cavity has a finesse as low as possible, or a cavity length as long as possible. Given the cost constraints, the final cavity length is set to 300 m.

To minimize loss, the filter cavity is a linear cavity situated along the Y arm of the LIGO interferometer. Both mirrors of the cavity have a 6-inch diameter and are triply suspended and mounted on isolated in-vacuum optical tables. The beam size has a diameter of 18.5 mm (28.6 mm) on the input (end) mirror. The designed filter cavity has $\gamma_{\mathrm{design}} = 2\pi \times 42$ Hz, using an input coupler

power transmissivity of $T_{\text{in}} \approx 1000$ ppm [3] and assuming 60 ppm optical loss, to approximately match $\Omega_{\text{SQL}} = \sqrt{2}\gamma_{\text{FC}} = 2\pi \times 59$ Hz for a circulating arm power of 500 kW.

5.6 Alignment Challenges

The beautiful theories of frequency-dependent squeezing assume that everything is aligned and coupled well in the real system, which is very nontrivial to achieve. In this section, we will discuss some of the challenges when aligning optical beams in LIGO, one of the most complex optical systems.

5.6.1 Squeezer alignment

Fig. 5-10 shows the pictures of the squeezer, which is a traveling-wave bow-tie cavity doubly resonant at both pump (532 nm) and fundamental (1064 nm) light. The pump field is generated from a single harmonic generator on an in-air table. The green beam is then coupled to the fiber, which is fed through the vacuum chamber and aligned to the input mirror of the squeezer.

Since the spontaneous parametric down-conversion process heavily depends on the phase-matching between the pump and down-converted fields, which is very sensitive to the temperature of the crystal. We detune the crystal temperature from optimal for initial alignment to prevent a nonlinear process. We swept the PZT on the cavity mirror and could see the transmitted cavity flashes, which were used to fine-tune the alignment [86].

Once the initial alignment is done, we should be able to see the transmitted light on a camera. The spatial mode of the light might not be the fundamental mode that has a nice and round circle. We can fine-tune the input beam to find the 00 mode. At this stage, we should have enough signal for Pound-Drever-Hall (PDH) locking [87]. If the cavity can be locked on resonance, we can further tune the alignment until we see a stable lock on 00 mode and maximize the transmitted power.

The final step of alignment is to scan the PZT such that transmitted light sees through a whole

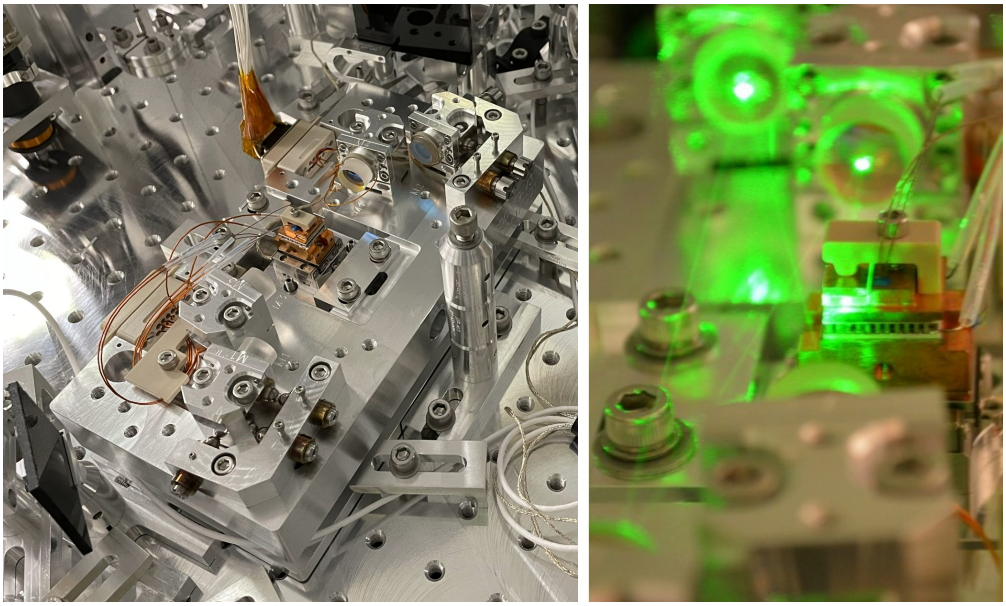

Figure 5-10: Pictures of (a) the squeezer bow-tie cavity [10] (b) when it is locked on green resonance [11].

FSR. If the cavity is mode-mismatched, we would see higher-order mode peaks in a single FSR. Minimizing these peaks will optimize the final alignment to the cavity.

The alignment for red locking is similar. We can send a coherent red beam known as the seed to the squeezer cavity. Since we don't have a PDH signal for red, we lock the red on resonance by dithering the PZT at high frequency (~kHz) and demodulating the beatnote of the reflected light. The bandwidth of the dither-lock is lower than the dither frequency, but we only need it to see the transmitted seed light whose alignment is defined by the squeezer cavity. In nominal operation, we don't have the seed and the dither-locking loop.

The transmitted seed beam when the squeezer is on red resonance would be co-aligned with the squeezed vacuum. It can be used as a proxy beam to do power budgeting and estimate losses.

5.6.2 Faraday alignment

The seed beam (co-aligned with squeezed vacuum) will be retro-reflected after being directed to the filter cavity. The retro beam will then propagate through two Faraday isolators, two PSAMS mirrors, and other relay optics before coupling with interferometer output at the output Faraday isolator. A beam aligned well to the filter cavity will have the perfect retro-reflected beam. However, we didn't have a filter cavity in some of our early experimental works.

To optimize the retro alignment, we added another waveplate in the path to re-direct the retro-reflected beam back to the squeezer cavity. If the retro beam is truly following the same path back, it will be aligned back to the squeezer cavity again [88]. This allows us to align the beams downstream without a filter cavity, especially through the Faraday isolators to estimate its throughput efficiency.

5.6.3 Align to interferometer

The alignment of the seed beam (co-aligned with the squeezed beam) to the interferometer is independent of the existence of the filter cavity, which acts as a retro-reflector of the squeezed beam. To simplify the anti-symmetric part of LIGO (known as differential arm, DARM), we misaligned the folded cavity mirror (SR2) such that the seed beam would not see the signal-recycling cavity but a single bounce from the signal recycling mirror (SRM). The seed beam is directed to the output Faraday isolator, single-bounced by SRM, and enters the anti-symmetric (AS) port of LIGO. It is easy to check the alignment by looking at the AS port camera and searching for the seed beam.

Once the seed beam is on camera, it can be aligned properly by the quadrant photodiode (QPD) at the AS port. After this is done, we should be able to see the seed beam coupled to the output mode cleaner (OMC) cavity. The fine-tuning of the alignment can be done by maximizing the resonant peak of the fundamental mode at the transmission photodiode.

5.6.4 Filter cavity alignment

Once the filter cavity is installed and qualified for vacuum, we opened the gate valve to merge the vacuum of the squeezer chamber (HAM7), filter cavity, and chamber (HAM8) that hosts the filter cavity end mirror (FC2). The first step to aligning a filter cavity is to find the transmitted beam from the input mirror (FC1). It is non-trivial to search for a laser beam landing on a 6-inch optics from 300-meter away. The required angular resolution is $6\,\text{in}/300\,\text{m} = 500 \times 10^{-6}$ rad.

Remember that a lossless filter cavity requires the end mirror to be perfectly reflective, which implies that there won't be any transmitted beam. To solve this problem, we coated the mirrors to be dual-reflective on both green 532 nm and red 1064 nm. The green finesse is much lower than red, so we can use green to search for transmissions and perform preliminary locking before handing it over to red. By changing the input alignment of the green beam, we were able to find the transmitted beam through the viewport of the HAM8 chamber.

The next step is to retro-reflect the beam from FC2 back to FC1. It's very difficult to find the retro beam back to HAM7 if FC2 is misaligned, given the 300-m long baseline. Therefore, we set up a lens and a mirror near the HAM8 viewport to reflect the FC2 transmitted beam back to FC2, which reflects the retro beam again through the viewport. This baseline is much shorter so we can align FC2 to overlap these reflected beam spots [89, 90]. This rough alignment of FC2 will help us find the green beam reflected back to FC1 and even on the in-air photodiode that measures the reflection of the green light.

After FC2 is aligned, we can adjust FC1 to reflect the retro beam back to FC2. This part is almost as difficult as finding the first light in the filter cavity. Nonetheless, scanning the full range of the FC1 actuator should allow us to find the beam and overlap with the first light that passes through the cavity. We were able to see the cavity flashes when FC1 and FC2 are roughly aligned. The rest of the work is very standard to align any cavities such as the squeezer cavity mentioned above.

5.7 Length Sensing and Control

The beautiful theories of frequency-dependent squeezing discussed in Chapter 4 didn't mention one important reality - that the whole system moves around the mathematically optimized point and is continuously disturbed by the outside environment. To suppress the environmental noise and maintain the system at the optimal operating point, we deploy hundreds of control loops to stabilize the LIGO detector [91]. In this chapter, we will focus on the sensing and control of the length degree of freedom of cavities and optical paths.

Before diving into the control system, there's an important lesson I learned on what "control" often means in LIGO context. Coming from a Mechanical Engineering field, I often take control as a way to control the dynamics of the system, for example, to actuate a torsional pendulum to a desired position with minimal overshoot, steady-state error, etc. However, "control" in LIGO usually means to suppress the free-running error. LIGO cares more about the noise suppression at steady state than the dynamics for the system to reach a steady-state. The different take on the control system was confusing to me when I first started working on LIGO.

5.7.1 Squeezing control overview

The goal for the length sensing and control (LSC) is to stabilize two things

- Squeezing angle ϕ. This is the relative phase between the squeezed vacuum and the interferometer output light.

- Filter cavity detuning $\Delta\omega$. This is the frequency detuning of the cavity from the resonance of the carrier field.

Fig. 5-11 shows the experimental overview of the length sensing and control for the frequency-dependent squeezing system. The whole system is divided into colored blocks for each control

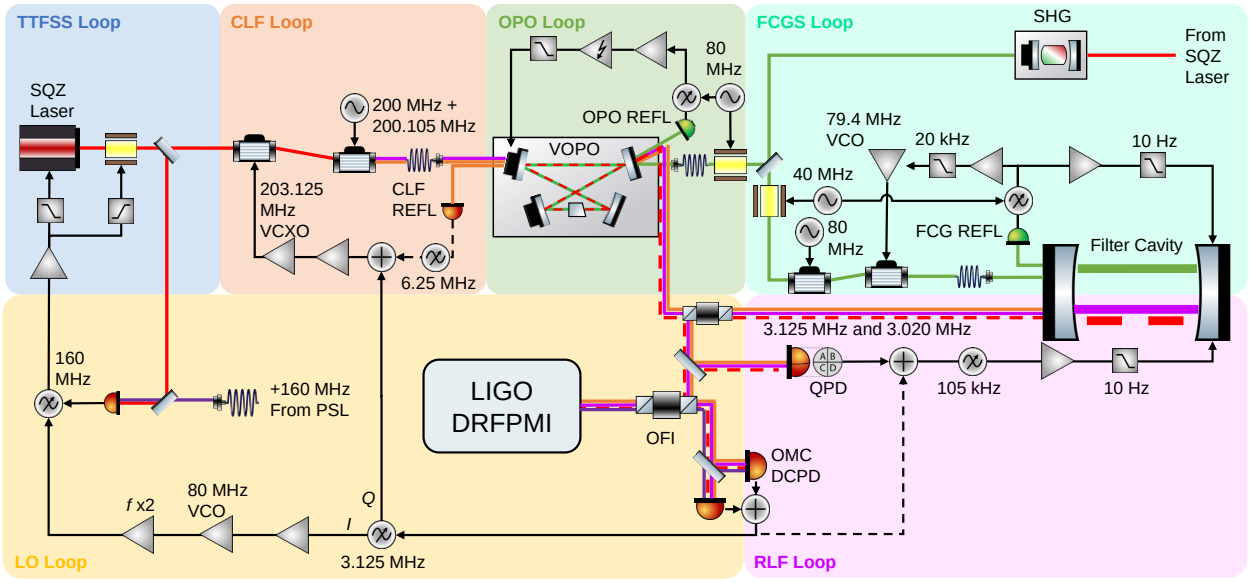

Figure 5-11: Overview of the length sensing and control loops for the L1 squeezing system in Observing Run 4 [12].

loop. The right two blocks (FCGS and RLF) are for filter cavity control, while the left blocks are for squeezing angle control. We will explain the simplest one first.

5.7.2 TTFSS loop

The table-top frequency stabilization servo (TTFSS) is the loop that phase-locks the SQZ laser with the interferometer light such that the generated squeezed vacuum has a frequency reference with respect to the carrier light. The phase-locking loop (PLL) is very standard. We double pass the light from the pre-stabilized laser (PSL), which is the laser source for LIGO [92,93], through an acousto-optic modulator (AOM) to generate 160-MHz sideband. These sidebands are then routed to the squeezer table with a long optical fiber, beaten against the SQZ laser, and read out by heterodyning. The error signal is fed back to both the PZT of the SQZ laser (for large dynamic range) and the electro-optic modulator (EOM, for large bandwidth). The total bandwidth is around 300 kHz.

5.7.3 OPO loop

The squeezer, sometimes referred to as an optical parametric amplifier (OPA) or optical parametric oscillator (OPO), is locked on dual resonance of 532-nm pump light and 1064-nm carrier light. We use a standard PDH loop to sense error signals and feed them back to the cavity length by a PZT actuator. The pump light is generated by a single harmonic generator from the SQZ laser, so the pump beam is phase-locked with the SQZ laser. We use EOM to produce the 80-MHz sidebands and demodulate the beatnote on the reflection (REFL) photodiode. The temperature control loop allows the fine-tuning of the phase-matching condition for the spontaneous parametric down conversion process. The down-converted and entangled photon pairs (squeezed vacuum) will propagate from the OPO REFL port to the filter cavity.

5.7.4 CLF loop

The coherent locking field (CLF) uses the technique of coherent control to witness and lock the phase of the squeezed vacuum [94, 95]. Normally when we phase-lock two laser beams, we can use either heterodyne or homodyne readout to sense the relative phase fluctuations. However, it is difficult to do this with a squeezed vacuum because it is not a coherent beam.

To sense the phase of the squeezed vacuum, we can measure the squeezing it produces, but the measured squeezing level is fluctuating too quickly or we don't have enough bandwidth to control it. Instead, we send a co-propagating auxiliary field that is a single-side sideband at 3.125 MHz, which is the CLF field. Unlike the spontaneous parametric down conversion that produces squeezed photon pairs $\omega \pm \Omega$ from one pump photon 2ω, the nonlinear process converts one pump photon and CLF photon at $\omega + \Omega_{\mathrm{CLF}}$ to $2(\omega + \Omega_{\mathrm{CLF}})$ and one $\omega - \Omega_{\mathrm{CLF}}$, known as the difference frequency generation. Since both the CLF field and squeezed vacuum are from the same pump field, they are phase-coherent with each other.

The CLF REFL PD will see the CLF field beating with the converted CLF to produce a $2\Omega_{\mathrm{CLF}}$ beatnote. Feeding back this error signal to the frequency actuator AOM will phase-lock the CLF

field with the pump field and therefore with the squeezed vacuum. The transmitted CLF field will co-propagate with the squeezed vacuum and serve as its phase witness.

We generate the CLF by two AOMs with opposite directions of photon momentum. The first AOM gives 203.125-MHz sideband, and the second AOM kicks back 200 MHz to produce the final 3.125 MHz CLF field. We do this trick to generate sideband at a very low radio frequency and even audio frequency range [4].

5.7.5 LO loop

The local oscillator (LO) loop phase-locks the CLF field with respect to the output carrier light from the interferometer output. At the transmission of output mode cleaner (OMC) cavity, there are a pair of photodiode that readout gravitational wave signals and all noises, known as OMC DCPD. We demodulate the 3.125-MHz beatnote between CLF and carrier light and feed the error signal to the SQZ laser.

By locking CLF to the squeezed vacuum and then locking CLF to the output light, we eventually phase-lock the squeezed vacuum to the interferometer output. This is the idea of coherent control of squeezed vacuum, by using CLF as a proxy field to bridge the connection between squeezed vacuum and output carrier light.

5.7.6 FCGS loop

Filter cavity green sensing (FCGS) is a preliminary control loop to lock the filter cavity at a frequency detuning from the resonance. As mentioned in Section 5.6.4, the FC mirrors are dual coated with green finesse (370) much lower than red (7000). This allows us to hierarchically lock the filter cavity from green to red.

The filter cavity is stabilized first by the FCGS loop. We pick some green light from the SHG and add 40-MHz sideband to it via EOM. Then the green light passes through two AOMs that are

used to actuate the frequency of the light. The PDH signals are fed back to the AOM first for a wider dynamic range. Once the green lock is achieved, we transfer the error signal from AOM to suspensions of FC2, known as the mass feedback.

The relatively low green finesse allows the FCGS loop to engage fast enough to catch the green resonance with freely swinging cavity mirrors. We notice that engaging the TTFSS loop helps reduce the noise of the SQZ laser, and thus helps the locking of the filter cavity on green.

5.7.7 RLF loop

With the filter cavity locked on green, the last step is to lock it on the red resonance at the right frequency detuning with the resonant locking field (RLF). RLF field is co-generated with CLF from the same AOM so they are always co-aligned. Unlike CLF field with frequency shift of 3.125 MHz, RLF is generated at $\Omega_{\mathrm{RLF}} = 203.125 - 200.105 = 3.02\,\mathrm{MHz}$. By design, the FSR of the filter cavity is $c/2L$, and

$$6 \times \mathrm{FSR} = 6 \times \frac{c}{2L} = 6 \times \frac{299\,792\,458\,\mathrm{m/s}}{2 \times 297.85\,\mathrm{m}} = 6 \times 503.26\,\mathrm{kHz} = 3.0196\,\mathrm{MHz} \tag{5.21}$$

which is the RLF frequency. Therefore, RLF is exactly on the resonance of the filter cavity, but 6 FSR away from carrier resonance.

To find the red resonance, we lock the filter cavity on green and scan the 79.4-MHz voltage-controlled oscillator (VCO). The mass feedback will move the FC mirror to follow the green resonance. We can dither-lock the OPO on the seed light to help find the first red resonance of the filter cavity.

After finding the red resonance, we can optimize the alignment of the red beam by maximizing FC transmission, minimizing higher-order peaks in cavity sweep, etc. When we send the CLF and RLF to the filter cavity near red resonance, we will sense the PDH signal from the QPD on the FC reflection. The RLF would be resonant in the cavity, but the CLF is 105-kHz away and outside

the FC full linewidth of 84 Hz. So the RLF plays the role of "local oscillator", and CLF is the "sideband" in this case. Their beatnote is demodulated at 105 kHz and fed back to FC2. Note that the resonance of the CLF field would also give a 105-kHz error signal, but it's not the right field to be resonant in the filter cavity.

A stable green locking loop will stabilize the cavity length to have a root-mean-square (RMS) motion less than the linewidth of the red resonance. This allows us to hand over the mass feedback from green to red. This is similar to the lock acquisition of the 4-km arm cavity [96, 97]. The FCGS will disengage and the green beam will be blocked to the filter cavity once the RLF loop is stabilized.

The detuning frequency $\Delta\omega$ can be controlled via the selection of the RLF frequency offset from the carrier laser, namely

$$\Omega_{\mathrm{RLF}} = 3.0196\,\mathrm{MHz} + \frac{\Delta\omega}{2\pi} \tag{5.22}$$

The demodulation frequency also has to change correspondingly. This part of the control system is digital so it's easier to adjust for best filter cavity performance [98].

This concludes the nominal loop topology for the squeezing system in Observing Run 4. The loop bandwidth is summarized in Table 5.1.

Table 5.1: Bandwidth of individual control loops of the squeezing system [19, 20].

	TTFSS	OPO	CLF	LO	RLF
Bandwidth	300 kHz	3.2 kHz	1.1 kHz	4.1 kHz	50 Hz

5.7.8 Alternative topology

Fig. 5-11 shows the nominal control scheme employed in Observing Run 4. The dashed line in the schematics offers an alternative loop topology. Two dashed signal lines offer different error signals.

The first one is the RLF loop. We use the 1% pick-off light from the squeezed path to measure

the 105-kHz RLF-CLF beatnote. This means a 1% loss of the squeezed vacuum. Alternatively, we can measure the RLF signals on the OMC DCPD. We didn't try it during commissioning but it should work in principle.

The CLF loop also has an alternative error signal. Instead of measuring the $2\Omega_{\mathrm{CLF}}$ at the CLF REFL PD, we can use the Q-quadrature of the demodulated 3.125-MHz signal from the DCPD. The reason is that the converted CLF sideband records phase information of the pump field. It will be read out by beating with regular CLF (manifested on CLF REFL RF6) or the carrier light (OMC DCPD RF3-Q). In fact, we observe a more stable squeezing level when we use RF3-Q to control the phase between CLF and pump [99]. The drawback is that the RF3-Q error signal has an error slope that is dependent upon the demodulate phasing. It sometimes changes from lock to lock.

5.8 Alignment Sensing and Control

While length sensing and control (LSC) is responsible for stabilizing frequencies and phases, alignment sensing and control (ASC) is engaged to stabilize the angular pointing of optical beams or alignment to the cavity [100–102]. The ASC loop bandwidth is usually much lower than that of LSC because the alignment drifts are slow.

There are two major ASC loops to control alignments of the squeezed vacuum to the filter cavity and the squeezed vacuum to the interferometer. We will discuss each one separately.

5.8.1 Filter cavity ASC

The filter cavity alignment is sensed by the 105-kHz wavefront sensor (WFS), which demodulates the 105-kHz RLF-CLF beatnote from each quadrant of the QPD. This is a common technique used in LIGO for various ASC loops [103, 104]. A misaligned filter cavity would move the REFL beam spot on the QPD, which would see the change of demodulated signal from all of the four quadrants. Therefore, they are good sensors for the FC alignment.

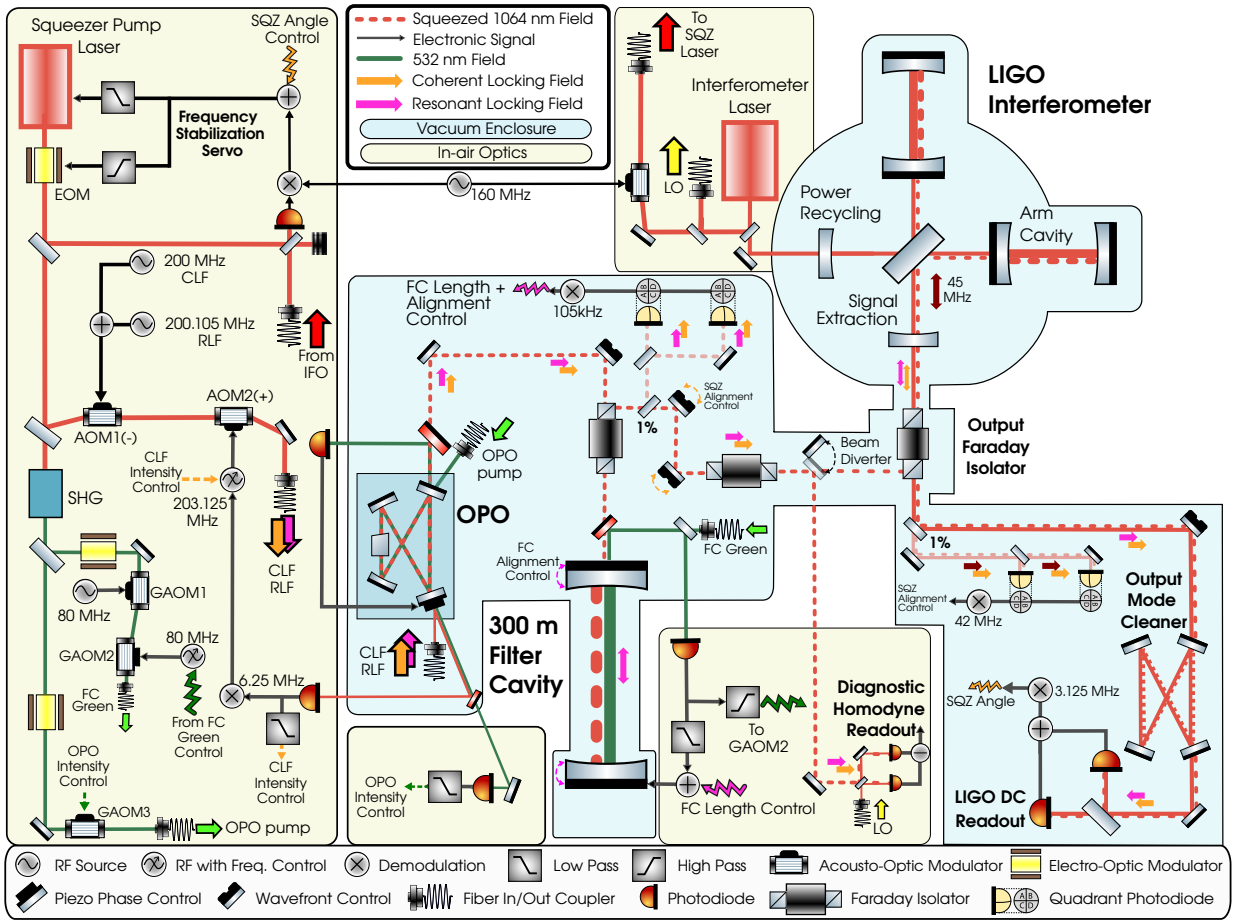

Figure 5-12: A complete overview of the squeezing system, including LSC loops, ASC loops, and ISS [3].

We diagonalize these WFS signals such that they are independently witnessing the pitch/yaw alignment of FC1/2. These signals are then fed back to the optics stage of the FC triple suspension [105]. The bandwidth of the FC ASC loops is less than 0.1 Hz to control slow driftings.

In addition, we have an alignment dithering system (ADS) to center the beam on the FC mirrors. We dither FC1/2 at a low frequency in pitch/yaw. If the beam is not at the center of the optics, the demodulated RLF-CLF signal would sense the oscillation at the dither frequency with amplitude proportional to the distance of the beam spot from the center of optics. The ADS system was not employed in real-time, but a one-time action to center the beam spots on the FC mirrors [106].

5.8.2 Squeezing ASC

The SQZ ASC is responsible for keeping the squeezed vacuum aligned with the interferometer output field to ensure an optimal squeezing injection all the time. We pick off 1% of the beam after the output Faraday isolator and send them to the two QPD, known as anti-symmetric A and B (AS-A, AS-B). Note that this pick-off is inevitably a 1% loss of the squeezed vacuum and the gravitational wave signal.

The 3-MHz CLF (co-propagated with SQZ) will beat with the 45-MHz sideband (co-propagated with interferometer light) to form a 42-MHz RF signal on the WFS QPD. We use the same method as above to sense the alignment drift [107].

Besides the ASC loops, we also have various intensity stabilization servo (ISS) to control the squeezing level. The CLF intensity is controlled by stabilizing the 6.25-MHz RF power on the CLF REFL PD. The pump intensity is stabilized by controlling the transmitted pump power. These ISS also help to maintain the stable reference offset for various ASC loops.

5.9 Observation of Frequency-Dependent Squeezing

Everything aforementioned in this thesis culminates with the observation of frequency-dependent squeezing at both LIGO detectors.

Fig. 5-13 shows the frequency-dependent squeezing working at both detectors. It's the first demonstration of the technique on real gravitational-wave detectors that benefit astrophysical observations. The unsqueezed are shown in black. The frequency-independent squeezing (without filter cavity) is shown in green, which has high-squeezing at high frequency but suffers from extra quantum radiation pressure noise at low frequency. With a filter cavity that provides the frequency-dependent phase rotation, we can achieve broadband squeezing as shown in purple traces. The estimate of non-quantum ("classical") noises and the model for unsqueezed quantum noise are also shown in the plot.

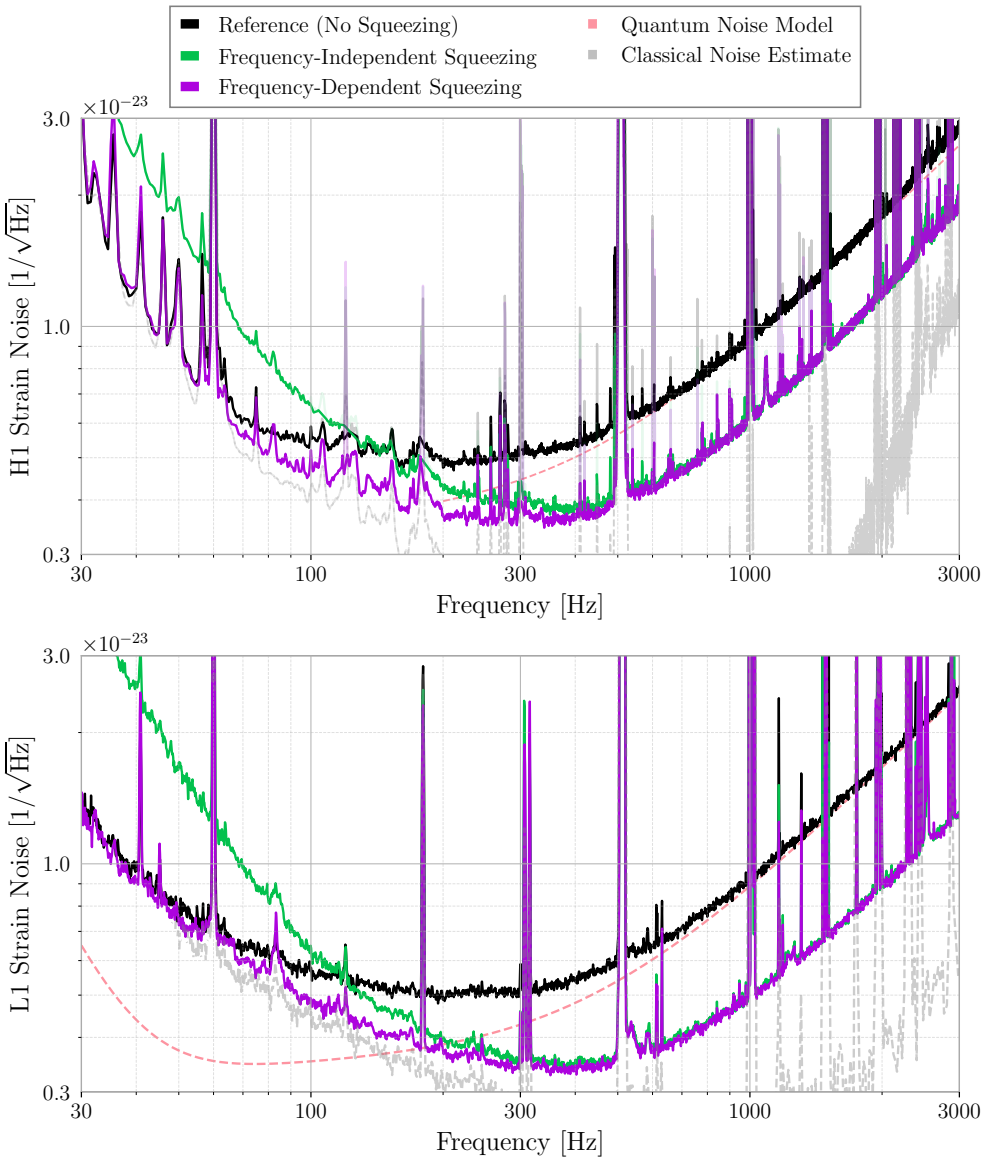

Figure 5-13: Observation of frequency-dependent squeezing in LIGO Hanford (top) and Livingston (bottom) detectors. The total interferometer noises see squeezing of 4.0 dB (Hanford) and 5.8 dB (Livingston) at high frequencies, and up to 1–2 dB from 60–100 Hz [3].

While Fig. 5-13 shows the experimental observations of the frequency-dependent squeezing, there are lots of work to do in order to understand the whole system, especially the quantum noise part. In the next chapter, we will solve the full interferometer to understand all the losses and

degradations to squeezing. More importantly, the squeezed quantum noise can be shown to surpass the Standard Quantum Limit, a milestone in the field of quantum measurement.

5.10 Impact of Squeezing to LIGO

Besides frequency-dependent squeezing, many instrument upgrades have been implemented to increase the sensitivity of both LIGO detectors [2] more than before [108–110]. A figure of merit of LIGO's sensitivity is the SenseMon range or binary neutron star (BNS) range [111]. It corresponds to the radius of the sensitive volume of the Universe for 1.4–1.4 $M_\odot$ neutron star binary systems (assuming a detection threshold with a matched-filter signal-to-noise ratio of 8 in a single detector), integrated over the interferometer antenna pattern, and averaged over all binary inclinations and orientations [112]. The analytical expression is [113]

$$\text{BNS range} = \left(\frac{5M^{5/3}\theta^2}{96\pi^{4/3}\rho_0^2} \int_0^\infty df \frac{f^{-7/3}}{S_h(f)} \right)^{1/2} \tag{5.23}$$

where $\theta = 1.77$ accounts for the averaging over the binary positions and orientations, $\rho_0 = 8$ is the minimal SNR, and $M = 1.2M_\odot$ is the binary chirp mass of a pair of 1.4-$M_\odot$ neutron stars. The BNS range weights heavily at the low-frequency part of the detector's total noise $S_h(f)$, motivating the frequency-dependent squeezing that reduces the quantum radiation pressure noise at low frequencies.

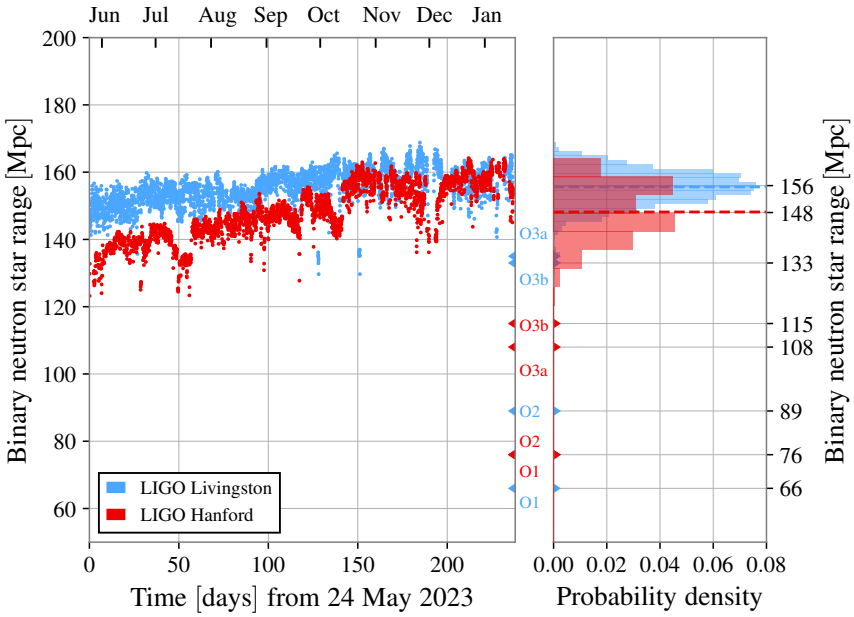

Figure 5-14: The BNS range trends for the LIGO Hanford (red) and LIGO Livingston (blue) observatories during the first half of the fourth observing run. The left plot shows the hourly binary neutron star range over time of the LIGO Hanford and LIGO Livingston detectors during O4a. The right plot shows the range histograms of each site, with the Hanford Observatory range being bimodal. Both detectors achieved ranges over 160 Mpc during the run, with the Livingston detector achieving close to 170 Mpc [2].

Fig. 5-14 shows the BNS range of both LIGO detectors during the first part of Observing Run 4 (O4a). The median of the LIGO Livingston detector is 156 Mpc, compared to O3's median range of 133 Mpc. The increase of the range is credited to the instrument upgrade at the front lines of all noise sources.

Fig. 5-15 shows the total noise budget of the Livingston detector during O4a. The measured noise is the total detector noise with frequency-dependent squeezing. The sum of known noises includes analytical noises from the model (dashed lines like quantum, thermal, and residual gas) and projected noises from all other sources listed in the legend.

The detector noise is limited by quantum shot noise and laser noise at high frequencies (> 500 Hz) [114, 115]. The coating Brownian noise limits the detector at the mid-frequency band

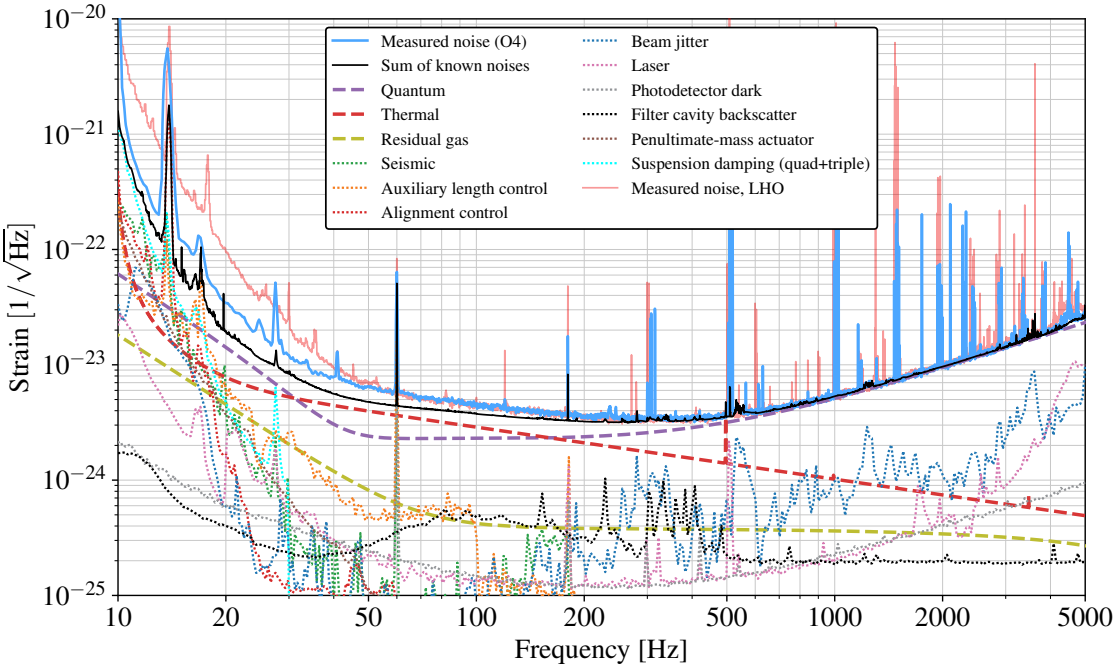

Figure 5-15: Noise budget of LIGO Livingston Observatory [2].

(50–500 Hz) [116]. Below 50 Hz, the noise contributions are complicated. Quantum radiation pressure noise can be a limiting factor, while the control noises, including LSC loops [96] and ASC loops [100], are comparable to the quantum noise. The measured noise of the twin Hanford detector is also shown in the background for comparison.

There is still a noticeable gap between the sum of known noises and the total measured noise. The reason is largely due to the underestimation of coating Brownian noise measured from witness samples [117], and scattered noise from stray light that couples the beam tube motions to the phase noise of the output light. Ongoing effort have been put to investigate the mysterious noises in LIGO.

Fig. 5-16 shows the cumulative detection of gravitational-wave events since the first Observing Run (O1) [118–120]. Thanks to the instrument upgrade including frequency-dependent squeezing, the detection rate or the slope of the curve nearly doubles in O4, compared to O3.

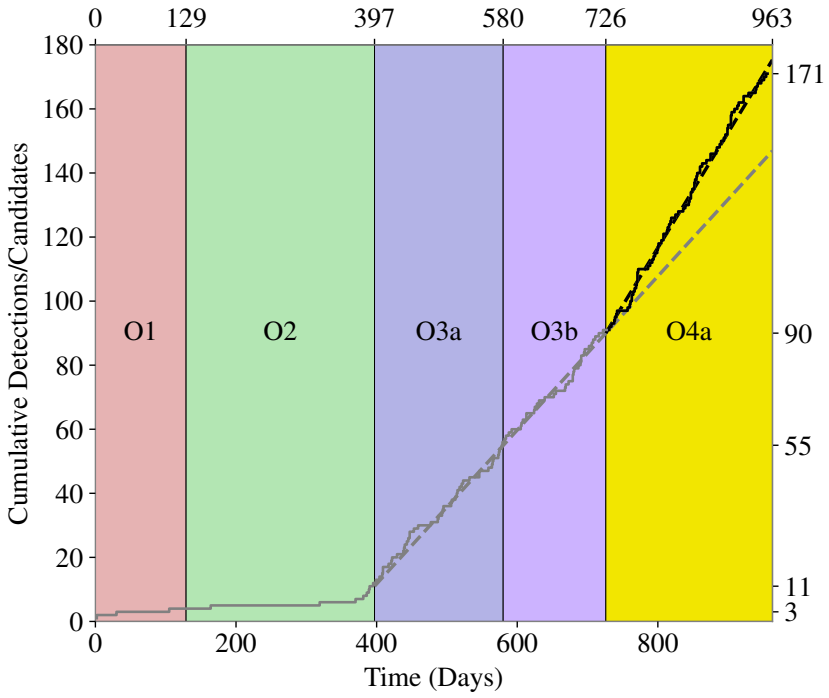

Figure 5-16: Cumulative events up to January 9, 2024, including the entirety of O4a. O4a entries are preliminary candidates identified in online real-time triggers [2].

The success of the squeezing experiment, along with other technological advances at many other fronts of the detector in O4, paves the way for the designed goal of A+ upgrade with 750 kW of arm power and 6 dB broadband squeezing. Assuming that we could find a new coating material that reduces the coating Brownian noise by a factor of 2, the A+ LIGO would be able to see more than half of the total black holes that exist in our known Universe. Next-generation detectors like Cosmic Explorer (CE) and Einstein Telescope (ET) are motivated to detect all binary compact objects in the known Universe.

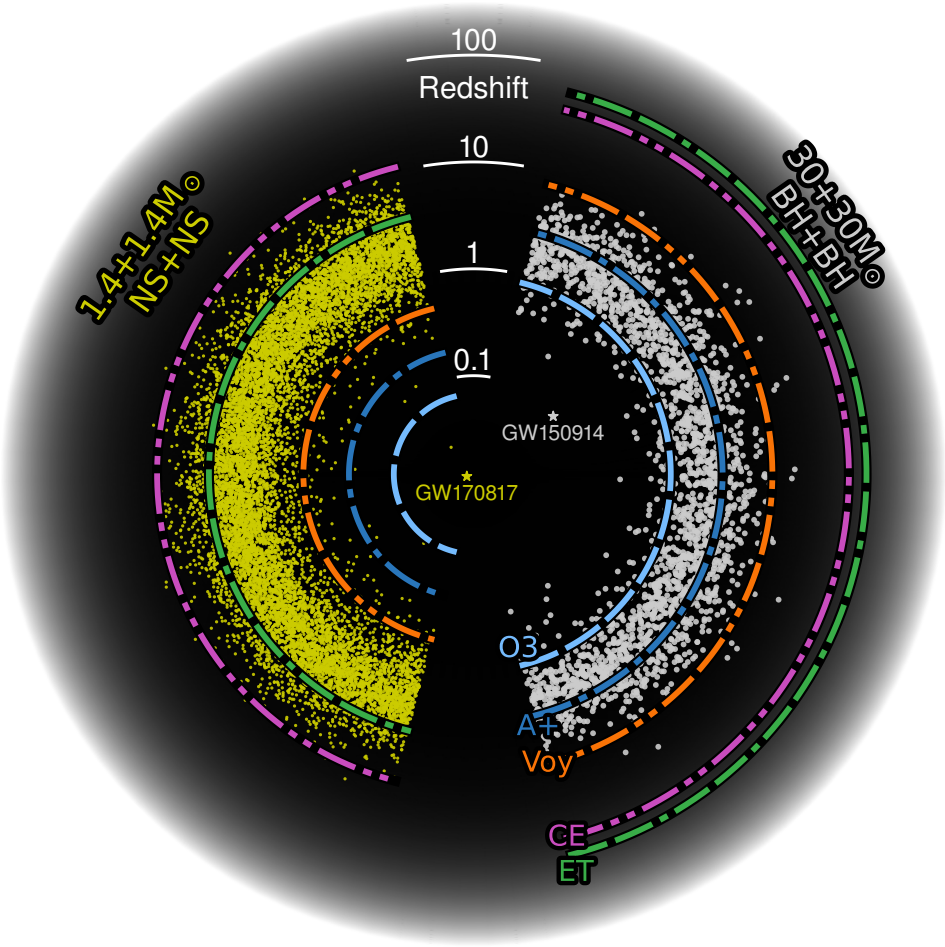

Figure 5-17: The cosmic history of binary stellar remnant mergers, and the range of current and proposed detectors that are possible to see them [13].

6 LIGO BREAKS STANDARD QUANTUM LIMIT

The Standard Quantum Limit (SQL) describes an apparent limit on how well you can measure the position of an object with light. As discussed in previous chapters, the discrete nature of light yields a fundamental quantum noise to the measurement precision. Although the power of the light can be increased to reduce the relative shot noise, it will cause a stronger quantum back-action to the measured object. This is the result of the Heisenberg uncertainty principle.

The heuristic model of the uncertainty principle is the Heisenberg's microscope. It is a thought experiment came up by Heisenberg to grasp the intuition of the uncertainty principle.

This chapter discusses about the quantum noise of LIGO Livingston Observatory that is squeezed below the SQL [1].

6.1 Heisenberg's Microscope

Suppose that we are measuring the position of a particle under a microscope. Given the aperture size a of the lens and the wavelength λ of the light, we can resolve the angular resolution up to the diffraction limit, which is known as the Rayleigh criterion.

$$\Delta\theta \sim \frac{\lambda}{a} \tag{6.1}$$

Therefore, the position uncertainty of the particle is

$$\Delta x \sim L\Delta\theta \tag{6.2}$$

where L is the distance between the particle and the lens.

When we measure the position of the particle, we actually "see" the photon scattered from the particle. The scattering of the photon from the particle will lead to a recoil to the particle itself. This is the quantum back-action.

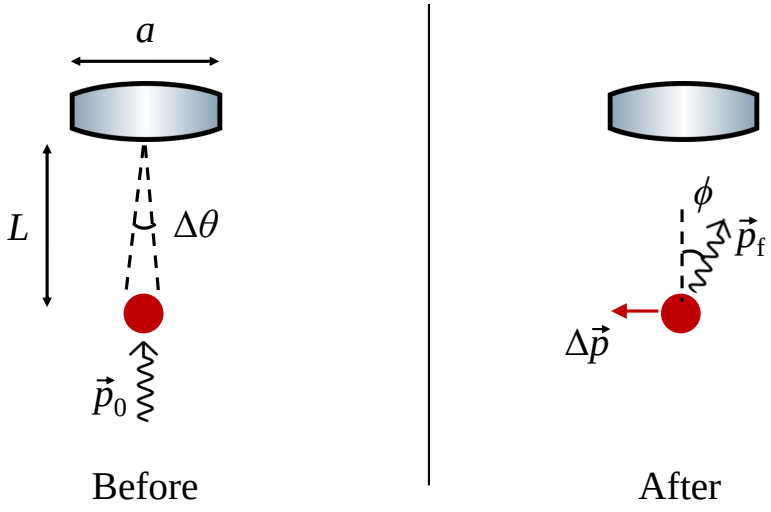

Figure 6-1: Set-up of the Heisenberg's microscope thought experiment.

Fig. 6-1 shows the set-up of the thought experiment. The momentum conservation gives

$$\Delta p \sim p_0\phi \sim \frac{\hbar}{\lambda}\frac{a}{L} \tag{6.3}$$

The scatter angle ϕ has to be smaller than a/L to be able to go through the lens. Therefore, we have

$$\Delta x\Delta p \sim \frac{L\lambda}{a}\frac{\hbar a}{\lambda L} \sim \hbar \tag{6.4}$$

If we wish to increase the position uncertainty, we need a smaller wavelength to probe the

particle harder with a higher-energy photon. However, this would lead to a higher momentum uncertainty. It's clear to see the trade-off between uncertainties of conjugate observables.

The Heisenberg's microscope is a one-off measurement of the particle, whereas in LIGO, we perform a continuous measurement of the mirror. The direct implication of the uncertainty principle in continuous measurement is the Standard Quantum Limit.

6.2 Standard Quantum Limit

The Heisenberg uncertainty principle asserts that the product of the uncertainties in the measurements of conjugate observables (like position and momentum) cannot be less than $\hbar/2$. When we measure the position x of an object with an uncertainty Δx, it inevitably disturbs its momentum by $\Delta p \geq \hbar/(2\Delta x)$. After a time interval τ, the object with mass m will evolve with an additional uncertainty in position $\Delta x'$ due to the momentum disturbance, $\Delta x' = \tau \Delta p/m = \hbar\tau/(2m\Delta x)$. A highly precise measurement ($\Delta x \to 0$) will result in the next position measurement being entirely unpredictable ($\Delta x' \to \infty$) due to quantum back-action [121–125]. The minimal achievable uncertainty is attained when $\Delta x = \Delta x' = \sqrt{\hbar\tau/(2m)}$, referred to as the Standard Quantum Limit (SQL) [126]. While the SQL is relevant to measurements of microscopic particles, it also limits the measurements conducted by the LIGO interferometric detectors, which measure the differential positions of a pair of 40-kg arm cavity mirrors.

In the continuous measurement context like LIGO, the SQL can be easily seen from the unsqueezed quantum noise model developed in Section 4.2.2, namely Eq. (4.52)

$$S(\Omega) = \frac{h_{\mathrm{SQL}}^2}{2}\left(|\mathscr{K}(\Omega)| + \frac{1}{|\mathscr{K}(\Omega)|}\right) \tag{6.5}$$

where

$$h_{\mathrm{SQL}}(\Omega) = \sqrt{\frac{8\hbar}{m\Omega^2 L^2}} \tag{6.6}$$

is the SQL represented in the strain noise of the interferometer. The first term is due to quantum back-action from the quantum radiation pressure noise, while the second term is the imprecision noise due to quantum shot noise. No matter how hard we probe the mirror (changing the value of $\mathcal{K}$), we are always limited by the SQL, dictated by Heisenberg's uncertainty principle. This is true even in the ideal case where the whole system is lossless. Any realistic experimental degradation will increase the quantum noise [127, 128].

Eq. (6.5) enforces the SQL because it is an incoherent superposition of quantum back-action and imprecision noise, as we probe the mirror with uncorrelated photons. When we send entangled photon pairs like squeezing, we can manipulate the quantum correlation between light and mirror due to ponderomotive squeezing [36]. Quantum correlation has been observed in many experiments, including LIGO [45, 46, 129, 130]. As alluded in Eq. (4.65), the squeezed quantum noise is (Eq. (4.65))

$$S_{\mathrm{SQZ}}(\Omega) = 2\hbar\omega_0 B^2(|\mathcal{K}|^2+1)[e^{2r}\sin^2(\phi-\theta) + e^{-2r}\cos^2(\phi-\theta)] \tag{6.7}$$

When we have a perfect filter cavity that creates $\phi = \phi(\Omega) = \theta(\Omega)$, the squeezed quantum noise can surpass the SQL near the SQL frequency Ω_{SQL} where $|\mathcal{K}(\Omega_{\mathrm{SQL}})| = 1$

$$S_{\mathrm{FDSQZ}}(\Omega_{\mathrm{SQL}}) = h^2_{\mathrm{SQL}}(\Omega_{\mathrm{SQL}})e^{-2r} < h^2_{\mathrm{SQL}} \tag{6.8}$$

Given our success with frequency-dependent squeezing as shown in the previous chapter, it might seem trivial to claim that our quantum noise is below SQL. However, LIGO measures not only quantum noise but also non-quantum ("classical") noises that have comparable or even a factor of three higher than quantum noises in amplitude, depending on the frequency of measurement. Precisely quantifying the classical noise and obtaining the underlying quantum noise is the most difficult part of the work.

Since LIGO measures the total noise of the interferometer, the classical noise can be obtained

trivially by subtracting the total noise with an accurate quantum noise model. As discussed in Chapter 3, the full quantum noise model is very complicated and has a lot of parameters. For each cavity, we have optical losses and mis-detunings. Between two cavities, we have mode-mismatches. The parameter space can easily go above 30. A clever parameter estimation is required to find the correct model.

In the following sections, we will infer the quantum noise model provided by the Gravitational Wave Interferometer Noise Calculator (GWINC) by isolating a simpler subsystem and fitting its parameters [58]. Then we can use these parameters to infer new parameters introduced in the full system. We would be able to find all parameters in a stepwise fashion.

All of the experiments obtained in this chapter were also done at LIGO Livingston Observatory. Qualitatively similar results have also been observed in LIGO Hanford Observatory. The first measurement we fit first is the sensing function.

6.3 Analysis of Sensing Function

The sensing function is the optical gain (g_{cal} in Eq. (4.51)) that converts the measured optical power fluctuation in Watt to the change of the length difference between two arms of LIGO, known as differential arm lengths (DARM). The sensing function depends only on the unsqueezed interferometer's response to the arm-length perturbations, mostly including degradation of the output path and responses of the signal-recycling cavity (SRC, sometimes also called a sideband-extraction cavity, SEC). Therefore, we can isolate and infer the SRC parameters by fitting the sensing function.

LIGO employs an active calibration system known as the Photon Calibrator (Pcal) [55]. The system actively modulates the differential arm length by sending an amplitude-modulated laser beam on the test mass. Therefore, we can directly measure the interferometer's sensing function by sweeping the Pcal laser frequency.

The calibration team infers coupled-cavity pole (f_{cc}) and SRC spring information at low frequencies from the s [131]. Nevertheless, the f_{cc} uses single-cavity transfer function to approximate the coupled cavity, and it is not correct if we have mode-mismatches. Therefore, we infer SRC parameters ourselves from sensing functions produced by GWINC, which has these parameters:

Table 6.1: The major 9 GWINC parameters that affect the sensing function.

Physical quantity	**GWINC variable name**	**Symbol**
Arm power	ArmPower	P_{arm}
Readout loss	1 - PhotoDetectorEfficiency	Λ_{RO}
Mode-mismatch between IFO and OMC	MM_IFO_OMC	Υ_{OMC}
Mode-mismatch phase of IFO to OMC	MM_IFO_OMCphi	Υ_{OMC} phase
SRC loss	BSLoss	Λ_{SR}
Mode-mismatch between Arm and SRC	MM_ARM_SRC	Υ_{SR}
Mode-mismatch phase of Arm to SRC	MM_ARM_SRCphi	Υ_{SR} phase
SRC Gouy phase	SRCGouy_rad	ψ_{SR}
SRCL detuning	SRM.Tunephase	$\Delta\phi_{\text{SR}}$

6.3.1 Parametric study

We perform a parametric study to understand how each GWINC parameter affects the sensing function. We first find a canonical set of parameters that closely represents the truth, and then perturb each parameter independently from the canonical set. The change of the modeled sensing function is plotted concerning each perturbed dimension.

There are two scenarios with the arm to SRC mismatch Υ_{SR}, controlled by the parameter is_OPD. When is_OPD is true, the thermal lensing is more dominant than quadratic mode-mismatch, creating the optical path distortion (OPD) and thus the name of the parameter. Mathematically, the transfer function of the arm cavity (assuming lossless) with OPD is

$$\mathbf{h}_{\text{OPD}} = \mathbf{U}\mathbf{r}_{\text{arm}}\mathbf{U} \tag{6.9}$$

whereas the no-OPD transfer function is

$$\mathbf{h}_{\mathrm{NoOPD}} = \mathbf{U}^{\dagger}\mathbf{r}_{\mathrm{arm}}\mathbf{U} \tag{6.10}$$

where $\mathbf{U}$ is the scatter matrix to convert the field to the arm cavity basis. The no-OPD case is the standard quadratic mode-mismatch picture as discussed in Section 4.4. The OPD case assumes strong thermal lensing due to the absorption of high circulating power in the arm cavity. The truth might be a combination of both instead of a binary case. Anyway, we will analyze both cases separately.

Fig. 6-2 shows how the sensing function from GWINC is affected by IFO parameters. The title shows the canonical parameter set where we perturb from. For each subplot, the title says the perturbed parameter. The various values of such parameters are labeled in the legend. The sensing function is therefore very sensitive to Υ_{SR}.

The top row represents the degeneracy between arm power and readout loss/mode-mismatches. With only 0.1% of Υ_{SR} and 5% of Υ_{OMC}, Υ_{OMC} is quite degenerate with readout loss, and both of them affect the sensing function in a similar way as arm power. Note that it is with small Υ_{SR}.

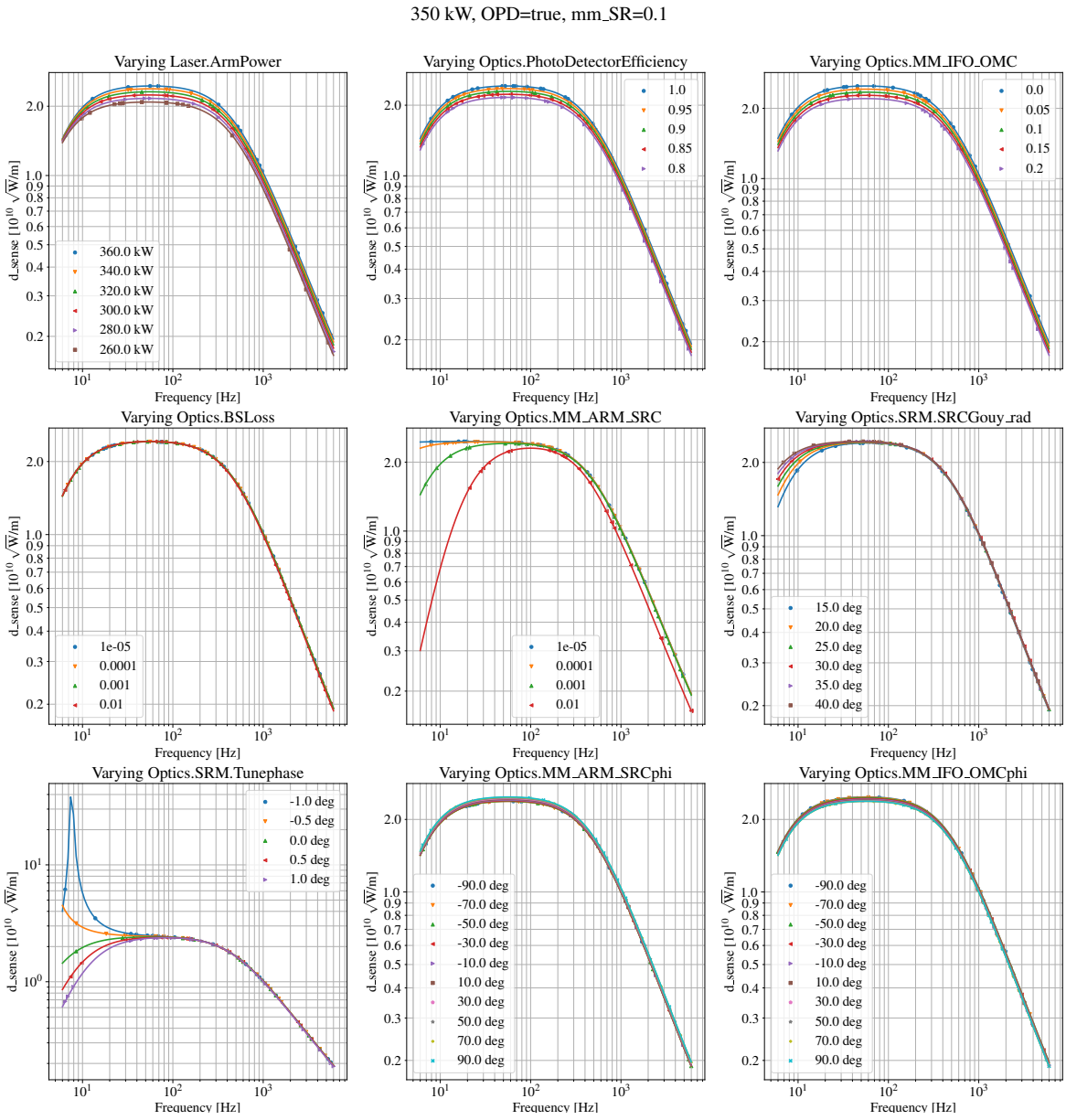

Figure 6-2: Parametric study of the sensing function as we perturb model parameters from a canonical set. The perturbed GWINC parameter is labeled in the title of each subplot. Roughly degenerate parameters are plotted in the same row [14].

The center row represents loss/mismatches in SRC. The simple SRC loss changes the coupled cavity pole by a tiny bit, as the high frequency of the sensing function changes but not the low

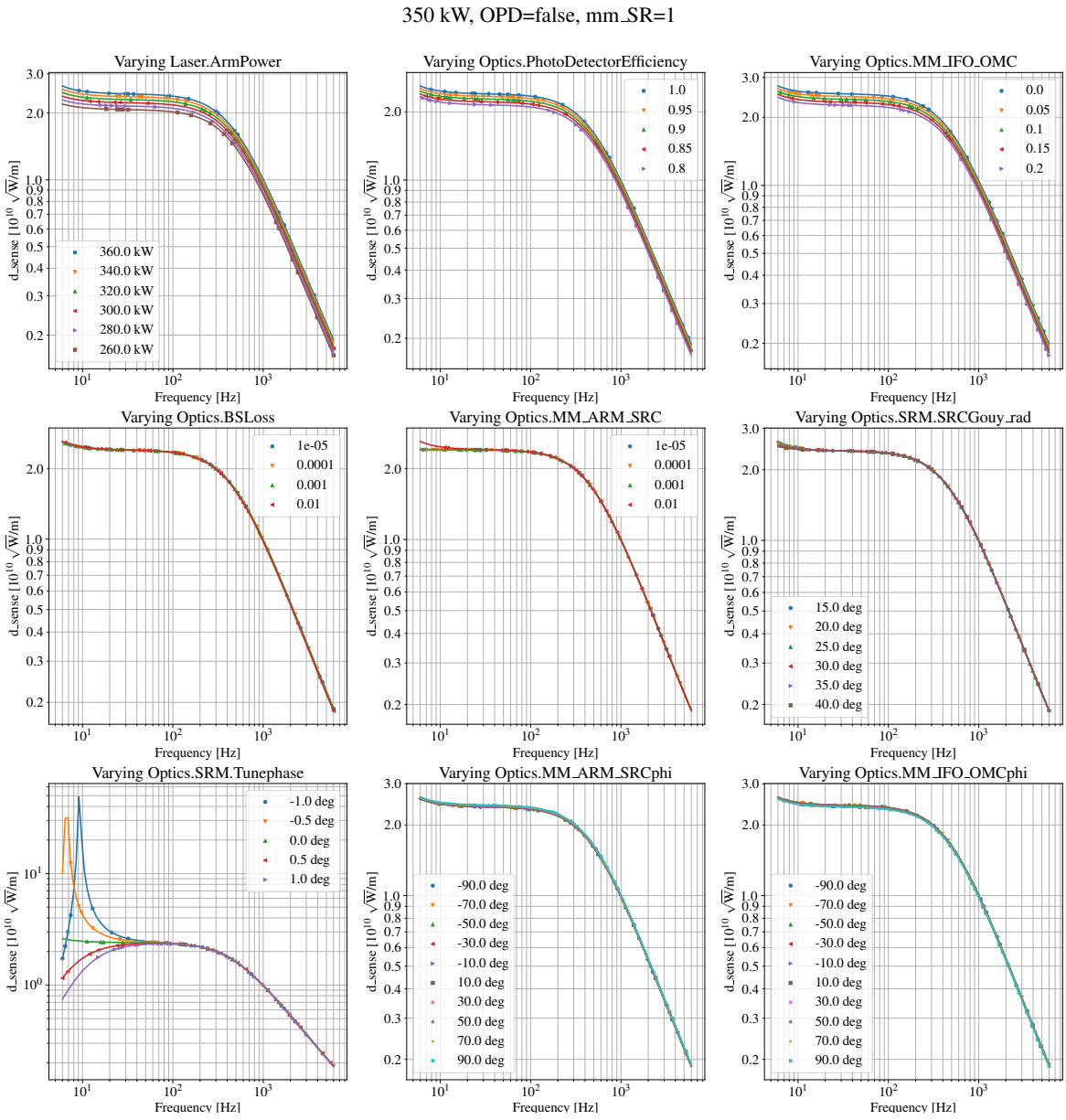

Figure 6-3: Parametric study of the sensing function in the case where quadratic mode-mismatch is dominant (OPD = false) [14].

frequency. Υ_{SR} doesn't change the cavity pole by much, but they affect the SRC spring heavily due to the extra mismatch phasing. At low Υ_{SR}, it affects the sensing function like SRCL detuning. When it's large, it also reduces high-frequency optical gain.

The SRC Gouy phase is kind of a hidden parameter that can change over thermalizing. A higher Gouy phase damps the spring by changing the mismatch phasing that reduces the mis-rotation when coherently summed with 00 modes.

The bottom row represents another phasing due to cavity detuning and mismatches. The SRCL detuning affects the spring heavily as expected. Note that it could counteract the effect due to Υ_{SR} so they form a degenerate pair. The other mismatch phasings contribute relatively less than other phasings. Given the low-frequency shape of the measured Pcal sweep, the Υ_{SR} couldn't be too high and therefore the mismatch phasing doesn't matter much. They would definitely matter with squeezing.

Fig. 6-3 shows the case where is_OPD is false so the thermal lensing is less dominant than quadratic mode-mismatch. The sensing function is not super sensitive to Υ_{SR}. We need at least 1% of arm to SRC mismatch to see any effect.

Without thermal lensing, Υ_{SR} affects the SRC spring in the opposite way, making it more pro-spring. Everything else is pretty much the same as the OPD=true case. The mismatch phasings are not significant here.

6.3.2 MCMC on the calibration sweep

The sensing function from GWINC (d_sense) is in the unit of $\sqrt{\text{W}}$/m. To convert it to W/m, we need to multiply it with the square root of the power of the interferometer light measured on DCPD. We manually fit the Pcal data first with both OPD scenarios, as shown in Fig. 6-4.

There's a factor of two difference between the GWINC model and the measured sensing function. I couldn't find the missing factor but I will still fit the scale anyway. The GWINC model with the parameter set agrees fairly well with measured data.

Knowing one set of parameters that's close to the truth, we can perform a Monte-Carlo-Markov-Chain (MCMC) method to infer those parameters that could significantly affect the sensing function. We have 5 degrees of freedom in the MCMC run: scale factor, SRC loss, SRCL offset, ARM

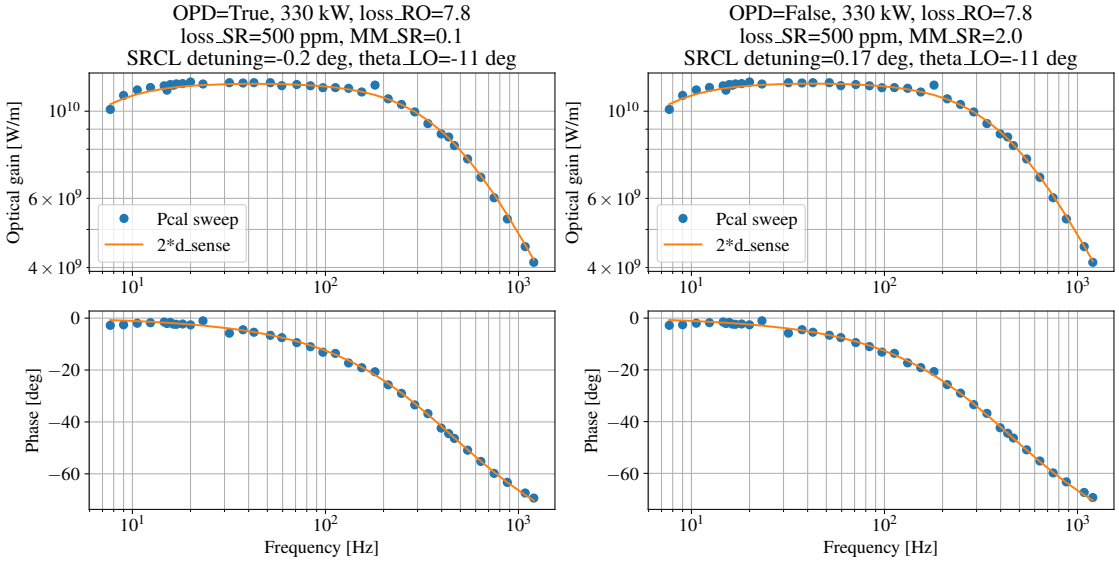

Figure 6-4: Comparison between measured Pcal sweeps and GWINC model of sensing function. The parameter set is shown on top of the plot, which is the initial point for MCMC [14].

to SRC mismatch, and IFO to OMC mismatch. The arm power and readout loss are absorbed in the scale factor. The initial walkers are distributed perturbatively around the parameter set. The MCMC result for the case where OPD is true is shown in Table 6.2.

Table 6.2: MCMC result of fitting sensing function assuming OPD is true.

Parameter	**MCMC result**
scale	$2.01^{+0.07}_{-0.04}$
SRC loss	$-42.33^{+1.47}_{-3.96}$ dB
SRCL detuning	$-0.20^{+0.12}_{-0.28}$ deg
Arm to SRC mode-mismatch	$-61.34^{+6.30}_{-5.54}$ dB
IFO to OMC mode-mismatch	$-24.25^{+5.01}_{-5.26}$ dB

For the strong thermal lensing case (Table 6.2), we've set the upper bound of Υ_{SR} to be -60 dB (0.1%). The distribution of the Υ_{SR} also shows that the likelihood of it being above -60 dB is very

small, which means that the arm to SRC mode-mismatch has to be incredibly small $< 0.1\%$. This is against other evidences of thermal effects observed in LIGO. Therefore, we will not assume a strong thermal lensing case in the GWINC model.

Table 6.3: MCMC result of fitting sensing function assuming OPD is false.

Parameter	**MCMC result**
scale	$1.93^{+0.05}_{-0.01}$
SRC loss	$-65.89^{+16.71}_{-22.51}$ dB
SRCL detuning	$0.14^{+0.01}_{-0.03}$ deg
Arm to SRC mode-mismatch	$-31.46^{+0.63}_{-3.06}$ dB
IFO to OMC mode-mismatch	$-39.75^{+14.37}_{-14.44}$ dB

In the case where thermal lensing is negligible (Table 6.3), the MCMC constrains the scale and SRCL detuning pretty well. Other parameters like losses and mismatches are not well constrained as they are pretty degenerate and absorbed in the scale factor. The Υ_{SR} already has an upper bound to be more than -30 dB (3%), which is a reasonable non-ideality. Note that these degrees of freedom are not orthogonal with each other; we can see a strong correlation between scale factor and Υ_{OMC}, SRCL detuning and Υ_{SR}, etc.

In conclusion, we choose the default case where quadratic mismatch dominates and gives the most reasonable SRC parameters for later analysis. The SRC parameters inferred from sensing functions are

Table 6.4: Inferred parameters from Pcal sweep measurements.

Parameter	**MCMC result**
Arm to SRC mode-mismatch	2.8%
SRCL detuning	0.14 degree

6.4 Analysis of Strain Noise Difference

The quantum noise can be directly modeled with GWINC. However, it can't be directly observed since we can only measure the total strain noise of the unsqueezed interferometer.

$$S_{\text{total}} = S_{\text{Quantum}} + S_{\text{Classical}} \tag{6.11}$$

Although we can't measure classical noises, we have an important knob, the squeezing angle ϕ, to actively change the quantum noise of the interferometer, as seen in Eq. (4.65) (written here again)

$$S_{\text{Quantum}}(r,\phi) = \frac{h_{\text{SQL}}^2}{2}\left(|\mathcal{K}| + \frac{1}{|\mathcal{K}|}\right)[e^{2r}\sin^2(\phi-\theta) + e^{-2r}\cos^2(\phi-\theta)] \tag{6.12}$$

To simplify the problem, we misalign the filter cavity and send frequency-independent squeezing (ϕ has no frequency-dependence) to the interferometer. Assuming the classical noise is stationary, we can subtract the frequency-independent squeezed total noise with unsqueezed total noise

$$S_{\text{diff}} = S_{\text{total}}(r,\phi) - S_{\text{total}}(r=0) = S_{\text{Quantum}}(r,\phi) - S_{\text{Quantum}}(r=0) \tag{6.13}$$

which is the quantum noise difference because the classical noise contributions are subtracted out. The quantum noise difference is something we can measure and is directly modeled by GWINC, providing a nice fitting strategy.

The quantum noise S_{Quantum} has much more parameters than r and ϕ in the realistic case where there is degradation. Many parameters are very degenerate, as seen in the previous section on the sensing function. To constrain the parameter space, we took 11 different squeezing angles while attempting to keep other parameters to be the same. The goal is to find a common set of parameters that accurately models the noise difference for each ϕ.

While the strain noise difference samples the relative change of the noise level, we still need

a measurement of the absolute strain noise. The NULL channel of the output is ideal for this. We will explain it in the next subsection.

6.4.1 SUM, NULL, and XCORR

The DC readout uses two OMC DCPDs instead of one, so we can actually take advantage of that by finding useful information from these two PDs. Let the OMC output field be $\vec{B}$ for the classical part and $\vec{b}$ for the quantum mechanical part. A beamsplitter h_{BS} splits the output into two fields entering two independent PDs.

$$\begin{bmatrix} \vec{A}_1 \\ \vec{A}_2 \end{bmatrix} = h_{BS} \begin{bmatrix} \vec{B} \\ 0 \end{bmatrix} \tag{6.14}$$

and for quantum parts

$$\begin{bmatrix} \vec{a}_1 \\ \vec{a}_2 \end{bmatrix} = h_{BS} \begin{bmatrix} \vec{b} \\ \vec{d} \end{bmatrix} \tag{6.15}$$

where the ideal BS has zero loss and amplitude reflectivity $r = 1/\sqrt{2}$.

There's no classical field entering from the other port of the BS, but the vacuum fluctuation $\vec{d}$ always exists. The power measured on each PD is

$$P_1(\Omega) = \sqrt{2\hbar\omega_0}\vec{B}^\dagger(r^2\vec{b} + rt\vec{d}) \tag{6.16}$$

$$P_2(\Omega) = \sqrt{2\hbar\omega_0}\vec{B}^\dagger(t^2\vec{b} - rt\vec{d}) \tag{6.17}$$

The SUM of the DCPD is what we use to observe gravitational waves:

$$P_{\mathrm{SUM}} = \sqrt{2\hbar\omega_0}\vec{B}^\dagger\left[(r^2 + t^2)\vec{b} + (rt - rt)\vec{d}\right] \tag{6.18}$$

and the NULL is the difference

$$P_{\mathrm{NULL}} = \sqrt{2\hbar\omega_0}\vec{B}^{\dagger}\left[(r^2 - t^2)\vec{b} + 2rt\vec{d}\right] \tag{6.19}$$

Ideally, $r = t = 1/\sqrt{2}$ and the usual SUM channel is recovered as if there's only one PD measuring all the OMC transmitted light.

The NULL can be used as a reference of an unsqueezed condition because the field $\vec{b}$ that contains radiation pressure noise (quantum correlations) gets subtracted out. The measured field $\vec{d}$ is purely vacuum. Note that this is opposite to the balanced homodyne readout as discussed in Section 3.3.2.

The other useful channel is the XCORR when we cross-correlate individual PD signals [132].

$$S_{1\times2}(\Omega) = \frac{1}{2\pi\delta(\Omega - \Omega')/2}\langle 0|P_1(\Omega){P_2}^{\dagger}(\Omega')|0\rangle_{sym} \tag{6.20}$$

$$= 2\hbar\omega_0\frac{\langle 0|\vec{B}^{\dagger}(r^2\vec{b} + rt\vec{d})(t^2\vec{b}^{\dagger} - rt\vec{d}^{\dagger})\vec{B}|0\rangle_{sym}}{2\pi\delta(\Omega - \Omega')/2} \tag{6.21}$$

$$= 2\hbar\omega_0 r^2t^2\vec{B}^{\dagger}(\langle\vec{b}\vec{b}^{\dagger}\rangle - \langle\vec{d}\vec{d}^{\dagger}\rangle)\vec{B} \tag{6.22}$$

The vacuum state $\langle\vec{d}\vec{d}^{\dagger}\rangle$ is just **1**, but the $\langle\vec{b}\vec{b}^{\dagger}\rangle$ contains quantum correlations from quantum radiation pressure noise (QRPN). At high frequencies, the shot noise cancels out so the rest of the measured cross-correlation spectrum is just classical noise. At low frequencies, the QRPN still exists in $\vec{b}$.

It can be verified that

$$S_{\mathrm{SUM}} = S_1 + S_2 + S_{1\times2} + S_{2\times1} \tag{6.23}$$

This holds true when we add classical noise to the equation. The classical sidebands can be organized in parallel to the quantum part, although it's not quantum by nature

$$P_{\mathrm{SUM}} = \sqrt{2\hbar\omega_0}\vec{B}^{\dagger}\left[(r^2 + t^2)\vec{b} + (rt - rt)\vec{d}\right] + \vec{B}^{\dagger}\vec{b}_c \tag{6.24}$$

$\vec{b}_c$ is not a quantum operator and it is very small. The PSD of the SUM channel is

$$S_{\mathrm{SUM}} = 2\hbar\omega_0(r^2+t^2)^2\vec{B}^\dagger\langle\vec{b}\vec{b}^\dagger\rangle\vec{B} + \underbrace{\frac{\vec{B}^\dagger\langle\vec{b}_c\vec{b}_c^\dagger\rangle\vec{B}}{2\pi\delta(\Omega-\Omega')/2}}_{S_c} \tag{6.25}$$

It can be shown that

$$S_1 = 2\hbar\omega_0\vec{B}^\dagger(r^4\langle\vec{b}\vec{b}^\dagger\rangle + r^2t^2\langle\vec{d}\vec{d}^\dagger\rangle)\vec{B} + r^4S_c \tag{6.26}$$

$$S_2 = 2\hbar\omega_0\vec{B}^\dagger(t^4\langle\vec{b}\vec{b}^\dagger\rangle + r^2t^2\langle\vec{d}\vec{d}^\dagger\rangle)\vec{B} + t^4S_c \tag{6.27}$$

$$S_{1\times2} = 2\hbar\omega_0\vec{B}^\dagger(r^2t^2\langle\vec{b}\vec{b}^\dagger\rangle - r^2t^2\langle\vec{d}\vec{d}^\dagger\rangle)\vec{B} + r^2t^2S_c \tag{6.28}$$

What's different with the vacuum state is that they cross-correlate negatively, whereas the classical part cross-correlates positively. This makes sense because shot noise is a local noise on each individual PD. There is no cross-correlation on that.

Fig. 6-5 shows the calculated SUM, NULL, and XCORR channels. In fact, we could obtain the NULL spectrum either by subtracting cross-correlation from the SUM, or just directly calculating the PSD of the difference of two DCPD time series. The results are verified to be approximately the same. In this plot, the blue "GDS" curve is the PSD calculated from GDS-STRAIN channel. The orange "SUM" curve is calculated from the DCPD SUM channel CAL-DELTAL_EXTERNAL. A frequency-dependent correction function is applied to make sure the GDS and SUM are identical. This correction will also be applied to individual PD signals from CAL-DELTAL. The red "NULL" curve is calculated from the difference of the raw time series of two PD (CAL-DELTAL_A and CAL-DELTAL_B), and the purple "XCORR" is the cross-spectral density of two raw time series. The "SUM - NULL" curve is verified to overlap with XCORR. The "GDS - XCORR" curve, however, deviates from the NULL at low frequencies. This is because the difference between GDS and XCORR are small and have a large uncertainty after subtraction. The NULL channel is best to estimate the calibrated shot noise (after subtracting the gray DARK trace). The pink "XORR,

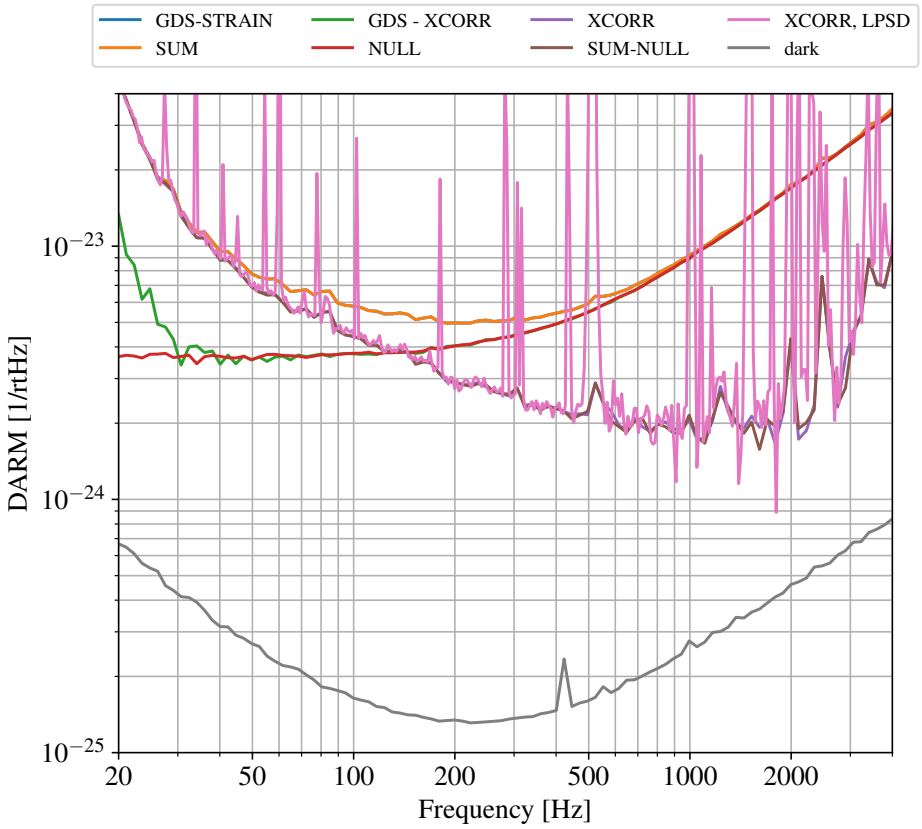

Figure 6-5: Comparison of SUM, NULL, and XCORR channel measured on OMC DCPD [14].

LPSD" uses a different algorithm to obtain cross-PSD as a sanity check [133]; it is equal to the XCORR curve.

Since the NULL PSD is cleaner at low frequencies compared with subtraction, we will use (NULL noise - dark) noise as the shot noise from now on. The dark noise is a factor of 30 smaller at high frequency and a factor of 7 smaller at low frequency, in ASD.

The other nice thing with NULL is that it is independent of the squeezing set-up because the quantum correlations created in the quantum modes $\vec{b}$ are subtracted out. The NULL channel serves as a real-time measurement of the shot noise at all times.

6.4.2 Uncertainty analysis

We follow [46] for the uncertainty propagation. It is nice to follow the notation used in the previous literature. We redefine

$$D_s = S_{\text{total}}(r, \phi) \tag{6.29}$$

for squeezed total noise, and

$$D_r = S_{\text{total}}(r = 0) \tag{6.30}$$

for unsqueezed total noise, or "reference" total noise as used in [46]. The noise difference is

$$S = D_s - D_r \tag{6.31}$$

with uncertainty

$$\Delta S^2 = S^2 \delta G^2 + \Delta D_s^2 + \Delta D_r^2 + C^2(\delta N_t^2 + \delta N_m^2) \tag{6.32}$$

where

- $\delta G_{cal}(\Omega)$ is the reported combined calibration error and uncertainty estimate [134],
- $\Delta D(\Omega)$ is the statistical uncertainty due to PSD estimation, and
- $\delta N(\Omega)$ describes the non-stationary changes in the classical noise C contributions, where $\delta N_t(\Omega)$ is time-nonstationarity and $\delta N_m(\Omega)$ is the operating mode nonstationarity between unsqueezed and squeezed operating modes [135].

We also follow the convention in [46] and use Δ to describe the 1-σ uncertainty of the variable and use δ for the relative uncertainty $\delta D = \Delta D / D$.

Since we don't have the unsqueezed quantum noise model M_r, we can't do subtraction to obtain the classical noise C, but we can replace it with D_r which would only overestimate the uncertainty at high frequencies where the error is already small. It won't underestimate the error.

6.4.3 Re-binning power spectral density

The statistical uncertainty δD of the PSD scales inversely with the square root of the number of averages, which is proportional to the product of the duration T of the time series and the frequency bin width f

$$\delta D = \frac{1}{\sqrt{T f}}. \tag{6.33}$$

We first take the linear FFT of the raw time series to estimate the total noise PSD. For each frequency bin, we take the median statistics to indirectly remove potential glitches in the time series, as described in our previous work [46].

The linearly spaced PSD has the constant frequency bin width, for which we choose a frequency resolution of 0.0625 Hz. To reduce the statistical uncertainty and fit the model, we re-bin the PSD into a log-spaced frequency bins. Each new frequency bin collects all the energy of the old frequency bins that fall into the bin so that the total spectral energy is conserved. The statistical uncertainty of the new PSD with log-spaced and larger bin width still follows the relation of Eq. (6.33).

The raw PSD measures the total differential displacement between the two pairs of arm cavity mirrors, which contain many peaks and resonances including harmonics of the 60-Hz power line and 500-Hz violin mechanical modes of test masses suspensions, etc. These peaks would inflate the energy of our re-binned PSD. Therefore, we remove all the known noise peaks before re-binning.

6.4.4 Non-stationarity verification

The stationarity uncertainty has two contributing terms: time-nonstationarity $\delta N_t(\Omega)$ that captures slow thermal drifts of the interferometer, and mode-nonstationarity $\delta N_m(\Omega)$ that contains changes introduced by different operating modes of the interferometer, namely with and without squeezing.

The time-nonstationarity δN_t occurs due to thermal drifts of the interferometer. We follow the

same calculation from [46]

$$\delta N_t^2 \approx \frac{\mathcal{N}_\Sigma^2}{n} \tag{6.34}$$

where n is the number of observed unsqueezed strain noise at various times, and

$$\mathcal{N}_\Sigma^2 = \frac{2}{n(n-1)} \sum_{i \neq j}^{n} \mathcal{N}_{ij}^2 \tag{6.35}$$

where $\mathcal{N}_{ij}^2$ is the pairwise relative non-stationarity between two such discontiguous segments with PSD D_i and D_j

$$\mathcal{N}_{ij} = 2\frac{D_i - D_j}{D_i + D_j} \tag{6.36}$$

For the faster averaging timescales used in our measurements, slow drifts can be reduced with longer averaging times, similar to statistical PSD estimation. Therefore, both of drifts and statistical uncertainties are reduced after the re-binning process.

To measure the unsqueezed total noise as closely as the configuration with frequency-dependent squeezing, we set up the squeezing configuration but without the squeezed vacuum generated. Specifically, we leave both the squeezer and filter cavity locked on resonance but without the non-linear parametric down-conversion process.

Experimentally, we dither-lock the squeezer on red but don't send any pump light so there is no squeezed vacuum generated. The red resonance allows the transmission of CLF and RLF fields. However, they are only one-side RF sidebands because we don't have a difference frequency generation without the pump. The filter cavity is also locked on resonance with RLF-CLF beatnote to mimic the nominal operation with frequency-dependent squeezing. The demodulation phasing and control loop gains are re-tuned for single-side RLF-CLF [136]. If there is any extra technical noise introduced with frequency-dependent squeezing, for example backscatter noise driven by filter cavity length fluctuations, the interferometer would sense it in the total noise spectra in both configurations. The subtracted strain noise should not have any extra classical noise contributions.

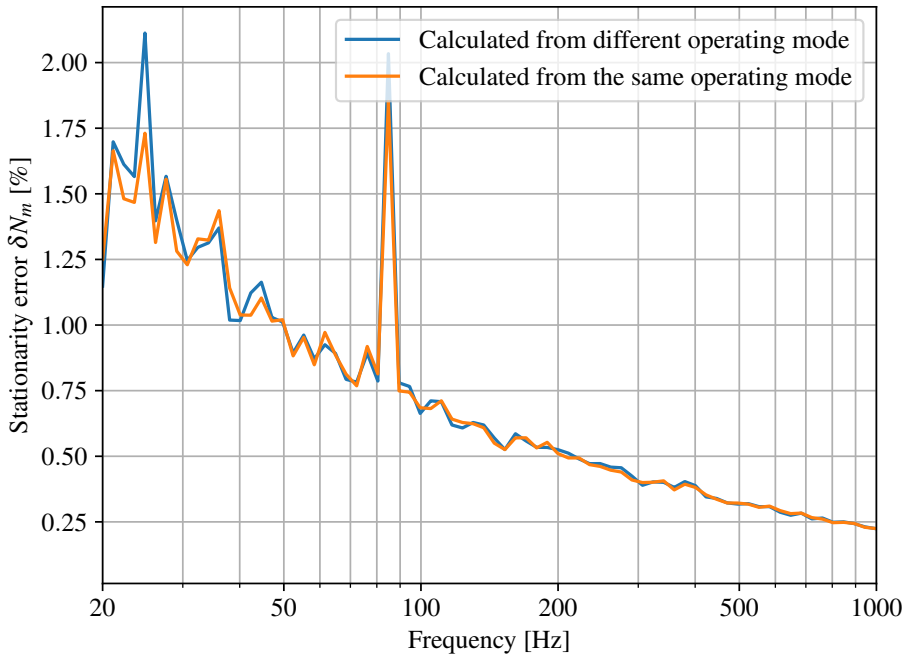

Figure 6-6: Comparison of the δN_m using two PSDs measured in the same unsqueezed operating mode (e.g. two segments with the squeezer beam diverter open), or measured in two different unsqueezed operating modes (e.g. with squeezer beam diverter open and beam diverter closed). Both uncertainties are the same, suggesting the squeezer system does not introduce excess technical noise in the full detectors [1, 14].

To confirm if there are any excessive noises including backscatter, we compare the total unsqueezed interferometer noise with the following two operating modes. The first one is to open the squeezer beam diverter to mimic the frequency-dependent squeezing case as mentioned above, and the second one is to close the squeezer beam diverter on the injection path such that no backscattered light can be transmitted between the interferometer and squeezing system.

We have two PSD of each mode and calculate $\delta N(\Omega)$ following Eq. (6.34). For two δN_m calculated, we select D_i and D_j using PSDs of the same and different operating modes.

Fig. 6-6 shows that the stationarity uncertainty curves are nearly identical between two PSDs taken at the same operating mode or different operating modes, confirming that the mode-nonstationarity

contribution to the total stationarity uncertainty is negligible.

Calibration uncertainty $\delta G_{cal}(\Omega)$ are estimated in the same way as [46]. Note that it is a form of systematic error instead of statistical error. Therefore, the calibration error is added to the total uncertainty after re-binning, since it can not be reduced by averaging. The contributions of aforementioned uncertainties to the total uncertainty are shown in Fig. 6-12.

6.4.5 Data taking procedures

As hinted by the estimation of statistical noise (Eq. (6.33)), we prefer to take the strain noise for a duration as long as possible. However, LIGO is a billion-dollor instrument that needs to observe gravitational waves. So we decided to limit our time to 20 minutes for each PSD, which gives a statistical uncertainty comparable to other sources of errors.

Things to check before taking data:

- Check if the calibration is working. It is preferable to have recent Pcal sweep data for sensing function inference.
- Check if individual OMC DCPD time series are calibrated. This is usually handled by CALDELTAL pipeline.
- Disengage unnecessary loops. For example, the alignment dithering (ADS) and squeezing to interferometer alignment sensing (SQZ ASC) loops are off.
- Optimize squeezer. This includes crystal temperature (TEC), mirror alignment (ZM), and mode-matching (PSAMS).
- Mis-align the filter cavity end mirror.
- Any known scattering sources (e.g. HVAC) that can be disabled for a short period while we take data? We want stationary, non-drifting, non-scattering-noise, and non-glitching classical noise background for the analysis.

- The interferometer has to be locked for at least 3 hours so it is well-thermalized. Otherwise, the classical noise is changing across different measurements.

There are preferences for squeezing angle selection. We found that anti-squeezing isn't very useful to us because it will inflate the quantum noise near the calibration lines, which biases the calibration process [14]. The best squeezing angles are those creating maximal squeezing at 40–4000 Hz. We typically select them such that the squeezing dips occurs uniformly in the log-spaced frequencies. These squeezing angles are negative, so we also need one or two positive squeezing angles less than 10 degrees. The phase-squeezing (where max squeezing happens at high frequencies) is defined with zero squeezing angle.

The unsqueezed data should be taken with a squeezer dither-locked on red and the pump shuttered. The ISS for CLF and LO loop should be re-tuned. We can also just close the beam diverter but we need to verify that both scenarios give the same unsqueezed noise (Fig. 6-6).

Ideally, the data is taken with 20-minute unsqueezed + 20-minute squeezing at angle ϕ_1 + 20-minute squeezing at angle ϕ_2. We can repeat this cycle 6 times to acquire a total of 12 spectra. We will also need to take one unsqueezed noise at the end of the test. The total time required is 6 hours and 20 minutes. However, there might be lock loss during this time period due to earthquakes, etc. If so, we take the rest data in the next lock with an interferometer thermalized. The non-stationaries between these two locks should be small, and they are included in the non-stationarity uncertainty.

6.4.6 Parametric study

We perform a parametric study similar to Section 6.3.1 to understand how each parameter affects the strain noise difference. The studied parameters are summarized in Table 6.5.

Table 6.5: The relevant 16 GWINC parameters that affect the sensing function.

Physical quantity	**GWINC variable name**	**Symbol**
Squeezing angle		θ_{SQZ}
SRCL detuning	SRM.Tunephase	$\Delta\phi_{\mathrm{SR}}$
SRC Gouy phase	SRCGouy_rad	ψ_{SR}
Mode-mismatch between Arm and SRC	MM_ARM_SRC	Υ_{SR}
Mode-mismatch phase of Arm to SRC	MM_ARM_SRCphi	Υ_{SR} phase
Mode-mismatch between IFO and OMC	MM_IFO_OMC	Υ_{OMC}
Mode-mismatch phase of IFO to OMC	MM_IFO_OMCphi	Υ_{OMC} phase
Mode-mismatch between SQZ and OMC	MM_SQZ_OMC	Υ_{SQZ}
Mode-mismatch phase of SQZ to OMC	MM_SQZ_OMCphi	Υ_{SQZ} phase
Arm power	ArmPower	P_{arm}
Homodyne angle	Quadrature.dc	θ_{LO}
SRC loss	BSLoss	Λ_{SR}
Phase noise	SQZAngleRMS	ϕ^2_{rms}
Generated squeezing	AmplitudedB	
Injection loss	InjectionLoss	Λ_{INJ}
Readout loss	1 - PhotoDetectorEfficiency	Λ_{RO}

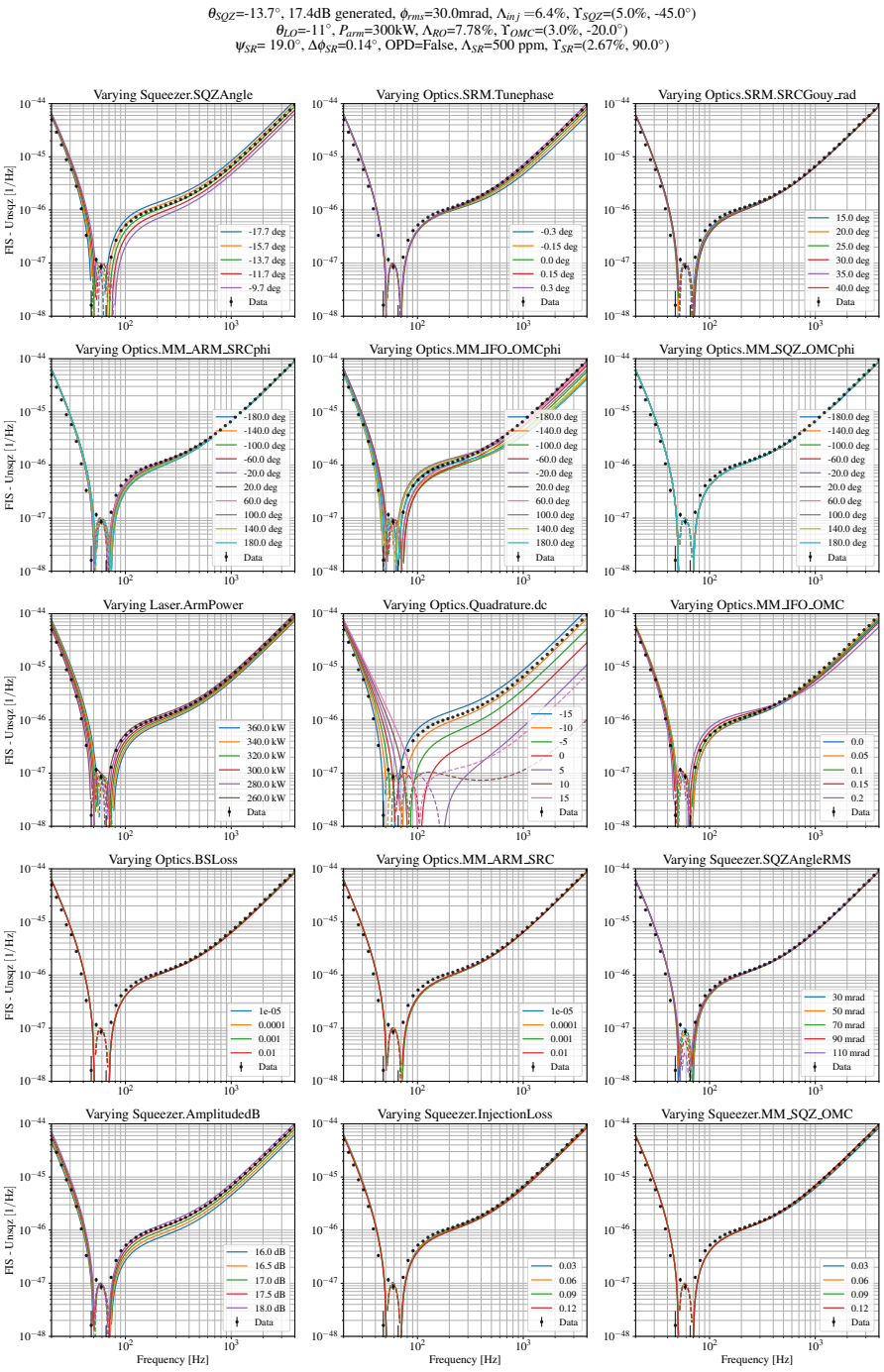

Figure 6-7: Parametric study of strain noise difference (frequency-independent squeezing - unsqueezed total noise) [14].

Fig. 6-7 shows the parametric study. We manually find a canonical set of parameters that are pretty close to the truth (as seen in the super-title of the figure). We perturb parameters around the canonical setting and see how each one affects the strain noise differences.

For each subplot, the title says the perturbed parameter. The various values of such parameters are labeled in the legend. The solid curve is the positive of the difference, and the dashed curve is the negative part of the difference that is flipped to the positive side. The negative difference means that the squeezed noise is less than the unsqueezed noise, meaning that we are squeezing there.

We can possibly observe some constraints from the squeezed spectra. At high frequencies, the strain difference sets a bound on the arm power. The higher the power, the lower the absolute noise difference is. This is because the shot noise scales inversely with arm power, so the difference is less for higher power. The phase parameters only reduce the difference as the squeezing angle is not optimized. Similarly, loss and phase noise also reduce differences in one way. More generated squeezing increases the difference, but it will plateau as the optical losses prevent more squeezing from being observed. This gives an upper bound of the arm power, in this case, is 280–300 kW. Note that this is different from the arm power calculated from power recycling gain (PRG), which gives 310 kW. We will discuss it a bit later.

At low frequency, the arm power and squeezing are degenerate. The loss will affect the QRPN, but it's small for a small loss of around 10%. This can set a lower bound of injected squeezing using the upper bound of arm power.

Note that Fig. 6-7 only shows 15 of the total 16 parameters in Table 6.5. The missing parameter is the readout loss, which is totally decoupled from the strain noise difference! This is counter-intuitive, but it helps us to break one of the most important degeneracies - between arm power and loss.

The preliminary study is done to remove parameters that don't make any difference [14]. We will also use parameters obtained from sensing function Table 6.1. To explain this, we can define the readout loss as an effective beam splitter with amplitude reflectivity $r = \sqrt{1 - \text{loss}}$. The quantum

noise in power is

$$S_P = 2\hbar\omega_0 r\boldsymbol{B}^\dagger(r^2\langle aa^\dagger\rangle + t^2\langle vv^\dagger\rangle)r\boldsymbol{B} \tag{6.37}$$

where a is the quantum field from interferometer and v is the vacuum fluctuations introduced by readout loss. The LO power $\boldsymbol{B}$ is also reduced by readout loss. Without squeezing, a is identical to v at high frequency and larger than v at low frequency.

$$S_P \propto r^2(r^2(1+\mathcal{K}^2)+t^2) \propto r^2(1+\mathcal{K}^2r^2) \tag{6.38}$$

where $\mathcal{K}$ is the optomechanical coefficient. Note that the sensing function also depends on the loss:

$$g^2 \propto r^4 \tag{6.39}$$

Therefore, increasing the loss would decrease the sensitivity S_P/g^2 at high frequency ($1/r^2$), but doesn't change anything at low frequency limit (r cancels).

When we inject squeezing and take the strain noise difference, the difference PSD is

$$\Delta S_P = 2\hbar\omega_0 r\boldsymbol{B}^\dagger(r^2\langle a_{(FIS)}{a_{(FIS)}}^\dagger\rangle - r^2\langle a_{(UNS)}{a_{(UNS)}}^\dagger\rangle)r\boldsymbol{B} \propto r^4 \tag{6.40}$$

The vacuum are the same between the two $v_{FIS} = v_{UNS}$ and get subtracted out completely. Therefore the difference DARM is $\Delta S_h = \Delta S_P/|g|^2$; so no more dependence on r broadbandly.

Besides readout loss, the strain noise difference is also less sensitive to Λ_{SR} and Λ_{INJ}. These losses are mostly adjusting how much squeezing we can observe, which is removed when we take the difference of two strain noises. We will infer them from a different observable.

Υ_{SR} slightly changes the observable at around 100 - 1000 Hz, below 2e-47 (so near squeezing). Υ_{SQZ} only changes spectra above 100 Hz near squeezing (-12 to 12 degrees of relative squeezing angle). Υ_{OMC} heavily affects broadbandly and creates an interesting twist at 500-700 Hz when it's around 20%.

The generated squeezing and P_{arm} pretty much serves as a scaling factor, except that the arm power flips scaling sign at SQL frequency. Phase noise is also effectively a loss that only impacts the squeezing instead of anti-squeezing.

The mismatch phase between SQZ and OMC, Υ_{SQZ} phase, also affects the DARM difference negligibly. It's probably because the amount of scattered squeezed fields are too small, and the scattered back squeezed fields are even less so their actual phase doesn't matter. The scattered back fields scale with the product of all mismatches along the path. Even 10% mismatches along the path would contribute to 1%.

On the contrary, the Υ_{SR} phase and Υ_{OMC} phase change the DARM difference heavily because they affect the phase of the main laser and therefore LO angle. In addition, Υ_{SR} phase and ψ_{SR} are pretty much the same, where they only affect at the band of ~60 - 1000 Hz.

The SQZ angle θ_{SQZ} determines the squeezing level. The SRCL detuning $\Delta\phi_{\text{SR}}$ also changes the squeezing level, but it only affects frequencies above 100 Hz.

We can also categorize the parameters based on the bandwidth it affects:

- Broadband: SQZ_dB > P_{arm} > Υ_{OMC} + phase
- Above 100 Hz: $\Upsilon_{\text{SQZ}} \sim \phi_{\text{rms}} \sim \theta_{\text{SQZ}} \sim \Delta\phi_{\text{SR}}$
- 100 - 1000 Hz: $\psi_{\text{SR}} \sim \Upsilon_{\text{SR}}$ + phase
- Negligible: $\Lambda_{\text{INJ}} > \Lambda_{\text{SR}} > \Upsilon_{\text{SQZ}}$ phase $\sim \Lambda_{\text{RO}}$

The three parameters affecting 100-1000 Hz have very similar impacts on the observable shape. Therefore, we can reduce them to one for simplicity, and we pick Υ_{SR} phase as the representative because it gives the largest dynamic range. We can down-select it along with the top two types as the most influential parameters and plot them.

Fig. 6-8 shows that only these 5 parameters are able to move the frequency of the dip, namely where the squeezed quadrature gets read out.

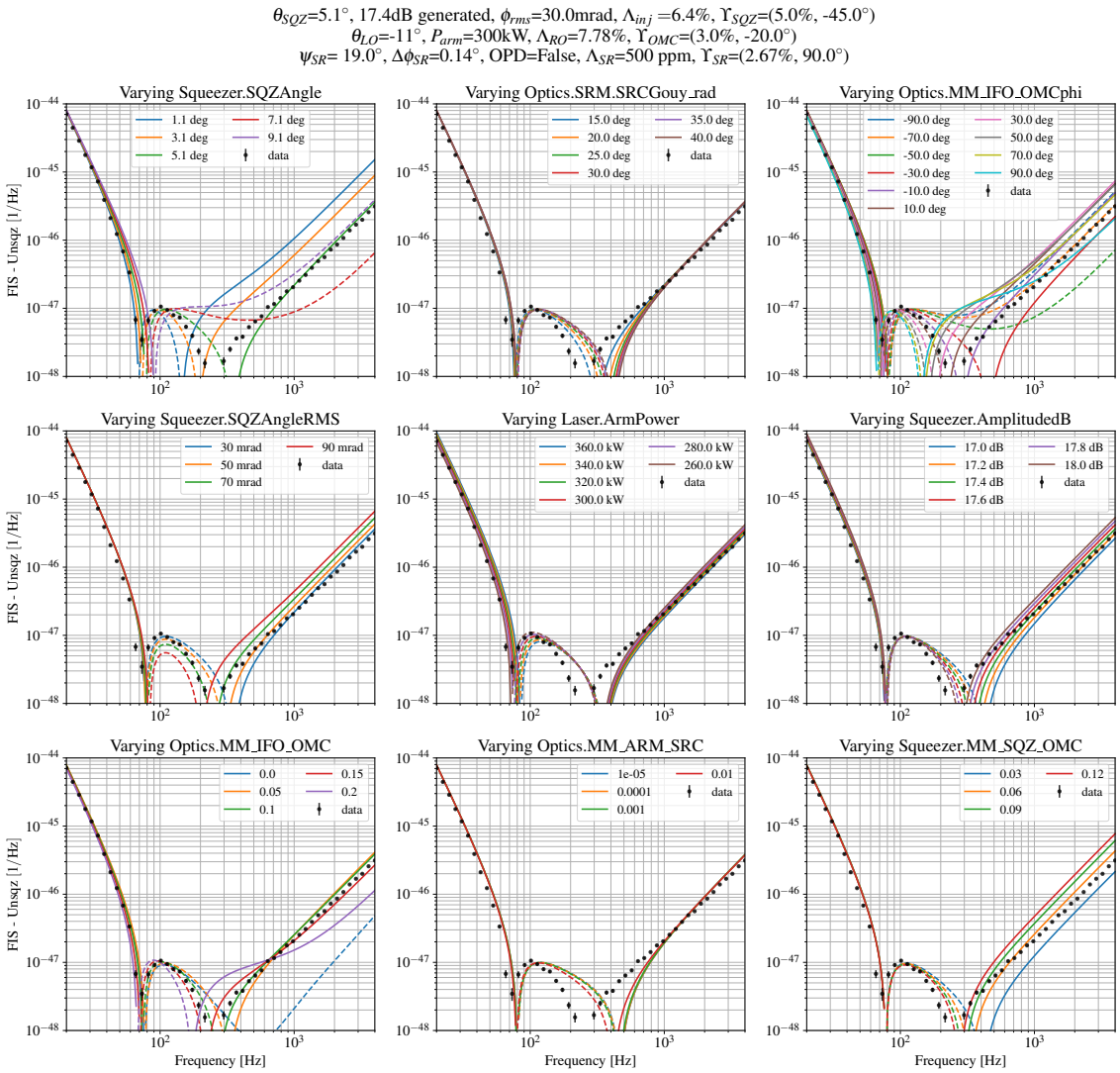

Figure 6-8: Parametric study of down-selected parameters [14].

- θ_{SQZ}
- ψ_{SR} (or equivalently other SR phasing parameters)
- Υ_{OMC}
- Υ_{OMC} phase

- P_{arm}

There is no single parameter from them that can move the dip without messing with other things. Therefore, we need to tweak all of them to find a set that fits the data. Adding them to the ϕ_{rms}, Υ_{SQZ} and Λ_{RO}, we have total 8 parameters to fit.

Having some understanding of which parameters are useful and how they affect our observable, we can start fitting them with MCMC. We will allow each parameter to change for each measurement and fit them separately first.

6.5 MCMC on Individual Quantum Noise Difference

As discussed in previous section, we want to find a common set of parameters that fits all of the strain noise differences. These parameters not only include those 8 plotted before, but also the squeezing angle for each of the total 11 measurements. These are almost 20 degrees of freedom, too much for MCMC.

We can start simply by fitting individual noise differences separately. It is also necessary to see if we are even able to fit the measurement, as a proof-of-principle test. The 8 parameters we down-selected from the previous section affect different frequency bands:

- Broadband: θ_{SQZ}, P_{arm}, Υ_{OMC} + phase
- Above 100 Hz: Υ_{SQZ}, ϕ_{rms}
- 100 - 1000 Hz: ψ_{SR}

Besides the strain noise difference, we also fit the shot noise from NULL to make sure the scale level is correct. This requires another parameter

- Broadband: Λ_{RO}

So total of 8 degrees of freedom for each individual data. Since each parameter is free to change for each measurement. they are "over-fitting" in some sense because some of them are common. For example, the readout loss Λ_{RO} is not expected to change in a single lock. Still, we are trying to see if it is even possible to fit these PSD differences + NULL PSD.

6.5.1 Set-up

A flat prior isn't a good practice for Bayesian analysis, especially when we have certain knowledge about the parameters. Even the truth is outside a few sigmas of the standard deviation of the prior, it will still have enough likelihood to counter prior reduction and increase the posterior overall.

We choose a Gaussian likelihood despite that one of the uncertainties, the calibration uncertainty, is asymmetrical. The reason is that the log- likelihood of Gaussian is a closed form, whereas the skewed Gaussian is numerical and gives $-\infty$ when we have a small log-likelihood. This limits the space the walkers can explore. We average the positive and negative error bars for Gaussian likelihood.

On the computer cluster (ldas-pcdev6.ligo-la.caltech.edu), each GWINC run takes about $210\times 60/128/2000/2 = 0.025$ sec. To model one measurement, we need to run it twice to model DARM difference. Therefore, running one MCMC with 256 walkers and 3000 steps takes $0.025\times2\times256\times 3000/3600 = 10.6$ hours

6.5.2 Result

We first fit each individual strain noise and NULL spectra measured at various squeezing angle. This doesn't require the interferometer parameters to be common, namely they are allowed to change for different measurements. This assumption is not realistic because parameters like arm power shouldn't change in a single thermalized lock, but it allows us to see if it's even possible, in

principle, to fit all PSD differences.

Each parameter of the model is classified as:

- Fixed: the parameter is fixed for all individual measurements. They are summarized in the title of the plot below.
- Independent: MCMC will change independent parameters to optimize individual measurement.

Table 6.6: Set-up of the MCMC on the individual strain noise difference.

		MCMC Set-up		Inferred
	Fixed/	Prior	Initial walker	Common/
	Chosen	Gaussian $(-\sigma, \sigma)$	Flat probability	Independent
Interferometer parameters				
Circulating power in arm cavity	270 kW			
Arm to SEC mismatch	2.7%			
Arm to SEC mismatch phase	0˚			
SEC round-trip detuning phase	0.14˚			
SEC round-trip Gouy phase		(20, 50) ˚	10˚ - 80˚	Independent
Readout angle	-11˚			
Total readout loss		(8, 10) %	1% - 15%	Independent
IFO to OMC mismatch		(4, 12) %	1% - 15%	Independent
IFO to OMC mismatch phase		(-40, -10) ˚	-60˚ - -20˚	Independent
Squeezing parameters				
Generated squeezing	17.4 dB			
Squeezing angle				Independent
Total Injection efficiency	92.9%			
SQZ to OMC mismatch		(1, 8) %	1% - 12 %	Independent
SQZ to OMC mismatch phase	-45˚			
Phase noise (RMS)		(20, 30) mrad	10 - 70 mrad	Independent

The initial parameters are summarized in Table 6.6. The prior probability is Gaussian with

the 16th-84th percentile shown in the Prior column for each parameter. The initial walkers are distributed with a flat probability in the range shown in the initial walker column. The fixed parameter is not touched by MCMC. Independent parameters inferred by MCMC for each individual data are plotted against the squeezing angles of each measurement, as shown in Fig. 6-9.

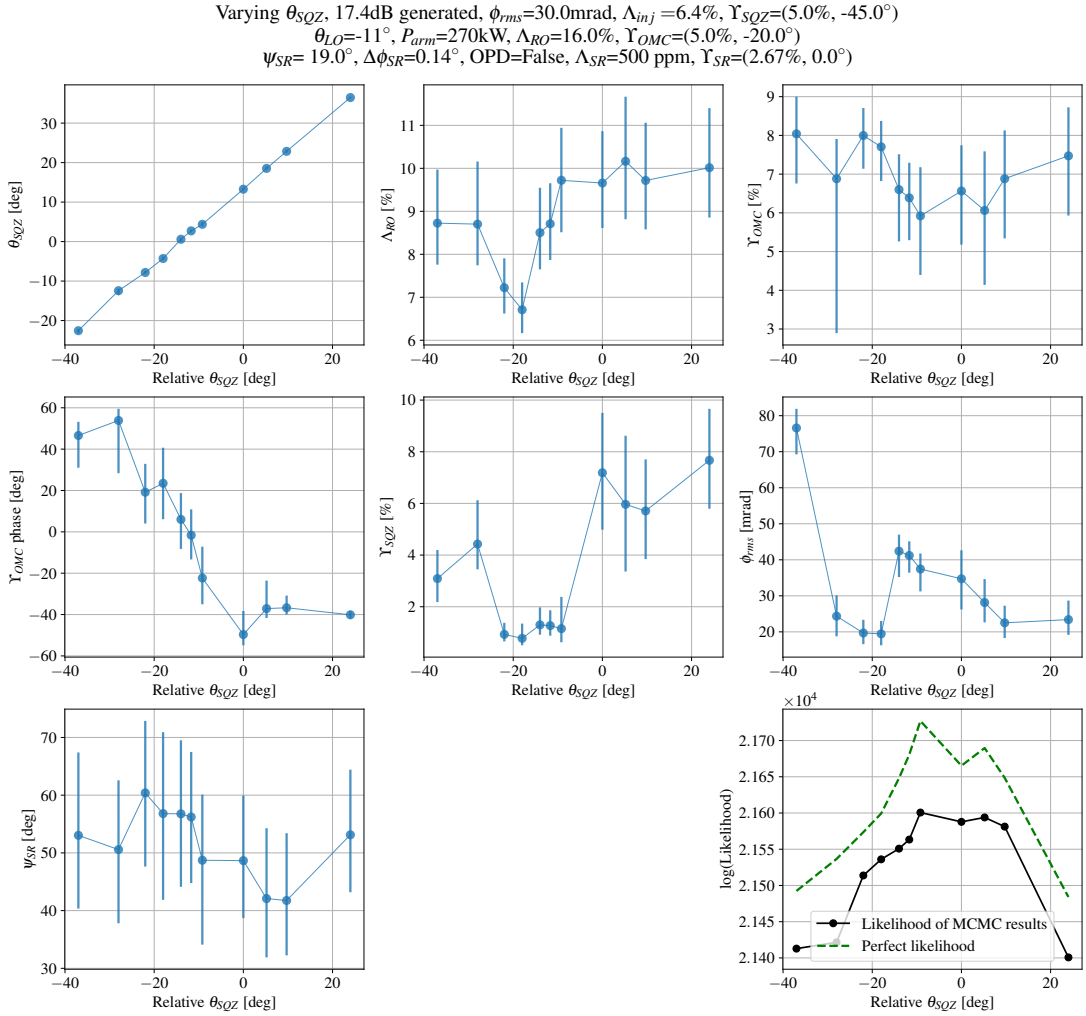

Figure 6-9: Result of MCMC on individual measurement at various squeezing angles [14].

The inferred squeezing angle is shown to be linearly correlated with the input squeezing angle, which makes sense because it is the parameter that we actively change to get various measurements.

There is a non-zero offset between two angles, namely $\theta_{\mathrm{SQZ}} = 0$ (phase squeezing) corresponds to ~12 degree in GWINC model. This is due to the non-zero homodyne angle and other phasing degradations.

Other parameters shouldn't depend on the relative θ_{SQZ} because they are not actively changed. The readout loss has a little dependency with the squeezing angle given their error bars. The IFO parameters like Υ_{OMC} and ψ_{SR} vary a little bit to the squeezing angle, which is promising to us after we set them to be common parameters.

The parameters that change with squeezing angles are Υ_{OMC} phase, Υ_{SQZ}, and ϕ_{rms}. Phase noise is known to change with different squeezing angles (different locking point changes the control loop). The Υ_{OMC} phase is changed probably because it tries to mimic the change of the phase of squeezed vacuum due to X/Y arm cavity mode-mismatch or differential loss, which leads to the non-zero LO angle and is not modeled in the current version of GWINC (superQK branch). The Υ_{SQZ} is also drifting because SQZ ASC was not engaged during the data taking. Keep in mind that we are actually "over-fitting" the individual measurement in some senses, since we allow parameters that shouldn't change over time to be a variable that fits the individual strain noise difference. Our goal is to find a set of common parameters that fit all of the data simultaneously. This would be the physical case close to the reality.

The last subplot shows how good the MCMC result is at each squeezing angle. The green is the perfect likelihood where the residuals are zero. The MCMC likelihood is pretty close to the theoretical maximum likelihood, proving that the MCMC fitting is reasonably good. Now that we've demonstrated the possibility of modeling the strain noise difference, we can proceed to finding the common set of parameters that fit all of the measurements simultaneously.

6.6 MCMC on All Quantum Noise Difference

Knowing that it's possible to fit individual strain noise differences, we now try to fit all of them simultaneously. The initialized parameters are categorized as:

- "Fixed" parameters are fixed across all squeeze angle datasets. For example, the signal recycling cavity parameters we inferred earlier are assumed to be the same for all.
- "Chosen" parameters are selected and different for each squeeze angle dataset. For example, the squeezing angle is actively changed to obtain different squeezing PSD.
- "Common" parameters are shared degrees of freedom that MCMC infers a single value across all squeeze angle datasets. For example, the power within the arm cavity should be the same across measurements, and we use MCMC to infer its exact number.
- "Independent" parameters are degrees of freedom of MCMC infers differently for each squeeze angle dataset.

We can only allow one independent parameter because of the time constraint. To fit all 11 measurements simultaneously, we have 22 more parameters for MCMC because each measurement has a unique squeezing angle and phase noise. The time to run it with 10000 steps per walker is $0.025 \times 27 \times 10000 \times 54/3600 = 100$ hours, which is way too long to iterate.

Instead, we choose the squeezing angle and phase noise for each measurement, given the fitted values from the previous section. The set-up and results are shown in Table 6.7.

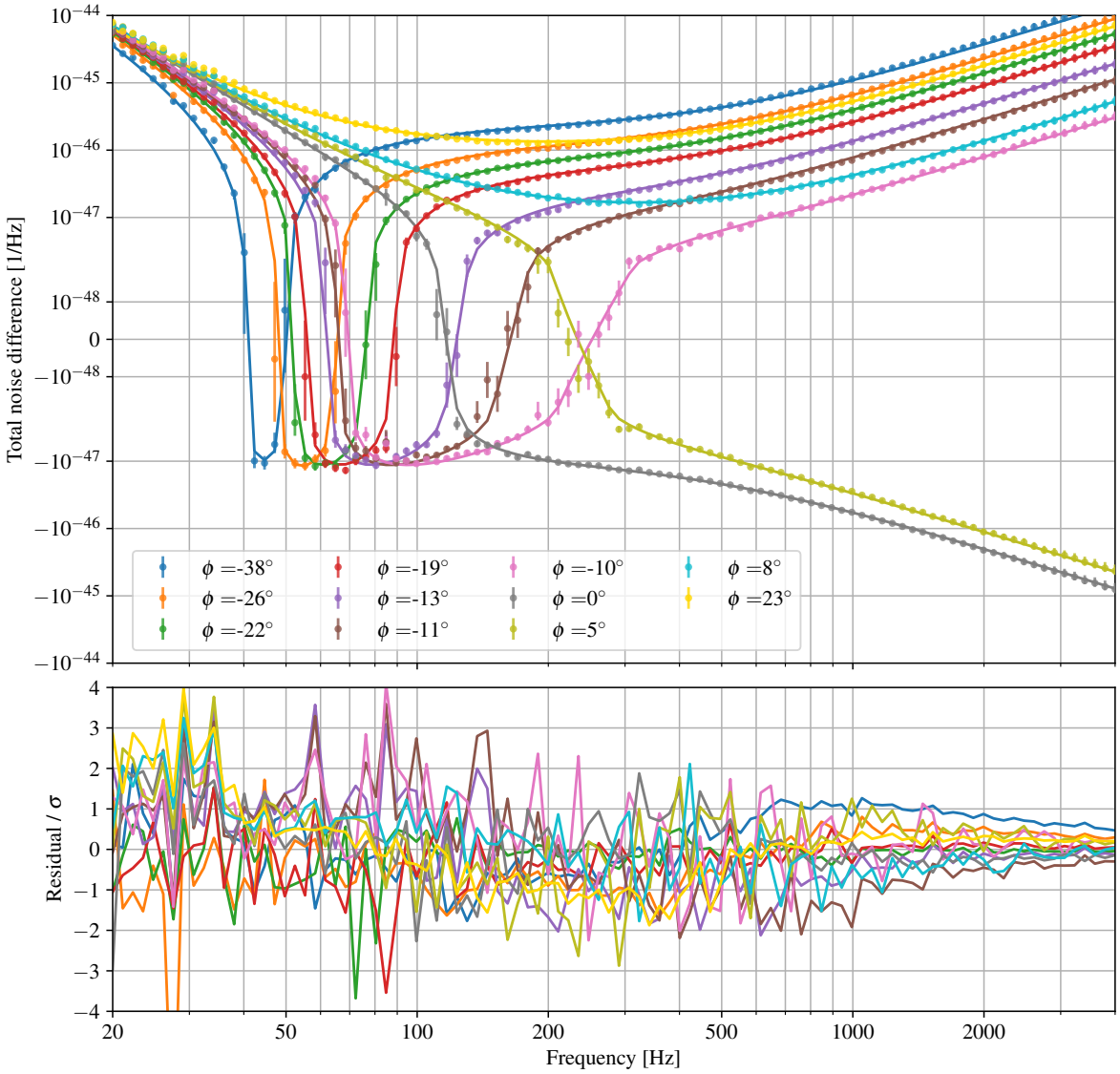

Figure 6-10: Inference results on the difference of total noise between frequency-independent squeezed and unsqueezed interferometer at various squeezing angles. The negative PSD difference means that the quantum noise is being squeezed. The residual between the model and measurements are normalized by the 1-σ uncertainty and shown in the bottom plot [1, 14].

Fig. 6-10 shows the best model that is able to minimize residuals for all strain noise differences. Notably, the arm power is inferred to be around 260 kW instead of 300 kW calculated from power recycling gain (PRG). The underestimation of the arm power raised lots of eyebrows when we first reported the analysis, as PRG calculation has been reliable since the Observing Run 3. Interestingly, the recent measurement of arm power using radiation pressure agreed with our analysis [137]. This is encouraging and validating our inference method on interferometer parameters.

Don't forget that we also fit NULL channels of all the measurements at the same time. The NULL channels are much easier to fit than strain noise differences. The results are shown in Fig. 6-11.

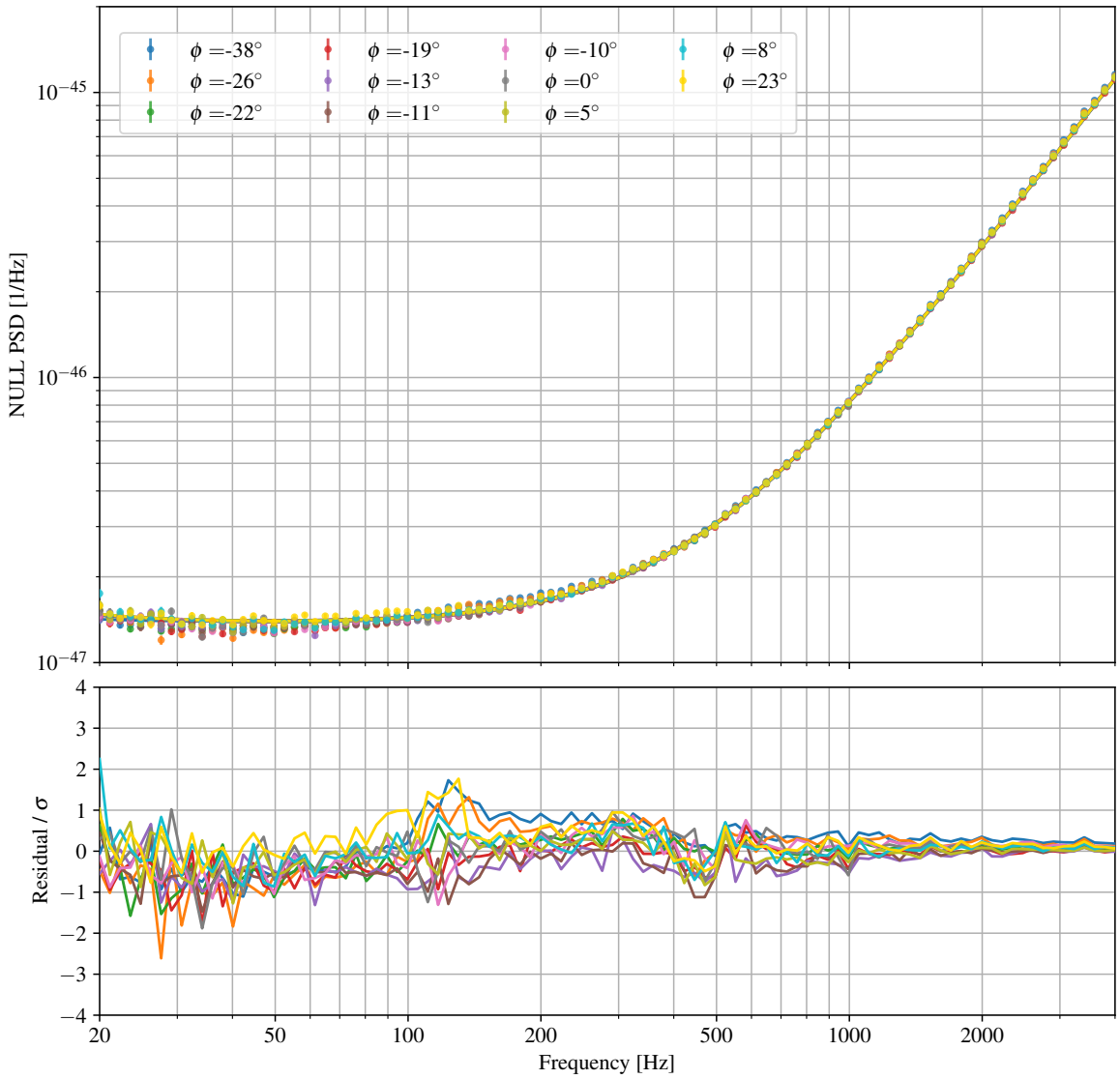

Figure 6-11: Inference results on the NULL channels, which are fit at the same time as the strain noise differences (Fig. 6-10).

This concludes the most difficult part of the inference. We've obtained all the parameters of the full LIGO, except for the filter cavity. We will fit filter cavity parameters in the next section.

6.7 MCMC on Frequency-Dependent Squeezing

The inferred interferometer parameters fully determine the unsqueezed quantum noise model M_r, which can be used to subtract for classical noise.

$$C = D_r - M_r \tag{6.41}$$

The classical noise stays the same when we are squeezing with or without the filter cavity, as proved in Section 6.4.4. The nominal squeezed quantum noise is

$$Q(\Omega) = D_s(\Omega) - (D_r(\Omega) - M_r(\Omega)). \tag{6.42}$$

The total uncertainty of $Q(\Omega)$ is

$$\Delta Q^2(\Omega) = Q^2(\Omega)\delta G^2_{cal}(\Omega) + [\Delta D_s^2(\Omega) + \Delta D_r^2(\Omega) + \Delta M_r^2(\Omega) + \tag{6.43}$$

$$(D_r(\Omega) - M_r(\Omega))^2(\delta N_t^2(\Omega) + \delta N_m^2(\Omega))] \tag{6.44}$$

where the new uncertainty $\Delta M_r(\Omega)$ is the uncertainty of the unsqueezed reference quantum noise model. It can be calculated by feeding the MCMC chains to the GWINC model.

We plot the noise spectrum in units of amplitude spectral density (ASD) $q(\Omega) = \sqrt{Q(\Omega)}$. The relative error in ASD is

$$\delta q(\Omega) = \frac{1}{2}\delta Q(\Omega) \tag{6.45}$$

$$= \sqrt{\frac{\delta G^2_{cal}(\Omega)}{4} + \frac{1}{4Q^2(\Omega)}\left[\Delta D_s^2(\Omega) + \Delta D_r^2(\Omega) + \Delta M_r^2(\Omega) + C^2(\Omega)(\delta N_t^2(\Omega) + \delta N_m^2(\Omega))\right]}. \tag{6.46}$$

Fig. 6-12 shows the contributions of each uncertainty. The statistical uncertainty dominates

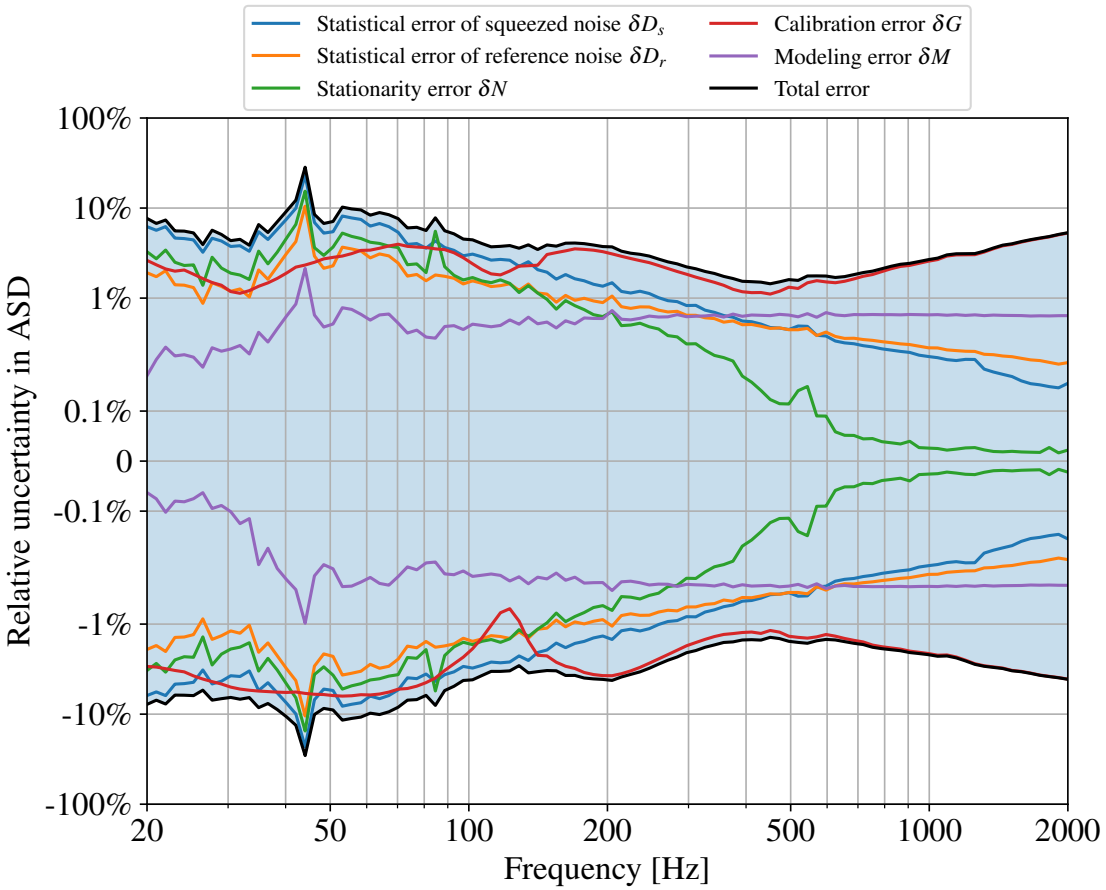

Figure 6-12: Total uncertainty budget of inferred quantum noise from various error sources [1, 14].

both positive and negative error bars at low frequency due to the small frequency bin width (Eq. (6.33)). At high frequencies above 500 Hz, the statistical error decreases as there are more averages available per bin width. Both statistical and stationarity error are symmetrical, whereas the calibration error and modeling error are not. The calibration error, obtained from the calibration pipeline [134], dominates at a high frequency above 200 Hz.

With the frequency-dependent squeezing quantum noise and uncertainties, we can find the filter cavity parameters to model it directly with GWINC. The set-up of MCMC and results are summarized in the Table 6.7

Table 6.7: Parameters of the LIGO Livingston detector inferred using Markov Chain Monte Carlo (MCMC) methods.

		MCMC Set-up		Inferred
	Fixed/	Prior	Initial walker	Common/
	Chosen	Gaussian $(-\sigma, \sigma)$	Flat probability	Independent
Interferometer parameters				
Circulating power in arm cavity		(270, 320) kW	270 - 310 kW	$257^{+3.9}_{-1.6}$ kW
Arm to SEC mismatch	2.7%			
Arm to SEC mismatch phase	0°			
SEC round-trip detuning phase	0.14°			
SEC round-trip Gouy phase		(20, 50) °	20° - 70°	$43.0^{+4.5}_{-5.2}$ °
Readout angle	-11°			
Total readout loss		(8, 10) %	6% - 10%	$8.0^{+1.2}_{-0.5}$ %
IFO to OMC mismatch		(6, 8) %	4% - 10%	$3.6^{+0.5}_{-0.5}$ %
IFO to OMC mismatch phase				Independent
Squeezing parameters				
Generated squeezing	17.4 dB			
Squeezing angle	Chosen			
Total Injection efficiency	92.9%			
SQZ to OMC mismatch		(1, 8) %	1% - 8 %	$1.1^{+1.3}_{-0.2}$ %
SQZ to OMC mismatch phase	-45°			
Phase noise (RMS)	Chosen			
Filter cavity parameters				
Length	300 m			
Detuning		(−28, −25) Hz	−31 Hz - −26 Hz	−25.6 Hz
Finesse	7000			
Full-linewidth	71 Hz			
Input coupler transmission		(800, 900) ppm	750 ppm - 880 ppm	797 ppm
Derived round-trip loss				100 ppm
Squeezer to FC mismatch	0.2%			
Squeezer to FC mismatch phase		(−180, 180) °	−180° - 180°	−65°
Length noise (RMS)		(0.1, 1) pm	0.1 pm - 2 pm	0.2 pm

This concludes the parameter estimation of the quantum noise for the LIGO Livingston Observatory. We will show the fitted quantum noise result in the next section.

6.8 Sub-SQL Performance

Without further ado, let's see the quantum noise with nominal frequency-dependent squeezing.

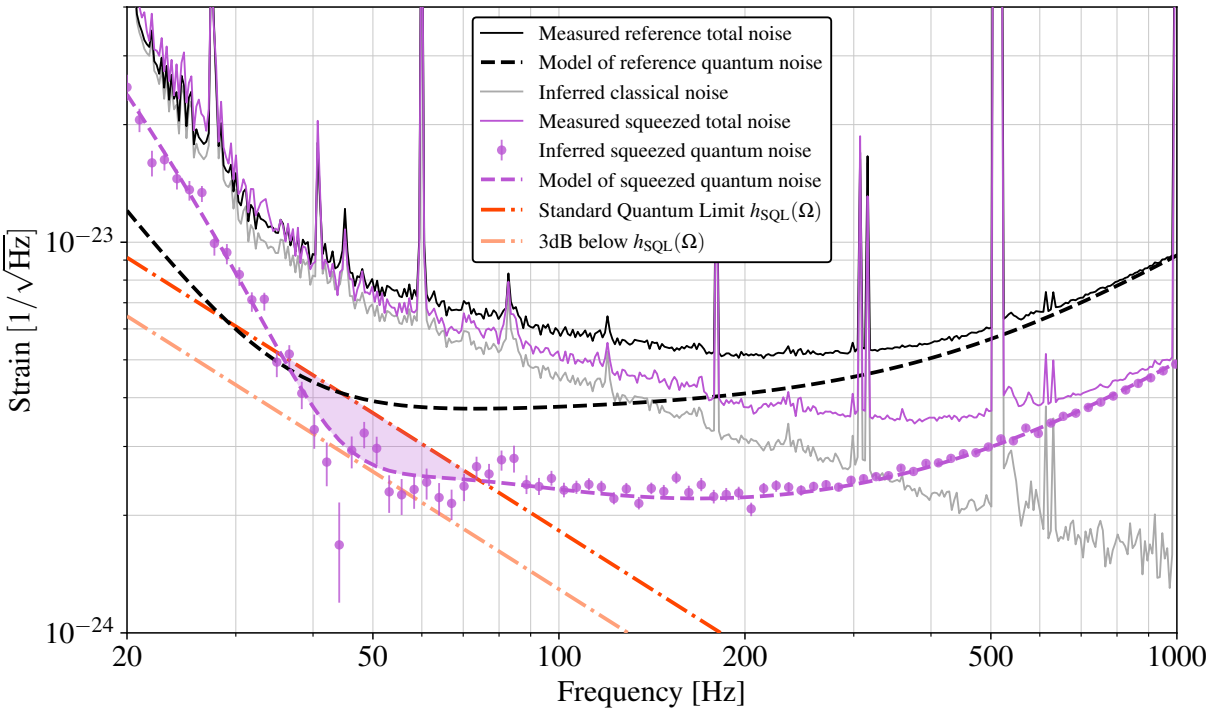

Figure 6-13: Strain sensitivity of the LIGO L1 interferometer. The squeezed quantum noise surpasses the standard quantum limit h_{SQL} by up to 3 dB in the shaded region between 35–75 Hz. This configuration is representative of the nominal detector noise during O4, demonstrating the use of quantum correlations to directly improve astrophysical sensitivity [1].

The total detector noise spectrum is an incoherent sum of the classical and quantum noise. The unsqueezed reference total noise (solid black) is measured without squeezing injection. An

unsqueezed quantum noise model (dashed black) is subtracted from the measured reference total noise to obtain an estimate of the underlying classical noise (gray). The inferred detector quantum noise with squeezing (purple dots) is obtained by subtracting the classical noise estimate (gray) from the measured squeezed total noise spectra (solid purple). The dashed purple trace shows a fitted model of frequency-dependent squeezed noise spectra, given our best knowledge of the detector and squeezer parameters.

Considering all measurement uncertainties, the LIGO detector operates with sub-SQL quantum noise at more than 3-σ statistical confidence, as enabled by frequency-dependent squeezing.

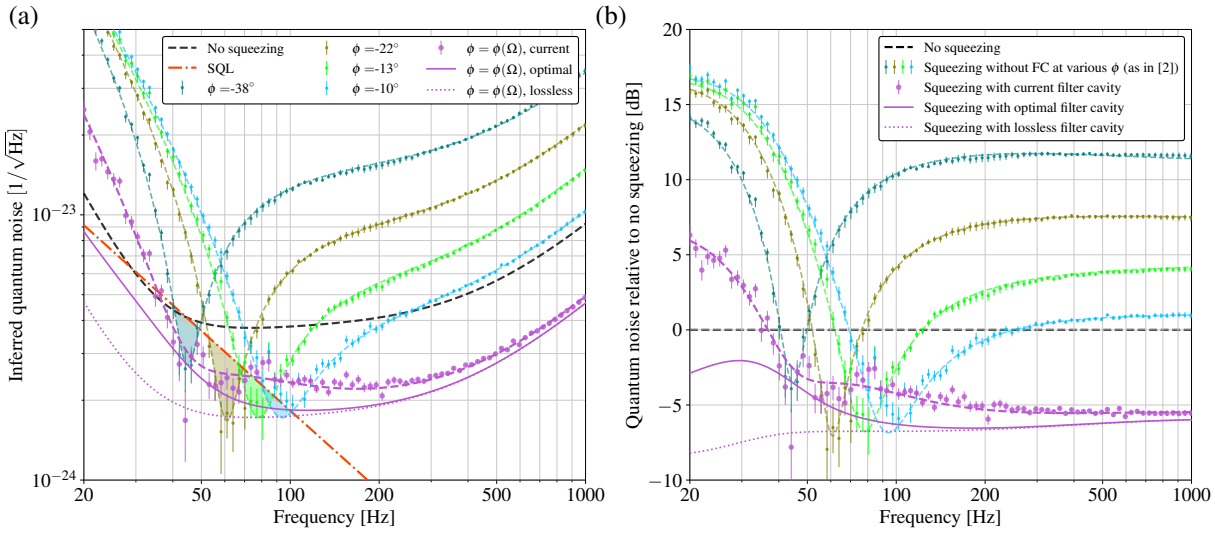

Figure 6-14: Quantum noise reduction in strain amplitude spectral density. Blue, olive, lime, and teal traces show the inferred quantum noise with frequency-independent squeezing injected at four different squeeze angles ϕ. The three purple traces show the quantum noise with three frequency-dependent squeezing configurations [1].

Fig. 6-14 compares the sub-SQL performance with frequency-independent squeezing (constant squeezing angle ϕ) and frequency-dependent squeezing ($\phi = \phi(\Omega)$). The sub-SQL dip can be produced by sending squeezing at a fixed angle, as previously observed [46]. However, the dip has a very narrow frequency range. Although we can move the dip frequency by changing the squeezing angle, it is not an optimal configuration for maximum sensitivity at all frequencies. As

mentioned in the main text, frequency-dependent squeezing can theoretically achieve the sub-SQL envelope that covers all dips that frequency-independent squeezing can achieve (dotted purple).

6.9 Future Filter cavity Upgrade

While the current frequency-dependent squeezing configuration achieves quantum-noise suppression above 35 Hz (see the dashed purple "current FC" curve in Fig. 6-14), frequency-independent squeezing models and measurements all suggest that an optimal filter cavity would yield significantly greater quantum noise reduction at astrophysically-important low frequencies (solid purple "optimal FC" curve).

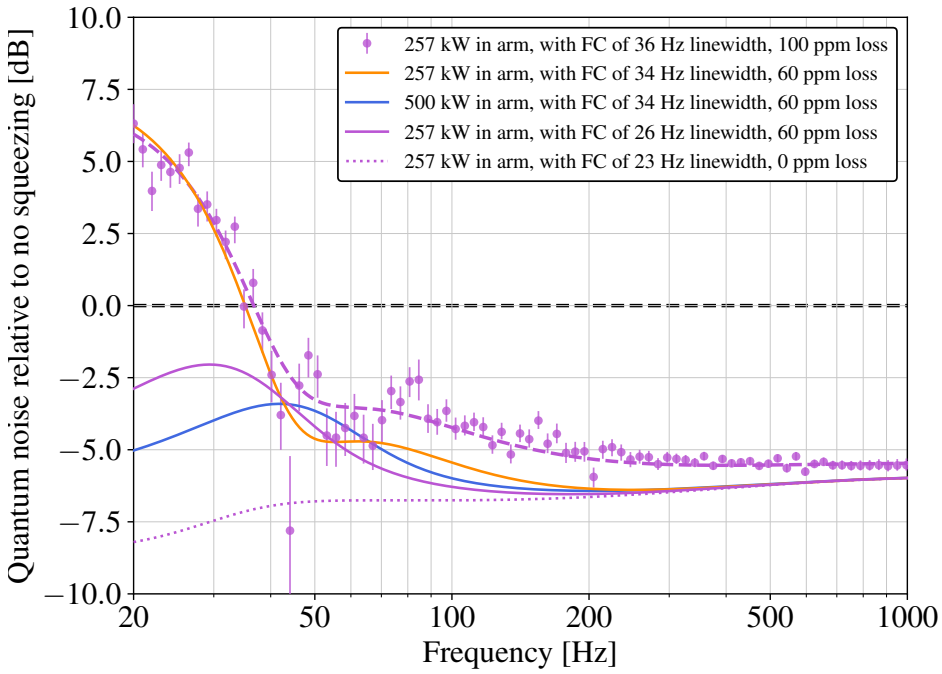

Figure 6-15: Comparison of the quantum noise with various filter cavity configurations.

The discrepancy between the current and optimal filter cavity arises from the mismatch between

the current SQL frequency and the filter cavity linewidth. In the lossless case, the optimal filter cavity would have an equal half-width-half-maximum linewidth γ_{FC} and detuning both determined by the SQL frequency, $\gamma_{\mathrm{FC}} = \Omega_{\mathrm{SQL}}/\sqrt{2}$ [138]. The current filter cavity was designed to have $\gamma_{\mathrm{FC}} = 2\pi\times 42$ Hz, using an input coupler power transmissivity of $T_{\mathrm{in}} \approx 1000$ ppm [3] and assuming 60 ppm optical loss, to approximately match $\Omega_{\mathrm{SQL}} = \sqrt{2}\gamma_{\mathrm{FC}} = 2\pi \times 59$ Hz. However, the current SQL frequency is at $\Omega_{\mathrm{SQL}} = 2\pi \times 37$ Hz. Since Ω_{SQL} is proportional to the square root of arm power as in Eq. (4.71), the optimal filter cavity curve in Fig. 6-14 could be approached by either reducing the filter cavity linewidth (reducing T_{in}, solid purple) or increasing the current arm power from 260 kW to 500 kW, as shown in Fig. 6-15. This is because a higher circulating laser power couples back action into the measurement over a larger bandwidth, requiring a higher bandwidth filter cavity to compensate.

With frequency-dependent squeezing, the LIGO A+ detectors now operate with quantum-limited sensitivity surpassing the SQL, as envisioned for the first time over two decades ago [36]. The methods described here enabled us to accurately model quantum noise through the complex optical systems of the LIGO interferometers, with important insights that inform the next steps toward the A+ target of 6 dB of broadband squeezing enhancement.

Concepts for future upgrades in the LIGO facilities and the next generation of gravitational-wave detectors like Cosmic Explorer [139] and Einstein Telescope [140] include the ambitious goal of 10 dB squeezing enhancement. Techniques and methods presented here are fundamental to achieving this goal and further enhancing the scientific potential of gravitational-wave observatories.

7 POINT ABSORBER LIMITS TO GW DETECTOR

In the previous chapters, we have explored squeezed state of light as a way to reduce quantum noise. Alternatively, we still have to increase the amount of optical power in the arm cavity to reduce quantum shot noise and enable the optimal filter cavity. However, unintended micron-scale contaminants known as point absorbers on the arm cavity mirrors can absorb the light circulating in the cavity, causing thermoelastic deformation of the mirror surfaces and increasing losses by scattering light out of the fundamental cavity mode. This point absorber effect is a significant limiting factor in some high-power cavity experiments, such as the Advanced LIGO gravitational wave detector. In this chapter, we present an analytical approach to understanding the point absorber effect from first principles and simulate its impact on increased scattering. We statistically calculate the achievable circulating power in current and future gravitational-wave detectors based on various point absorber configurations. Our theoretical formulation is validated experimentally by comparing it with the scattered power measured in the arm cavity of Advanced LIGO using in-situ photodiodes. This understanding is a crucial tool in the global effort to design future gravitational wave detectors capable of supporting high optical power and thereby reducing quantum noise.

7.1 Introduction

A wide variety of precision optical experiments rely on resonant optical cavities to enable precise measurements of space, time, and spacetime itself. These experiments often require high optical intensity incidents on the mirrors of the cavity to boost the signal-to-noise ratio. However, unintended defects may be deposited on the reflective surface of the mirror during the coating process or exposure to a dusty environment [141]. These localized defects, known as "point absorbers", absorb optical power and cause undesired thermal effects on the optics under irradiation, especially in cavities containing high circulating power. The point absorber becomes a limiting factor in various precision measurement experiments that require a high-finesse cavity with low round-trip loss, such as cavity QED [142], axion detection [143], qubit experiments [144], and gravitational-wave detectors [145–147]. It is thus necessary to develop a quantitative understanding of the point absorber effect in high-power optical cavities.

With a 4 km long baseline and a circulating power of more than 200 kW, the arm cavity of Advanced Laser Interferometer Gravitational-Wave Observatory (aLIGO) serves as a good example of the point absorber effect [110]. aLIGO is a dual-recycled Fabry-Pérot Michelson interferometer designed to measure tiny perturbations of spacetime with unprecedented precision [145]. One of the fundamental noises that limit aLIGO's performance is quantum shot noise, which can be reduced either by increasing the arm power or by manipulating the quantum states of light through squeezing [62]. However, arm power can be limited by point absorbers (studied here), other thermal distortions [148], and a variety of instabilities [100, 149–151]. The arm power during the third Observing Run O3 was limited to one-third of the designed value of 750 kW, mainly due to point absorbers on the mirror [110, 145] that scatter light out of the fundamental cavity mode.

Point absorbers were known to exist since the first observing run. Many analyses have been carried out to understand how they deform the optics and scatter light out of the cavity [141, 152, 153]. In this paper, we provide a more general approach from first principles. The traditional formalism is

extended to include arbitrary heating functions with any nonlinear boundary conditions, such as the Stefan-Boltzmann law. With the correction from nonlinear boundary condition, we can make more accurate statistical estimations of the arm power for the next planned upgrade of aLIGO (known as "A+") and the next generation of gravitational-wave detectors with a variety of potential point absorber configurations.

We start by calculating the differential temperature profile from a single-point absorber heating with proper boundary conditions. Then the thermoelastic deformation of the mirror is derived using the thermoelasticity equation. Next, this deformation is incorporated in an FFT-based simulation to obtain the field in the arm cavity, which is used to calculate its round-trip loss and achievable power. In addition, we simulate the low-angle scattered light intensity and compare this with in-situ measurements. Our results reveal a good match between these measurements and simulation, thus confirming our understanding of point absorbers.

7.2 Temperature Solution

Point absorber deteriorates the performance of an optical resonator through a mechanism of absorbing laser power, thermally expanding the mirror, and scattering excessive light. We will model the process step-by-step. The analytical solution of the differential temperature is shown first.

Consider a cylindrical optics with radius a and height h. Select the cylindrical coordinate system at the center of the mirror with z direction pointing towards the high-reflective (HR) side and cavity. One point absorber is put at the center of HR side for circular symmetry. When the cavity is locked, the system is stationary, and the heat equation simplifies to the Laplace equation.

$$\nabla^2 T = 0 \tag{7.1}$$

where $T(r, z)$ is the differential temperature higher than the ambient T_∞. The boundary conditions

have a heating intensity $I(r)$ due to the absorption of a Gaussian intensity by the absorber plus thermal radiation on all of its surfaces.

$$\begin{cases} -K\dfrac{\partial}{\partial z}T\left(r, z=\dfrac{h}{2}\right) = -I(r) + \epsilon\sigma\left[\left(T_\infty + T\left(r, z=\dfrac{h}{2}\right)\right)^4 - T_\infty^4\right] \\ -K\dfrac{\partial}{\partial r}T(r=a, z) = \epsilon\sigma\left[\left(T_\infty + T\left(r=a, z\right)\right)^4 - T_\infty^4\right] \\ -K\dfrac{\partial}{\partial z}T\left(r, z=-\dfrac{h}{2}\right) = -\epsilon\sigma\left[\left(T_\infty + T\left(r, z=-\dfrac{h}{2}\right)\right)^4 - T_\infty^4\right] \end{cases} \tag{7.2}$$

where K is thermal conductivity, ϵ is emissivity/absorptivity, and σ is Stefan-Boltzmann constant. By linearizing the radiative term for small T, the exact solution of the Laplace equation can be expressed in Dini series [154].

$$T(r,z) = \sum_k \left\{J_0\left(\frac{kr}{a}\right)\right\}\begin{Bmatrix} e^{kz/a} \\ e^{-kz/a}\end{Bmatrix} = \sum_k J_0\left(\frac{\zeta_k r}{a}\right)\left(A_k e^{\zeta_k z/a} + B_k e^{-\zeta_k z/a}\right) \tag{7.3}$$

with $\{\zeta_k\}$ solved from the Robin boundary condition of the cylindrical side. The coefficients A_k and B_k are then solved from the other two boundary conditions in (Eq. (7.2)). Although Dini series method provides an exact solution to the temperature, it becomes computationally expensive as the number of effective terms is inversely proportional to the absorber size. For a point absorber of a few microns, the computations require effective terms on the order of 10^5, and the exponent exceeds the maximum of the finite floating-point number in double precision. A simple yet good approximation is desired.

Semi-infinite approximation simplifies the solution by treating the optics as a semi-infinite solid [155]. Take the Hankel transform of the second-order partial differential equation with respect

to r, we get

$$-k^2\tilde{T}(k,z) + \partial_z^2\tilde{T}(k,z) = 0 \tag{7.4}$$

where

$$\tilde{T}(k,z) = \mathscr{H}_0[T(r,z)] = \int_0^\infty \mathrm{d}r\, r\, J_0(kr)T(r,z) \tag{7.5}$$

The angular dependence is removed due to symmetry. The solution of Eq. (7.4) is simply

$$\tilde{T}(k,z) = A(k)e^{kz} + B(k)e^{-kz} \tag{7.6}$$

Assuming a semi-infinite solid, we can drop the second term. The conditions $T(r \to \infty, z) = T(r, z \to -\infty) = 0$ are already used, so the only one left is the radiative boundary condition at HR surface:

$$-K\frac{\partial}{\partial z}T\left(r, z = \frac{h}{2}\right) = -I(r) + g\left(T\left(r, z = \frac{h}{2}\right)\right) \tag{7.7}$$

$g(T)$ is generally a non-linear function but can be linearized for small T. We present a general way of solving it first. Let the heating source be fully from a point absorber:

$$I(r) = \frac{P_{abs}}{\pi w^2}e^{-r^2/w^2} = \epsilon I_{abs}e^{-r^2/w^2} \tag{7.8}$$

where P_{abs} is the power absorbed, w is the absorber radius, and I_{abs} is the laser intensity at point absorber. The intensity profile is not necessarily Gaussian, but we choose it to simplify calculations, since it's an eigenfunction of useful transformations.

Take Hankel transform again on both sides of the boundary condition at the HR surface:

$$-K\partial_z\tilde{T}(k, z = h/2) = \mathscr{H}_0\Big[-I(r) + g\Big(T(r, z = h/2)\Big)\Big] = H(k) \tag{7.9}$$

Therefore

$$\tilde{T}(k,z) = A(k)e^{kz} = -\frac{H(k)e^{k(z-h/2)}}{Kk} \tag{7.10}$$

We are most interested in the temperature profile at HR surface $T_{HR}(r) = T(r, z = h/2)$

$$\begin{aligned} T_{HR}(r) &= \mathscr{H}_0^{-1}\left[\tilde{T}\left(k, z = \frac{h}{2}\right)\right] \\ &= \frac{2}{\pi K}\int_0^r dr' r' \left(I(r') - g\left(T_{HR}(r')\right)\right)\frac{1}{r}\mathscr{K}\left(\frac{r'^2}{r^2}\right) \\ &\quad + \frac{2}{\pi K}\int_r^\infty dr' \left(I(r') - g\left(T_{HR}(r')\right)\right)\mathscr{K}\left(\frac{r^2}{r'^2}\right) \end{aligned} \tag{7.11}$$

where $\mathscr{K}$ is the complete elliptic integral of the first kind (not the optomechanical coupling coefficient from the previous chapters). This is a nonlinear integral equation with no analytical solution. An approximate solution can be achieved by either linearizing the boundary function g or solving it successively with feedback.

The linearized boundary solution has been given in [155]. We just summarize them here. If we assume small T, the boundary condition can be linearized as

$$g(T_{HR}(r)) = \epsilon\sigma\left[\left(T_\infty + T_{HR}(r)\right)^4 - T_\infty^4\right] \approx 4\epsilon\sigma T_\infty^3 T_{HR}(r) \tag{7.12}$$

Plug back to Eq. (7.9) and Eq. (7.10)

$$T_{HR}(r) = \int_0^\infty dk k J_0(kr)\frac{\tilde{I}(k)}{Kk + 4\epsilon\sigma T_\infty^3} = \frac{\epsilon I_{abs} w^2}{2K}\int_0^\infty dk J_0(kr)\frac{e^{-k^2w^2/4}}{1 + 4\epsilon\sigma T_\infty^3/(Kk)} \tag{7.13}$$

The complete temperature function can also be solved:

$$\tilde{T}(k, z) = e^{k(z-h/2)}\tilde{T}_{HR}(k) \tag{7.14}$$

Instead of summing infinite Dini series, the semi-infinite solution integrates absorbed intensity in the spatial frequency domain weighted by Bessel functions. Both methods are compared in Fig. 7-1 for various absorber sizes.

The semi-infinite solution can be well fitted with an analytical expression (Fig. 7-1), which

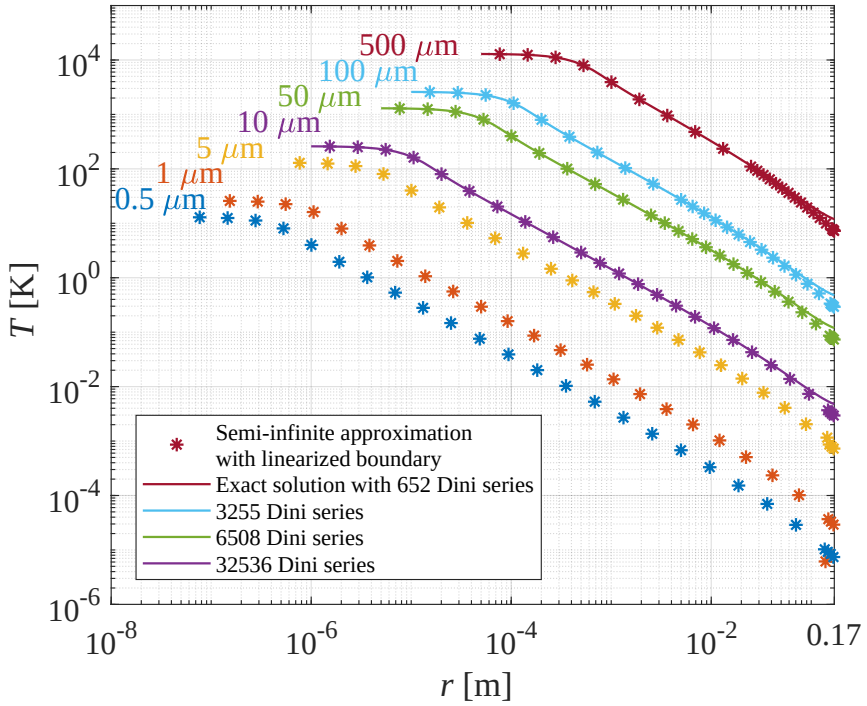

Figure 7-1: There are two approximations that can be applied: semi-infinite approximation and linearized boundary approximation. This plot shows that semi-infinite approximation and exact differential temperature solutions using Dini series agree very well, given different point absorber radii. The incident intensity on the centered absorber is 4.1×10^7 W/m^2 (unity thermal emissivity), which is equivalent to the center intensity of the 240-kW beam on ETM of aLIGO arm cavity. Note that the number of Dini series required increases inverse proportionally to the absorber size.

unveils the physics of absorber heating.

$$T_{HR}(r) \approx \frac{\sqrt{\pi}}{2} \frac{\epsilon I_{abs} w}{K} \frac{1}{(1 + (r/(0.46w))^{3.2})^{1/3.2}} \tag{7.15}$$

For small absorbed power P_{abs}, the heat from the point absorber is primarily dissipated by conduction. This estimation breaks down for large absorbed power. For example, if we have $P_{abs} = 10$ mW, $w = 10$ μm and $K = 1.38$ W/mK for fused silica optics, we would have $T_{HR}(0) = 204$ K larger than the ambient, invalidating the linearization assumption. Alternatively, the correction will matter if the radiative contribution becomes significant. This motivates us to find the solution

to the general boundary condition.

The nonlinear integral equation (Eq. (7.11)) can be solved by successive approximation with feedback [156,157]. Start the zeroth iteration by guessing a solution $T_0(r)$ such as the solution from the linearized boundary condition mentioned before. The real solution is denoted as $T_S(r)$. The zeroth error function is defined as

$$\varepsilon_0(r) = T_0(r) - T_S(r) \tag{7.16}$$

Send it to Eq. (7.11) and keep the first non-trivial order of the error.

$$g_0(r) = \epsilon\sigma\left[\left(T_\infty + T_0\right)^4 - T_\infty^4\right] = g_S(r) + 4\epsilon\sigma(T_\infty + T_0)^3\varepsilon_0 + \mathcal{O}(\varepsilon^2) \tag{7.17}$$

Assume the error has weak variation over radius: $\varepsilon_0(r) \approx \varepsilon_0$.

$$\begin{aligned} T(T_0(r)) &= \frac{2}{\pi K}\left[\int_0^r dr' \frac{r'}{r}\left(I(r') - g_0(r')\right)\mathscr{K}\left(\frac{r'^2}{r^2}\right) + \int_r^\infty dr'\left(I(r') - g_0(r')\right)\mathscr{K}\left(\frac{r^2}{r'^2}\right)\right] \\ &= T_S(r) - \varepsilon_0\frac{8\epsilon\sigma}{\pi K}\left[\int_0^r dr' \frac{r'}{r}(T_\infty + T_0)^3\mathscr{K}\left(\frac{r'^2}{r^2}\right) + \int_r^\infty dr'(T_\infty + T_0)^3\mathscr{K}\left(\frac{r^2}{r'^2}\right)\right] \\ &= T_S(r) - \varepsilon_0 C_0(r) \\ &= T_S(r) - (T_0(r) - T_S(r))C_0(r) \end{aligned} \tag{7.18}$$

Therefore, the solution is

$$T_S(r) = \lim_{i\to\infty} T_i(r) \tag{7.19}$$

where

$$T_{i+1} = \frac{T(T_i) + C_i T_i}{1 + C_i} \tag{7.20}$$

As T_i approaches real solution, $T(T_i) = T_i$ and $T_{i+1} = T_i$. Iterate the solution until it converges.

For small point absorbers, the temperature is relatively low, and the radiative corrections are negligible. The linearized boundary solution is very accurate. However, the correction becomes

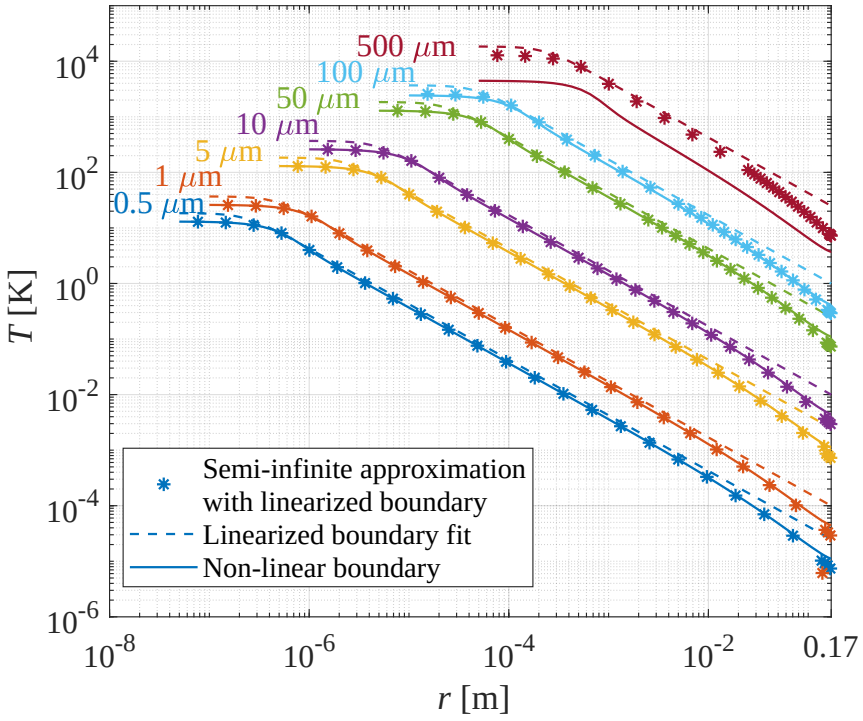

Figure 7-2: Solution of temperature profile under linearized and nonlinear boundary conditions. The parameters are the same as Fig. 7-1. The analytical fit of the approximation is Eq. (7.15).

significant for absorbers with radii larger than 100 μm, up to a factor of three in the 500-μm case. The nonlinear boundary solution is necessary for unusually large point absorbers.

The solution of the temperature distribution allows us to proceed on solving the thermoelastic deformation of the mirror surface induced by point-absorber heating.

7.3 Displacement Solution

Given the temperature distribution $T(r, z)$ solved in previous section, we can find the displacement vector field $\mathbf{u}$ of the mirror next. We follow Hello and Vinet's formalism, but apply it to the

semi-infinite solution [158]. The elasticity equation to solve is the static Navier-Cauchy equation:

$$\nabla \cdot \mathbf{T} = T_{ij;j} = 0 \tag{7.21}$$

where T_{ij} is the stress tensor and the semicolon stands for covariant derivative. The gravity is not included because we are interested in the net thermal effect caused by the point absorber. The stress tensor has a thermoelastic stress-strain relationship:

$$T_{ij} = -\lambda\Theta g_{ij} - 2\mu E_{ij} + (3\lambda + 2\mu)\alpha T g_{ij} \tag{7.22}$$

where $E_{ij} = (u_{i;j} + u_{j;i})/2$ is the strain tensor, Θ =Tr(E) is the expansion of the body, and g_{ij} is the 3-D metric. Other constants are μ (first Lamé coefficient), λ (second Lamé coefficient), and α (thermal expansion coefficient). The stress tensor (T_{ij}) should not be confused with temperature distribution $T(r, z)$. Under a differential temperature $T(r, z) = T_{abs} - T_{\infty}$, the mirror undergoes an additional expansion of αT in all directions. Assuming axial symmetry and no rotation, we have $u_{\phi} = 0$ and remove one component of Eq. (7.21). The other remaining two coupled partial differential equations are broken down in terms of our most interesting variable u_i:

$$u_{i;j} = u_{i,j} + \Gamma_{ijl} u_l \tag{7.23}$$

where comma stands for partial derivative. The Christoffel symbols are $\Gamma_{\phi\phi r} = \Gamma_{\phi r\phi} = \frac{1}{r}$, $\Gamma_{r\phi\phi} = -\frac{1}{r}$, and all rest are zero. The surviving components of the strain tensor are

$$E_{rr} = u_{r;r} = u_{r,r} + \Gamma_{rrl} u_l = u_{r,r} \tag{7.24}$$

$$E_{\phi\phi} = u_{\phi;\phi} = u_{\phi,\phi} + \Gamma_{\phi\phi l} u_l = \frac{u_r}{r} \tag{7.25}$$

$$E_{zz} = u_{z;z} = u_{z,z} + \Gamma_{zzl} u_l = u_{z,z} \tag{7.26}$$

$$E_{rz} = \frac{1}{2}(u_{r;z} + u_{z;r}) = \frac{1}{2}(u_{r,z} + \Gamma_{rzl} u_l + u_{z,r} + \Gamma_{zrk} u_k) = \frac{1}{2}(u_{r,z} + u_{z,r}) \tag{7.27}$$

The new stress-strain relationship is

$$\begin{cases} T_{rr} = \lambda(\Theta - 3\alpha T(r,z)) + 2\mu(E_{rr} - \alpha T(r,z)) = \lambda\Theta + 2\mu E_{rr} - (3\lambda + 2\mu)\alpha T(r,z) \\ T_{\phi\phi} = \lambda(\Theta - 3\alpha T(r,z)) + 2\mu(E_{\phi\phi} - \alpha T(r,z)) = \lambda\Theta + 2\mu E_{\phi\phi} - (3\lambda + 2\mu)\alpha T(r,z) \\ T_{zz} = \lambda(\Theta - 3\alpha T(r,z)) + 2\mu(E_{zz} - \alpha T(r,z)) = \lambda\Theta + 2\mu E_{zz} - (3\lambda + 2\mu)\alpha T(r,z) \\ T_{rz} = 2\mu E_{rz} \end{cases} \tag{7.28}$$

All other components of the stress tensor are zero. In the steady-state condition with no external pressure (ignoring gravitational contribution), the total force **F** acting on the volume element is zero:

$$\mathbf{F} = -\int_{\partial V} \mathbf{T} \cdot d\mathbf{A} = -\int_{V} \nabla \cdot \mathbf{T} dV = 0 \tag{7.29}$$

So

$$\nabla \cdot \mathbf{T} = T_{ij;j} = T_{ij,j} + \Gamma_{ijl} T_{lj} + \Gamma_{jjl} T_{il} = 0 \Rightarrow \begin{cases} T_{rj;j} = \dfrac{\partial T_{rr}}{\partial r} + \dfrac{\partial T_{rz}}{\partial z} + \dfrac{T_{rr} - T_{\phi\phi}}{r} = 0 \\ T_{\phi j;j} = \dfrac{\partial T_{r\phi}}{\partial r} + \dfrac{\partial T_{z\phi}}{\partial z} + \dfrac{3T_{r\phi}}{r} = 0 \\ T_{zj;j} = \dfrac{\partial T_{rz}}{\partial r} + \dfrac{\partial T_{zz}}{\partial z} + \dfrac{T_{rz}}{r} = 0 \end{cases} \tag{7.30}$$

The second equation is trivial because all $T_{i\phi} = 0$. These two coupled partial differential equations can be represented in the variable u_i of interest.

$$\begin{cases} (\lambda+2\mu)\partial_r^2 u_r + (\lambda+\mu)\partial_r\partial_z u_z + \mu\partial_z^2 u_r + \dfrac{\lambda+2\mu}{r}\partial_r u_r - \dfrac{\lambda+2\mu}{r^2}u_r = \alpha(3\lambda+2\mu)\partial_r T(r,z) \\ (\lambda+2\mu)\partial_z^2 u_z + (\lambda+\mu)\partial_r\partial_z u_r + \mu\partial_r^2 u_z + \dfrac{\lambda+\mu}{r}\partial_z u_r + \dfrac{\mu}{r}\partial_r u_z = \alpha(3\lambda+2\mu)\partial_z T(r,z) \end{cases} \tag{7.31}$$

One solution of $u_i(r,z)$ that satisfies Eq. (7.31) is [158]

$$\begin{cases} u_r(r,z) = \dfrac{\alpha(3\lambda+2\mu)}{2(\lambda+\mu)}\dfrac{1}{r}\displaystyle\int_0^r dr' r' T(r',z) + \dfrac{\lambda+2\mu}{2\mu(3\lambda+2\mu)}(Ar+Brz) \\ u_z(r,z) = \dfrac{\alpha(3\lambda+2\mu)}{2(\lambda+\mu)}\left[\displaystyle\int_{h/2}^z T(r,z')dz' - \int_0^r \frac{dr'}{r'}\int_0^{r'} \partial_z T(r'',h/2)r''dr'' + C\right] \\ \qquad - \dfrac{\lambda}{\mu(3\lambda+2\mu)}\left(Az + \dfrac{Bz^2}{2}\right) - \dfrac{\lambda+2\mu}{4\mu(3\lambda+2\mu)}Br^2 \end{cases} \tag{7.32}$$

where A, B, C are constants constrained by realistic boundary conditions.

$$T_{rr}(a,z) = 0 \qquad \text{and} \qquad u_z(a,h/2) = 0 \tag{7.33}$$

Expand the first one:

$$\begin{aligned} T_{rr}(a,z) &= (\lambda+2\mu)u_{r,r} + \frac{\lambda}{r}u_r + \lambda u_{z,z} - \alpha(3\lambda+2\mu)T(a,z) \\ &= -\frac{P_{abs}}{2\pi K}\frac{\mu\alpha(3\lambda+2\mu)}{\lambda+\mu}\frac{1}{a}\int_0^\infty dk e^{k(z-h/2)}\frac{e^{-k^2w^2/8}}{1+4\epsilon\sigma T_\infty^3/(Kk)}\frac{J_1(ka)}{k} + A + Bz \\ &= 0 \end{aligned} \tag{7.34}$$

These constants A, B are used to approximately compensate the stress T_{rr} variation at the edge along the thickness. Since A, B are relatively small compared to the other terms, they are calculated with linearized $T(r, z)$. We are most interested in the HR surface deformation in the axial direction.

$$h(r) = u_z(r, h/2) = \frac{\alpha(3\lambda + 2\mu)}{2(\lambda + \mu)K} \int_0^r \frac{dr'}{r'} \int_0^{r'} dr'' r''(-I(r'') + g(r'')) - \frac{\lambda + 2\mu}{4\mu(3\lambda + 2\mu)} Br^2 + C' \tag{7.35}$$

where C' is enforced by $h(a) = 0$.

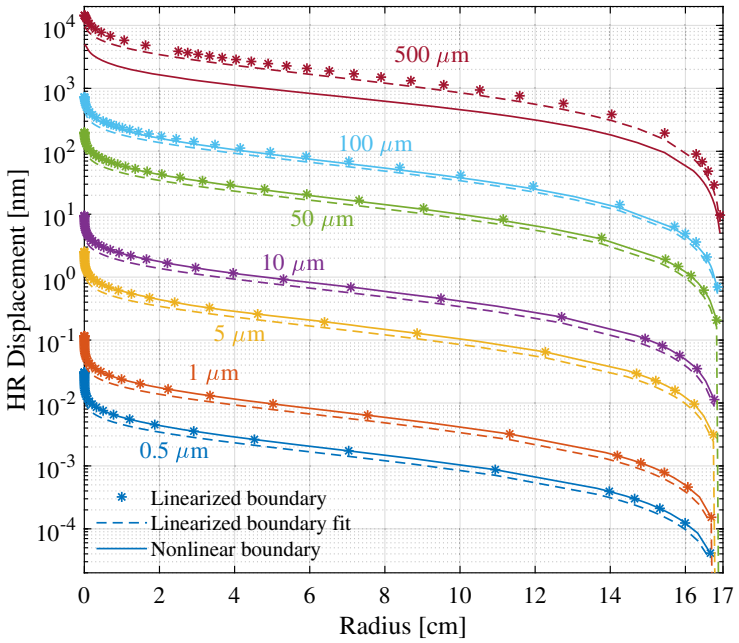

Figure 7-3: Thermoelastic displacements on the HR surface by various point absorber radii (labeled near each curve). The edge of the 17-cm radius optic has zero deformation. The incident intensity on the centered absorber is 4.1×10^7 W/m^2, equivalent to the center intensity of the 240 kW beam on the mirror of aLIGO arm cavity. Analytic fits to the linearized boundary solution (Eq. (7.36)) are also shown [5].

The simple linearized boundary solution overestimates the surface displacement as it does on the temperature. A micro-absorber can cause surface deformation on the scale of nm in height and cm in size. The analytical fit of displacement is:

$$h(r) \approx 0.12 \left(\frac{3\lambda + 2\mu}{\lambda + \mu} \right) \frac{\epsilon I_b w^2 \alpha}{K} \ln \left(\frac{a^2}{r^2 \left(1 - \frac{w^2}{a^2} \right) + w^2} \right) \tag{7.36}$$

The important caveat of failing of Eq. (7.36) holds at high absorbed power. With the deformation known, we can superpose it onto the test mass phase map data and calculate fields in a static cavity.

7.4 Arm Power Limited by Point Absorber

Advanced gravitational-wave detectors are Michelson interferometers using Fabry–Perot cavities as arms to increase optical power and thus the signal produced by gravitational-wave strain. The arm power is further increased by the addition of a mirror at the symmetric port of the interferometer to form a power-recycling cavity [50, 145]. However, the power buildup can be degraded by the point absorber effect as follows.

Without any thermoelastic deformation, the round-trip loss in the cavity is constant, and the arm power is linearly proportional to the input power with the slope set by the round-trip loss of the cold cavity (gray lines in Fig. 7-4). However, the thermoelastic deformation from the point absorbers contributes to the optical loss by scattering light out of the fundamental cavity mode. Thus, an increase in arm power leads to an increase in the optical loss of the arm, which decreases the optical gain of the power recycling cavity [141]. As a result, for sufficiently high power levels the arm power saturates and becomes largely independent of the input power.

Understanding the limitations of point absorbers on the achievable arm power in realistic situations with multiple absorbers is important in planning future detectors—for example, the next-generation gravitational-wave detector Cosmic Explorer (CE) [139, 159]. CE will achieve a factor of ten increase in sensitivity relative to A+ by scaling up the A+ design to use 40 km long arm cavities and increasing the arm power by a factor of two. The key parameters of the coupled arm cavities of both detectors are summarized in Table 7.1.

Table 7.1: Parameters of the Y-arm cavity of LIGO Livingston Observatory measured in Observing Run O3b and the proposed Cosmic Explorer. Note that, with the exception of the optical gain and round-trip loss, the A+ design parameters are the same as those of aLIGO.

Parameter	**aLIGO**	**CE**
Designed arm power	750 kW	1.5 MW
Optical gain of:		
Power recycling cavity	40	76
Arm cavity	270	280
Round-trip loss of:		
Power recycling cavity	500 ppm	500 ppm
Cold arm (no absorber)	66 ppm	40 ppm
Cavity length	3995 m	40 km
Mirror		
Aperture	34 cm	70 cm
Material	Fused Silica	Fused Silica
Temperature	290 K	290 K
Beam radius on:		
Input mirror	5.2 cm	12 cm
End mirror	6.1 cm	12 cm

To investigate the achievable arm power in CE and the upcoming A+ observing runs, we conducted a Monte Carlo statistical analysis of round-trip loss by calculating fields under a thousand-point absorber maps generated on the arm cavity mirrors. For each map, the absorber locations are uniformly distributed; radii are governed by a Rayleigh distribution, and number are governed by a Poisson distribution with mean number density one per 60 cm^2, characteristic of coated aLIGO mirrors. We investigate the cases of mean absorber radius $\langle w \rangle = 5\,\mu\mathrm{m}$ (optimistic) and larger absorbers with $\langle w \rangle = 12\,\mu\mathrm{m}$ (pessimistic). The FFT-based simulation package Stationary Interferometer Simulation (SIS) [160] is used to calculate the field amplitudes in the cavity given these point absorber maps. The round-trip loss for each map is calculated at several arm powers from

which the power recycling gain is computed. The recycling gain is then converted to the input power required to reach a given arm power.

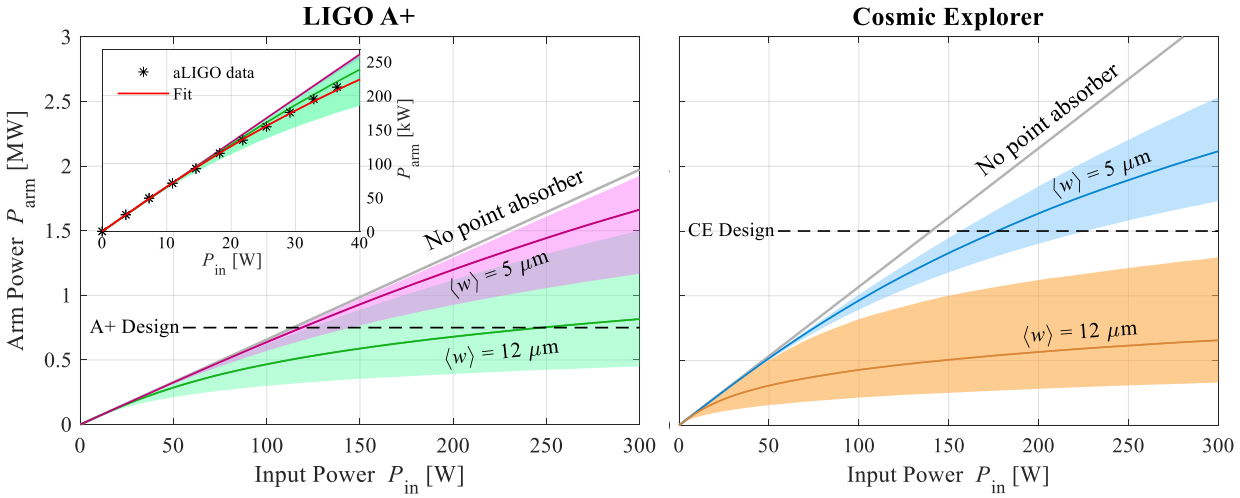

Figure 7-4: Circulating power in the arm cavity versus input power for two different detectors and mean radii of point absorbers (optimistic 5 µm and pessimistic 12 µm). The solid line is the median with shadings corresponding to the 16th and 84th percentile. The gray lines (no absorber case) increase linearly with the initial slopes set by the round-trip loss of the cold cavity (Table 7.1), and the designed power is 750 kW for A+ and 1.5 MW for CE. In the absence of point absorbers, the required input power is 120 W for A+ and 140 W for CE. In the zoomed-in graph, the data points collected from LIGO Livingston Observatory throughout Observing Run O3b are fit to obtain the radii of point absorbers. It is statistically more confident for A+ to achieve the designed power with $\langle w \rangle = 5$ µm [5].

Fig. 7-4 shows the results for these two cases for both the A+ and CE arm cavities. The medians are shown as solid lines and the shadings correspond to the 16th and 84th percentile. The arm power saturation is evident in the $\langle w \rangle = 12$ µm case and, while it may be possible for A+ to reach its 750 kW design arm power, it is unlikely that CE would ever reach its design of 1.5 MW with absorbers of this size. On the other hand, our analysis suggests that point absorbers with $\langle w \rangle = 5$ µm pose little risk of damaging the A+ arm power, but it requires on average 30% more input power for CE to achieve the designed goal. In both cases, the point absorbers limit the arm power of CE more significantly than that of A+.

This statistical model is consistent with measured arm powers in the LIGO Livingston observatory during Observing Run O3, which deviates from linear growth at high power due to the point absorber effect. This data, shown in the inset graph of Fig. 7-4, is fit to yield a 12.6 µm radius absorber and 66 ppm round-trip loss of the cold cavity. The thermal absorptivity is taken as unity to break its degeneracy with the radius of the point absorber (Eq. (7.36)). The data sits in the predicted region of the pessimistic case. These results are also consistent with measurements of the total absorbed power of the point absorber [161].

7.5 Experimental Verification

Knowing the absorber radii, beam position, and cavity parameters, we can calculate the scattered fields through FFT simulation and compare the theoretical modeling with measurements. Inside the arm cavity, there are four silicon photodiodes (PDs) mounted on each of the baffles installed in front of the test mass optics to block and monitor scattered light. As the power in the interferometer increases, the absorbers cause thermoelastic aberration of the HR surface of the test mass, which in turn results in an increased scattering. PD1 and PD4 facing the cavity sample the Airy patterns of scattered light, as shown in Fig. 7-5(a, d).

There were roughly a dozen point absorbers scattered around the surface of the end mirror, including one dominant absorber with the largest size near the center of the mirror (Fig. 7-5 (b)). After the Observing Run O3, we moved the beam spot at 23 locations on the end mirror to change the intensity incident on the absorbers while fixing the beam spot on the input mirror (Fig. 7-5). Simulations of each of these 23 alignments reveal that this large and centrally located absorber dominates the optical scatter (Fig. 7-4). The FFT results are shown in Fig. 7-5(e-f) for each of the 23 spot locations. We moved the beam to the same location repeatedly at indices 12, 17, 18, and 23. It is seen that the measurements at these indices are equal, indicating that our measurements are reproducible over a week. The simulation is capable of predicting the magnitude and variation of

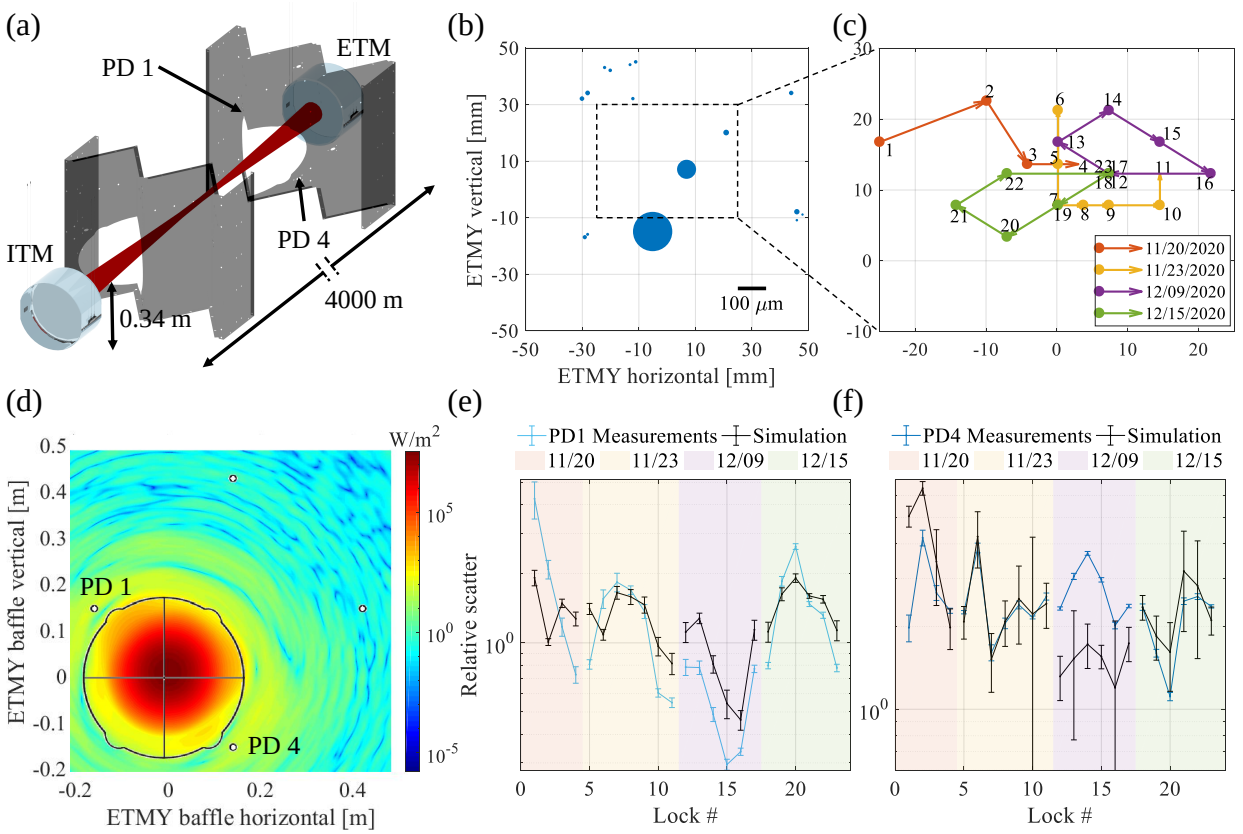

Figure 7-5: (a) Schematics of the Y arm cavity of LIGO Livingston Observatory with photodiodes (PD1 and PD4) marked. (b) Map of point absorbers on ETMY with the scale bar marked. (c) Beam trajectory on ETMY over four days while the beam location on ITMY is fixed. Note that we couldn't put the beam very close to the largest (dominant) absorber, which would scatter significantly and disrupt the lock acquisition. (d) Intensity distribution of the field incident on the end mirror baffle with a through-hole at the origin. (e-f) Experimental measurement (with 5×error bar) of normalized scatter power landing on PD1 and PD4 versus FFT simulation with point absorber formulation incorporated. The error bar of simulation is due to the 3 mm uncertainty of beam position. The data is taken at 23 beam spot locations on the end mirror at four different days. The relative scatter of clean optics without any absorber is roughly an order of magnitude lower than the plotted simulation curve (not shown).

the low-angle scatter, even though the field amplitude shows a great amount of structure along the radial distance from the beam center. The consistency between data and simulation lends further credibility to our modeling and improves our understanding of the point absorber effect. Without

the scattering due to point absorbers, the simulated relative scatter magnitude is roughly a factor of ten lower, and the simulated variations show little coherence with the PD measurements.

7.6 Future Implications

In summary, we carried out an analytical approach to the point absorber problem in a high-power resonant cavity. We propose an analytical solution to the thermoelastic deformation of the optics with arbitrary point absorber heating function and boundary conditions. Both temperature and displacement profiles are derived and incorporated in the state-of-the-art FFT-based optical simulation. With a more advanced and accurate understanding of the point absorber effect, we make a statistical prediction of arm power in current and future gravitational-wave detectors for different mean radii of point absorbers. Our analysis of resonant field power in the cavity suggests that point absorbers of mean 5 µm radii will not prevent future gravitational-wave detectors from achieving their design sensitivity. Active research is being carried out to mitigate both the size and number of point absorbers on future optics. Finally, our formulation shows a strong coherence with data when compared with in-situ measurements of scattered light, thus confirming our model.

Future analyses on the distortion of phase and mode-shape of the fields from point absorbers are needed to estimate the degradation on the Michelson contrast, which impacts the signal-to-noise ratio and thus the sensitivity of the gravitational wave detectors.

8 CONCLUSION & OUTLOOK

In summary, this thesis focuses on two ways to reduce the quantum noise in gravitational-wave detectors by sending an exotic quantum state of light (squeezing) or sending more quanta of light (powering up). These are the only methods to reduce the quantum noise in the foreseeable future without drastically changing the infrastructure of the detector (for example, increasing mirror mass or arm length). Tremendous efforts have been put to reduce quantum noise in these two front lines, and we will certainly continue improving the detector and achieve the A+ design goal of 750 kW in the arm and 6 dB broadband squeezing.

While powering up is a standard way to reduce quantum noise, we have lots of known challenges operating with a good fraction of Megawatts stored in the arm cavity. The point absorber is a potential limit to the arm power (Chapter 7). Our result suggests that a mean absorber radius $\langle w \rangle = 5$ µm (optimistic) is unlikely to stop us, but larger absorbers with $\langle w \rangle = 12$ µm (pessimistic) will certainly limit us from possibly achieving the designed arm power for both current and next-generation gravitational-wave detectors [5].

Squeezed state of light provides an alternative way to mitigate the quantum noise (Chapter 2). We formulate the direct calculation of quantum noise from first principles (Chapter 3). The theory can be easily extended to higher-order spatial modes or reduced to an approximated form commonly used in literature (Chapter 4). This bottom-up approach is the most intuitive understanding of squeezing as far as I know, although the essential physics has been covered by many other excellent works [33, 35, 36, 39].

Squeezing was introduced to convert LIGO to a quantum nondemolition detector by cleverly taking advantage of the quantum correlations between light and mirror at a high operating power [36]. It motivates the design that is finally realized in actual gravitational-wave detectors after two decades of research and development [3]. We thoroughly discussed the frequency-dependent squeezing system (Chapter 5), whose filter cavity enables us to prepare the quantum state and surpass the Standard Quantum Limit (SQL) [1]. It is a milestone in the field of quantum metrology and precision measurement.

With frequency-dependent squeezing, the LIGO detector is operating with quantum noise below the Standard Quantum Limit (Chapter 6). Together with other upgrades, both LIGO are detecting gravitational waves with an event rate doubled compared to the last observing run [2]. With more detections, we would collect enough statistics to constrain the distribution of mass, redshift, and spin properties of compact object populations [120, 162]. It allows us to study the formation and evolutionary pathways of these objects. With a higher signal-to-noise ratio, we can perform precise studies such as testing general relativity and constraining the equation of state of neutron stars [163, 164]. On multi-messenger astronomy, LIGO will be co-observing with the Rubin Observatory that is planning to operate in early 2025. With the state-of-the-art low-latency pipelines, we are ready to observe astrophysical events that release both gravitational and electromagnetic wave signals, for example, binary neutron star mergers [111, 165].

Looking into the future, we still have plenty of compact binary coalescence farther away in the Universe waiting to be detected. The era of multi-messenger astronomy had just begun. The mission of reducing quantum noise will continue by increasing the arm power and the broadband squeezing levels. Both efforts are not parallel with each other but rather enable each other mutually, as we see that the optimal filter cavity would require a higher arm power than the current. Nonetheless, we will have to drastically change our infrastructure by increasing the arm cavity length and mirror mass, as will be done by the next-generation gravitational-wave detectors to see even older cosmological history of the Universe imprinted in gravitational waves.

A LIST OF ACRONYMS

A+: A+ intrument upgrade of LIGO.

ABCD matrix: A ray-transfer matrix analysis that has four elements

AC: Alternating Current

ADS: Alignment Dither System

aLIGO: Advanced LIGO

AOM: Acousto-Optic Modulator

AR: Anti-reflective

AS: Anti-Symmetric

ASC: Angular (or Alignment) Sensing and Control

ASD: Amplitude Spectral Density

BH: Black Hole

BnC: Paper by Buonanno and Chen [39]

BNS: Binary Neutron Star

BS: Beam Splitter

Caltech: California Institute of Technology

CE: Cosmic Explorer

CLF: Control Locking Field

DARM: Differential Arm Length

dB: Decibel

DC: Direct Current (time-independent part)

DC Readout: Direct Current Readout of gravitational wave

DCPD: Often referred to as the photodiode at the transmission port of the output mode cleaner cavity

DnD: Paper with title starting “Decoherence and Degradation” [35]

DRFPMI: Dual-recycled Fabry-Pérot Michelson Interferometer

EOAM: Electro-Optic Amplitude Modulator

EOM: Electro-Optic Modulator

ET: Einstein Telescope

ETM: End Test Mass

ETMX/Y: End Test Mass of X/Y arm

FC: Filter Cavity

FC1: Filter Cavity input mirror

FC2: Filter Cavity end mirror

FCGS: Filter Cavity Green Sensing

FFT: Fast Fourier Transform

FP: Fabry-Pérot Cavity

FSR: Free Spectral Range

GAOM: Acousto-Optic Modulator for green light

GW: Gravitational Wave

GWINC: Gravitational Wave Interferometer Noise Calculator

H1: LIGO Hanford Interferometer

HAM: Horizontal Axis Module, a vacuum chamber hosting LIGO optical system

HAM7: The vacuum chamber hosting squeezer cavity

HAM8: The vacuum chamber hosting filter cavity end mirror

HG: Hermite-Gaussian

HOM: Higher-Order Mode

HR: High-Reflective

HVAC: Heating, Ventilation, and Air Conditioning

Hz: Hertz

IFO: Interferometer

in: Inch

IR: Infrared

ISS: Intensity Stabilization Servo

ITM: Input Test Mass

ITMX/Y: Input Test Mass of X/Y arm

kHz: kilohertz

KLMTV: Paper written by Kimble, Levin, Matsko, Thorne, and Vyatchanin [36]

L1: LIGO Livingston Interferometer

lb: Pound

LG: Laguerre-Gaussian

LHO: LIGO Hanford Observatory, same as H1

LIGO: Laser Interferometer Gravitational Wave Observatory

LLO: LIGO Livingston Observatory, same as L1

LO: Local Oscillator

LSC: Length Sensing and Control

MCMC: Markov Chain Monte Carlo

MHz: Megahertz

MICH: Michelson cavity length

MIT: Massachusetts Institute of Technology

Mpc: Megaparsec

NS: Neutron Star

NULL: The difference channel of two detection photodiodes

O3, O4: Oberving Run 3, 4

OFI: Output Faraday Isolator

OM2: The second mirror before the output mode cleaner

OMC: Output Mode Cleaner

OPA: Optical Parametric Amplifier

OPD: Optical Path Distortion

OPO: Optical Parametric Oscillator

Pcal: Photon Calibrator

PD: Photodiode

PDH: Pound-Drever-Hall locking technique

PLL: Phase-Locking-Loop

PPKTP: Periodically Poled Potassium Titanyl Phosphate, a nonlinear crystal

ppm: parts per million

PRC: Power-Recycling Cavity

PRG: Power-Recycling Gain

PRM: Power-Recycling Mirror

PSAMS: Piezo-deformable optics on Suspended Active Matching Stages

PSD: Power Spectral Density

PSL: Pre-Stabilized Laser

PZT: Piezoelectric Transducer

QND: Quantum non-demolition

QPD: Quadrant Photodiode

QRPN: Quantum Radiation Pressure Noise

rad: Radian

REFL: Reflected light port

RF: Radio Frequency

RIN: Relative Intensity Noise

RLF: Resonant Locking Field

RMS: Root-Mean Square

ROC: Radius of Curvature

rtHz: Square root Hertz

SAMS: Suspended Active Matching Stages

SEC: Signal Extraction Cavity, also known as signal-recycling cavity

SHG: Single Harmonic Generator

SIS: Stationary Interferometer Simulation

SNR: Signal-to-Noise Ratio

SPDC: Spontaneous Parametric Down Conversion

SQL: Standard Quantum Limit

SQZ: Squeezing

SR2: The optic before signal-recycling mirror

SRC: Signal-Recycling Cavity

SRCL: Signal-Recycling Cavity Length

SRM: Signal-Recycling Mirror

SUM: The sum channel of two detection photodiodes

TCS: Thermal Compensation System

TEC: Temperature Control

TEM: Transverse Electromagnetic Mode

TEM00: Fundamental 00 Transverse Electromagnetic Mode

TRANS: Transmission light port

TTFSS: Table Top Frequency Stabilization Servo

UGF: Unity Gain Frequency

VCO: Voltage Controlled Oscillator

VOPO: in-Vacuum Optical Parametric Oscillator

WFS: Wave Front Sensors

XCORR: The cross-correlation of two detection photodiodes

ZM: Relay mirror in the Squeezing path

B USEFUL DIAGRAMS

Here are some useful diagrams related to squeezing system.

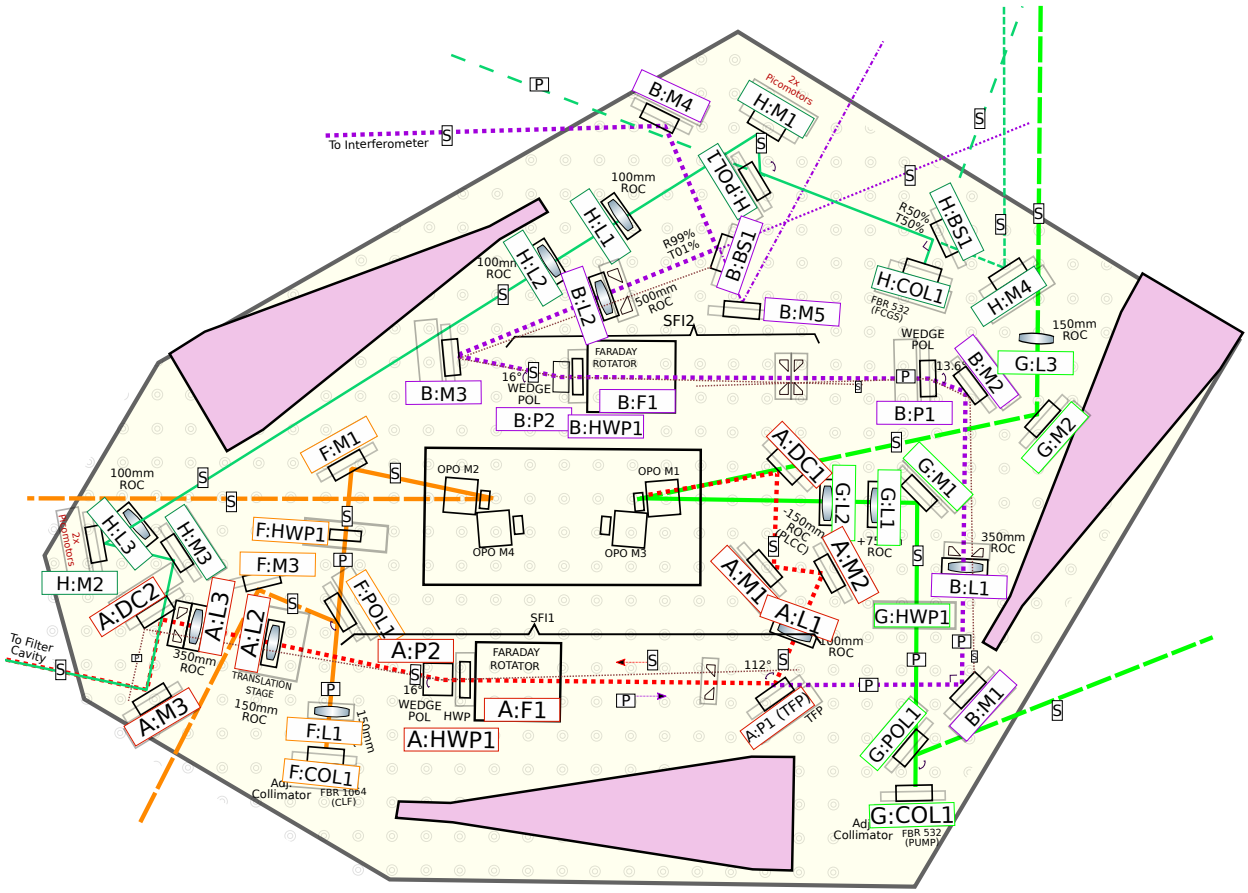

Figure B-1: Optical layout of VOPO platform. All the optical components are labeled [15].

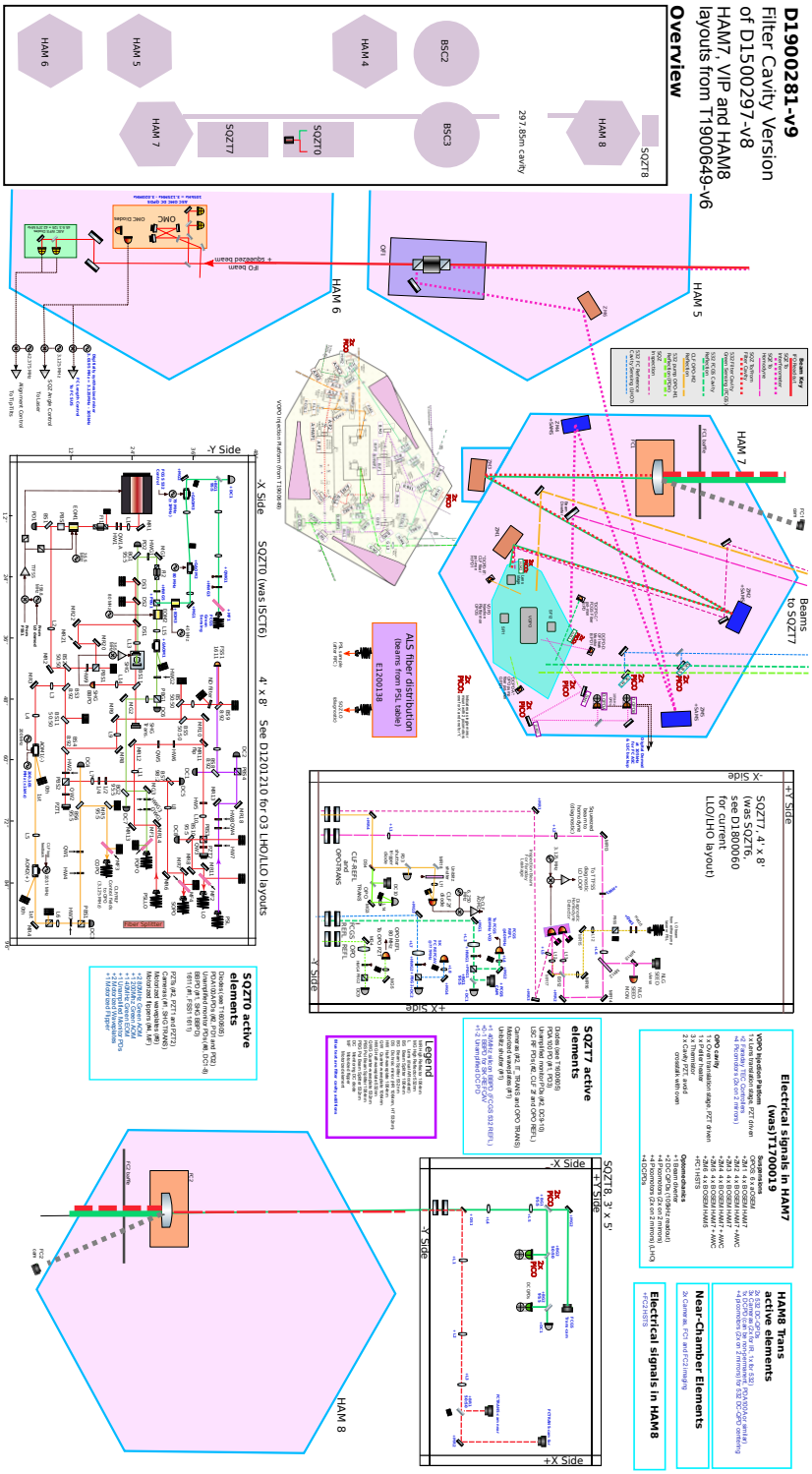

Figure B-2: Overall layout of the entire squeezing subsystem [16].

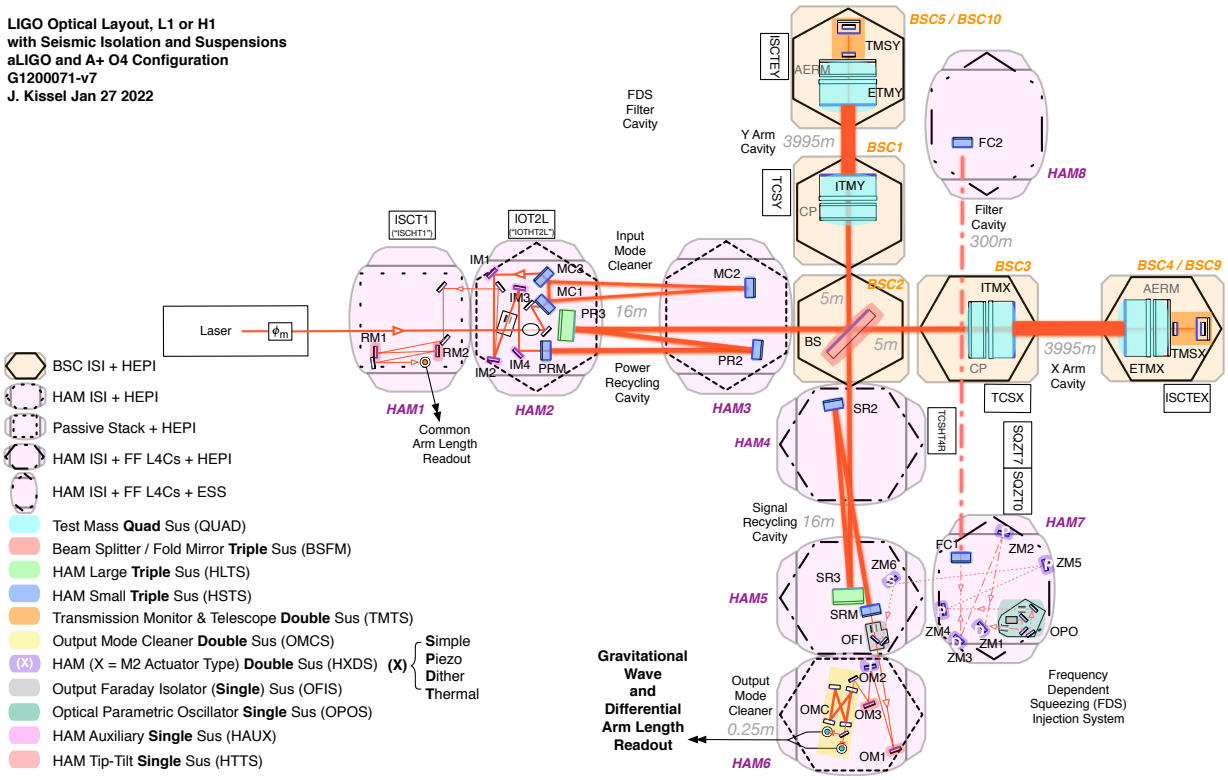

Figure B-3: Optical layout of LIGO with seismic isolation and suspensions labeled. [17]

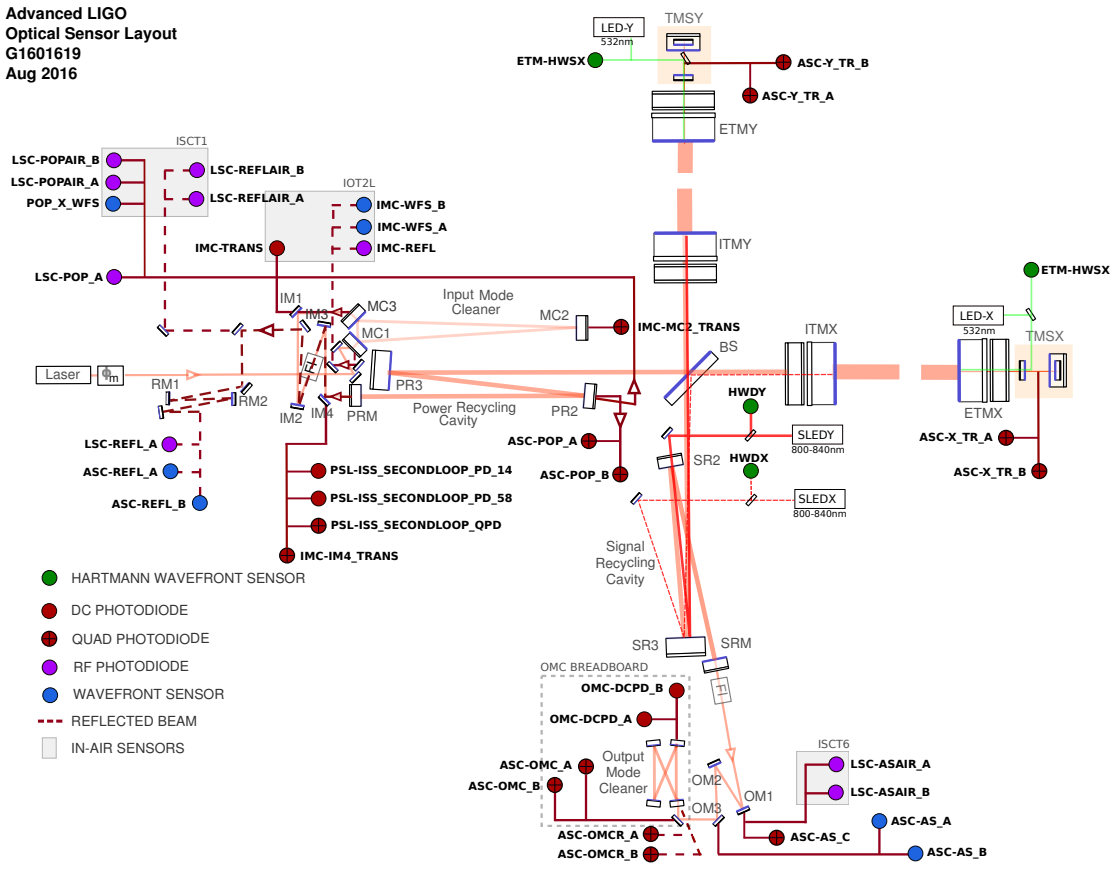

Figure B-4: Layout of optical sensors in LIGO. [18]

Bibliography

[1] W. Jia, V. Xu, K. Kuns, M. Nakano, L. Barsotti, M. Evans, N. Mavalvala, *et al.*, "Squeezing the quantum noise of a gravitational-wave detector below the standard quantum limit," *Science*, (in press), 2024.

[2] E. Capote, W. Jia, N. Aritomi, M. Nakano, V. Xu, *et al.*, "Sensitivity and performance of the Advanced LIGO detectors in the fourth observing run," 2024. (in prep).

[3] D. Ganapathy, W. Jia, M. Nakano, V. Xu, N. Aritomi, T. Cullen, N. Kijbunchoo, S. E. Dwyer, A. Mullavey, L. McCuller, and members of the LIGO O4 Detector Collaboration, "Broadband Quantum Enhancement of the LIGO Detectors with Frequency-Dependent Squeezing," *Phys. Rev. X*, vol. 13, p. 041021, Oct. 2023.

[4] D. Ganapathy, V. Xu, W. Jia, C. Whittle, M. Tse, L. Barsotti, M. Evans, and L. McCuller, "Probing squeezing for gravitational-wave detectors with an audio-band field," *Phys. Rev. D*, vol. 105, p. 122005, Jun 2022.

[5] W. Jia *et al.*, "Point absorber limits to future gravitational-wave detectors," *Phys. Rev. Lett.*, vol. 127, p. 241102, Dec 2021.

[6] L. Barsotti, L. McCuller, M. Evans, and P. Fritschel, "The A+ design curve," *LIGO Document: LIGO-T1800042*, 2018.

[7] D. Griffith, "A+, SUS, HAM Piezo Double Suspension (HPDS, PSAMS, P-SAMS) Assembly," Drawing LIGO-D2000532-v3, CIT, Oct. 2021.

[8] V. Srivastava, G. Mansell, C. Makarem, M. Noh, R. Abbott, S. Ballmer, G. Billingsley, A. Brooks, H. T. Cao, P. Fritschel, D. Griffith, W. Jia, M. Kasprzack, M. MacInnis, S. Ng, L. Sanchez, C. Torrie, P. Veitch, and F. Matichard, "Piezo-deformable mirrors for active mode matching in advanced LIGO," *Opt. Express*, vol. 30, pp. 10491–10501, Mar 2022.

[9] W. Jia, "Noise testing of the Piezo-SAMS - LVK March Meeting," Presentation LIGO-G2100567-v1, MIT, Mar. 2021.

[10] A. Mullavey *et al.*, "VOPO cavity mirror swap." aLIGO LLO Logbook, Apr. 2021. https://alog.ligo-la.caltech.edu/aLOG/index.php?callRep=55506.

[11] L. McCuller, "Coalescing with frequency-dependent squeezing," Presentation LIGO-G2300668-v1, Caltech, Mar. 2023.

[12] W. Jia, "A+ O4 LLO Squeezing LSC Diagram Layout," Drawing LIGO-G2301114-v1, MIT, May 2023.

[13] E. D. Hall, "Cosmic Explorer: A Next-Generation Ground-Based Gravitational-Wave Observatory," *Galaxies*, vol. 10, no. 4, 2022.

[14] W. Jia, "LLO O4 GWINC Quantum Noise Model," Technical report LIGO-T2300439, MIT, Jan. 2024.

[15] L. McCuller, S. Biscans, and L. Barsotti, "Frequency dependent squeezing final optical layout," Technical report LIGO-T1900649-v8, MIT, Dec. 2020.

[16] L. McCuller, L. Barsotti, S. Biscans, P. Fritschel, and D. Sigg, "Overview of Frequency-Dependent Squeezing layout for O4: HAM7, HAM8, SQZT0, SQZT7, SQZT8," Drawing LIGO-D1900281-v9, MIT, Nov. 2020.

[17] J. Kissel, "LIGO Seismic Isolation and Suspensions Cartoon," Drawing LIGO-G1200071-v8, LHO, July 2023.

[18] T. Hardwick and C. Ingram, "aLIGO Optical Sensors Graphic (PSL 1064 nm beam)," Drawing LIGO-G1601619-v2, LSU, July 2018.

[19] M. Nakano *et al.*, "Control loop summary of TTFSS, OPO, and CLF." aLIGO LLO Logbook, July 2022. https://alog.ligo-la.caltech.edu/aLOG/index.php?callRep=60808.

[20] M. Nakano *et al.*, "SQZ finalizing before O4." aLIGO LLO Logbook, May 2023. https://alog.ligo-la.caltech.edu/aLOG/index.php?callRep=65100.

[21] R. A. Hulse and J. H. Taylor, "Discovery of a pulsar in a binary system," *Astrophys. J., Lett., v. 195, no. 2, pp. L51-L53*, 1 1975.

[22] B. P. Abbott *et al.*, "Observation of gravitational waves from a binary black hole merger," *Phys. Rev. Lett.*, vol. 116, p. 061102, Feb 2016.

[23] B. Schutz, "Fundamentals of gravitational radiation," in *A First Course in General Relativity*, p. 202–266, Cambridge University Press, 2022.

[24] A. Einstein, 1916.

[25] A. Einstein, 1918.

[26] R. X. Adhikari, "Gravitational radiation detection with laser interferometry," *Rev. Mod. Phys.*, vol. 86, pp. 121–151, Feb 2014.

[27] R. J. Glauber, "Coherent and incoherent states of the radiation field," *Phys. Rev.*, vol. 131, pp. 2766–2788, Sep 1963.

[28] P. Carruthers and M. M. Nieto, "Coherent States and the Forced Quantum Oscillator," *American Journal of Physics*, vol. 33, pp. 537–544, 07 1965.

[29] E. Schrodinger, "Der stetige Ubergang von der Mikro- zur Makromechanik," *Naturwiss.*, vol. 14, pp. 664–666, 1926.

[30] R. J. Glauber, "Coherent and incoherent states of the radiation field," *Phys. Rev.*, vol. 131, pp. 2766–2788, Sep 1963.

[31] L. Susskind and J. Glogower, "Quantum mechanical phase and time operator," *Physics Physique Fizika*, vol. 1, pp. 49–61, Jul 1964.

[32] C. Gerry and P. Knight, "Nonclassical light," in *Introductory Quantum Optics*, p. 150–194, Cambridge University Press, 2004.

[33] L. McCuller *et al.*, "LIGO's quantum response to squeezed states," *Phys. Rev. D*, vol. 104, p. 062006, Sep 2021.

[34] C. Whittle, K. Komori, D. Ganapathy, L. McCuller, L. Barsotti, N. Mavalvala, and M. Evans, "Optimal detuning for quantum filter cavities," *Phys. Rev. D*, vol. 102, p. 102002, Nov 2020.

[35] P. Kwee, J. Miller, T. Isogai, L. Barsotti, and M. Evans, "Decoherence and degradation of squeezed states in quantum filter cavities," *Phys. Rev. D*, vol. 90, p. 062006, Sep 2014.

[36] H. J. Kimble, Y. Levin, A. B. Matsko, K. S. Thorne, and S. P. Vyatchanin, "Conversion of conventional gravitational-wave interferometers into quantum nondemolition interferometers by modifying their input and/or output optics," *Phys. Rev. D*, vol. 65, p. 022002, Dec 2001.

[37] C. M. Caves and B. L. Schumaker, "New formalism for two-photon quantum optics. I. Quadrature phases and squeezed states," *Phys. Rev. A*, vol. 31, pp. 3068–3092, May 1985.

[38] B. L. Schumaker and C. M. Caves, "New formalism for two-photon quantum optics. II. Mathematical foundation and compact notation," *Phys. Rev. A*, vol. 31, pp. 3093–3111, May 1985.

[39] A. Buonanno and Y. Chen, "Quantum noise in second generation, signal-recycled laser interferometric gravitational-wave detectors," *Phys. Rev. D*, vol. 64, p. 042006, Jul 2001.

[40] K. S. Thorne and R. D. Blandford, *Modern Classical Physics: Optics, Fluids, Plasmas, Elasticity, Relativity, and Statistical Physics*, ch. 6.4, p. 303. Princeton University Press, 2017.

[41] W. B. Davenport and W. L. Root, "Spectral analysis," in *An Introduction to the Theory of Random Signals and Noise*, pp. 87–111, Wiley, 1987.

[42] J. Cripe, N. Aggarwal, R. Lanza, A. Libson, R. Singh, P. Heu, D. Follman, G. D. Cole, N. Mavalvala, and T. Corbitt, "Measurement of quantum back action in the audio band at room temperature," *Nature*, vol. 568, pp. 364–367, Apr. 2019.

[43] N. Aggarwal, T. J. Cullen, J. Cripe, G. D. Cole, R. Lanza, A. Libson, D. Follman, P. Heu, T. Corbitt, and N. Mavalvala, "Room-temperature optomechanical squeezing," *Nat. Phys.*, vol. 16, pp. 784–788, July 2020.

[44] T. P. Purdy, R. W. Peterson, and C. A. Regal, "Observation of radiation pressure shot noise on a macroscopic object," *Science*, vol. 339, no. 6121, pp. 801–804, 2013.

[45] T. P. Purdy, K. E. Grutter, K. Srinivasan, and J. M. Taylor, "Quantum correlations from a room-temperature optomechanical cavity," *Science*, vol. 356, no. 6344, pp. 1265–1268, 2017.

[46] H. Yu, L. McCuller, M. Tse, *et al.*, "Quantum correlations between light and the kilogram-mass mirrors of LIGO," *Nature*, vol. 583, pp. 43–47, July 2020.

[47] F. Acernese *et al.*, "Quantum back-action on kg-scale mirrors - observation of radiation pressure noise in the advanced virgo detector," *Phys. Rev. Lett.*, vol. 125, p. 131101, Sep 2020.

[48] M. Aspelmeyer, T. J. Kippenberg, and F. Marquardt, "Cavity optomechanics," *Rev. Mod. Phys.*, vol. 86, pp. 1391–1452, Dec 2014.

[49] M. Yap *et al.*, "Broadband reduction of quantum radiation pressure noise via squeezed light injection," *Nature Photonics*, vol. 14, pp. 19–23, Oct. 2020.

[50] B. J. Meers, "Recycling in laser-interferometric gravitational-wave detectors," *Phys. Rev. D*, vol. 38, pp. 2317–2326, Oct 1988.

[51] J. Mizuno, K. A. Strain, P. G. Nelson, J. M. Chen, R. Schilling, A. Ruediger, W. Winkler, and K. Danzmann, "Resonant sideband extraction: A New configuration for interferometric gravitational wave detectors," *Phys. Lett. A*, vol. 175, pp. 273–276, 1993.

[52] E. D. Hall *et al.*, "Gravitational-wave physics with Cosmic Explorer: Limits to low-frequency sensitivity," *Phys. Rev. D*, vol. 103, p. 122004, Jun 2021.

[53] D. Ganapathy, L. McCuller, J. G. Rollins, E. D. Hall, L. Barsotti, and M. Evans, "Tuning Advanced LIGO to kilohertz signals from neutron-star collisions," *Phys. Rev. D*, vol. 103, p. 022002, Jan 2021.

[54] T. T. Fricke, N. D. Smith-Lefebvre, R. Abbott, R. Adhikari, K. L. Dooley, M. Evans, P. Fritschel, V. V. Frolov, K. Kawabe, J. S. Kissel, B. J. J. Slagmolen, and S. J. Waldman, "DC readout experiment in Enhanced LIGO," *Classical and Quantum Gravity*, vol. 29, p. 065005, feb 2012.

[55] S. Karki, D. Tuyenbayev, S. Kandhasamy, B. P. Abbott, T. D. Abbott, E. H. Anders, J. Berliner, J. Betzwieser, C. Cahillane, L. Canete, C. Conley, H. P. Daveloza, N. De Lillo, J. R. Gleason, E. Goetz, K. Izumi, J. S. Kissel, G. Mendell, V. Quetschke, M. Rodruck, S. Sachdev, T. Sadecki, P. B. Schwinberg, A. Sottile, M. Wade, A. J. Weinstein, M. West, and R. L. Savage, "The Advanced LIGO photon calibrators," *Review of Scientific Instruments*, vol. 87, no. 11, p. 114503, 2016.

[56] A. D. Viets, M. Wade, A. L. Urban, S. Kandhasamy, J. Betzwieser, D. A. Brown, J. Burguet-Castell, C. Cahillane, E. Goetz, K. Izumi, *et al.*, "Reconstructing the calibrated strain signal in the Advanced LIGO detectors," *Classical and Quantum Gravity*, vol. 35, p. 095015, Apr. 2018.

[57] G. W. Ford, J. T. Lewis, and R. F. O'Connell, "Quantum Langevin equation," *Phys. Rev. A*, vol. 37, pp. 4419–4428, Jun 1988.

[58] The LIGO Scientific Collaboration. https://pypi.org/project/gwinc/.

[59] L. Barsotti, J. Harms, and R. Schnabel, "Squeezed vacuum states of light for gravitational wave detectors," *Reports on Progress in Physics*, vol. 82, p. 016905, dec 2018.

[60] R. Schnabel, "Squeezed states of light and their applications in laser interferometers," *Physics Reports*, vol. 684, pp. 1–51, 2017.

[61] J. Aasi, J. Abadie, B. P. Abbott, R. Abbott, T. D. Abbott, M. R. Abernathy, C. Adams, T. Adams, P. Addesso, R. X. Adhikari, C. Affeldt, O. D. Aguiar, P. Ajith, B. Allen, E. Amador Ceron, D. Amariutei, S. B. Anderson, W. G. Anderson, K. Arai, M. C. Araya, C. Arceneaux, S. Ast, S. M. Aston, D. Atkinson, P. Aufmuth, C. Aulbert, L. Austin, B. E. Aylott, S. Babak, P. T. Baker, S. Ballmer, Y. Bao, J. C. Barayoga, D. Barker, B. Barr, L. Barsotti, M. A. Barton, I. Bartos, R. Bassiri, J. Batch, J. Bauchrowitz, B. Behnke, A. S. Bell, C. Bell, G. Bergmann, J. M. Berliner, A. Bertolini, J. Betzwieser, N. Beveridge, P. T. Beyersdorf, T. Bhadbhade, I. A. Bilenko, G. Billingsley, J. Birch, S. Biscans, E. Black, J. K.

Blackburn, L. Blackburn, D. Blair, B. Bland, O. Bock, and Bodiya, "Enhanced sensitivity of the LIGO gravitational wave detector by using squeezed states of light," *Nature Photonics*, vol. 7, pp. 613–619, Aug. 2013.

[62] M. Tse *et al.*, "Quantum-Enhanced Advanced LIGO Detectors in the Era of Gravitational-Wave Astronomy," *Phys. Rev. Lett.*, vol. 123, p. 231107, Dec 2019.

[63] F. Acernese *et al.*, "Increasing the Astrophysical Reach of the Advanced Virgo Detector via the Application of Squeezed Vacuum States of Light," *Phys. Rev. Lett.*, vol. 123, p. 231108, Dec 2019.

[64] The LIGO Scientific Collaboration, "A gravitational wave observatory operating beyond the quantum shot-noise limit," *Nature Physics*, vol. 7, p. 962, 2011.

[65] J. Lough, E. Schreiber, F. Bergamin, H. Grote, M. Mehmet, H. Vahlbruch, C. Affeldt, M. Brinkmann, A. Bisht, V. Kringel, H. Lück, N. Mukund, S. Nadji, B. Sorazu, K. Strain, M. Weinert, and K. Danzmann, "First Demonstration of 6 dB Quantum Noise Reduction in a Kilometer Scale Gravitational Wave Observatory," *Phys. Rev. Lett.*, vol. 126, p. 041102, Jan 2021.

[66] H. Grote, K. Danzmann, K. L. Dooley, R. Schnabel, J. Slutsky, and H. Vahlbruch, "First long-term application of squeezed states of light in a gravitational-wave observatory," *Phys. Rev. Lett.*, vol. 110, p. 181101, May 2013.

[67] J. Aasi *et al.*, "Advanced LIGO," *Classical and Quantum Gravity*, vol. 32, p. 074001, 2015.

[68] A. Wade *et al.*, "A squeezed light source operated under high vacuum," *Sci. Rep.*, vol. 4, p. 18052, Dec 2015.

[69] E. Oelker, G. Mansell, M. Tse, J. Miller, F. Matichard, L. Barsotti, P. Fritschel, D. E. McClelland, M. Evans, and N. Mavalvala, "Ultra-low phase noise squeezed vacuum source for gravitational wave detectors," *Optica*, vol. 3, pp. 682–685, Jul 2016.

[70] R. W. Boyd, "Chapter 2 - wave-equation description of nonlinear optical interactions," in *Nonlinear Optics (Fourth Edition)* (R. W. Boyd, ed.), pp. 65–135, Academic Press, fourth edition ed., 2020.

[71] S. Dwyer, *Quantum noise reduction using squeezed states in LIGO*. PhD dissertation, Massachusetts Institute of Technology, Department of Physics, 2013.

[72] A. Fernandez-Galiana *et al.*, "A compact actively damped vibration isolation platform for optical experiments in ultra-high vacuum," *arXiv:1901.09666*, 2019.

[73] M. Nakano *et al.*, "Escape efficiency measurement." aLIGO LLO Logbook, July 2022. https://alog.ligo-la.caltech.edu/aLOG/index.php?callRep=60851.

[74] M. Nakano *et al.*, "OPO scan of the green 532nm laser with the swapped PZT." aLIGO LLO Logbook, Apr. 2021. https://alog.ligo-la.caltech.edu/aLOG/index.php?callRep=55530.

[75] H. T. Cao, S. W. S. Ng, M. Noh, A. Brooks, F. Matichard, and P. J. Veitch, "Enhancing the dynamic range of deformable mirrors with compression bias," *Opt. Express*, vol. 28, pp. 38480–38490, Dec 2020.

[76] H. T. Cao, A. Brooks, S. W. S. Ng, D. Ottaway, A. Perreca, J. W. Richardson, A. Chaderjian, and P. J. Veitch, "High dynamic range thermally actuated bimorph mirror for gravitational wave detectors," *Appl. Opt.*, vol. 59, pp. 2784–2790, Mar 2020.

[77] S. S. Y. Chua, S. Dwyer, L. Barsotti, D. Sigg, R. M. S. Schofield, V. V. Frolov, K. Kawabe, M. Evans, G. D. Meadors, M. Factourovich, R. Gustafson, N. Smith-Lefebvre, C. Vorvick, M. Landry, A. Khalaidovski, M. S. Stefszky, C. M. Mow-Lowry, B. C. Buchler, D. A. Shaddock, P. K. Lam, R. Schnabel, N. Mavalvala, and D. E. McClelland, "Impact of backscattered light in a squeezing-enhanced interferometric gravitational-wave detector," *Classical and Quantum Gravity*, vol. 31, p. 035017, Feb. 2014.

[78] L. McCuller *et al.*, "IFO HAM7 backscatter tests." aLIGO LLO Logbook, July 2022. https://alog.ligo-la.caltech.edu/aLOG/index.php?callRep=60897.

[79] E. Genin, M. Mantovani, G. Pillant, C. D. Rossi, L. Pinard, C. Michel, M. Gosselin, and J. Casanueva, "Vacuum-compatible low-loss Faraday isolator for efficient squeezed-light injection in laser-interferometer-based gravitational-wave detectors," *Appl. Opt.*, vol. 57, pp. 9705–9713, Nov 2018.

[80] M. Evans, L. Barsotti, P. Kwee, J. Harms, and H. Miao, "Realistic filter cavities for advanced gravitational wave detectors," *Phys. Rev. D*, vol. 88, p. 022002, Jul 2013.

[81] S. Chelkowski, H. Vahlbruch, B. Hage, A. Franzen, N. Lastzka, K. Danzmann, and R. Schnabel, "Experimental characterization of frequency-dependent squeezed light," *Phys. Rev. A*, vol. 71, p. 013806, Jan 2005.

[82] L. McCuller, C. Whittle, D. Ganapathy, K. Komori, M. Tse, A. Fernandez-Galiana, L. Barsotti, P. Fritschel, M. MacInnis, F. Matichard, K. Mason, N. Mavalvala, R. Mittleman, H. Yu, M. E. Zucker, and M. Evans, "Frequency-Dependent Squeezing for Advanced LIGO," *Phys. Rev. Lett.*, vol. 124, p. 171102, Apr. 2020.

[83] F. Acernese *et al.*, "Frequency-Dependent Squeezed Vacuum Source for the Advanced Virgo Gravitational-Wave Detector," *Phys. Rev. Lett.*, vol. 131, p. 041403, Jul 2023.

[84] Y. Zhao, N. Aritomi, E. Capocasa, M. Leonardi, M. Eisenmann, Y. Guo, E. Polini, A. Tomura, K. Arai, Y. Aso, Y.-C. Huang, R.-K. Lee, H. Lück, O. Miyakawa, P. Prat, A. Shoda, M. Tacca, R. Takahashi, H. Vahlbruch, M. Vardaro, C.-M. Wu, M. Barsuglia, and R. Flaminio, "Frequency-Dependent Squeezed Vacuum Source for Broadband Quantum Noise Reduction in Advanced Gravitational-Wave Detectors," *Phys. Rev. Lett.*, vol. 124, p. 171101, Apr. 2020.

[85] L. McCuller and L. Barsotti, "Design Requirement Document of the A+ filter cavity and relay optics for frequency dependent squeezing," Technical report LIGO-T1800447-v7, MIT, Aug. 2020.

[86] A. Mullavey *et al.*, "HAM7 - Initial VOPO alignment and locking." aLIGO LLO Logbook, Dec. 2021. https://alog.ligo-la.caltech.edu/aLOG/index.php?callRep=58271.

[87] R. W. P. Drever, J. L. Hall, F. V. Kowalski, J. Hough, G. M. Ford, A. J. Munley, and H. Ward, "Laser phase and frequency stabilization using an optical resonator," *Appl. Phys. B*, vol. 31, no. 2, pp. 97–105, 1983.

[88] R. Goetz *et al.*, "Full SFI alignment and SFI2 throughput measurements." aLIGO LLO Logbook, June 2021. https://alog.ligo-la.caltech.edu/aLOG/index.php?callRep=56140.

[89] D. Ganapathy *et al.*, "Let there be light (FC locked)." aLIGO LHO Logbook, Nov. 2022. https://alog.ligo-wa.caltech.edu/aLOG/index.php?callRep=65881.

[90] L. McCuller *et al.*, "Filter cavity stably locked at 532." aLIGO LLO Logbook, Nov. 2022. https://alog.ligo-la.caltech.edu/aLOG/index.php?callRep=62400.

[91] A. Abramovici and J. Chapsky, "Examples," in *Feedback Control Systems: A Fast-Track Guide for Scientists and Engineers*, pp. 35–48, Boston, MA: Springer US, 2000.

[92] P. Kwee, C. Bogan, K. Danzmann, M. Frede, H. Kim, P. King, J. Pöld, O. Puncken, R. L. Savage, F. Seifert, P. Wessels, L. Winkelmann, and B. Willke, "Stabilized high-power laser system for the gravitational wave detector Advanced LIGO," *Opt. Express*, vol. 20, pp. 10617–10634, May 2012.

[93] F. Thies, N. Bode, P. Oppermann, M. Frede, B. Schulz, and B. Willke, "Nd:YVO4 high-power master oscillator power amplifier laser system for second-generation gravitational wave detectors," *Opt. Lett.*, vol. 44, pp. 719–722, Feb 2019.

[94] H. Vahlbruch, S. Chelkowski, B. Hage, A. Franzen, K. Danzmann, and R. Schnabel, "Coherent control of vacuum squeezing in the gravitational-wave detection band," *Phys. Rev. Lett.*, vol. 97, p. 011101, Jul 2006.

[95] S. Chelkowski, H. Vahlbruch, K. Danzmann, and R. Schnabel, "Coherent control of broadband vacuum squeezing," *Physical Review A*, vol. 75, p. 043814, Apr. 2007.

[96] K. Izumi and D. Sigg, "Advanced LIGO: length sensing and control in a dual recycled interferometric gravitational wave antenna," *Classical and Quantum Gravity*, vol. 34, p. 015001, dec 2016.

[97] A. Staley, D. Martynov, R. Abbott, R. X. Adhikari, K. Arai, S. Ballmer, L. Barsotti, A. F. Brooks, R. T. DeRosa, S. Dwyer, A. Effler, M. Evans, P. Fritschel, V. V. Frolov, C. Gray, C. J. Guido, R. Gustafson, M. Heintze, D. Hoak, K. Izumi, K. Kawabe, E. J. King, J. S. Kissel, K. Kokeyama, M. Landry, D. E. McClelland, J. Miller, A. Mullavey, B. O′Reilly, J. G. Rollins, J. R. Sanders, R. M. S. Schofield, D. Sigg, B. J. J. Slagmolen, N. D. Smith-Lefebvre, G. Vajente, R. L. Ward, and C. Wipf, "Achieving resonance in the Advanced LIGO gravitational-wave interferometer," *Classical and Quantum Gravity*, vol. 31, p. 245010, nov 2014.

[98] R. Bork, J. Hanks, D. Barker, J. Betzwieser, J. Rollins, K. Thorne, and E. von Reis, "advligorts: The Advanced LIGO Real-Time Digital Control and Data Acquisition System," 2020.

[99] M. Nakano *et al.*, "Efforts for long-term stability of the squeezing level." aLIGO LLO Logbook, Mar. 2023. https://alog.ligo-la.caltech.edu/aLOG/index.php?callRep=64103.

[100] L. Barsotti, M. Evans, and P. Fritschel, "Alignment sensing and control in advanced LIGO," *Classical and Quantum Gravity*, vol. 27, p. 084026, Apr. 2010.

[101] P. Fritschel, N. Mavalvala, D. Shoemaker, D. Sigg, M. Zucker, and G. González, "Alignment of an interferometric gravitational wave detector," *Appl. Opt.*, vol. 37, pp. 6734–6747, Oct 1998.

[102] E. Schreiber, K. L. Dooley, H. Vahlbruch, C. Affeldt, A. Bisht, J. R. Leong, J. Lough, M. Prijatelj, J. Slutsky, M. Was, H. Wittel, K. Danzmann, and H. Grote, "Alignment sensing and control for squeezed vacuum states of light," *Opt. Express*, vol. 24, pp. 146–152, Jan 2016.

[103] D. Z. Anderson, "Alignment of resonant optical cavities," *Appl. Opt.*, vol. 23, pp. 2944–2949, Sep 1984.

[104] E. Morrison, B. J. Meers, D. I. Robertson, and H. Ward, "Automatic alignment of optical interferometers," *Appl. Opt.*, vol. 33, pp. 5041–5049, Aug 1994.

[105] M. Nakano *et al.*, "FC WFS commissioning." aLIGO LLO Logbook, Jan. 2023. https://alog.ligo-la.caltech.edu/aLOG/index.php?callRep=63269.

[106] M. Nakano *et al.*, "Beam centering loop." aLIGO LLO Logbook, Mar. 2023. https://alog.ligo-la.caltech.edu/aLOG/index.php?callRep=64079.

[107] M. Nakano *et al.*, "Re-re-commissioning of AS42." aLIGO LLO Logbook, Apr. 2023. https://alog.ligo-la.caltech.edu/aLOG/index.php?callRep=64336.

[108] D. V. Martynov *et al.*, "Sensitivity of the Advanced LIGO detectors at the beginning of gravitational wave astronomy," *Phys. Rev. D*, vol. 93, p. 112004, Jun 2016.

[109] B. P. Abbott *et al.*, "GW150914: The Advanced LIGO Detectors in the Era of First Discoveries," *Phys. Rev. Lett.*, vol. 116, p. 131103, Mar 2016.

[110] A. Buikema *et al.*, "Sensitivity and performance of the Advanced LIGO detectors in the third observing run," *Phys. Rev. D*, vol. 102, p. 062003, Sep 2020.

[111] B. P. Abbott *et al.*, "GW170817: Observation of Gravitational Waves from a Binary Neutron Star Inspiral," *Phys. Rev. Lett.*, vol. 119, p. 161101, Oct 2017.

[112] H.-Y. Chen, D. E. Holz, J. Miller, M. Evans, S. Vitale, and J. Creighton, "Distance measures in gravitational-wave astrophysics and cosmology," *Classical and Quantum Gravity*, vol. 38, p. 055010, jan 2021.

[113] P. J. Sutton, "S3 Performance of the LIGO Interferometers as Measured by SenseMonitor," Technical report LIGO-T030276, CIT, Dec. 2003.

[114] K. Somiya, Y. Chen, S. Kawamura, and N. Mio, "Frequency noise and intensity noise of next-generation gravitational-wave detectors with RF/DC readout schemes," *Phys. Rev. D*, vol. 73, p. 122005, Jun 2006.

[115] J. B. Camp, H. Yamamoto, S. E. Whitcomb, and D. E. McClelland, "Analysis of light noise sources in a recycled Michelson interferometer with Fabry-Perot arms," *J. Opt. Soc. Am. A*, vol. 17, pp. 120–128, Jan 2000.

[116] V. Braginsky and S. Vyatchanin, "Thermodynamical fluctuations in optical mirror coatings," *Physics Letters A*, vol. 312, no. 3, pp. 244–255, 2003.

[117] S. Gras and M. Evans, "Direct measurement of coating thermal noise in optical resonators," *Phys. Rev. D*, vol. 98, p. 122001, Dec 2018.

[118] B. P. Abbott *et al.*, "GWTC-1: A Gravitational-Wave Transient Catalog of Compact Binary Mergers Observed by LIGO and Virgo during the First and Second Observing Runs," *Phys. Rev. X*, vol. 9, p. 031040, Sep 2019.

[119] R. Abbott *et al.*, "GWTC-2.1: Deep extended catalog of compact binary coalescences observed by LIGO and Virgo during the first half of the third observing run," *Phys. Rev. D*, vol. 109, p. 022001, Jan 2024.

[120] R. Abbott *et al.*, "GWTC-3: Compact Binary Coalescences Observed by LIGO and Virgo during the Second Part of the Third Observing Run," *Phys. Rev. X*, vol. 13, p. 041039, Dec 2023.

[121] V. B. Braginskiĭ and Y. I. Vorontsov, "Quantum-mechanical limitations in macroscopic experiments and modern experimental technique," *Sov. Phys. Usp.*, vol. 17, p. 644, May 1975.

[122] V. B. Braginsky, Y. I. Vorontsov, and K. S. Thorne, "Quantum Nondemolition Measurements," *Science*, vol. 209, pp. 547–557, Aug. 1980.

[123] V. B. Braginsky and F. Ya. Khalili, "Quantum nondemolition measurements: The route from toys to tools," *Rev. Mod. Phys.*, vol. 68, pp. 1–11, Jan. 1996.

[124] W. G. Unruh, "Quantum non-demolition," in *Gravitational Radiat. Collapsed Objects Exact Solut.* (C. Edwards, ed.), Lecture Notes in Physics, (Berlin, Heidelberg), pp. 385–426, Springer, 1980.

[125] W. G. Unruh, "Readout State Preparation and Quantum Non-Demolition," in *Quantum Optics, Experimental Gravity, and Measurement Theory* (P. Meystre and M. O. Scully, eds.), NATO Advanced Science Institutes Series, pp. 637–645, Boston, MA: Springer US, 1983.

[126] V. B. Braginsky, F. Y. Khalili, and K. S. Thorne, "Quantum nondemolition measurement," in *Quantum Measurement*, p. 50–63, Cambridge University Press, 1992.

[127] E. Oelker, L. Barsotti, S. Dwyer, D. Sigg, and N. Mavalvala, "Squeezed light for advanced gravitational wave detectors and beyond," *Opt. Express*, vol. 22, pp. 21106–21121, Aug 2014.

[128] S. Dwyer *et al.*, "Squeezed quadrature fluctuations in a gravitational wave detector using squeezed light," *Opt. Express*, vol. 21, pp. 19047–19060, Aug 2013.

[129] V. Sudhir, R. Schilling, S. A. Fedorov, H. Schütz, D. J. Wilson, and T. J. Kippenberg, "Quantum correlations of light from a room-temperature mechanical oscillator," *Phys. Rev. X*, vol. 7, p. 031055, Sep 2017.

[130] H. Yu, *Quantum Correlations in Advanced LIGO*. PhD thesis, Massachusetts Institute of Technology, Cambridge MA, 2020.

[131] E. D. Hall, C. Cahillane, K. Izumi, R. J. E. Smith, and R. X. Adhikari, "Systematic calibration error requirements for gravitational-wave detectors via the Cramér–Rao bound," *Classical and Quantum Gravity*, vol. 36, p. 205006, sep 2019.

[132] D. V. Martynov *et al.*, "Quantum correlation measurements in interferometric gravitational-wave detectors," *Phys. Rev. A*, vol. 95, p. 043831, Apr 2017.

[133] M. Tröbs and G. Heinzel, "Improved spectrum estimation from digitized time series on a logarithmic frequency axis," *Measurement*, vol. 39, no. 2, pp. 120–129, 2006.

[134] L. Sun *et al.*, "Characterization of systematic error in Advanced LIGO calibration," *Classical and Quantum Gravity*, vol. 37, p. 225008, oct 2020.

[135] D. Tuyenbayev, S. Karki, J. Betzwieser, C. Cahillane, E. Goetz, K. Izumi, S. Kandhasamy, J. S. Kissel, G. Mendell, M. Wade, A. J. Weinstein, and R. L. Savage, "Improving LIGO calibration accuracy by tracking and compensating for slow temporal variations," *Classical and Quantum Gravity*, vol. 34, p. 015002, Dec. 2016.

[136] W. Jia *et al.*, "Unsqueezed DARM with FC locked on single-side CLFRLF." aLIGO LLO Logbook, May 2023. https://alog.ligo-la.caltech.edu/aLOG/index.php?callRep=64982.

[137] V. Frolov *et al.*, "PRG calibration check." aLIGO LLO Logbook, Feb. 2024. https://alog.ligo-la.caltech.edu/aLOG/index.php?callRep=69558.

[138] C. Whittle, K. Komori, D. Ganapathy, L. McCuller, L. Barsotti, N. Mavalvala, and M. Evans, "Optimal detuning for quantum filter cavities," *Phys. Rev. D*, vol. 102, p. 102002, Nov. 2020.

[139] M. Evans *et al.*, "Cosmic Explorer: Science, Observatories, Community," Tech. Rep. CE–P2100003, Cosmic Explorer, 2021.

[140] M. Punturo *et al.*, "The Einstein Telescope: a third-generation gravitational wave observatory," *Classical and Quantum Gravity*, vol. 27, no. 19, p. 194002, 2010.

[141] A. F. Brooks *et al.*, "Point absorbers in Advanced LIGO," *Appl. Opt.*, vol. 60, pp. 4047–4063, May 2021.

[142] C. J. Hood, H. J. Kimble, and J. Ye, "Characterization of high-finesse mirrors: Loss, phase shifts, and mode structure in an optical cavity," *Phys. Rev. A*, vol. 64, p. 033804, Aug 2001.

[143] H. Liu, B. D. Elwood, M. Evans, and J. Thaler, "Searching for axion dark matter with birefringent cavities," *Phys. Rev. D*, vol. 100, p. 023548, Jul 2019.

[144] J. Majer, J. Chow, J. Gambetta, J. Koch, B. Johnson, J. Schreier, L. Frunzio, D. Schuster, A. Houck, A. Wallraff, A. Blais, M. Devoret, S. Girvin, and R. Schoelkopf, "Coupling superconducting qubits via a cavity bus," *Nature*, vol. 449, pp. 443–7, 10 2007.

[145] The LIGO Scientific Collaboration, "Advanced LIGO," *Classical and Quantum Gravity*, vol. 32, p. 074001, mar 2015.

[146] F. Acernese *et al.*, "Advanced Virgo: a second-generation interferometric gravitational wave detector," *Classical and Quantum Gravity*, vol. 32, p. 024001, dec 2014.

[147] K. Somiya, "Detector configuration of KAGRA–the japanese cryogenic gravitational-wave detector," *Classical and Quantum Gravity*, vol. 29, p. 124007, jun 2012.

[148] C. Zhao, J. Degallaix, L. Ju, Y. Fan, D. G. Blair, B. J. J. Slagmolen, M. B. Gray, C. M. M. Lowry, D. E. McClelland, D. J. Hosken, D. Mudge, A. Brooks, J. Munch, P. J. Veitch, M. A. Barton, and G. Billingsley, "Compensation of strong thermal lensing in high-optical-power cavities," *Phys. Rev. Lett.*, vol. 96, p. 231101, Jun 2006.

[149] C. Blair *et al.*, "First Demonstration of Electrostatic Damping of Parametric Instability at Advanced LIGO," *Phys. Rev. Lett.*, vol. 118, p. 151102, Apr 2017.

[150] M. Evans *et al.*, "Observation of Parametric Instability in Advanced LIGO," *Phys. Rev. Lett.*, vol. 114, p. 161102, Apr 2015.

[151] J. A. Sidles and D. Sigg, "Optical torques in suspended Fabry Perot interferometers," *Physics Letters A*, vol. 354, pp. 167–172, May 2006.

[152] W. Winkler, K. Danzmann, A. Rüdiger, and R. Schilling, "Heating by optical absorption and the performance of interferometric gravitational-wave detectors," *Phys. Rev. A*, vol. 44, pp. 7022–7036, Dec 1991.

[153] E. Hall, "The effect of a point absorber in an arm cavity," *LIGO Document, LIGO-T1900038*, 2019.

[154] P. Hello and J.-Y. Vinet, "Analytical models of thermal aberrations in massive mirrors heated by high power laser beams," *Journal de Physique*, vol. 51, no. 12, pp. 1267–1282, 1990.

[155] P. P. Lu, A. L. Bullington, P. Beyersdorf, S. Traeger, J. Mansell, R. Beausoleil, E. K. Gustafson, R. L. Byer, and M. M. Fejer, "Wavefront distortion of the reflected and diffracted beams produced by the thermoelastic deformation of a diffraction grating heated by a gaussian laser beam," *J. Opt. Soc. Am. A*, vol. 24, pp. 659–668, Mar 2007.

[156] W. R. Mann and F. Wolf, "Heat transfer between solids and gasses under nonlinear boundary conditions," *Quarterly of Applied Mathematics*, vol. 9, no. 2, pp. 163–184, 1951.

[157] W. R. Mann and J. H. Roberts, "On a certain nonlinear integral equation of the Volterra type.," *Pacific Journal of Mathematics*, vol. 1, no. 3, pp. 431 – 445, 1951.

[158] P. Hello and J.-Y. Vinet, "Analytical models of transient thermoelastic deformations of mirrors heated by high power CW laser beams," *Journal De Physique*, vol. 51, pp. 2243–2261, 1990.

[159] E. D. Hall, K. Kuns, J. R. Smith, Y. Bai, C. Wipf, S. Biscans, R. X. Adhikari, K. Arai, S. Ballmer, L. Barsotti, Y. Chen, M. Evans, P. Fritschel, J. Harms, B. Kamai, J. G. Rollins, D. Shoemaker, B. J. J. Slagmolen, R. Weiss, and H. Yamamoto, "Gravitational-wave physics with Cosmic Explorer: Limits to low-frequency sensitivity," *Phys. Rev. D*, vol. 103, p. 122004, Jun 2021.

[160] H. Yamamoto, "SIS (Stationary Interferometer Simulation) manual," *LIGO Document, LIGO-T2000311-v2*, 2020.

[161] A. Brooks *et al.*, "HWS analysis of power-up with ETMY beam on different parts of the optic." aLIGO LLO Logbook, Mar. 2023. https://alog.ligo-la.caltech.edu/aLOG/index.php?callRep=52400.

[162] R. Abbott *et al.*, "Population of Merging Compact Binaries Inferred Using Gravitational Waves through GWTC-3," *Phys. Rev. X*, vol. 13, p. 011048, Mar 2023.

[163] The LIGO Scientific Collaboration, the Virgo Collaboration, and the KAGRA Collaboration, "Tests of General Relativity with GWTC-3," 2021.

[164] B. P. Abbott *et al.*, "GW170817: Measurements of Neutron Star Radii and Equation of State," *Phys. Rev. Lett.*, vol. 121, p. 161101, Oct 2018.

[165] S. S. Chaudhary, A. Toivonen, G. Waratkar, G. Mo, D. Chatterjee, S. Antier, P. Brockill, M. W. Coughlin, R. Essick, S. Ghosh, S. Morisaki, P. Baral, A. Baylor, N. Adhikari, P. Brady, G. C. Davies, T. D. Canton, M. Cavaglia, J. Creighton, S. Choudhary, Y.-K. Chu, P. Clearwater, L. Davis, T. Dent, M. Drago, B. Ewing, P. Godwin, W. Guo, C. Hanna, R. Huxford, I. Harry, E. Katsavounidis, M. Kovalam, A. K. Li, R. Magee, E. Marx, D. Meacher, C. Messick, X. Morice-Atkinson, A. Pace, R. D. Pietri, B. Piotrzkowski, S. Roy, S. Sachdev, L. P. Singer, D. Singh, M. Szczepanczyk, D. Tang, M. Trevor, L. Tsukada, V. Villa-Ortega, L. Wen, and D. Wysocki, "Low-latency gravitational wave alert products and their performance at the time of the fourth LIGO-Virgo-KAGRA observing run," *Proceedings of the National Academy of Sciences*, vol. 121, no. 18, p. e2316474121, 2024.